INVESTIGATION OF THE RELATIONSHIP BETWEEN NEGATIVE THERMAL EXPANSION AND OTHER THERMAL PROPERTIES OF FRAMEWORK OXIDES

by

Catherine Anne Kennedy

Submitted in partial fulfillment of the requirements
for the degree of Doctor of Philosophy

at

Dalhousie University
Halifax, Nova Scotia
March 2005

Your file Votre référence
ISBN: 0-494-00972-1
Our file Notre référence
ISBN: 0-494-00972-1

DALHOUSIE UNIVERSITY

To comply with the Canadian Privacy Act the National Library of Canada has requested that the following pages be removed from this copy of the thesis:

Preliminary Pages

Examiners Signature Page (pii)

Dalhousie Library Copyright Agreement (piii)

Appendices

Copyright Releases (if applicable)

Dedicated to my family and friends

Table of Contents

List of Figures

List of Tables

Abstract

Several framework solids exhibit negative thermal expansion (NTE) over a wide temperature range, *e.g.* ZrW_2O_8 exhibits NTE from 0.3 to 1050 K. Although NTE is observed in other materials, it occurs over much smaller temperature ranges. NTE in ZrW_2O_8 is associated with the low-energy modes corresponding to the correlated vibrations of the $[WO_4]^{2-}$ tetrahedra and their three nearest $[ZrO_6]^{8-}$ octahedra. This involves translation as well as libration, and low-energy optic modes play a central role. Thermal expansion and resistance to heat flow both originate in the anharmonic terms of the lattice dynamics. The influence of NTE in these framework materials on thermal conductivity was investigated by measuring thermal properties (thermal conductivity, κ, from *ca.* 2 to 390 K and heat capacity, C_P, from *ca.* 0.4 to 300 K) of ZrW_2O_8 and $HfMo_2O_8$.

Literature values of the C_P of ZrW_2O_8 showed more disagreement than one might expect. In this research, it was found that the discrepancy could be due to low thermal conductivity of ZrW_2O_8. The C_P of $HfMo_2O_8$ is reported here for the first time. Analysis of C_P reveals low-frequency modes that are not present in the binary oxides. A calculation of C_P of $HfMo_2O_8$ from HfW_2O_8, ZrW_2O_8, and $ZrMo_2O_8$ fits experimental C_P of $HfMo_2O_8$ better since each AB_2O_8 compound exhibits NTE and therefore has the low-frequency modes attributed to NTE. The thermodynamic calculations of the production of ZrW_2O_8 and $HfMo_2O_8$ from the appropriate oxides confirm that both are thermodynamically unstable with respect to the oxides.

The κ values of both ZrW_2O_8 and $HfMo_2O_8$ are exceptionally low: $\kappa_{dense}(ZrW_2O_8)$ is 0.91 W m^{-1} K^{-1} and $\kappa_{dense}(HfMo_2O_8)$ is 0.64 W m^{-1} K^{-1} at T = 300 K. Temperature-dependent κ values of ZrW_2O_8 and $HfMo_2O_8$ are glass-like, despite polycrystalline morphology. Through consideration of the C_P, phonon mean free path, and Grüneisen parameter, the κ behavior is attributed to the low-frequency modes which are also responsible for NTE. It is possible that other NTE framework oxides similar to those studied here will also exhibit this low, glass-like κ, hence low-frequency modes in materials could provide a basis for design of new materials with low κ.

List of Abbreviations and Symbols Used

A	cross-sectional area
α	thermal expansion coefficient (units = K^{-1})
α_V	volume thermal expansion coefficient
α_l	linear thermal expansion coefficient
$\alpha_{a,\ b,or\ c}$	thermal expansion coefficient for unit cell dimension a, b, or c
α_{ij}	thermal expansion tensor
B_T	bulk modulus (units = Pa)
C	heat capacity per unit volume (units = J K^{-1} m^{-3})
C_P	constant pressure heat capacity (units = J K^{-1} mol^{-1})
$C_{P,pl}$	heat capacity of platform, grease, and sample (if present)
$C_{P,s}$	heat capacity of sample
C_V	constant volume heat capacity
$C_{V,D}$	Debye heat capacity
$C_{V,E}$	Einstein heat capacity
C_σ	heat capacity at constant stress
C_ε	heat capacity at constant strain
c_{ijkl}^T	isothermal elastic constant tensor
χ_T	isothermal compressibility (units = Pa^{-1})
D	thermal diffusivity (units = m^2 s^{-1}) or Debye mode contribution to DOS
E	Einstein mode contribution to DOS
E_Y	Young's modulus
e	thermal effusivity (units = W s m^{-2} K^{-1})
ε	surface emissivity
ϕ	porosity
G	Gibbs energy (units = J K^{-1}) or shear modulus (units = Pa)
$\Delta_{prod}G$	Gibbs energy of production

$\vec{G}$	wavevector of momentum transfer on a lattice
$g(v)$	density of states
γ_i	Grüneisen Parameter in terms of vibrational mode *i*
γ_T	average Grüneisen Parameter from thermodynamic data
h	Planck's constant = 6.626 0693(11) × 10^{-34} J s
$\hbar$	= $h/2\pi$ = 1.054 571 68(18) × 10^{-34} J s
H	enthalpy (units =J mol^{-1})
$\Delta_{trs}H$	enthalpy of transition
$\Delta_{prod}H$	enthalpy of production
I	current
J_U	thermal energy flux (units = W m^{-2})
$J_{phonons}$	thermal energy flux of phonons
K	thermal conductance (units = W K^{-1})
K_g	thermal conductance of grease
K_w	thermal conductance of wires
k_B	Boltzmann constant = 1.380 6505(24) × 10^{-23} J K^{-1}
$\bar{k}$	wavevector
κ	thermal conductivity (units = W m^{-1} K^{-1})
κ_{min}	minimum thermal conductivity
λ	phonon mean free path (units = m)
M	metal atom
N_A	Avogadro's constant = 6.022 1415(10) x 10^{23} mol^{-1}
n	number of atoms per unit volume (units = m^{-3})
$n(T)$	concentration of phonons at a given temperature
ν	vibrational frequency
ν_D	Debye frequency
ν_E	Einstein frequency
ν_i	frequency per phonon branch
p	number of atoms in the primitive cell
$P_{average}$	average power supplied by DSC furnace

$P(t)$	heater power supplied by PPMS
P_{rad}	radiative heat loss
p_i	number of phonon modes per frequency branch i
ρ	density
$\dot{q}$	applied power
q	heat pulse
$\vec{Q}$	wavevector transfer
θ	characteristic temperature
θ_D	Debye temperature
θ_D^e	effective Debye temperature
θ_E	Einstein temperature
R	rectangular shaped mode contribution to DOS
r	distance between two atoms
S_A	surface area
$\Delta_{trs}S$	entropy of transition
σ	electrical conductivity (units = Ω^{-1} m^{-1})
σ_T	Stefan-Boltzmann constant = 5.670 400(40) x 10^{-8} W m^{-2} K^{-4}
R	resistance or ideal gas constant = 8.314 472(15) J mol^{-1} K^{-1}
t	time
T_g	glass transition temperature
T_b	heat sink temperature
$T_{pl}(t)$	temperature of platform, grease, and sample (if present)
$T_s(t)$	temperature of sample
T_{trs}	transition temperature
T_{sample}	temperature of DSC sample furnace
$T_{\text{reference}}$	temperature of DSC reference furnace
T_i	initial temperature during DSC or adiabatic calorimetry C_P measurement
T_f	final temperature during DSC or adiabatic calorimetry C_P measurement
ΔT_∞	asymptotic temperature differential
τ	time constant

U	internal energy
V	voltage or volume
V_m	molar volume (units = m^3 mol^{-1})
$V(x)$	interatomic potential energy
v	speed of sound
v_i	polarization of speed of sound
v_m	average phonon velocity or speed of sound
v_l	longitudinal speed of sound
v_t	transverse speed of sound
x_d	distance of atoms from their equilibrium distance at absolute zero
Z	number of formula units per unit cell
ASTM	American Society for Testing and Materials
CTE	coefficient of thermal expansion
DOS	density of states
DSC	differential scanning calorimetry
FM	formula mass
IR	infrared
ITS-90	International Temperature Scale of 1990
NIST	National Institute of Standards and Technology
RM	reference material
RR	resistance ratio
RUM	Rigid Unit Mode
NTE	negative thermal expansion
PDOS	phonon density of states
PLT-2000	Provisional Low Temperature Scale of 2000
PPMS	Physical Properties Measurements System
QD	Quantum Design
TTO	thermal transport option
XAFS	x-ray absorption fine structure

Acknowledgements

I would like to thank my supervisor Prof. Mary Anne White for the support and guidance she has provided throughout my PhD studies. Her patience and dedication to her graduate and undergraduate students has been an inspiration to me.

I would like to thank Prof. A.P. Wilkinson of the Georgia Institute of Technology for the $HfMo_2O_8$ sample. I would like to thank Prof. J. Boerio-Goates of Brigham Young University for the MoO_3 heat capacity data, and Prof. M. Sorai of Osaka University, and Prof. Y. Yamamura of the Japan Advanced Institute of Science and Technology for the HfW_2O_8 heat capacity data.

Thanks to Prof. Jeff Dahn in the Physics Department for the use of his lab equipment and to his students, especially Dr. Zhaohui Chen and Dr. Mark Obrovac, for their help in using the equipment. I would also like to thank Andy George in the Physics Department for use of the high temperature, high vacuum equipment.

I would also like to thank the past and present members of the MAW lab group for their support and for being such great people with whom I had the pleasure of sharing a lab. They are Dr. Liyan Qui, Dr. Bi-Zeng Zhan, Dr. Robert Marriott, John Neima, Mike Jakubinek, Dr. Doug MacLaren, Dr. Gerry MacKay, Hamid Rafiee, Maria Stancescu, and Rong Sun. A special thanks to Patricia Laws, also a former lab member, for reading my thesis and for the helpful comments and encouragement she has provided.

I would like to thank the Department of Chemistry and the support staff members who helped with technical details during my time in the Department of Chemistry: Brian Millier, Rick Conrad, Mike Boutilier, Ross Shortt, and Juergen Mueller.

Last but not least I would like to thank my family, friends, and all the folks from Catalone for their encouragement throughout my educational journey. Special thanks to Aaron for support and encouragement in these final months of writing.

Chapter 1. Thermal Properties of Solids: Theory

1.1. Motivation for Project

Understanding of the thermal properties of a material is of fundamental importance in that this knowledge can lead to better understanding of the theories in chemistry, physics, and engineering, can help uncover links between structure and properties, and can help provide insight into applications of the material. The thermal properties of materials discussed in this thesis consist mainly of heat capacity, thermal expansion, thermal conductivity, and various related properties.

There have been devastating reminders in the past as to the importance of thermal properties of materials. One example is the Space Shuttle Challenger accident on January 28, 1986 when all seven crewmembers lost their lives. As outlined in the Report of the Presidential Commission on the Space Shuttle Challenger, commonly known as the Roger's Commission report, one of the contributing factors to the explosion was "...the failure of the pressure seal in the aft field joint of the right Solid Rocket Motor...due to a faulty design unacceptably sensitive to a number of factors...the effects of temperature, physical dimensions, the character of materials, the effects of reusability, processing, and the reaction of the joint to dynamic loading".[1] To put it in simple terms, at the cold temperatures experienced during the launch that day, the thermo-mechanical properties of the o-ring were such that it would not seal as well as if the weather had been warmer.

This dramatic example illustrates how further knowledge of thermal properties of materials could help prevent mechanical failure, and the characterization of thermal properties is important for many other applications. Studying thermal properties also can

shed light on the structure and dynamics of materials. In this thesis, I use the study of the thermal properties of materials as a means to better understand how the property of shrinking on heating, as in the case of zirconium tungstate, instead of expanding per usual, is linked to thermal conductivity.

The purpose of this Chapter is to give an introduction to the theory of thermal properties of non-metallic solids. Chapter 2 will introduce the methods and procedures used in the measurement of thermal properties. The experimental methods and procedures for each system are discussed in more detail in the subsequent chapters. A significant part of this project was to measure heat capacities as a function of temperature and two different calorimeters were used to do so. In Chapter 2, the results of measurement of standard calorimetry materials are given. In Chapter 3 and Chapter 4, the thermal properties of zirconium tungstate (ZrW_2O_8) and hafnium molybdate ($HfMo_2O_8$), are discussed respectively. Chapter 5 consists of final conclusions and future consideration for related studies.

1.2. Heat Conduction in Non-Metallic Solids: Phonons

In insulating solids, heat is carried by vibrations of the atoms in the lattice. In metallic solids, electrons also carry the heat. In this project, only non-metallic materials are considered, so the concept of phonons is very important. Consider a material at $T = 0$ K; the atoms in a lattice are fluctuating around their equilibrium positions (due to zero-point energy). As the temperature is raised, the atoms will gain thermal energy and the fluctuations of the atoms increase. The more thermal energy a lattice possesses, the more the atoms on the lattice will vibrate. These vibrations pass through the lattice by "lattice

waves" also known as "phonons". A phonon is a quantum unit of crystal wave energy. Phonons will travel at the speed of sound that is characteristic of the material. Heat conduction and phonons are related and will be discussed in more detail in later sections.

1.3. Heat Capacity of Solids

1.3.1. Introduction

Heat capacity is the amount of energy needed to raise a unit of mass of material by a unit of temperature. When the temperature of a material is raised, the result is that the internal energy of that material will be raised. However, the amount by which the temperature increases depends on the conditions under which the material is being influenced. Under constant volume conditions, the heat capacity is defined as

$$C_V = \left(\frac{\partial U}{\partial T}\right)_T \qquad 1.1$$

where U is the internal energy of the material. At constant pressure, the heat capacity is defined as

$$C_P = \left(\frac{\partial H}{\partial T}\right)_P \qquad 1.2$$

where H is the enthalpy. C_V is fundamentally the more useful quantity for predicting or modeling heat capacity since theoretical models are generally more concerned with the calculation of internal energy, which is directly related to C_V. However, C_P is more practical to experimentally measure since it is easier to maintain processes at constant pressure than at constant volume.[2]

Enthalpy is related to internal energy through the following relationship

$$H = U + PV \tag{1.3}$$

where P is the pressure in the system and V is the volume. C_P differs from C_V by the work needed to change the volume of the system to maintain constant pressure as follows (for a cubic solid or an isotropic liquid or gas):[3]

$$C_P - C_V = \frac{\alpha_V^2 TV}{\chi_T} \tag{1.4}$$

where the volume coefficient of thermal expansion constant is $\alpha_V = V^{-1}(\partial V/\partial T)_P$ and the isothermal compressibility is $\chi_T = -V^{-1}(\partial V/\partial P)_T$. The reciprocal of χ_T is the bulk modulus, $B_T = \chi_T^{-1}$. For pressures up to about 1 GPa, χ_T and B_T of a solid can be approximated as constant.[4]

The conversion of C_P to C_V is much more complicated for anisotropic solids and requires knowledge of the thermal expansion tensors and the elastic constants of the material.[5] For an anisotropic crystal, C_P and C_V are related to the heat capacities at constant stress, C_σ, and constant strain, C_ε. The condition of constant stress can mean constant pressure, so $C_P = C_\sigma$, and therefore[6]

$$C_P - C_V \cong C_P - C_\varepsilon = C_\sigma - C_\varepsilon = VT\left(c_{ijkl}^T \alpha_{ij} \alpha_{kl}\right). \tag{1.5}$$

where c_{ijkl}^T is the isothermal elastic constant tensor and α_{ij} is the thermal expansion tensor. Equation 1.5 depends on the symmetry of the crystal under consideration.

If the temperature dependent thermal expansion data and compressibility data are not available, the Nernst-Lindemann empirical relationship[7]

$$C_P - C_V = AC_P^2T \qquad 1.6$$

can be used to find the temperature dependence of (C_P - C_V) given that $A = V\alpha_V^2 / C_P^2\chi_T$ is assumed to be temperature independent.[8] If A is calculated from V, B_T, α_l at one temperature, it can be used to calculate (C_P - C_V) over a wide range of temperature without serious error.[9]

1.3.2. Theoretical Models for Heat Capacity

1.3.2.1. Early Models

Dulong and Petit suggested one of the earliest generalization concerning heat capacity in 1819.[10] They explained that for many insulating solids at room temperature, the experimental heat capacity was approximately 25 J K^{-1} mol^{-1} or $3R$ where R is the ideal gas constant. The Dulong-Petit value of $3R$ is approached for many simple monatomic crystals as the temperature is increased.[11]

The Dulong-Petit Law can be understood through the theory of equipartition of energy developed by Boltzmann.[9] To know an atom's position, three coordinate positions must be specified. Therefore, a molecule with p atoms has $3p$ degrees of freedom. A polyatomic molecule's motion can be described in terms of three types of motion; vibrational, rotational, and translational. The principle of equipartition states that each rotational and translational degree of freedom contributes $\frac{1}{2}k_BT$ to the internal energy, U, where k_B is the Boltzmann constant. Vibrational motions contribute $2\times\frac{1}{2}k_BT$ to U since these motions have both kinetic and potential energy.

In a solid, each atom contributes three degrees of freedom that correspond to

vibrational motions of the atoms in the lattice. Therefore, per atom, $U = 3\times2\times\frac{1}{2}k_BT$, and from Equation 1.1, $C_V = 3k_B$ in a solid. Since $k_B\times N_A = R$, where N_A is Avogadro's number, on a molar basis, $C_V = 3R$.

Dulong and Petit's Law was further extended when it was discovered that the molar heat capacity of a compound is often nearly equal to the sum of the heat capacity of the constituent atoms. This is referred to as the Newmann-Kopp Law. It can be used to describe simple solids such as binary compounds and alloys.[9] Deviations will occur for the majority of systems in which the chemical properties (*i.e.* bonding environment) and the physical properties (*i.e.* lattice dynamics) change upon compound formation.

1.3.2.2. Einstein Model

The Dulong and Petit Law failed to describe the decrease in C_P as temperature goes below room temperature. This was solved almost 100 years later by Einstein when he considered heat capacity by applying quantum theory to the thermal vibrations of atoms in solid.[12]

The heat capacity of a crystal can be determined from the amount of energy that is stored in the vibrations of the atoms in the lattice. Consider a crystalline material. The crystal would consist of atoms held at their lattice sites by interatomic forces. Oscillations or vibrations in the lattice would cause the atoms to be displaced from their respective positions. There are $3p$ normal vibrational modes in a crystal, where p is the number of atoms in the primitive cell. These modes are described by phonons.

The heat capacity of a crystal is the sum of all C_i, the contributions of each vibrational mode i to the heat capacity. The heat capacity of all lattice vibrations in the

crystal, C_{vib}, is related to the spectrum of frequencies or phonon density of states, $g(\nu)$ $\left[\int_0^\infty g(\nu)d\nu = 1\right]$ in the following manner:

$$C_{vib} = 3pN_A k_B \int_0^\infty \frac{x^2 e^x}{(e^x - 1)^2} g(\nu)d\nu \qquad 1.7$$

where $x = h\nu/k_B T$ and h is Planck's constant.

The phonon density of states of a crystal can be very complicated. Einstein's model treats solids as a collection of independent three-dimensional harmonic oscillators which vibrate at a single frequency given by the Einstein frequency, ν_E. Therefore, in this model $g(\nu)d\nu = 0$ for $\nu \neq \nu_E$, and $g(\nu)d\nu = 1$ for $\nu = \nu_E$. The Einstein heat capacity function is:[12]

$$C_{V,E} = 3R\left(\frac{\theta_E}{T}\right)^2 \frac{e^{\theta_E/T}}{\left(e^{\theta_E/T} - 1\right)^2} \qquad 1.8$$

where the vibrational temperature, $\theta_E = h\nu/k_B$, is referred to as the Einstein temperature.

The Einstein function agrees well for the temperature dependence of the heat capacity in the high temperature region; as T is increased above θ_E, C_V approaches the Dulong-Petit value for a monatomic solid ($C_V \approx 3R$).[10] The Einstein function also agrees with the observation that C_V approaches 0 J K^{-1} mol^{-1} as $T \rightarrow 0$ K, but at low temperatures the values tend to be lower than the experimental values.

1.3.2.3. Debye Model

Debye[13] devised a heat capacity model that more correctly predicted the low temperature experimental heat capacity values, *i.e.* that the heat capacity approaches $C_V =$

0 J K^{-1} mol^{-1} with a limiting value proportional to T^3.[11,14] He takes into account the fact that atoms (or molecules) in a solid vibrate with a distribution of frequencies instead of oscillating at a single frequency. Debye suggested that the frequency distribution be approximated by $g_D(\nu) = a\nu^2$ up to a cut-off frequency of $\nu = \nu_D$ above which $g(\nu) = 0$. In this equation, $a = 9p/\nu_D^3$ is a proportionality constant dependent on the material, and $g_D(\nu)$ is defined so that $g_D(\nu)d\nu$ is the number of frequencies between ν and $\nu + d\nu$.

The Debye heat capacity is:[13]

$$C_{V,D} = 9R\left(\frac{T}{\theta_D}\right)^3 \int_0^{\theta_D/T} \frac{x^4 e^x}{\left(e^x - 1\right)^2} dx \qquad 1.9$$

where $\theta_D = h\nu_D/k_B$ is the Debye temperature and $x = h\nu/k_BT$.

In the limit as T $\rightarrow$ 0, the Debye equation becomes:

$$C_V = \frac{12}{5}\pi^4 N_A k_B \left(\frac{T}{\theta_D}\right)^3 \qquad 1.10$$

i.e. $C_V \propto T^3$ for $T < \theta_D/100$ for nonmetals. This is referred to as the Debye-T^3 law.

The density of states distribution given by the Debye function is more like that of an actual simple crystal than the Einstein function, as shown in Figure 1.1 (when compared to solid argon).[15] The vibrational density of states will vary from crystal to crystal. However, the Debye model shows the same characteristics for many simple crystalline solids and approaches T = 0 K as a function of T^3, in agreement with experimental heat capacities. The heat capacities given by the Einstein and Debye models are shown in Figure 1.2.

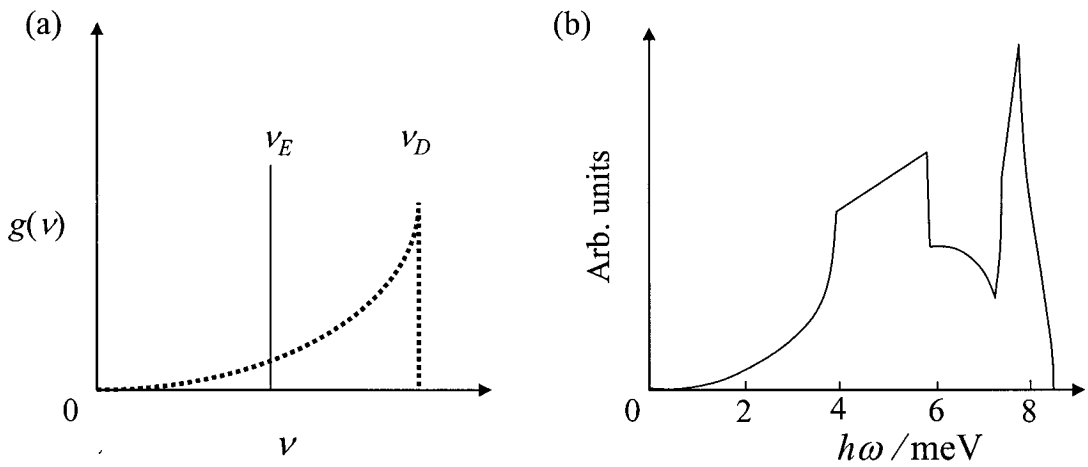

Figure 1.1. Frequency distributions. (a) Distribution of frequencies given by Debye, ν_D (---) and Einstein, ν_E (—) and (b) phonon density of states of argon, restyled from reference 15.

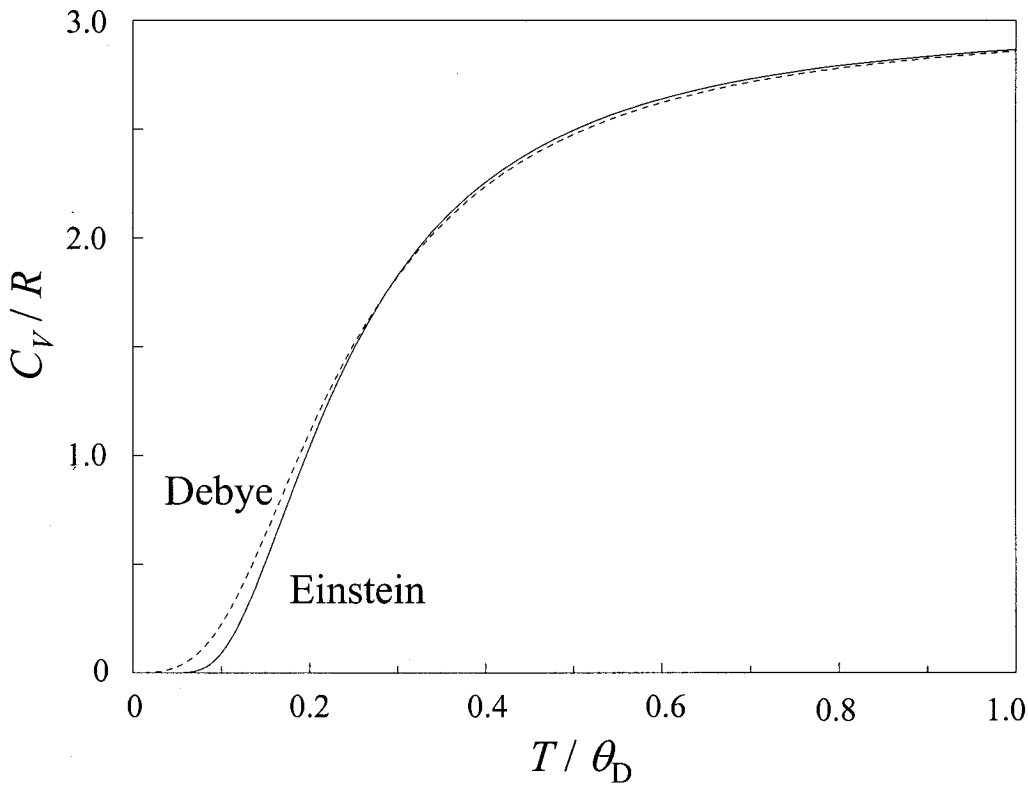

Figure 1.2. The Einstein and Debye heat capacity functions for monatomic solids.

1.3.3. Calculation of Heat Capacity using Spectroscopic Methods

In principle, the heat capacity of a material can be calculated if the complete phonon dispersion curve of the material is known. Infrared and Raman spectroscopies can be used to obtain the phonon frequencies and inelastic neutron scattering can be used to measure the phonon density of states, PDOS, of a material.

1.3.3.1. Inelastic Neutron Scattering

Neutrons provide an ideal probe of lattice dynamics, and in principle, neutron scattering is the only available technique for measuring phonon dispersion curves across the whole Brillouin zone.[16] Neutrons are scattered from matter with a change in the wavevector, $\vec{Q}$, called the scattering vector or wavevector transfer, and a change in the energy, $\hbar\omega$, called the energy transfer.

In elastic scattering, the energy transfer is zero. Elastic neutron scattering can be used for diffraction purposes as a complement to x-ray diffraction.

In inelastic scattering, the energy transfer has a non-zero value and involves the interaction between the neutron and one or more phonon. The neutron either absorbs the phonon and is scattered with a gain in energy, or it creates a phonon and is scattered with a loss in energy. The phonon density of state spectrum of a crystal is measured using inelastic neutron scattering. The PDOS gives the distribution of frequencies for the entire unit cell.

1.3.3.2. IR and Raman Spectroscopy

Infrared and Raman spectroscopies provide methods of measuring phonon frequencies that are complementary to neutron scattering. Photons do not interact with phonons in the same manner that neutrons do. As a result, photons will only be scattered or absorbed by phonons with very long wavelengths.[16]

In infrared spectroscopy, photons can be absorbed to create phonons of the same frequency and wavevector. This technique involves shining a polychromatic beam of radiation on the sample and measuring the frequencies at which absorption occurs, typically in the infrared region of the electromagnetic spectrum, hence the name. The long-wavelength infrared photon from the light source will cause a local dielectric polarization of the crystal which will oscillate in time. No absorption of the photons will occur if the crystal cannot respond to this forced vibration. However, if the photon radiation frequency is the same as the phonon frequency, the crystal will respond to this forced vibration through a change in the local dipole moment, and the photon will be absorbed. In infrared spectroscopy, unlike neutron scattering, absorption only occurs for the set of normal modes (infrared active modes) that change the dipole moment of the system. The set of infrared active modes for a crystal can be determined from group theory.

In Raman scattering, as in neutron scattering, photons can be scattered with either absorption or creation of phonons. In this type of spectroscopy, monochromatic light in the visible region of the electromagnetic spectrum is used and photons are scattered by the sample with a change in frequency. Raman active modes are those that change the polarizability of the system.

1.3.3.3. Relationship to C_V

The motion of atoms in a lattice can be described by the dispersion relationship, which gives the distribution of wavevectors as a function of frequencies of the allowable vibrations. A solid containing p atoms per unit cell will have $3p$ modes, or dispersion branches. In three of these $3p$ branches the atoms move together as in ordinary sound vibrations, hence these are called acoustic branches. Acoustic modes have a strong dispersion and large frequency range from $\omega = 0$ to some cut-off frequency. Acoustic branches are known as such because the dispersion relation at small wavevector, given by $\vec{k}$, is of the form $\omega = v \times \vec{k}$ which is characteristic of sound waves, where v is the speed of sound.[17] Another characteristic of acoustic branches is that $\omega(\vec{k})$ is zero when $\vec{k}$ is zero.

An acoustic mode is one in which all ions in a unit cell move in phase as a unit and the dynamics are dominated by the interaction between cells.[17] The acoustic branches can be further classified into longitudinal and transverse branches where there is one longitudinal mode for every two transverse modes. Figure 1.3 schematically shows the motions for acoustic vibrations in monatomic crystal. Figure 1.4(a) shows in-phase acoustic modes for a diatomic crystal.

The remainder of the branches, $3p$ - 3, are known as optical branches. Optic modes can interact with light and have a smaller dispersion of frequencies.[17] The optic mode shown in Figure 1.4(b) shows motion for the two different types of atoms with an oscillating dipole.[18]

Acoustic modes are vibrations due to movement of the entire unit cell which manifest as an array of frequencies; therefore the Debye heat capacity equation better

describes acoustic modes. Optic modes are motions due to internal vibrations which would manifest at more discrete frequencies hence they are modelled well by the Einstein heat capacity equation.[14]

To use experimental C_P data in a theoretical analysis in terms of solid-state dynamics, density of states, or decomposition into component vibrational contributions using the Debye or Einstein heat capacity modes, C_P must be converted to C_V using Equations 1.4, 1.5 or 1.6 depending on the available information. The heat capacity can be calculated using Einstein and Debye heat capacity models for the optical and acoustic modes, respectively. IR and Raman spectroscopy are used to obtain frequencies of optic modes while the acoustic modes are modeled by the Debye temperature obtained from experiments. For each optic mode, the number of phonon modes per branch of frequency, p_i, can be evaluated from the PDOS spectrum. There are different methods in which this assignment can be made. These will be discussed further in Chapter 3.

The Einstein heat capacity contribution as a function of temperature, $C_E(T)$, can be calculated using the following set of equations:

$$C_E(T) = \sum_i \frac{p_i C_i}{Z}, \; C_i(T) = N_A k_B \frac{(x_i)^2 e^{x_i}}{\left(e^{x_i} - 1\right)^2}, \; x_i = \frac{h\nu_i}{k_B T} \qquad 1.11$$

where ν_i is the frequency of each phonon mode and Z is the number of formula units per unit cell.

The Debye heat capacity as a function of temperature, $C_D(T)$ can be calculated using Equation 1.9 and the characteristic Debye temperature and dividing this by Z. The total calculated heat capacity is $C_V(T) = C_E(T) + C_D(T)$.

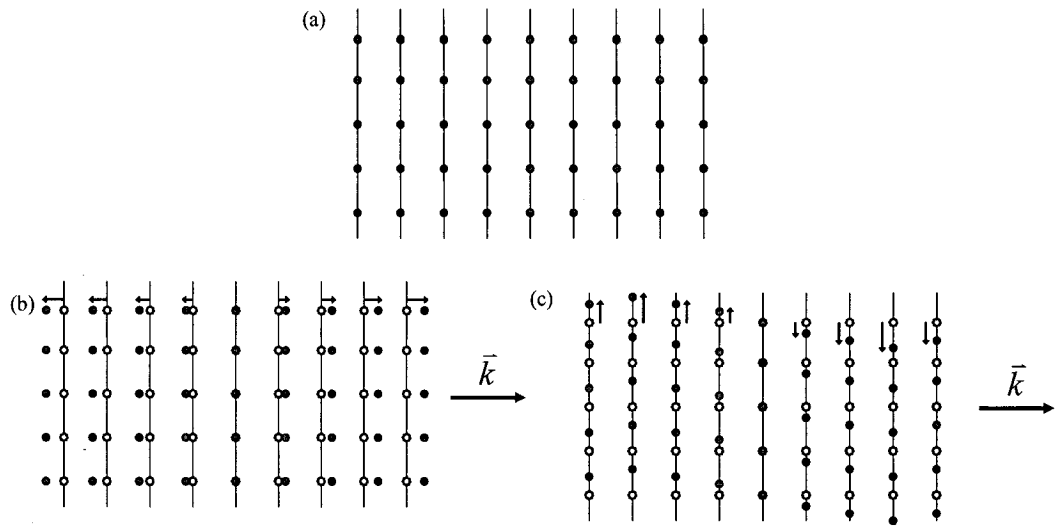

Figure 1.3. Planes of atoms in a monatomic two-dimensional lattice (a) at equilibrium, (b) as displaced during the passage of a longitudinal wave, and (c) as displaced during passage of a transverse wave.

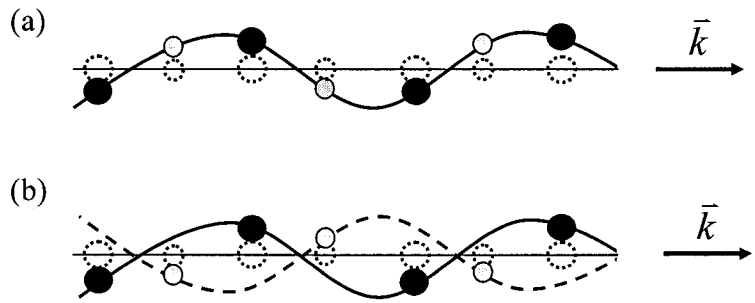

Figure 1.4. A schematic of transverse atomic motions (near the zone boundary) in a one-dimensional diatomic crystal for (a) an acoustic mode and (b) an optical mode. Equilibrium positions shown as dotted-lined circles. Adapted from reference (18).

1.4. Anharmonic Crystal Interactions

1.4.1. Introduction

When atoms in a crystal lattice gain thermal energy, they vibrate about their lattice equilibrium positions. In the case of a perfectly harmonic lattice, the atoms will vibrate so that their average displacement in any direction is centered on the lattice site. Atomic interactions in that type of lattice can be described by the harmonic

approximation. Consider the simple case of a diatomic molecule. From Hooke's Law, the interatomic potential energy[19] of two atoms separated by a distance x_d from their equilibrium distance at absolute zero can be described as:

$$V(x_d) = cx_d^2 \qquad 1.12$$

where $V = 0$ at $x_d = 0$ and c is related to Hooke's law force constant. The schematic in Figure 1.5 shows the true interatomic potential in comparison to a harmonic approximation (a parabola). Some of the consequences of a hypothetical purely harmonic lattice according to Kittel[20] are that: 1) two lattice waves, also known as phonons, do not interact, nor does a single lattice wave decay or change form over time, 2) there is no thermal expansion, and 3) heat capacity becomes constant at temperatures above the Debye temperature, θ_D.

In real crystals, none of the above consequences is realized; all real lattices are anharmonic. In an anharmonic lattice, the potential energy between bonded atoms is better described by a higher than quadratic relationship between V and x_d that considers anharmonic terms in the potential as in:[19]

$$V(x_d) = cx_d^2 - gx_d^3 - fx_d^4 \qquad 1.13$$

where the cubic term represents the asymmetry of the mutual repulsion of the atoms and the quadric term represents the softening of the vibrations at larger amplitudes.[20] The true interatomic potential is parabolic (harmonic) only at the very bottom of the energy well as shown in Figure 1.5. Going higher up in the energy well, the two sides become asymmetric.

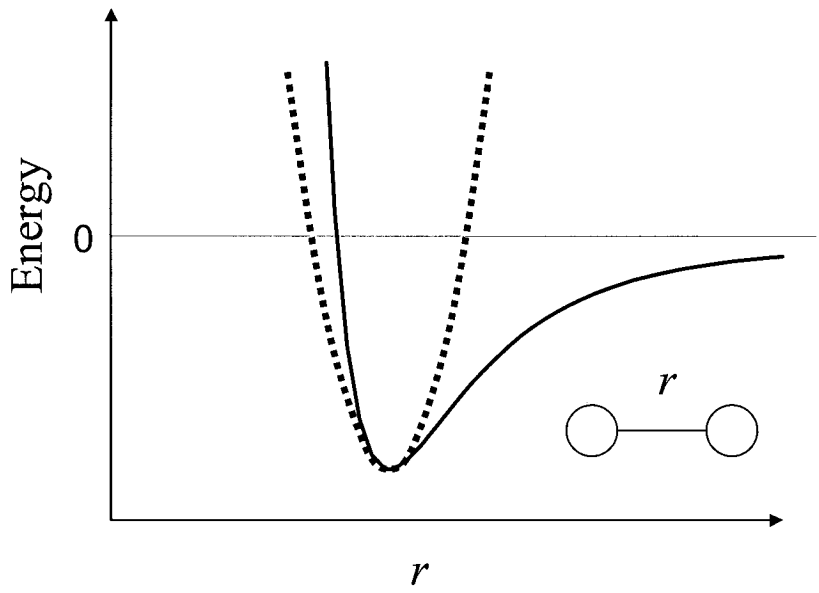

Figure 1.5. The interatomic potential of two atoms separated by distance r for a harmonic oscillator (---) and an anharmonic oscillator (—).

Real crystal interactions are anharmonic in nature, but at low energies (low temperatures), the anharmonic potential is close to harmonic. Contrary to the consequences in the harmonic list from Kittel[20] given above, in a real crystal system lattice waves will interact with each other causing a resistance in the flow of the phonons (quantified by measuring thermal conductivity) and the thermal expansion in crystals is non-zero (with some exceptions). In turn, these phenomena must be due to the anharmonic interactions in crystals.

Anharmonicity is an important factor in thermodynamics. Thermal expansion is of major importance in this project. The thermal expansion of chemical bonds arises due to the anharmonicity of interatomic interactions. Thermal conductivity is a direct consequence of anharmonic phonon-phonon interactions and the Grüneisen parameter quantifies the degree of anharmonicity in a material. The significance of these properties will be discussed in more detail in the following sections.

1.4.2. Thermal Expansion

The thermal expansion of materials arises due to the anharmonicity in interatomic interactions. The coefficient of thermal expansion can be expressed as the ratio of the change in length of a line segment in a body per unit of temperature change, relative to its length.

The thermal expansion coefficient can be given along a particular direction in the unit cell of crystal; for example where a is the unit cell dimension, α_a is given by:

$$\alpha_a = \frac{1}{a}\left(\frac{\partial a}{\partial T}\right)_P \qquad 1.14$$

or for a isotropic thermal expansion, one can consider the linear thermal expansion, α_l

$$\alpha_l = \frac{1}{l}\left(\frac{\partial l}{\partial T}\right)_P . \qquad 1.15$$

Consider the interatomic potential for a diatomic molecule as presented in Figure 1.6. This figure shows the interatomic potentials for both a harmonic and an anharmonic oscillator. An indication of the expansion of the bond length as the temperature is increased is shown. Figure 1.6 illustrates how there would be no thermal expansion for an harmonic lattice, while for an anharmonic lattice, there would be non-zero expansion.[21]

For a perfectly harmonic crystal lattice, the atoms experience thermally excited motion, but the motion is centered on the same lattice site at all temperatures. The displacement of the atoms is independent of the energy level; therefore as the temperature is increased, r stays the same and there will be no thermal expansion. For an anharmonic crystal lattice, the asymmetry in the potential for the interatomic interactions leads to an

increase in the displacement from the minimum energy lattice site as a function of energy of the system. This gives rise to thermal expansion, shown in Figure 1.6. At low energies, the anharmonic potential becomes more harmonic-like. The unit cell dimensions would approach a constant value as the temperature approaches absolute zero, therefore $\alpha \rightarrow 0$ as $T \rightarrow 0$.

Some values of the coefficient of thermal expansion are given in Table 1.1 for selected materials at various temperatures. For most materials, $\alpha > 0$, but there are some exceptions, for example where $\alpha \sim 0$. Invar is an alloy that is considered to have zero thermal expansion at room temperature.[22] In the room temperature region, a rod of Invar of 1 m in length would increase by 0.000025 mm over $\Delta T = 25$ K, while under the same conditions, a 1 m aluminum rod would increase by 0.058 mm.

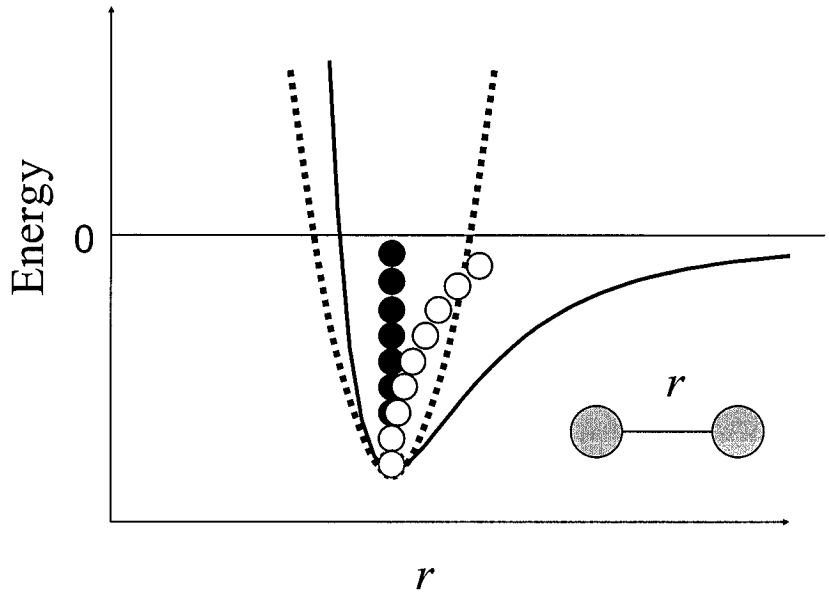

Figure 1.6. The average displacement of the interatomic separation distance from the minimum energy separation distance as a function of energy in the system: • a harmonic lattice (zero thermal expansion); and ○ an anharmonic lattice (non-zero thermal expansion). Also shown is the interatomic potential of two atoms separated by distance r for a harmonic oscillator (---) and an anharmonic oscillator (—). Styled after reference 19.

There are also cases where $\alpha < 0$, such as in Pyrex at room temperature and quartz at $T = 50$ K. Other materials exhibit $\alpha < 0$ over very wide temperature ranges, including siliceous faujasite (25 K > T < 573 K)[23] and zirconium tungstate (0.3 < T < 1050 K).[24] The above explanation illustrates why positive thermal expansion occurs, but it does not explain why negative thermal expansion would arise. The cause of negative thermal expansion (NTE) is not identical for all systems in which it arises. However, in all NTE systems, there is still regular or positive thermal expansion between neighboring atoms, but there must be some mechanism that more than counteracts the positive thermal expansion and leads to net negative thermal expansion. Negative thermal expansion will be discussed in more detail in Chapter 3.

Table 1.1. Values of thermal expansion of selected materials at various temperatures. Obtained from reference 19 unless otherwise indicated.

Material	T / K	α_a / 10^{-6} K^{-1}
Al	50	3.8
Al	300	23.2
Cu	50	3.8
Cu	300	16.8
Ice	100	12.7
Ice	200	37.6
Diamond	50	0.004
Diamond	300	1.0
Invar[22]	300	0.01
Pyrex	50	56.2
Pyrex	300	-2.3
Siliceous faujasite[23]	300	-4.2

Thermal expansion in materials is directly related to the strength of the forces between the molecules or atoms. Material with stronger forces, *i.e.* harder materials, will have lower thermal expansion. Diamond is a very hard material due to its strong covalent bonding and has a much lower coefficient of thermal expansion than softer materials, such as ice.

If the magnitude of the Debye temperature is known, it would provide insight into the degree of thermal expansion in a solid. θ_D is a measure of the force constant between the molecules or atoms in a solid and hence reflects the strength of intermolecular interactions. High intermolecular interaction strength would result in larger value of θ_D. Subsequently, diamond has a higher value of θ_D than ice does.

The coefficient of thermal expansion, α_V or α_l, can be measured experimentally by using diffraction techniques (either elastic neutron diffraction or x-ray diffraction) to measure lattice parameters as a function of temperature. Alternatively, α_V can be measured directly using capacitance dilatometry. Previous experiments on the thermal expansion from other research labs were used for this thesis and the measurement techniques will be referred to in each instance.

Thermal expansion is an important property to consider for many engineering applications. The coefficient of thermal expansion is based on the intrinsic nature of the material, so it can vary greatly from material to material. Even though mismatching in thermal expansion can lead to useful applications such as bimetallic strip thermometers, it also can lead to problems and potentially failure in a system. For example, interfaces shared by two materials with different thermal expansion properties could result in thermal stress leading to cracks or separation at the interfaces. Materials that have high coefficients of thermal expansion exhibit poor thermal shock resistance, *i.e.* rapid cooling or heating would result in temperature gradients that cause cracks. Most materials exhibit anisotropic behavior, *i.e.* α is different along the three axes of the unit cell. This could also lead to microcracks. For engineering purposes, low thermal expansion coefficients and control of α are desirable.

1.4.3. Thermal Conductivity

1.4.3.1. Introduction

Thermal conductivity describes the ability of a material to transport heat; hence it is a transport property that describes the motion of heat from the hotter to the cooler. The flux of thermal energy, J_U, is the amount of heat transmitted across a unit area per unit time during the steady-state flow of heat the down a rod with a temperature gradient, dT/dx.[20] The thermal conductivity coefficient, κ, of a solid is defined by:

$$J_U = -\kappa\left(\frac{dT}{dx}\right). \qquad 1.16$$

A simple theory of thermal conductivity was derived by Debye for gases (based on the kinetic theory of gases) and can be used by analogy for insulating solids as well where phonons carry the heat. The Debye equation for thermal conductivity is

$$\kappa = \frac{Cv_m\lambda}{3} \qquad 1.17$$

where C is the heat capacity per unit volume, v_m is the average phonon velocity, and λ is the phonon mean free path of a particle between collisions. The phonon mean free path is the average distance a phonon can travel along a path before being thrown off by an obstacle. The obstacle could be another phonon, an imperfection in the crystal, or a crystal boundary.

The derivation of the elementary kinetic theory that leads to Equation 1.17 specifically for the flux of phonons is as follows.[18] Consider a rod in which a temperature gradient has been established as in Figure 1.7. The phonons will diffuse from the hotter region, concentration of the phonons given by $n(T+\Delta T)$, to the cooler

region where the concentration of phonons is $n(T)$.

The temperature difference, ΔT, between the ends of the free path of the particle in the x direction, distance λ_x, is given by

$$\Delta T = \frac{dT}{dx}\lambda_x = \frac{dT}{dx}v_x\tau \qquad 1.18$$

where τ is the average time between collision and v_x is the phonon velocity along the x direction. The difference in the number of phonons between the two regions is given by

$$\Delta n = n(T+\Delta T) - n(T) = \frac{\partial n}{\partial T}\Delta T = v_x\tau\frac{\partial n}{\partial T}\frac{dT}{dx}. \qquad 1.19$$

The thermal flux of phonons across a point between the two regions in the x direction is

$$J_{phonons} = -\Delta n\tau\frac{3pv_x}{V} \qquad 1.20$$

where $3p/V$ is the number of phonons modes per unit volume (equal to three × the number of atoms per unit volume). The negative sign accounts for the fact that the flow of heat is in the opposite direction of the temperature gradient. By combining Equations 1.19 and 1.20, one can write

$$J_{phonons} = -v_x^2\tau\frac{3p}{V}\frac{\partial n}{\partial T}\frac{dT}{dx}. \qquad 1.21$$

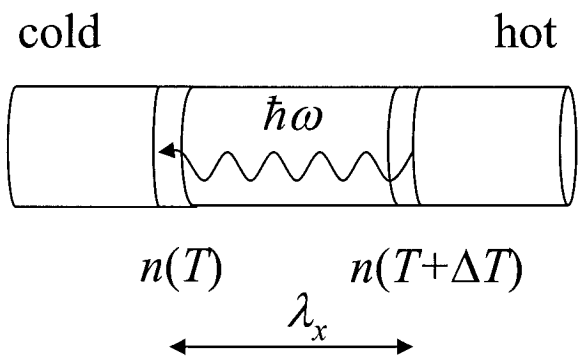

Figure 1.7. Phonon drift in a rod leading to finite value of thermal conductivity in a solid. Styled after reference 18.

The phonon flux is converted to a thermal energy flux by assuming that each phonon carries an average energy of $\hbar\omega$. The thermal energy flux will therefore be $J_U = \hbar\omega \times J_{phonons}$. When all directions of phonon motion are considered, then $v_x^2 = v_m^2/3$ where v_m is the average phonon velocity. Since the heat capacity per unit volume is given by the quantity $\frac{3p}{V}\hbar\omega\frac{\partial n}{\partial T}$, the flux of thermal energy is

$$J_U = \frac{Cv_m^2\tau}{3}\frac{dT}{dx}. \qquad 1.22$$

By comparing Equations 1.16 and 1.22, and since the phonon mean free path is $\lambda = v_m\tau$, the Debye equation for thermal conductivity, Equation 1.17, is reached.

The thermal conductivity of a solid can be measured directly by attaching thermocouples a known distance apart on a crystal and applying power, $\dot{q}$. The thermal gradient dT/dx can be measured, and κ is given by:

$$\kappa = \frac{\dot{q}}{A}\frac{dx}{dT} \qquad 1.23$$

where A is the cross-sectional area of the crystal perpendicular to the heat flow. Figure 1.8 shows diagrammatically the measurement of thermal conductivity of a solid with well-defined geometry under steady-state conditions, *i.e.* the rate of power introduced to the top of the solid would match the loss at the bottom of the crystal therefore the temperature of the solid would not change.

In a crystal described by perfect harmonic oscillators, phonons do not couple with each other and they carry heat perfectly, therefore, there would be no resistance to heat flow and thermal conductivity would be infinite. Since heat flow is not infinite, there must be one or more mechanisms leading to resistance in the heat flow. The explanation to this problem for insulators was derived by Peierls.[25]

As shown in Figure 1.9, two phonons can interact with one another resulting in a phonon with a motion in the same general direction as the incident phonons. This action was termed a "normal" or "N" process by Peierls and he showed that this phonon interaction would not resist heat flow.

Peierls termed the phonon-phonon interaction that would lead to thermal resistance an "Umklapp" or "U" process, the translation from German meaning "turning back". This type of process, shown in Figure 1.9(b) involves two phonons that interact to form a resultant phonon whose direction is opposite that of the incident phonons, made possible by a momentum transfer to the lattice.

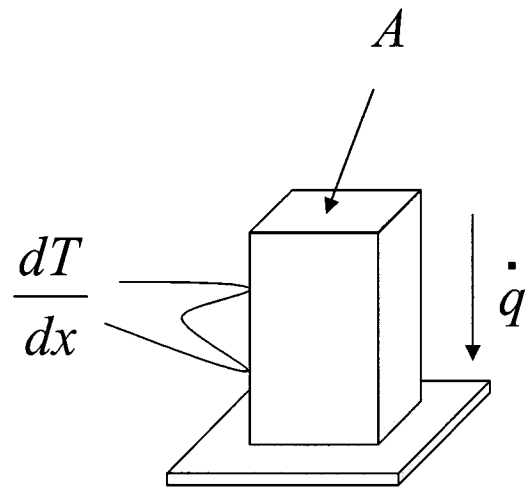

Figure 1.8. Schematic of the direct measurement of thermal conductivity of a solid, steady-state method. Styled after reference (19).

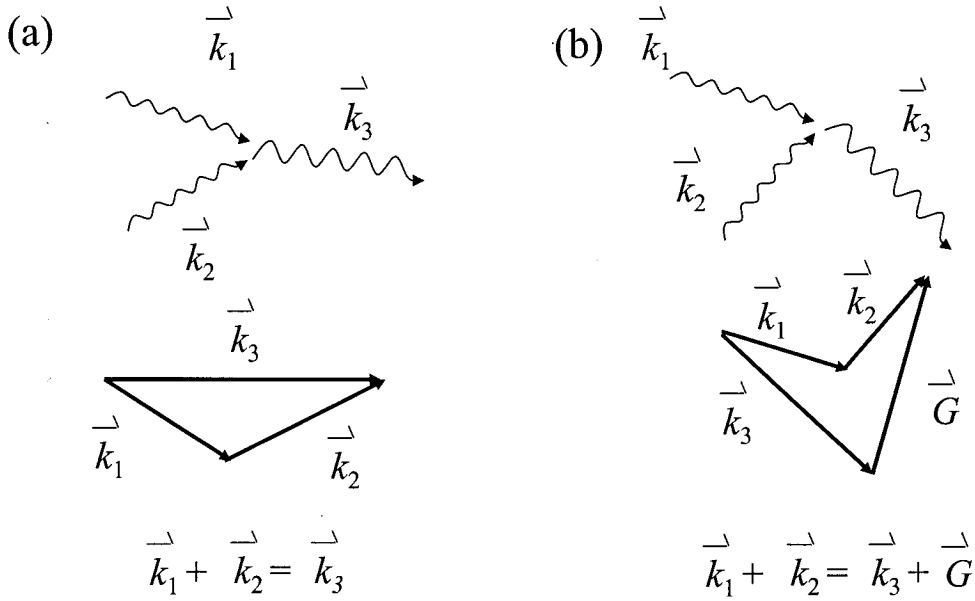

Figure 1.9. Peierls' explanation for heat flow resistance for a two phonon system shown schematically. $\vec{k}_1$ and $\vec{k}_2$ are the incident wavevectors of the two phonons and $\vec{k}_3$ is the wavevector of the resultant phonon. (a) "N" or "normal" process where there is no resistance to heat flow and (b) "U" or "Umklapp", *i.e.* "turning back" process that leads to resistance in heat flow. $\vec{G}$ represents the momentum transfer to the lattice. Styled after reference (19).

Equation 1.17 states that κ varies with the heat capacity, the average phonon velocity and the mean free path of the phonons. The average phonon velocity is a characteristic of the material and does not vary greatly with temperature so it assumed to be a constant. Phonon velocity is directly related to the strength of the interatomic (molecular) interactions that do not change much with temperature. The heat capacity of a solid was introduced and the manner in which C varies with temperature was discussed in Section 1.3. The heat capacity will behave in approximately the same way for a crystalline solid as for an amorphous solid. However, the mean free path of the phonons will differ greatly for a crystalline solid when compared to an amorphous solid.

For a crystalline solid at high temperature, κ depends mainly on λ since C is approximately constant for $T > \theta_D$ and as mentioned above, v_m is approximately constant over the entire temperature range. As the temperature is decreased, κ will increase as λ increases due to the fact that as the temperature is decreased, the distance a phonon can travel will increase since the available thermal energy is lower and fewer phonons will be excited. κ will reach a maximum as the temperature is decreased, since the crystal size or the average distance between imperfections will limit λ. At temperatures below this maximum mean free path, which occurs at approximately 10 % of θ_D,[9] κ will normally decrease with decreasing T since C will decrease proportionally to T^3 if the temperature is far below the Debye temperature of the material.

The thermal conductivity of an amorphous solid normally is lower than that of a crystalline material. This is a consequence of the lack of long-range order in the crystal structure, leading to the very short mean free path, λ, which is essentially temperature independent. κ decreases as the temperature decreases since as temperature is decreased,

fewer phonons will be excited. The dependence of thermal conductivity on temperature of a typical simple crystalline solid is very different than that of a typical amorphous solid,[26] as shown schematically in Figure 1.10.[27] The typical simple crystalline material has a maximum in the temperature dependence while the amorphous does not. Table 1.2 gives the thermal conductivities of various materials at $T = 300$ K.[28]

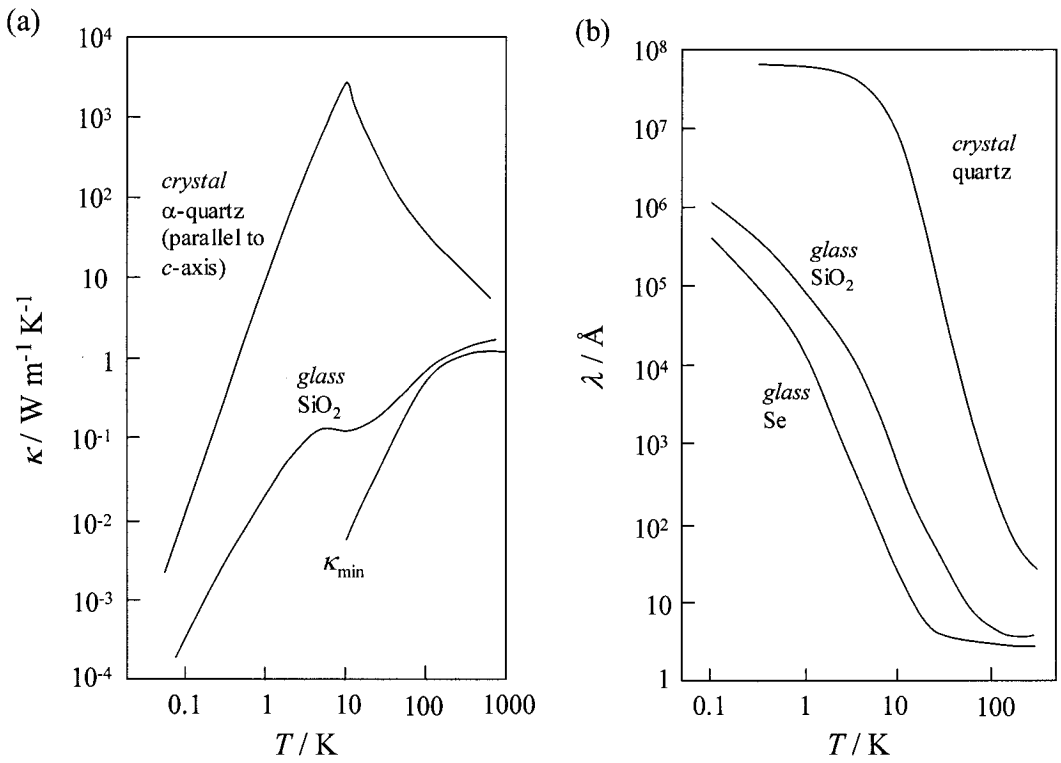

Figure 1.10. (a) The thermal conductivity of a simple insulating solid; crystalline and amorphous SiO_2. Also shown is κ_{min} for SiO_2 calculated with Equation 1.24. (b) Phonon mean free path for various solids, calculated with Equation 1.17. Redrawn from reference 27.

Table 1.2. Thermal conductivity of various materials at $T = 300$ K. (All data are from Touloukian *et al.*[28] unless otherwise noted.)

Material	**κ / W m^{-1} K^{-1}**	**Material**	**κ / W m^{-1} K^{-1}**
Diamond	2310	SiO_2 (crystalline, *c*-axis)	10.4
Graphite, *c*-axis	2000	SiO_2 (crystalline, *a*-axis)	6.2
Graphite, *a*-axis	9.5	SiO_2 (amorphous)	1.38
Copper[29]	398	Typical Silica aerogel[30]	0.017

1.4.3.2. Dynamic Disorder in Crystalline Materials, Reduction of κ

Studies of the thermal properties of inclusion compounds provide an interesting example of how dynamical disorder in crystalline materials could lower κ. A specific example is the case of Dianin's compound; its molecular structure is shown in Figure 1.11.

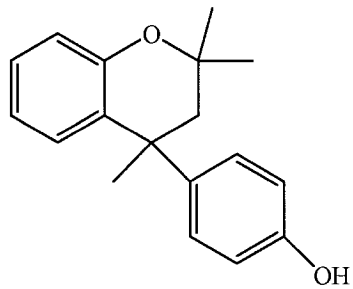

Figure 1.11. The molecular structure of Dianin's compound.

This molecule crystallizes to form a hexamer held together by hydrogen bonding. The crystal has the same structure with and without the presence of guests in the cages of host lattice. Its κ has been shown to be greatly reduced when two ethanol molecules, which are dynamically disordered, are present as guests in the cages.[31] This study, and similar studies on inclusion compounds,[32,33] show how the low-energy optic modes associated with the dynamical disorder of one or several molecules rattling around in the host cage can interact with the heat-carrying acoustic modes leading to a shortening of the mean free path of the phonons. In some cases the mean free path is shortened to such a large extent that the κ becomes glass-like.

Inclusion compounds such as Dianin's compound illustrate that even though their morphology is crystalline, they can behave like amorphous materials in terms of their thermal conductivity.

1.4.3.3. The Concept of Minimum Thermal Conductivity

At one theoretical extreme, a perfect lattice governed by purely harmonic interatomic interactions has infinite thermal conductivity. At the other extreme, one can imagine fully coupled phonons, leading to the concept of theoretical minimum thermal conductivity, κ_{min}.

The minimum thermal conductivity proposed by Cahill and Pohl considers the thermal conductivity within the Debye model, with the assumption that the scattering length is one half of the wavelength.[27] The expression κ_{min} is based on the random walk between Einstein oscillators of varying sizes and can be calculated for each of the transverse and longitudinal polarizations, v_i, as follows,[27]

$$\kappa_{min} = \frac{1}{2.48} k_B n^{2/3} v_i 2 \left(\frac{T}{\theta_D^e} \right)^2 \int_0^{\theta_D^e/T} \frac{x^3 e^x}{\left(e^x - 1\right)^2} dx \qquad 1.24$$

where n is the number density (number of atoms per unit volume), and θ_D^e is the *effective* Debye temperature. An analysis of low-temperature heat capacity where θ_D represents *only* the acoustic modes (3 out of $3p$ degrees of freedom in the unit cell) would lead to a true Debye temperature. When the whole lattice is treated as unconnected atoms, the effective Debye temperature can be calculated, working backwards from the speed of sound. An *effective* Debye characteristic temperature would refer to the case when all the lattice modes (3 acoustic and $3p$ - 3 optical) have been treated as Debye-like. The *effective* Debye temperature can be calculated from the speed of sound as[34]

$$\theta_D^e = \left(\frac{h}{2\pi k_B} \right) v_i \left(6\pi^2 n\right)^{1/3}. \qquad 1.25$$

The total κ_{min} is the sum of the contributions from two transverse and one

longitudinal mode. The transverse and longitudinal speeds of sound, v_t and v_l, respectively, are calculated from the experimentally determined bulk modulus, B_T, and shear modulus, G, using relationships for transverse and longitudinal waves[35]

$$v_t = \left(G/\rho\right)^{1/2}, \quad v_l = \left(\left(B_T + \tfrac{4}{3}G/\rho\right)\right)^{1/2} \qquad 1.26$$

where ρ is the density. The mean speed of sound can be calculated from the transverse and longitudinal speeds of sound, $v_m = 3^{1/3}\left[\left(\left(v_l\right)^{-3} + 2\left(v_t\right)^{-3}\right)\right]^{-1/3}$.[34]

When κ_{min} is compared with the experimental thermal conductivity, information on the effectiveness of the phonon-phonon coupling (and hence the thermal resistivity) of the material can be determined. Knowing the magnitude of the thermal resistivity in the crystal will give a measure of the degree of the anharmonicity in the lattice vibrations, since as Peierls showed, only an anharmonic intermolecular potential leads to thermal resistance due to Umklapp interactions.[20]

1.4.4. Grüneisen Parameter

As was mentioned in the previous sections, the resistance to heat flow is caused by anharmonic intermolecular interactions. Positive thermal expansion is a result of the anharmonic nature of bonds, so being able to quantify the anharmonicity in a solid would be useful in analysis of thermal conductivity and thermal expansion. The anharmonicity in a material can be quantified by determining the Grüneisen parameter, γ.

This dimensionless 'constant' is not necessarily constant, especially at low temperatures. The Grüneisen parameter can be defined for mode i in terms of the frequency of that mode ω_i and the volume, V:[14]

$$\gamma_i = -\left(\frac{\partial \ln \omega_i}{\partial \ln V}\right). \qquad 1.27$$

It can be determined directly by spectroscopic measurements under pressure. The overall Grüneisen parameter is the sum over all the modes, $\gamma = \sum_i \gamma_i$. For a harmonic solid, ω_i is independent of the volume so $\gamma = 0$ for all modes. Any deviation from zero in the Grüneisen parameter will therefore be an indication of the anharmonic interactions in the solid, the larger the magnitude, the larger the degree of anharmonicity.

If other thermodynamic parameters of the material are known, the Grüneisen parameter can be calculated as a function of temperature:[14]

$$\gamma_T = \frac{B_T V_m \alpha_V}{C_V} \qquad 1.28$$

where V_m is the molar volume. The calculation yields an averaged γ for all of the modes at the temperature being probed.

1.5. Conclusion

As mentioned throughout Chapter 1, the anharmonic interactions within crystal lattices are important to both thermal expansion and thermal conductivity. In the subsequent chapters, the thermal properties will be presented with particular attention paid to anharmonicity.

1.6. A Look Ahead

This thesis presents the thermal properties of selected materials that exhibit the

unusual property of negative thermal expansion. These materials are studied in order to investigate the relationship between negative thermal expansion and other thermal properties. The thermal conductivity and heat capacity of the NTE materials ZrW_2O_8 and $HfMo_2O_8$ are determined in order to establish a link between NTE and thermal conductivity.

The techniques used to characterize thermal conductivity and heat capacity are described in the coming chapter, along with the results of standard materials measurements. My goal in the subsequent chapters is to present low-temperature measurements of the thermal conductivity and heat capacity of ZrW_2O_8 and $HfMo_2O_8$ and to delineate the origins of its unusually low thermal conductivity.

Chapter 2. Experimental Methods and Calorimetry Standard Materials

2.1. Introduction

The experimental methods and techniques used for this thesis are discussed in this chapter. Also, the standardization of two calorimeters, a relaxation calorimeter from Quantum Design, QD, and a small sample adiabatic calorimeter designed by Van Oort and White[36] are described.

2.2. Measurement of Thermal Conductivity

2.2.1. Introduction

Historically thermal conductivity measurement was used as a powerful tool to investigate lattice defects or imperfection in solids.[37] Recently Mathis Instruments, a company located in New Brunswick, Canada, has developed a non-invasive method to test uniformity in pharmaceuticals products efficiently using thermal effusivity, e, a transport property based on the thermal conductivity, heat capacity and density of a material ($e = \sqrt{\kappa \rho C_P}$).[38]

The measurement of thermal conductivity allows for the study of interesting physical phenomena; however it is also an important property from a technological aspect. Materials with high and low thermal conductivity are of special interest. For example, high-thermally conductive materials such as diamonds and silicon are extensively studied for their use in thermal management devices for electronics.[37] Low-thermally conductive materials such as skutterudites and clathrates are studied for their use in high-efficiency thermoelectric applications.[39]

As new materials technologies emerge, techniques become available for experimental measurement of κ of materials such as thin films,[40,41] superlattices,[41] and nanomaterials;[42] however, the accurate measurement and characterization of bulk materials can still pose many challenges.[43] In Chapter 1, Figure 1.8, the steady-state method was described to directly measure of κ of bulk materials, and in the next section, the pulse-power method, or "Maldonado" technique used to measure the materials in this thesis is described in detail.

One challenge is the radiative loss of heat that was intended to flow through the sample, a factor that is difficult to quantify. Other heat loss mechanisms could occur through leads, heater, and through the interface made between the sample and leads. The thermal contact between the sample and leads must be sufficient. Thermal anchoring materials such as high-thermally conducting varnishes and epoxy can be used to insure thermal resistance sufficiently low as to not affect the results. There is additional uncertainty from determining the sample dimensions in order to calculate κ. If seemingly identical samples vary due to impurity and/or heat treatment, it is very difficult to correct or compensate. These differences can cause large variations in κ.

Even with the corrections introduced for these various heat losses and with careful experimental procedures, it is still difficult to obtain κ results with accuracies better than $\pm$ 10%.[44]

The thermal conductivity technique can be tested through the measurement of known standard materials recommended for different κ ranges. Pyrex and Pyroceram are suggested as low-thermal conductivity standards ($\kappa < 4$ to 5 W m^{-1} K^{-1}), calibrated 304 stainless steel for intermediate values ($\kappa < 20$ W m^{-1} K^{-1}), and graphite for higher values

($20 > \kappa < 100$ W m^{-1} K^{-1}).[43] Stainless steel 304 and graphite are available from the National Institute of Standards and Technology.[45]

2.2.2. Measurement of κ with a Physical Properties Measurement System

The Physical Properties Measurement System, PPMS, is a commercially available instrument from Quantum Design that allows rapid characterization of thermal (heat capacity, thermal conductivity), electrical and magnetic properties of materials. The κ determination is based on the pulse-power method developed by Maldonado.[46] The PPMS includes a puck for measuring thermal transport properties (thermal transport option, TTO) which can measure simultaneously the thermal conductivity, the Seebeck coefficient, $\alpha_S = \Delta V/\Delta T$, and the electrical resistivity of a sample as a function of temperature. These properties can be measured from 1.9 to 390 K and under an applied magnetic field of up to 9 T, in a vacuum of 10^{-4} Torr. The details of the TTO have been published by Dilley *et al.* in 2002,[47] and the principles and procedures that they devised to measure thermal conductivity with the TTO are discussed in the following sections of this chapter.

The thermal conductivities of ZrW_2O_8 and $HfMo_2O_8$ were measured using the thermal transport option of the PPMS and the results are presented in Chapters 3 and 4 respectively. Since these materials are insulators[48,49] the electronic properties were not measured.

2.2.3. Principles and Procedures

There are two different methods for measuring thermal conductivity with the PPMS. They are the called the Continuous Measurement Mode and the Single Measurement Mode. The methods are described in the following sections. In both cases, heat is applied to a small pellet or bar of sample and the temperature is monitored in response to this. Thermal conductivity is determined by the thermal response when consideration has been taken of the effects of the attachments (called shoes).

2.2.3.1. Continuous Measurement Mode

The continuous mode is named as such since measurements are taken continuously as the software adjusts parameters (such as the heater power and period) to optimize the measurements. This mode is the faster way to obtain data since the system does not have to reach equilibrium before beginning the measurement of temperature. The instrument can simply be set up to scan at a slow rate ($\leq$ 1 K min^{-1}) over a given temperature range and will take measurements by using a curve fitting algorithm to determine the steady-state thermal properties by extrapolating the response of a short heat pulse, shown in Figure 2.1. In this method, the ΔT_{∞}, the difference in the hot and cold thermometer assuming that the system reached steady state and that the heater power was left on, is determined. ΔT_{∞} represents the asymptotic temperature drop across the sample if the heater is left on indefinitely. [47]

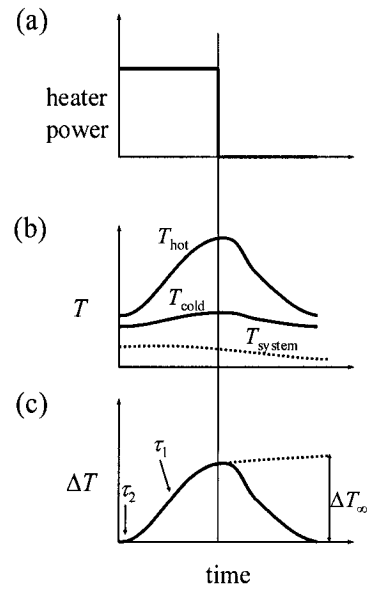

Figure 2.1. Idealized heat pulse and temperature response of hot and cold thermometers for the continuous measurement mode. (a) Heater power during square wave heat pulse, (b) temperature trace of hot, T_{hot}, and cold, T_{cold}, thermometer with PPMS base temperature, T_{system}, scanning at slow rate, and (c) temperature differential indicating the time constants (τ_1 and τ_2) and estimation of asymptotic temperature differential, ΔT_∞. Styled after reference 47.

In continuous measurement mode, the software that comes with the PPMS models the heat flow and automatically corrects for any heat loss that may occur. Once the heat pulse is applied to the sample, both the cold and hot thermometers are monitored over the entire heating pulse. When the heating cycle is finished, a non-linear least-squares fitting routine, which fits the data to an empirical formula, is launched to model the temperature data[47]

$$\Delta T_{model} = \Delta T_\infty \times \left[1 - \left(\tau_1 \times e^{(-t/\tau_1)} - \tau_2 \times e^{(-t/\tau_2)}\right)/\left(\tau_1 - \tau_2\right)\right] \qquad 2.1$$

where τ_1 and τ_2 are the long and short time-constants respectively indicated in Figure 2.1. τ_2 describes the behavior of the leads and the shoes, while τ_1 describes the behavior of the sample.

This process will optimize measurement parameters such as heater power and heat pulse period. A heat pulse is chosen to yield a temperature rise of a few kelvin. The uncertainty in κ is high if the temperature rise is too large during a heat pulse where κ changes rapidly with temperature. Due to a small magnitude of the thermal signal, errors in data are large if a temperature rise < 1% of the absolute temperature is chosen.[50]

Equation 2.1 is used to model the data taken during the heating. The cooling pulse is simultaneously fit by changing the sign of the model equation, $\Delta T_{\text{model,cooling}} = B - \Delta T_{\text{model,cooling}}$, where B is a constant. The thermal history of the material must be accounted for in this model due to long thermal diffusion times (τ_1). This is achieved by considering the residual effects of the two previous heat pulses in modeling the latest heat pulse and thus the first few data points measured must be discarded due to poor model fits.

From the heater power, $\dot{q} = I^2 R$ (I is current, R is resistance of the heater, in this case 2 kΩ) and the value of ΔT_∞, the thermal conductance, K (units W K^{-1}) can be determined as

$$K = \frac{\dot{q}}{\Delta T_\infty} . \qquad 2.2$$

The net heat conducted through the sample is estimated as the power dissipated in the heater resistor minus the losses due to radiation or thermal conduction loss down the leads of the shoe assemblies and thus K is established from the following:[50]

$$K = \left(\left(I^2 R - P_{\text{rad}} \right) / \Delta T \right) - K_{\text{shoes}} \qquad 2.3$$

where a standard estimate of the thermal conductance of the shoe assemblies is

$$K_{shoes} = aT + bT^2 + cT^3 \qquad 2.4$$

The parameters a, b, and c are constants, and P_{rad} is the radiative heat loss from the sample [47]

$$P_{rad} = \sigma_T \times (S_A / 2) \times \varepsilon \times \left(T_{hot}^4 - T_{cold}^4\right) \qquad 2.5$$

where σ_T = 5.670 × 10^{-8} W m^{-2} K^{-4} is the Stefan-Boltzmann constant, S_A is the total surface area, ε is the infrared emissivity of the radiating surface, and T_{hot} and T_{cold} are the average temperatures of the hot and cold thermometers respectively during the measurement. ε is the relative emissive power of a body compared to that of an ideal blackbody which has a surface emissivity of 1. Therefore, ε is the fraction of thermal radiation emitted from an object compared to the amount emitted if the body were a blackbody. ε is typically < 1. If ε is unknown, an approximate value depending on the nature of the sample is used.[50,51] This is only necessary for κ measurements for T > 200 K where some heater power is lost to thermal radiation from the hot end of the sample to the surrounding isothermal shield. Below 200 K radiative losses are negligible.

The factor of ½ in the total surface area is due to the fact that one half of the sample surface area is radiating at the hot temperature, the other half is at the cold temperature.[47] The radiative losses are difficult to estimate accurately, the errors of the measurements above T = 300 K are on the order of 1 mW K^{-1},[50] compared with typical thermal conductance of ~10 mW K^{-1} for the measurements reported here.

The thermal conductivity, κ, can be determined from the thermal conductance, the sample cross sectional area, A, and the length between the thermometers, l, as

$$\kappa = \frac{K \times l}{A}. \qquad 2.6$$

The standard deviations in the reported quantities of thermal conductivity are estimated using the QD software by estimating the quality of the curve fits to thermal conductivity through calculating the residual of the curve fit. It is assumed that the residual reflects the error in the estimation of ΔT and this is true when the data deviate from the curve in a random manner.

Systematic errors can be seen by inspecting the raw data file and are large if the curve fit does not properly represent the data. Systematic errors include a low period (length, in seconds, of the heater on/off cycle) to τ_1 ratio (this ratio should be around 8 for the model to fit well) or high-vacuum failure as well as other reasons outlined in the manual.[50] The residual, $R_{\Delta T}$, for the ΔT vs. time curve is calculated as follows:

$$R_{\Delta T} = \sqrt{\frac{\sum_i \left(\Delta T_i - \Delta T_{i,\text{model}}\right)^2}{N}} \qquad 2.7$$

where N is the number of data points in the curve, typically 64 for κ measurements. The error in the heater power also must be considered since $K = \dot{q}/\Delta T$. The standard deviation for the thermal conductivity, $\sigma(\kappa)$, is calculated as:

$$\sigma(\kappa) = \kappa \sqrt{\left(\frac{R_{\Delta T}}{\Delta T_\infty}\right)^2 + \left(\frac{2IR\partial I}{\dot{q}}\right)^2 + \left(\frac{0.2\dot{q}_{loss}}{\dot{q}}\right)^2 + \left(\frac{0.1 \times \Delta T_\infty K_{shoes}}{\dot{q}}\right)^2}. \qquad 2.8$$

The first term is the residual of the curve fit from Equation 2.7, and the second term propagates the error in the heater current, I, due to the digital-analogue converter where

the R is heater resistance. The third term is the error in the sample radiation term where 20% combined uncertainty in the estimation of surface area and emissivity is assumed, and the last term is the error in the thermal conductance leak from the shoe assemblies (K_{shoes} given in Equation 2.4) where a 10% uncertainty in this correction is assumed. All of these uncertainty estimates were assigned by QD and are built into the software.

Uncertainties in measuring the diameter and the height of the pellet are also included into the calculation of uncertainty for the thermal conductivity. Maximum and minimum κ are calculated assuming that the uncertainties in the height and diameter are both 0.02 mm.

2.2.3.2. Single Measurement Mode

The single measurement mode is slower but more direct than the continuous mode since the system is required to reach a steady state when the heater is in both the "on" and "off" states. The long time needed to reach steady state is a disadvantage of this mode over the continuous, but an advantage is that there is no need for a curve-fitting calculation.

For this method, ΔT vs. time data is first taken in the heater "off" state once the system settles. The user can designate whether the measurement style is timed or stability. For the purpose of measuring over large temperature ranges, stability is the preferred measurement style since it can be applied for the entire range of temperature. The time needed for the temperature to equilibrate depends greatly on the temperature at which κ is being measured. It can be specified as either a percentage of the temperature or a value of absolute temperature. Typically, a temperature stability of 0.1% dT/T is

used.

The stability mode waits in heater "off" mode until the temperature stability of the hot and cold thermometers is within the specified range. After applying heat, the system is set to wait for the same criterion to be met before taking final T_{hot} and T_{cold} measurements, see Figure 2.2, and the thermal conductance is determined as $K = \dot{q}/\Delta T$ where ΔT is T_{hot} - T_{cold}. Equations 2.3 to 2.5 are still applicable for calculating the heat loss due to radiation or thermal conduction loss via the leads of the shoe assemblies. The thermal conductivity is calculated from Equation 2.6.

The heat turns off after the criterion is achieved and moves to the next temperature setpoint where it will perform another measurement. In the timed mode, the system takes measurements of the temperature before applying a heat pulse (defined by the user), and then takes a final measurement at the end of the heat pulse.

In single mode, the magnitude of the heat pulse is selected by the user. Again, it is necessary to choose a heat pulse that yields a temperature rise of a few kelvin. Since the heat capacity and thermal conductivity vary with temperature, the magnitude of the heat pulse has to be chosen accordingly, or else the temperature difference would be too large. For an insulating sample, typical values of K were ~ 20 mW for $T > 40$ K, ~ 10 mW for 15 K $< T >$ 40 K, and 1 to 2 mW for $T < 15$ K. The required magnitude of the heat pulse changes greatly depending on the nature of the sample, thus initial test and adjustments need to be performed on unknown samples.

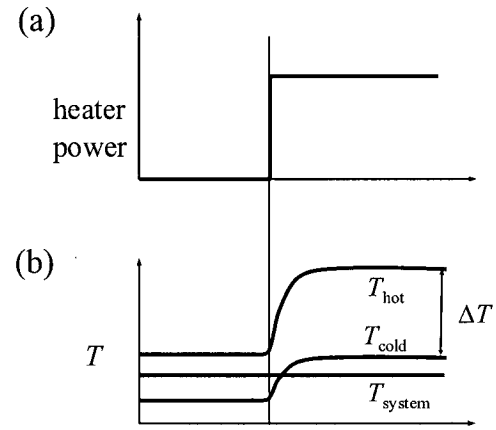

Figure 2.2. Idealized heat pulse and temperature response of hot and cold thermometer for single measurement mode. (a) Heater power during square wave heat pulse, (b) temperature trace of hot, T_{hot}, and cold, T_{cold}, thermometer with PPMS base temperature at constant temperature, T_{system}, and the temperature difference, ΔT.

2.2.4. The Thermal Transport Puck

The thermal transport puck is shown in Figure 2.3.[52] The puck can be operated using either a two-probe or a four-probe lead configuration. The pellets are placed between copper circular disks that have a diameter of 6.3 mm. The procedure for pressing pellets is discussed in the next section. These disks have two copper leads each, and are the two-probe configuration. Figure 2.4 shows the arrangement of the sample in the two-probe configuration.

The pellets are attached to the disks using thermally conductive epoxy (0.2 mm of silver-loaded epoxy, Tra-Bond 816H01 from Tra-Con, Inc.) to ensure sufficient thermal contact. Extreme care must be taken to ensure that the epoxy is evenly spread over the entire area of the pellet. If not, the thermal conductivity is greatly underestimated. This would cause variation among the thermal conductivity measurements of otherwise identical samples.

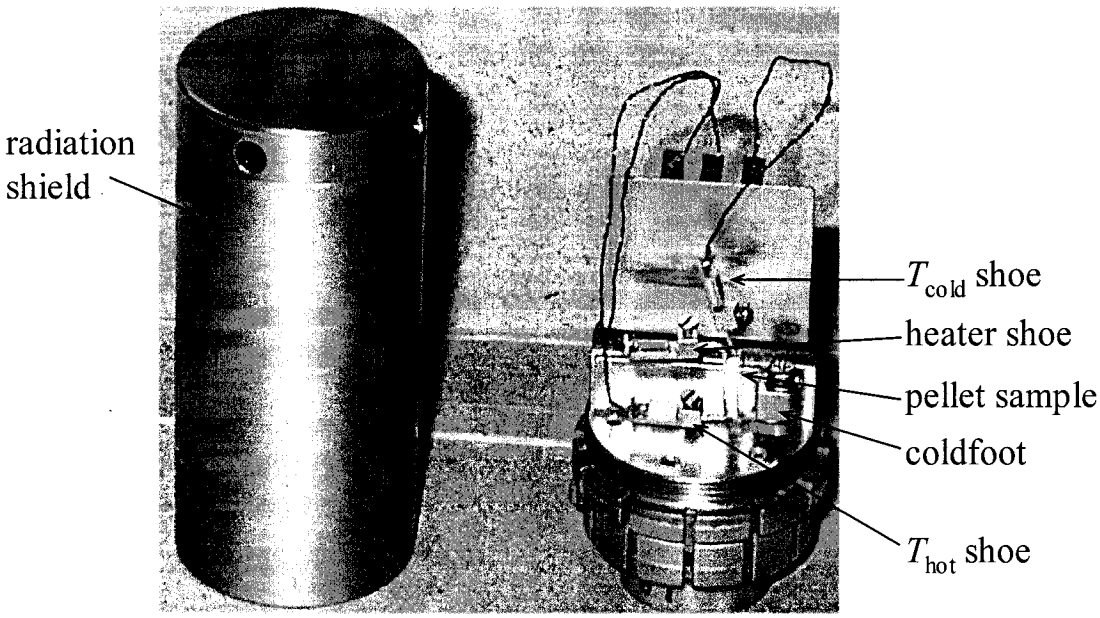

Figure 2.3. The PPMS thermal transport measurement puck from Quantum Design loaded with a pellet sample (for κ measurement).

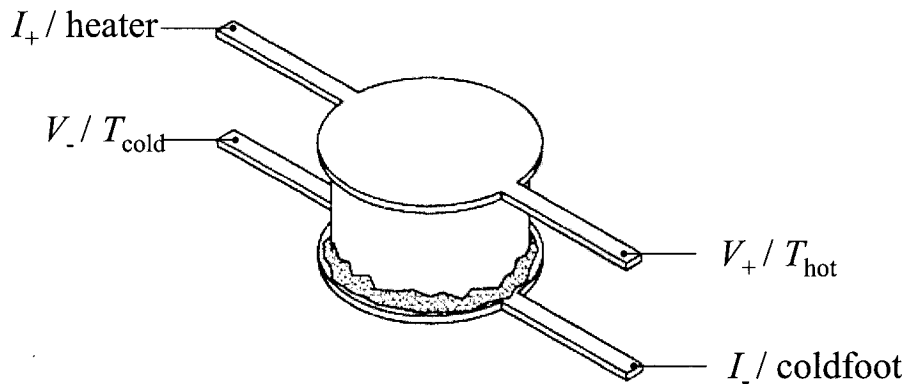

Figure 2.4. Two-probe lead configuration for pellet sample with disk shaped copper leads. From PPMS reference manual.[50]

To demonstrate the magnitude of the variance for an insulating material, consider the thermal conductivity of a material at 300 K. For this example, the sample has an area of 17.94 mm^2 and κ = 0.389 W m^{-1} K^{-1} at this temperature. If the thermal conductivity is recalculated considering the area of sample was not sufficiently thermally attached to the lead and only 80% was in thermal contact, then the thermal conductivity of the material is

actually 25% higher (0.485 W m^{-1} K^{-1}). After measuring the sample, there is no way of knowing if the epoxy is covering the entire area, therefore, it must be carefully attached (using thermally conductive epoxy) and inspected to check for good contact. The epoxy should be allowed to set for 24 hours before measuring the sample.

When the pellet is securely attached to the copper disks, the copper leads are screwed into the measurement puck shoes. Figure 2.3 shows a pellet sample with the shoes attached. The four shoes are a 2 kΩ metal film resistive heater, two calibrated Lake Shore thermometers and a fourth shoe that is directly attached to the puck base, which acts as a thermal sink. The two thermometers are Cernox™ 1050 sensors calibrated by Lake Shore, $T > 0.65$ K, with calibrations based on the International Temperature Scale of 1990 (ITS-90).[53] For $T < 0.65$ K, calibrations are based on the Provisional Low Temperature Scale of 2000 (PLT-2000).[54]

There are also voltage leads (V_+, V_-) attached to each thermometer shoe to measure the Seebeck coefficient and electrical resistivity. The heater shoe contains a current lead (I_+) used for electrical resistivity measurements and the second current lead (I_-) is on the shoe directly attached to the puck. The leads on the shoe assemblies for the thermometers and the heater are 50.8 mm long, 0.08 mm diameter wires, manganin alloy for the thermometers and PD-135 low-resistance copper alloy for the heater. These leads are designed to minimize thermal conduction from the sample to the puck. A radiation shield is placed over the puck once the sample is mounted to provide an isothermal environment during the measurements. The puck is inserted into the sample chamber through the top-loading Dewar and the sample chamber is evacuated to 10^{-4} Torr.

2.2.5. Pressing Powders into Pellets

ZrW_2O_8 and $HfMo_2O_8$ are powders, so they must be pressed into pellet form before attaching to the thermal transport puck. A sample press assembly, shown in Figure 2.5, was designed to press samples to the correct dimensions and configuration before being attached to heater/thermometer leads. The base was fabricated to the specified dimensions from stainless steel by the machinists in the Department of Chemistry at Dalhousie University. The plug and rod components were obtained from Small Parts, Inc. and are precision ground type 303 stainless steel per ASTM 582.[55]

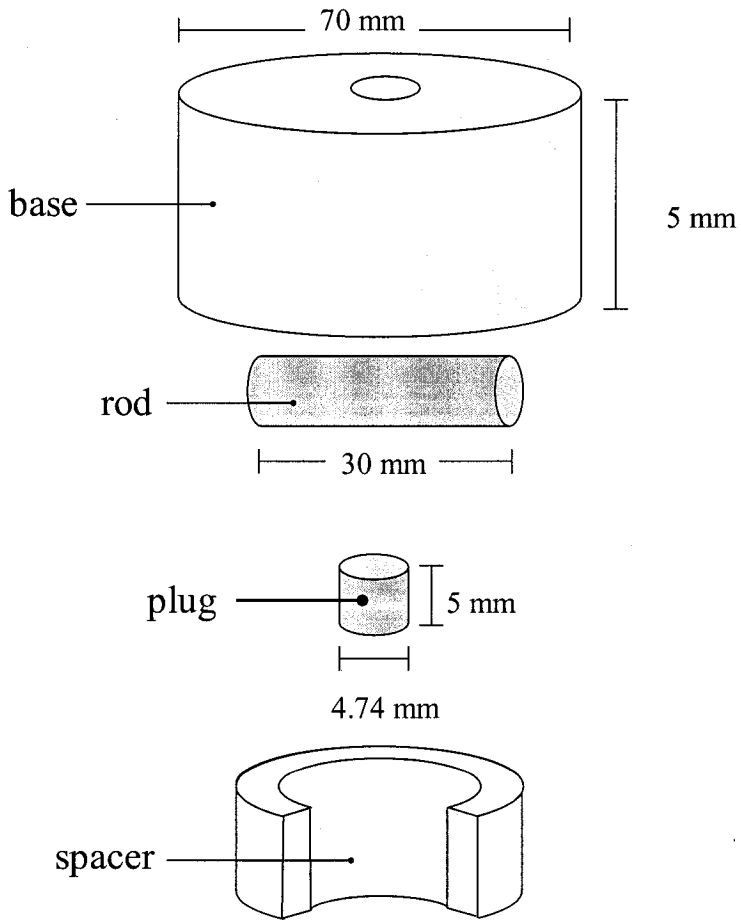

Figure 2.5. Schematic of pellet press assembly components.

To press samples, the procedure outlined in this section and shown schematically in Figure 2.6 was followed. The press assembly was arranged as shown in Figure 2.6(a). Approximately 100 mg of powder was placed on top of the rod, and the plug was placed on top of the powder. The assembly was then turned over as shown in Figure 2.6(b) and was placed in a hydraulic Carver Laboratory Press, Model B (from Fred S. Carver, Inc., maximum load of 24,000 lbs). A load of approximately 2000 lbs was exerted on the powder, corresponding to a pressure of approximately 0.5 GPa. To retrieve the pellet, the assembly was again inverted, the spacer was put in place as in Figure 2.6(c) and the entire assembly was placed in the lab press. Only a small amount of pressure was needed to push the plug and formed pellet out of the base.

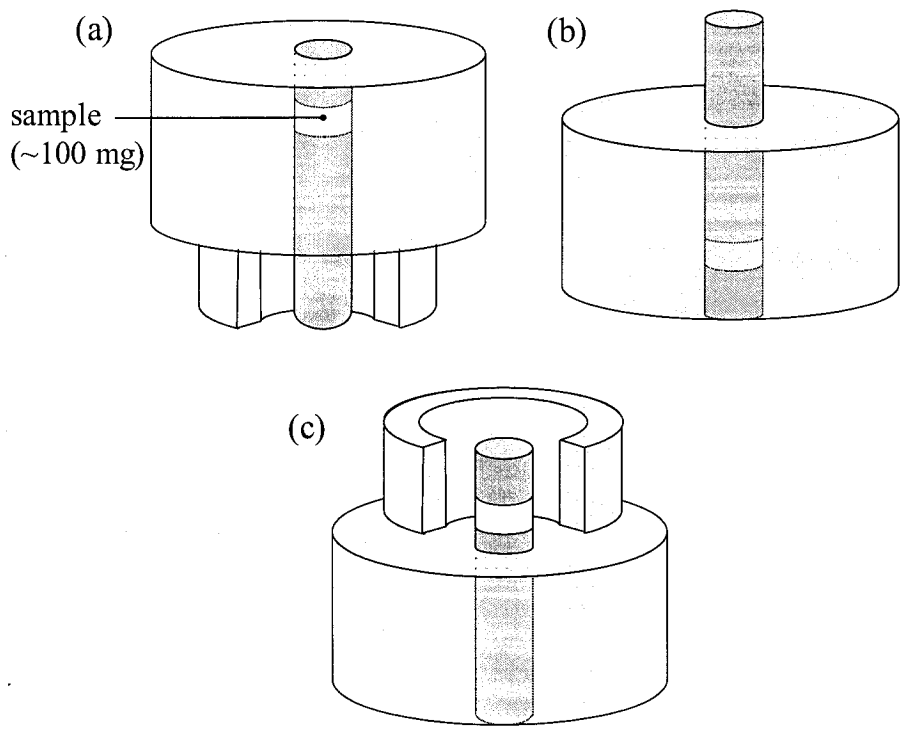

Figure 2.6. Procedure for pressing pellet with press assembly. (a) Place sample between rod and plug, (b) invert assembly to put in press, and (c) push pellet from the base.

The amount of powder needed to make a pellet shaped sample depends on the density of the material and its transport characteristics. The geometry of the sample is constrained in several ways. The area is constrained by the size of the pressing assembly (Figure 2.5). The thickness of the sample in pellet, l, is limited by the thermal diffusion time constant for the sample defined as $\tau \sim C \times l^2/\kappa$. Too thick a sample would result in excessively long measurement times while the minimum thickness is governed by the optimal temperature drop across the sample ($\Delta T \sim 0.03 \times T$). The maximum heater power, P, for the 2 kΩ heater in the PPMS is 50 mW where $P = \kappa \times \Delta T \times (A/l)$ and A is the sample area. If the ratio of the heater pulse period to the τ_l is less than 8 : 1, the curve-fitting software will not be able to adequately fit the data.[50] Also, if the pellets are too thin, it is difficult to epoxy them to the copper leads without causing a thermal short. To obtain good results, several pellets may have to be tested before the height is optimized.

2.2.6. Standard Materials

The accuracy and precision of the thermal conductivity option of the PPMS were determined previously for several NIST standard reference materials by the manufacturer and have been reported by Dilley *et al.*[47] The results for stainless steel and Pyrex glass are shown in Figure 2.7. Both samples were mounted in a two-probe configuration and were measured using continuous mode. The agreement of the κ data is excellent for both samples.

For thermal conductance, K, typical accuracies quoted by QD are the greater of ± 5% or an absolute K value for each of the following temperature ranges: ± 2 μW/K for T < 15 K, ± 20 μW K^{-1} for 15 K < T < 200 K, ± 0.5 mW/K for 200 K < T < 300 K, and ± 1

mW/K for $T > 300$ K. For measurements in this thesis, uncertainties in κ will include this uncertainty in K along with the uncertainties in measuring the diameter and the height of the pellet since $\kappa = (K \times l)/A$. A maximum and minimum κ are calculated assuming that the uncertainties in the height and diameter are both 0.02 mm.

Quantum Design includes a nickel calibration sample in their TTO user's kit. The nickel metal (grade 201) sample has a four-probe configuration and can be used as reference and calibration verification for all standard thermal transport measurements, including thermal conductivity.[50] The thermal conductivity of the nickel sample, measured three separate times over nine months, is shown in Figure 2.8 compared to literature data from 30 to 300 K from Powers *et al.*[56] on commercially pure nickel. The deviations from literature are shown in Figure 2.9. The PPMS measurements have good reproducibility over time, and match well with literature value, to within the uncertainty of the measurement. This sample is not considered a standard material by NIST; however it is useful for determining changes in the instrument over time. The high-temperature tail in thermal conductivity is common in samples with high thermal conductivity due to high thermal radiation of the sample, however, there are sample preparation techniques to follow that help manage the thermal radiation of samples.[50]

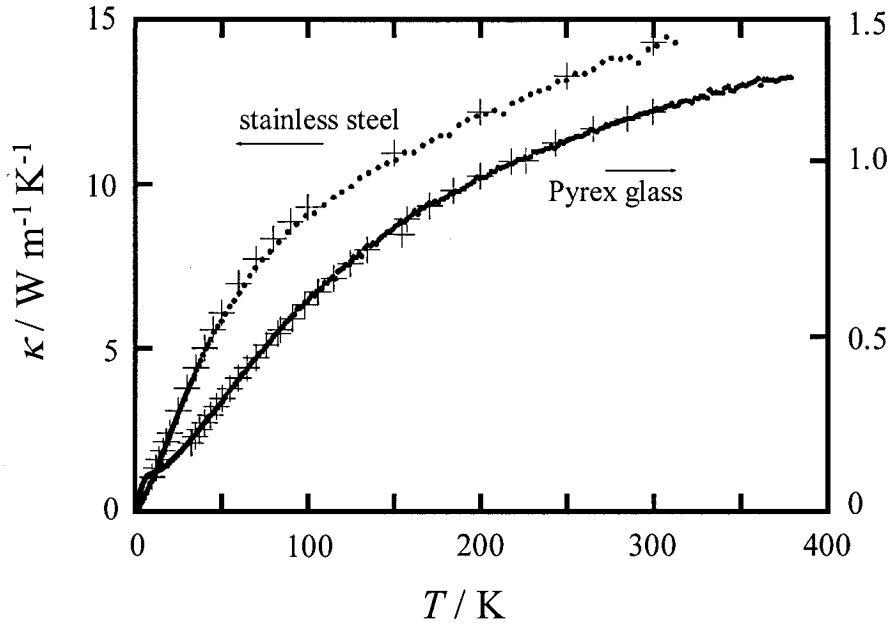

Figure 2.7. Temperature dependent thermal conductivity for stainless steel and Pyrex glass. • Quantum Design, + NIST. Redrawn from reference 47.

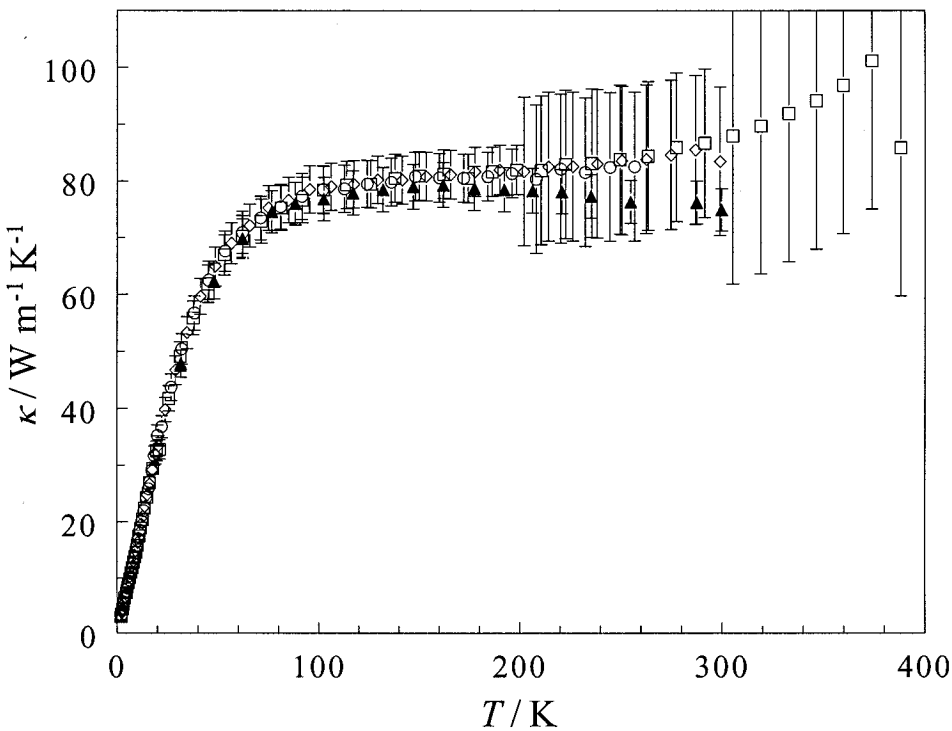

Figure 2.8. Thermal conductivities of nickel as a function of temperature. ○ PPMS 02/24/04; ◊ PPMS 08/06/04; □ PPMS 09/2/04; ▲ Power *et al.*[56]

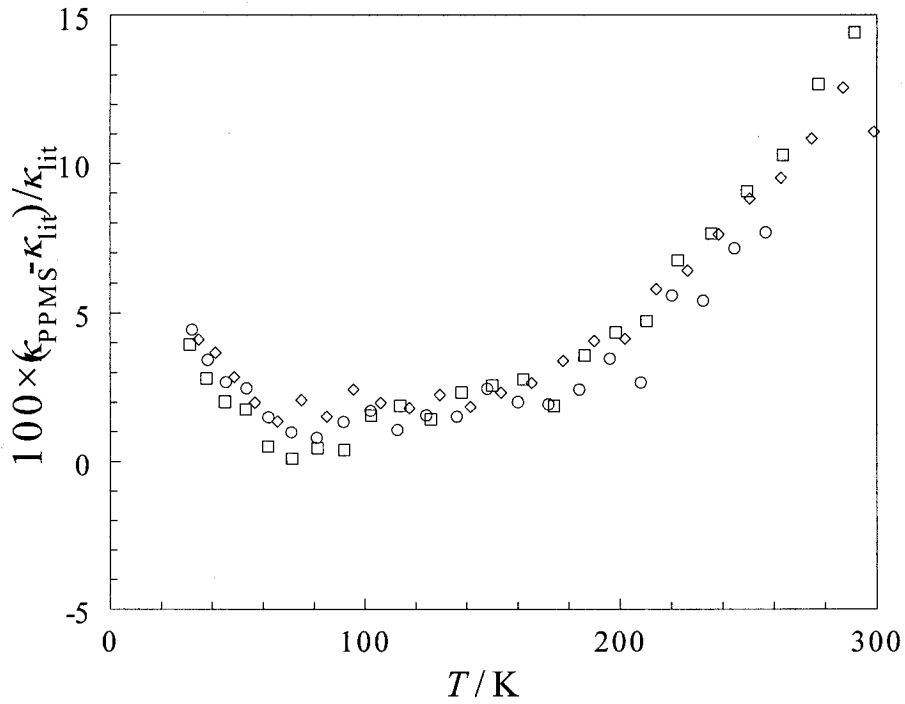

Figure 2.9. Relative thermal conductivity differences of nickel from smoothed literature source (Power *et al.*[56]) as a function of temperature. ○ PPMS 02/24/04; ◊ PPMS 08/06/04; □ PPMS 09/2/04.

2.2.7. Conclusions for Thermal Conductivity

Measuring thermal conductivity with the PPMS is possible for materials of various morphologies. Powdered samples can be pressed into a pellet configuration and can be carefully epoxied to copper plates to measure the thermal conductivity. κ can be measured in a temperature slewing mode where parameters need to be optimized to model ΔT, or in a steady-state mode where κ is measured from a direct temperature difference. As discussed in Chapter 3, the two modes show no discernable difference in κ for samples measured here.

Previous measurements on NIST standards show that this technique gives precise measurements for stainless steel and Pyrex glass, however the accuracies for measuring K vary with temperature. A small value of K at high T introduces a large uncertainty into

the measurement since uncertainty is the largest of 5% of K or 1 mW K^{-1} (1 mW K^{-1} is typically the larger of the two for my measurements). The uncertainties in measurements are typically > 10% at high temperatures.

It is important to epoxy the samples to the copper disks with great care since failure to do so will affect the surface area used for the calculation of κ. The quality of the thermal contact between the pellet shaped samples and the copper disks also seems to have a significant effect on measured κ.

2.3. Calorimetry

Accurate heat capacity data are essential to determine thermodynamic quantities, to reveal phase transitions, to give information on the entropies associated with these transitions, and to determine the order of the transitions. To be useful, the precision and accuracy of the heat capacity determination should be 1% or better, however, achieving this in practice depends greatly on whether the heat capacity of the sample is a substantial part of the total heat capacity (sample and calorimeter).[57]

The principles of calorimetry were first studied by Joseph Black (1728-1799) who established the concepts of latent and specific heat capacity.[58] His calorimeter consisted of a hollowed block of ice in which a material of known temperature was placed. Black's method was to measure the amount of ice melted by soaking it up with a sponge and weighing the water that the sponge absorbed.[59]

Since these early experiments, calorimetry has expanded to encompass many different types of methods and experimental instruments. A trend in the field of calorimetry has been the reduction of the sample size needed to make heat capacity

measurements accurately, with one of the most recent advances coming from Quantum Design: the relaxation calorimeter in the PPMS is capable of accurately measuring samples as small as 1 mg.[52]

The heat capacity measurements for this thesis were performed with two separate calorimeters, a small sample size automated calorimeter based on equilibrium methods and a commercially available calorimeter, PPMS, based on relaxation methods. A Perkin-Elmer® Pyris™ 1 power-compensated Differential Scanning Calorimeter, DSC, also was used for thermal analysis.

2.3.1. Adiabatic Calorimetry

2.3.1.1. Principles and Procedures

A description of the adiabatic heat-pulse calorimeter designed by Van Oort and White[36] along with measurement procedures are summarized in this section. The applied principle, $C = q/\Delta T$, which describes the heat capacity as heat, q, is applied to the sample and the temperature rise ΔT, is well known.

The applied heat pulse, q, is controlled by varying the time of heat pulse, t, and voltage, V, and measuring the rise in temperature,

$$q = \frac{V^2 t}{R} \qquad 2.9$$

where R = 590 Ω is the resistance of the heater. C_P at T_{avg} is obtained for a temperature determined from the average temperature, $T_{avg} = (T_i + T_f)/2$, where T_f is the final temperature, and T_i is the initial temperature.

This calorimeter, shown schematically in Figure 2.10, was designed so that a

relatively small amount sample (~5 cm^3) could be used. The heat capacity of material can be measured from $T = 40$ to 310 K with this apparatus. The sample vessel is made of copper that was gold-plated to prevent reaction with the sample. The vessel is hermetically sealed with a 0.5 mm indium wire o-ring. The sample vessel and the heater/thermometer assembly are hung from the lid of the adiabatic shield by a nylon filament loop. The sample vessel sits in a copper thermometer/heater assembly.

Temperature is measured over the range of 40 to 310 K using a four wire platinum resistance thermometer from Lake Shore Cryogenics (12.1 mm, Pt-103, 100 Ω at $T = 273$ K). The temperature is monitored as a resistance ratio, using a standard 100 Ω resistor at room temperature. The resistance ratio is determined using a 1 mA current in the forward and reverse direction. The thermometer is located in a small cylindrical cavity which extends up from the bottom of the assembly, fits into a corresponding cavity in sample vessel, and is held in place by low-temperature varnish (GE 7031). The heater consists of double silk wound Karma wire (2.6 m, 590 Ω) and is wound bifilarly around the heat/thermometer assembly held in place by GE 7031 varnish. Current is supplied to the heater using a constant DC voltage supply. The voltage and resistance measurements were made using a Hewlett Packard 3456A digital voltmeter.

Quasiadiabatic conditions in the system are maintained using an adiabatic shield that has its own heater composed of bifilary wound manganin wire (15 m, 100 Ω). The shield temperature is controlled proportionally based on the temperature difference between the shield and heater/thermometer assembly, measured using a copper-constantan thermocouple. The proportional component of the controller (set point) is adjusted as the system temperature changes.

The sample vessel, sample vessel lid, vessel screws and indium wire o-ring were stored within a vacuum desiccator before loading into calorimeter. Their masses as well as the sample mass were measured to within 0.1 mg. The sample was sealed in the vessel within an ultra-high-purity helium atmosphere to ensure that there is adequate thermal contact with the sample. To check for leaks in the seal, the sample vessel containing the sample of known mass was put under vacuum for at least 12 hours and the mass was measured at the end of the period to see if there was any mass change.

The vessel was then placed in the heater/thermometer assembly with a small amount of Apiezon T grease to ensure sufficient thermal contact between the two components. The assembly was hung from the lid of the adiabatic shield using the nylon filament loop shown in Figure 2.10.[60] The adiabatic shield was then suspended from the heat sink using three nylon filaments shown in Figure 2.11. All leads from the heater/thermometer assembly to the adiabatic shield and from the adiabatic shield to the calorimeter electronic board were soldered using thermal-free solder from Leeds and Northrup (70.44% Cd + 29.56% Sn, T_{melt} = 175 °C) which gives a low thermo-electric forces with respect to copper.[8]

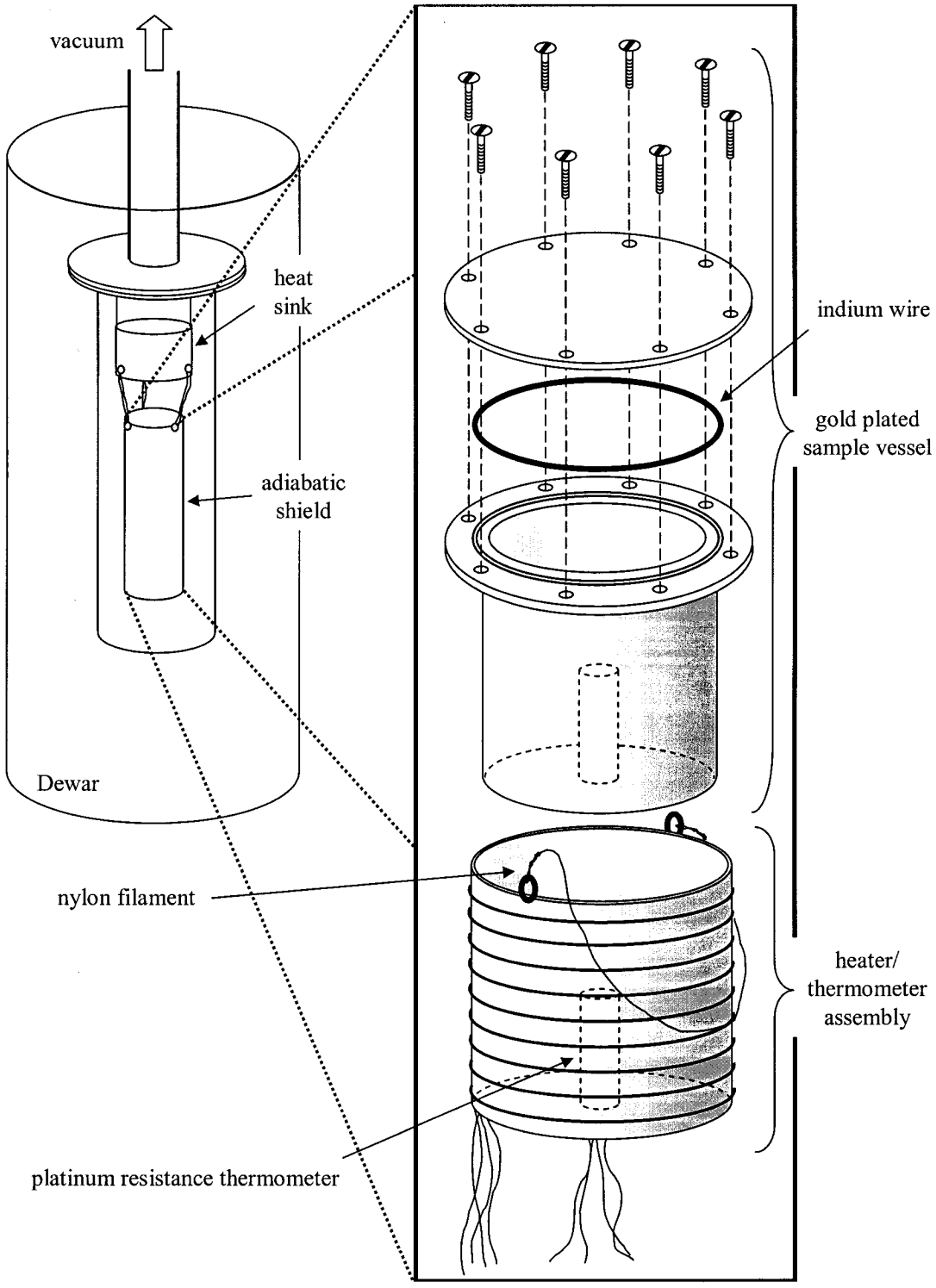

Figure 2.10. Schematic of small sample adiabatic calorimeter.[60] Used with permission from author.

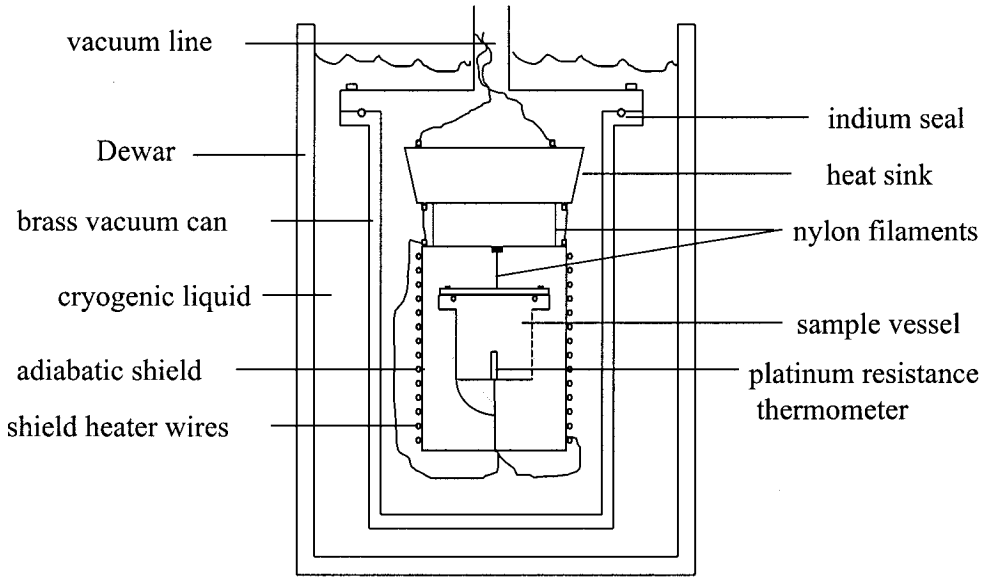

Figure 2.11. The inner cell of the adiabatic calorimeter showing the sample vessel hanging by a nylon filament in the inner brass vacuum can.

The calorimeter chamber must be evacuated to a pressure less than 1.5×10^{-5} Torr and once low pressure is achieved, the Dewar is slowly filled with either liquid nitrogen or liquid helium cryogen depending on the temperature range being studied.

A typical experiment required to determine the heat capacity is shown schematically in Figure 2.12. The method began by adjusting the set-point of the adiabatic shield controller, until the temperature drift was less than 5 $\mu K\ s^{-1}$. Data are collected every 45 seconds for 30 to 90 minutes (time of collection is dependent on temperature range) before and after the applying the heat pulse.

If the average temperature drift is higher than the designated value, the data were discarded. The temperature was measured as a resistance ratio, *RR*. The resistance ratios vs. time data collected before and after the pulse, excluding a short relaxation region after heat, were linearly extrapolated to the mid-point time of the pulse. These extrapolations provided the initial and final temperatures, T_i and T_f, respectively.

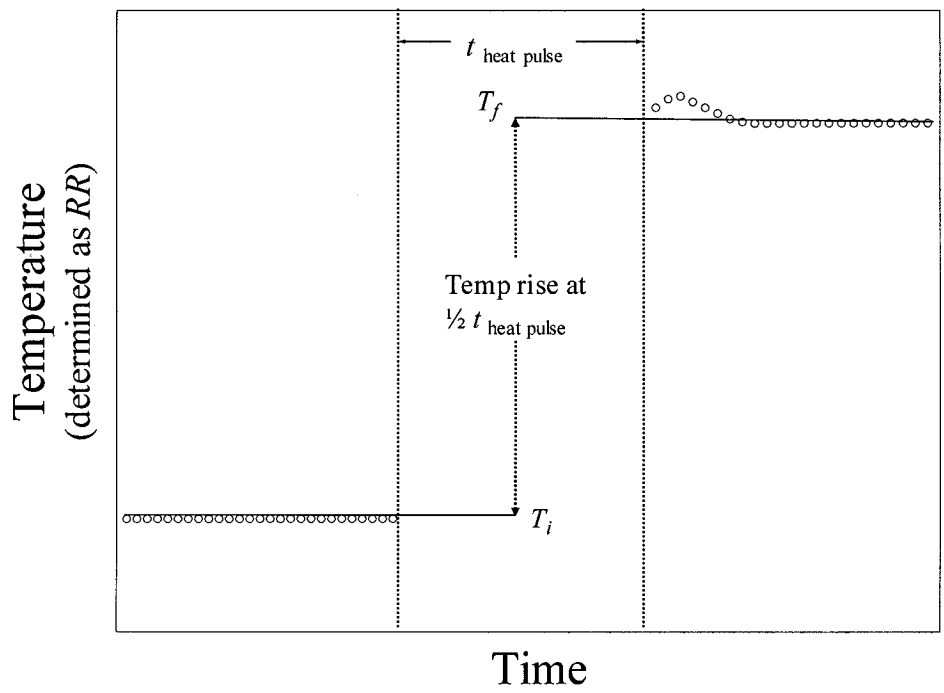

Figure 2.12. A typical adiabatic calorimeter experimental sequence.

The resistance of the heater was recorded in triplicate before and after the heat pulse. The applied voltage was recorded at the start, at the half way point of the heating period (during a pause in the heating process), and just before the end of the heating. The heat capacity of the sample is calculated as

$$C_P(T_{avg}) = \frac{q}{T_f - T_i} - C_P(vessel) \qquad 2.10$$

where the heat capacity of the empty vessel, C_P(vessel), had been determined previously and a quadratic spline fit was used to store this data within a custom made computer program. C_P(vessel) also includes corrections for the C_P of the grease and the indium wire. The accuracy and precision of this calorimeter were not determined in this thesis work but have been determined previously[36,61] and are discussed later in this chapter.

2.3.1.2. Standard Materials

Calorimetry Conference benzoic acid (C_6H_5COOH), a common reference material for adiabatic calorimeters, was used by Van Oort and White[36] to evaluate the accuracy of the small sample adiabatic calorimeter described for 50 K < T < 310 K. The benzoic acid was prepared for the Conference on Calorimetry by the National Bureau of Standards in March 1949.

This calorimeter was determined to be usually within ± 0.5% of the literature values[62] when 50% of the total heat capacity of the entire system arose from the benzoic acid at higher temperatures. The platinum resistance thermometer used in this calorimeter is not as accurate below 50 K, therefore the lowest-temperature heat capacity measurements cannot be considered as accurate compared to higher temperature measurements. Results from this study are shown in Figure 2.13.

A study on the heat capacity of NaOH conducted by Bessonette and White[61] showed accuracy to within 1.2% of the literature values with 45% of the total heat capacity being due to the NaOH at higher temperatures. Another comparison between a clathrate material ($Sr_8Ga_{16}Ge_{30}$) measured with this calorimeter[63] and a QD PPMS[64] show that the adiabatic calorimeter results are within ± 5% of the PPMS results for 80 K < T > 300 K, and are within ± 10% for 30 K < T < 80 K. However, the C_P of the sample in the adiabatic calorimeter only comprised of 15% of the total heat capacity at T = 300 K and 10% at T = 30 K.[63]

A more recent comparison of heat capacity measurements using both the adiabatic calorimeter and the PPMS are included in Chapter 3. The adiabatic calorimeter results are within ± 1% of the PPMS results for 90 K < T < 300 K, and are within 3% for 40 K <

$T < 90$ K with more than 30% of the total heat capacity being due to the sample at all temperatures.

Uncertainties for measurements with the adiabatic calorimeter in this thesis were calculated using standard propagation of errors based on the standard deviation of the sample mass, calorimeter mass, the addenda heat capacity measurement, and the total heat capacity measurement. This uncertainty is considered constant for $T = 50$ to 300 K and is based on the smallest contribution to the total heat capacity, $100 \times \delta C_P(\text{sample})/C_P(\text{total})$ for the sample. The resistance ratio sensitivity to temperature change, dRR/dT, is small for $T < 50$ K and causes more uncertainty in the ΔT measurement by adiabatic calorimetry. The uncertainties are given with the reported data.

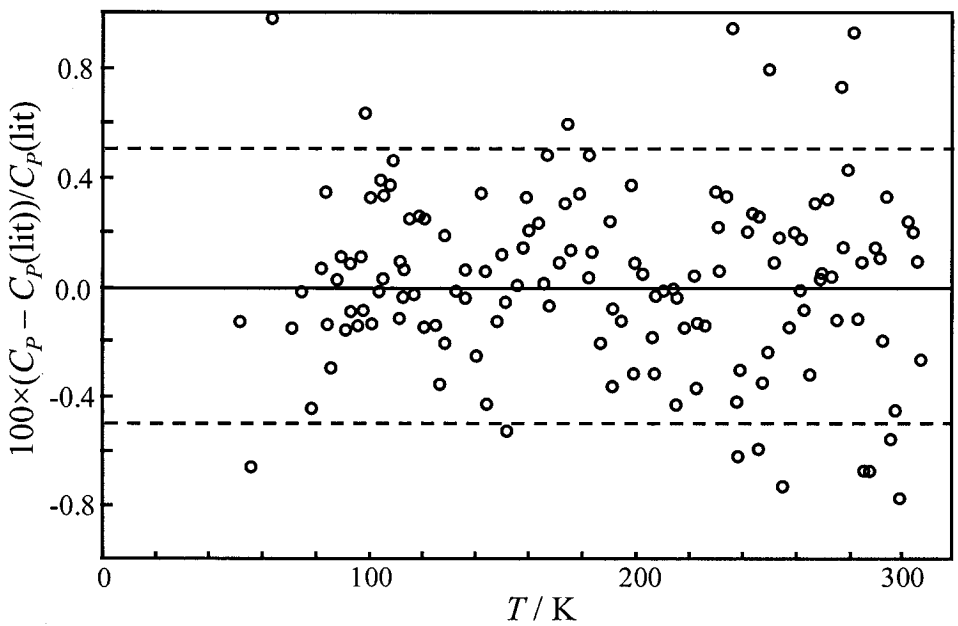

Figure 2.13. The relative difference between the heat capacity of benzoic acid measured by the adiabatic calorimeter and the reported literature values.[62] This diagram is restyled from Figure 2 of Van Oort and White.[36]

2.3.1.3. Conclusions for Adiabatic Calorimeter

The study conducted by Van Oort and White with the small sample adiabatic calorimeter found the calorimeter to be accurate to within 0.5%.[36] This was with 50% of the total measured heat capacity being from the sample contribution for $T = 50$ to 300 K. A more recent study shows a deviation of 1.2% from literature values with the sample contribution being > 45%. The resistance ratio sensitivity to temperature change, dRR/dT, is small for $T < 50$ K and thus causes more uncertainty in the ΔT measurement by adiabatic calorimetry.

2.3.2. Relaxation Calorimetry

2.3.2.1. Introduction

The second type of calorimeter used in this work is part of the PPMS system and is based on a heat-pulse calorimeter using thermal relaxation methods. The calorimeter described in the previous section has limitations on the sample size (needs ~ 5 cm^3 of sample) and the temperature range of measurement. The advantage of relaxation calorimeters is the small sample size; masses in the range of 1-200 mg can be measured. Relaxation calorimeters are faster than traditional heat-pulse adiabatic calorimeters and are typically more useful for lower temperatures measurements, to $T = 0.4$ K with the present PPMS.[14] There are limitations in the accuracy of the relaxation measurement technique that arise due to poor thermal contact between the sample and the platform. These two techniques complement each other; a more detailed comparison is presented later in this chapter.

Using the PPMS, the heat capacity is determined by modeling the thermal

response of the sample upon heating and is based on methods from Hwang *et al.*[65] There are two separate assemblies on which measurements can be made. The first assembly is used to measure samples over the temperature range of $T = 1.9$ to 400 K with a reported resolution of 10 nJ K^{-1} at $T = 2$ K.[52] This assembly will be referred to as the Helium-4 calorimeter system or hereafter called ^{4}He system, since ^{4}He is used as the cryogen. The system also is equipped with a Helium-3 calorimeter system, hereafter called ^{3}He system, and uses ^{3}He to reach temperatures as low as $T = 0.4$ K. The maximum achievable temperature for the ^{3}He system is $T = 350$ K.

2.3.2.2. Principles and Procedures

The PPMS relaxation calorimeter consists of a very small platform which is in thermal contact with a sample of unknown heat capacity and has a weak thermal link to a heat sink at constant temperature, T_b, as shown in Figure 2.14. The sample and the platform are heated to some temperature $T = T_b + \Delta T$ and then allowed to relax back down to T_b. A temperature increase ($\Delta T/T_b$) of 2% was employed for measurements made in this thesis.

The set-up procedure and thermal methods described in this section are applicable for the ^{4}He and ^{3}He assemblies and were adapted from the Hardware and Options Manual obtained from Quantum Design.[50] The platform/sample assembly for the relaxation calorimeter is shown schematically in Figure 2.15. This puck is plugged into the sample chamber within a Dewar from above. The assembly consists of 3×3 mm sapphire platform which is attached to the puck frame using 8 thin wires. A thin film heater and a Cernox sensor™ from Lake Shore Cyrotronics are attached to the back of the platform.

A radiation shield fits over the top of the puck. The system is evacuated to 10^{-4} Torr.

The software included with the PPMS employs two types of models for temperature decay. The first model is the Single-Tau Model. It operates under the assumption that there is good thermal contact between the sample and the platform, see Figure 2.14(a), so the temperature and heat capacity of the platform, grease, and sample (if present) are given by $C_{P,pl}$ and $T_{pl}(t)$. The thermal conductance of the wires, K_w needs to be considered.

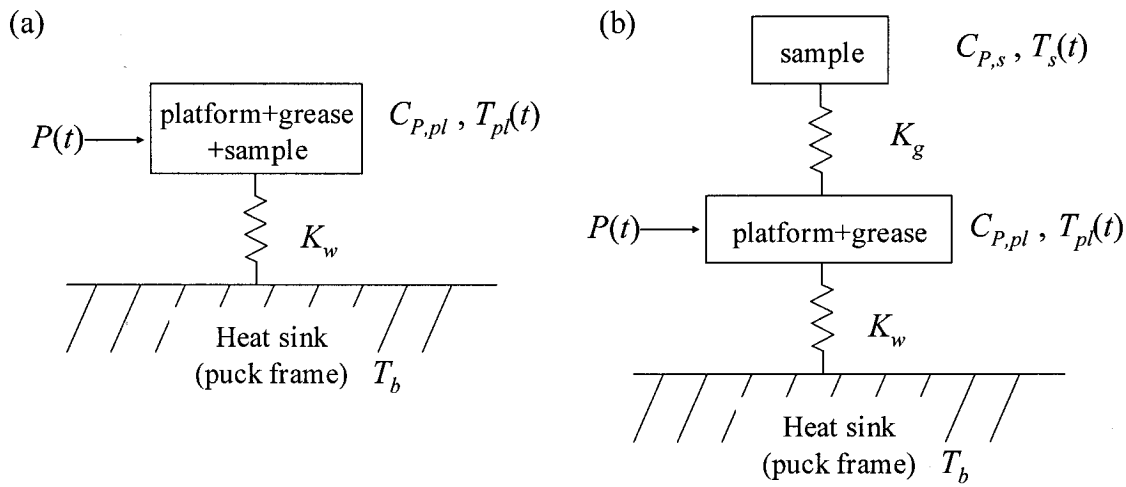

Figure 2.14. Schematic of the relaxation calorimeter. (a) Single-Tau Method, good contact is achieved between the sample and platform. Heat capacity and temperature of platform, grease, and sample (if present) are given by $C_{P,pl}$ and $T_{pl}(t)$ respectively. The platform is thermally connected to the puck (at a temperature T_b) by wires that have a thermal conductance K_w. $P(t)$ is the power used to heat sample. (b) Two-Tau Method™, the sample, described by heat capacity, $C_{P,s}$, and temperature, $T_s(t)$, is in poor thermal contact with the platform, described by heat capacity, $C_{P,pl}$, and temperature, $T_{pl}(t)$. The sample and platform are connected using thermally conductive grease that has a thermal conductance of K_g.

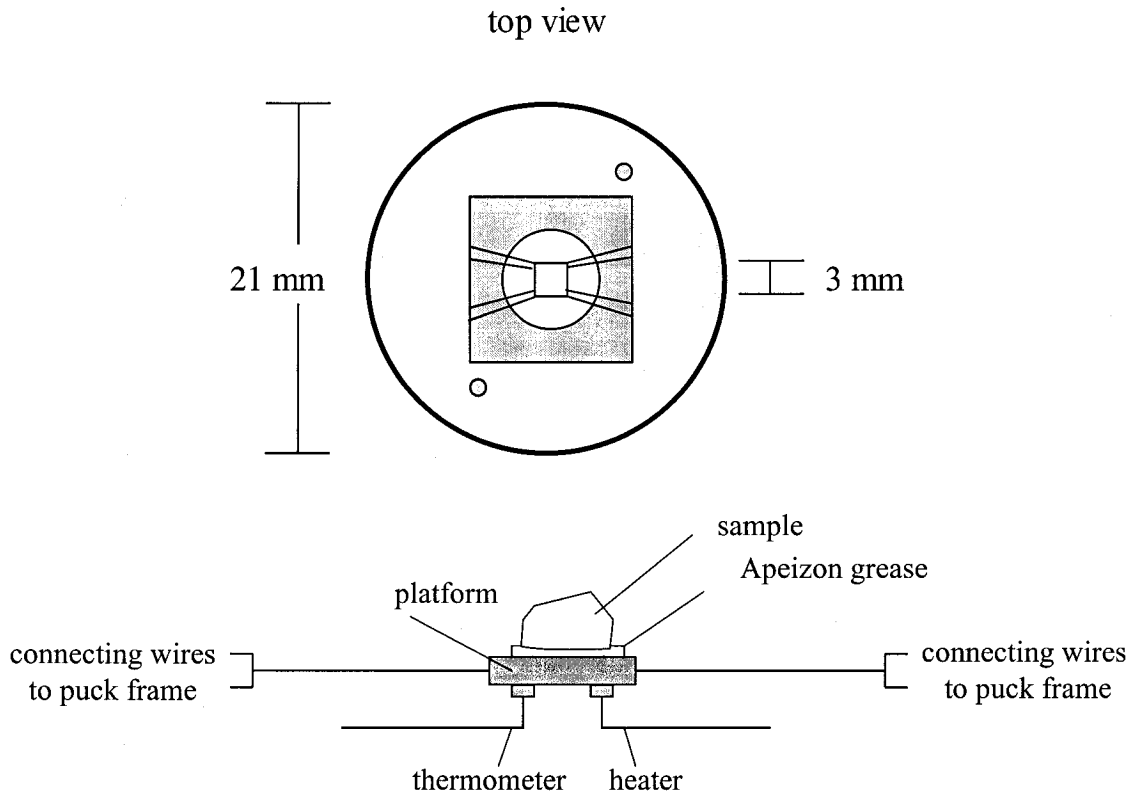

Figure 2.15. Schematic of the PPMS relaxation calorimeter puck assembly for the ^{4}He and ^{3}He systems.

To model the thermal response to the heat applied to the platform, the following heat balance equation is considered:

$$C_{P,pl}\frac{dT}{dt} = -K_w(T - T_b) + P(t) \qquad 2.11$$

where T_b is the temperature of the puck frame and $P(t)$ is the heater power (equal to the applied heat during the heating portion and zero when cooling). When the power being applied is discontinued, the temperature decay (back to T_b) is described by solving the heat balance differential equation (Equation 2.11) and the time constant, τ_1, is obtained from the temperature decay of the platform (including platform, grease and sample, if present):

$$T_{pl}(t) = T_b + \Delta T e^{-t/\tau_1}. \qquad 2.12$$

where $\tau_1 = C_{P,pl}/K_w$ characterizes the temperature relaxation between the sample holder (the platform) and the heat sink.[65]

Two separate measurements are required to determine the heat capacity of a sample. The first measures the heat capacity of the platform and the grease (using Single-Tau Model). This acts as an addendum for the second measurement in which the heat capacities of the platform, the grease, and the sample are considered (using the Single-Tau Model only if thermal contact between sample and platform is good and otherwise using the Two-Tau method, see below).

When the sample and platform are not in good thermal contact, the thermal conductance of the grease, K_g, has to be included, see Figure 2.14(b). A second time constant, τ_2, which arises from the poor thermal connection between the sample and platform is needed to model the heat capacity.[65] QD has named this the Two-Tau Model™.[52] Poor thermal contact has a tendency to distort the shape of the relaxation curve for these cases.

The heat balance equations for the platform and sample are

$$C_{P,pl}\frac{dT}{dt} = P(t) - K_w(T_{pl}(t) - T_b) + K_g(T_s(t) - T_{pl}(t)) \qquad 2.13$$

and

$$C_{P,s}\frac{dT}{dt} = -K_g(T_s(t) - T_{pl}(t)). \qquad 2.14$$

Solving Equations 2.13 and 2.14 to model the thermal relaxation

$$T_{pl}(t) = T_b + Ae^{-t/\tau_1} + Be^{-t/\tau_2} \qquad 2.15$$

gives two exponential decay functions, one with a long time constant, τ_1, and one with a short time constant, τ_2, as:

$$\tau_1 = \frac{1}{(A_\tau + B_\tau)}, \ \tau_2 = \frac{1}{(A_\tau - B_\tau)} \qquad 2.16$$

where τ_1 and τ_2 physically represent the thermal relaxation of the sample and the thermal relaxation of the platform, respectively. The expressions for A_τ and B_τ are:

$$A_\tau = \frac{K_w}{2C_{P,pl}} + \frac{K_g}{2C_{P,pl}} + \frac{K_g}{2C_{P,s}} \qquad 2.17$$

and

$$B_\tau = \frac{\sqrt{K_g^2C_{P,s}^2 + 2K_g^2C_{P,s}C_{P,pl} + K_g^2C_{P,pl}^2 + K_w^2C_{P,s}^2 + 2K_w^2C_{P,s}^2K_g - K_wC_{P,s}K_gC_{P,pl}}}{2C_{P,pl}C_{P,s}}. \qquad 2.18$$

Figure 2.16 gives a typical heat capacity measurement for a sample showing the thermal response.

Apiezon® grease is used to attach the sample to the puck platform. The grease is required to attach the sample to the platform but also to ensure that there is good thermal contact between them. Apiezon N grease is used from T = 0.4 K - 305 K and Apiezon H grease is used for experiments above T = 305 K. Both have good thermal transport properties, low vapour pressures, and are inert; however Apiezon N has a glass transition-like anomaly at approximately 215 K and a peak transition at approximately 290 K.[66] Samples masses are measured to ± 0.001 mg. The accuracy of the technique was verified by evaluating the heat capacities of Calorimetry Conference sapphire crystals and

National Institute of Standards and Technology (NIST) copper reference material, RM-5. The results of these measurements are discussed in Section 2.3.4.3.

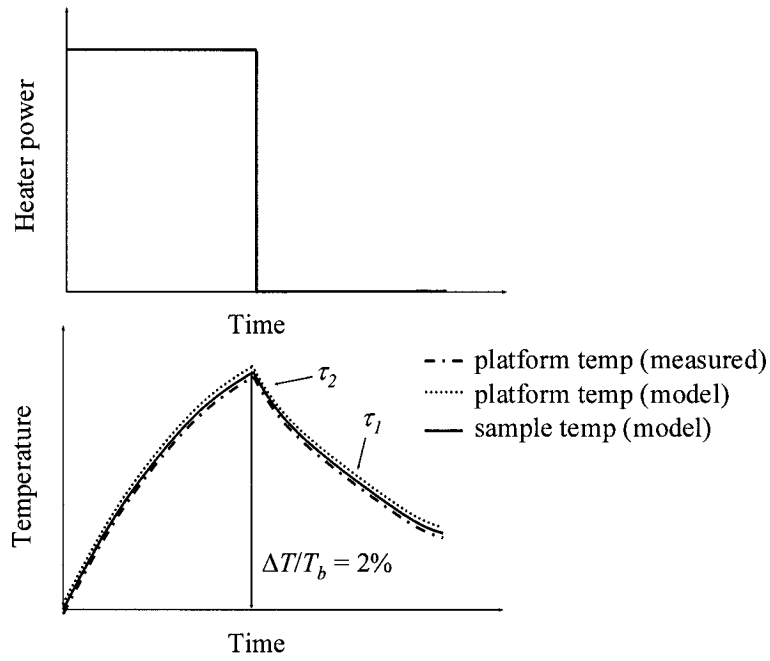

Figure 2.16. Typical temperature response to applied heat during the heat capacity measurement. Thermal relaxation is modeled using the Single-Tau or the Two-Tau™ method depending on quality of contact between sample and platform. This schematic shows the Two-Tau™ method to model temperature decay.

2.3.2.3. Standard Materials

When measuring samples with the PPMS that are single crystals or pressed-powders with low vapour pressures, the sample can be placed directly on the sample platform to perform the measurement. The accuracy of the ^{4}He heat capacity option of the PPMS was verified by measuring two high purity standard materials, synthetic sapphire (α-Al_2O_3), and high purity polycrystalline copper. The accuracy of the ^{3}He option was verified by measuring high-purity polycrystalline copper. The sapphire was obtained from the Conference on Calorimetry (March 1949) and copper (Reference Material 5) was obtained from National Institute of Standards and Technology (NIST).

2.3.2.3.1. PPMS ^{4}He System-Sapphire

Three sapphire crystals with masses of 13.567 ± 0.020 mg, 15.180 ± 0.020 mg, and 32.781 ± 0.010 mg were used for the heat capacity measurements from T = 1.83 K to T = 300 K.

Care was taken when selecting the optimal sample mass because too small a sample decreases accuracy since the heat capacity is additive, *i.e.* C_P(total) = C_P(sample) + C_P(plat). In order to ensure accurate heat capacity data, samples for the PPMS must be large enough that $100 \times C_P(\text{sample})/C_P(\text{total}) > 50\%$ for insulators and > 33% for metals.[76] However, too large a sample will lead to too long a time for the temperature of the sample to relax back to the initial temperature (before application of the heat pulse). The sample-to-platform contact is improved by the use of the appropriate grease, however, in some instances the thermal contact could be poor. The Two-Tao™ model estimates the sample-to-platform contact (called thermal coupling) as a percentage, 100% indicates perfect thermal contact, 0% indicates no thermal contact. Less than 90% would be considered poor thermal coupling, either due to too large a sample or poor contact. Both the sample contribution to the total heat capacity and the sample coupling must be considered to obtain accurate results.

The sapphire crystals were measured in three separate experiments. In each experiment, the sapphire crystal was placed directly on the Apiezon® N grease that was used for the addendum measurement. The data were collected in triplicate at approximately 5 K increments from T = 45 K to T = 300 K, and, from 1.83 K to 50 K, 50 data points were collected in a logarithmic temperature manner. The temperature rise was 2% of the set-point temperature and the Two-Tau™ method was used to compute the

heat capacity. The heat capacities and fraction of the heat capacity of the sapphire to the total heat capacity are shown in Figure 2.17.

The sapphire samples measured on the PPMS were compared to smoothed literature data for sapphire that were converted to the 1990 International Temperature Scale, ITS-90.[67] Relative differences, shown in Figure 2.18, were calculated from the smoothed equations for sapphire reported by Ditmars *et al.*[68] and Fugate and Swenson.[69] Archer[70] has reported smoothed values (spline fit) for the National Institute of Standards and Technology (NIST) based on ITS-90 where C_P data were reported from T = 10 K to 400 K. Archer's values[70] also are shown in Figure 2.18 along with values reported by Ditmars and Douglas,[71] Sorai *et al.*,[72] Viswanathan,[73] and White and Minges.[74] The literature values used in Figure 2.18 are those that show either measured or smoothed heat capacities below T = 70 K, therefore they do not include all of the over 220 reports dealing with the thermodynamic properties of sapphire noted by Castanet in 1984.[75]

The heat capacities measured with the ^{4}He option of the PPMS show accuracy and precision within 0.5% for $T > 80$ K and within 1% for $60 < T / \mathrm{K} < 80$. Below 60 K, the deviation of the PPMS sapphire data from the NIST data is large, approximately 40%. This is due to the fact that the sapphire heat capacity does not contribute significantly of the total heat capacity (< 30%) in this temperature range.

Lashley *et al.*[76] also have examined the accuracy of heat capacity measurements using the Quantum Design PPMS relaxation calorimeter and they also reported large deviation with sapphire for $T < 60$ K. This limits the use of sapphire as use as a standard test material below this temperature. Archer and Kirklin[77] have recognized this

phenomenon in their article on NIST standards for calorimetry and they recommended that copper is a more suitable material for this temperature range. Copper measurements are discussed below.

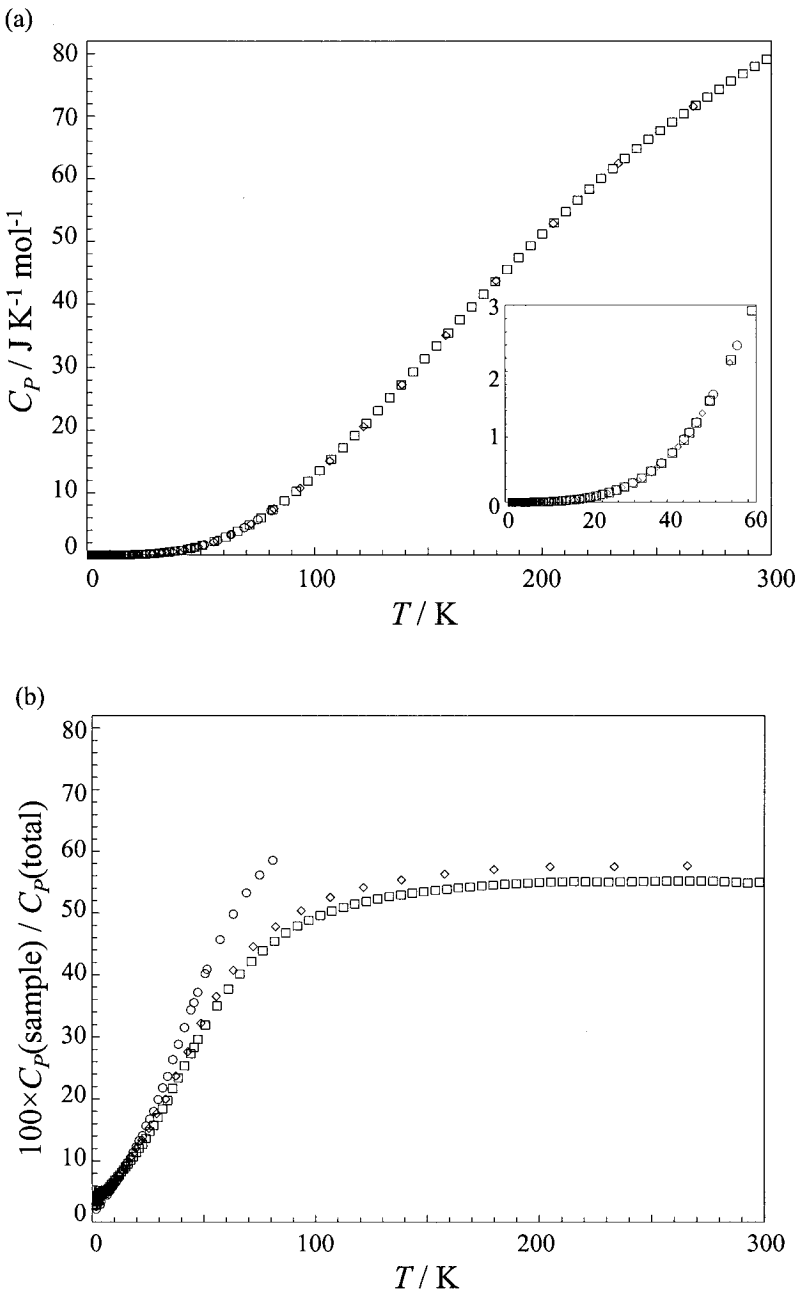

Figure 2.17. (a) Heat capacities of sapphire standard (MW = 101.961 g mol^{-1}) and (b) relative sample contributions of sapphire to the total heat capacity. ◊ 15.180 ± 0.020 mg crystal; □ 13.567 ± 0.020 mg crystal; ○ 32.781 ± 0.010 mg crystal. Error bars are not visible since the symbol is larger than the calculated uncertainty.

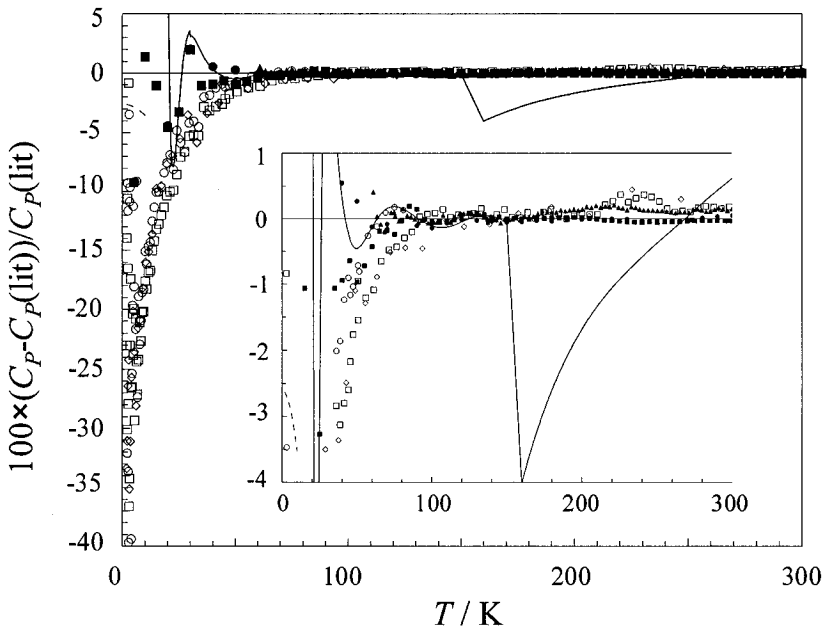

Figure 2.18. Relative heat capacity differences from smoothed literature data, C_P(lit), for sapphire. PPMS data for sapphire: ◊ 15.180 ± 0.020 mg crystal; □ 13.567 ± 0.020 mg crystal; ○ 32.781 ± 0.010 mg crystal. C_P(lit) has been calculated using the equations of Fugate and Swenson[69] for T < 30 K and Ditmars *et al.*[68] for T > 30 K. Literature data for sapphire: • Archer[70]; ■ Ditmars and Douglas[71]; ▲Sorai *et al.*[72]; ---- Viswanathan[73]; —White and Minges[74].

The estimated absolute uncertainty for the triplicate sapphire heat capacities measured with the PPMS were calculated using standard propagation of errors and are shown in Figure 2.19. The estimated uncertainties for sapphire (and for all other samples measured with the PPMS) were based on the greater of: the error calculated by twice the χ^2 statistics directly from the Quantum Design data; or the standard propagation of error based on the standard deviation of the sample mass, the addenda heat capacity measurement, and the total heat capacity measurement. The estimated uncertainties show that the precision of the measurement of sapphire with this technique is similar to accuracy, 1% for T > 80 K, but much larger below 80 K where the sample does not contribute much to the total C_P.

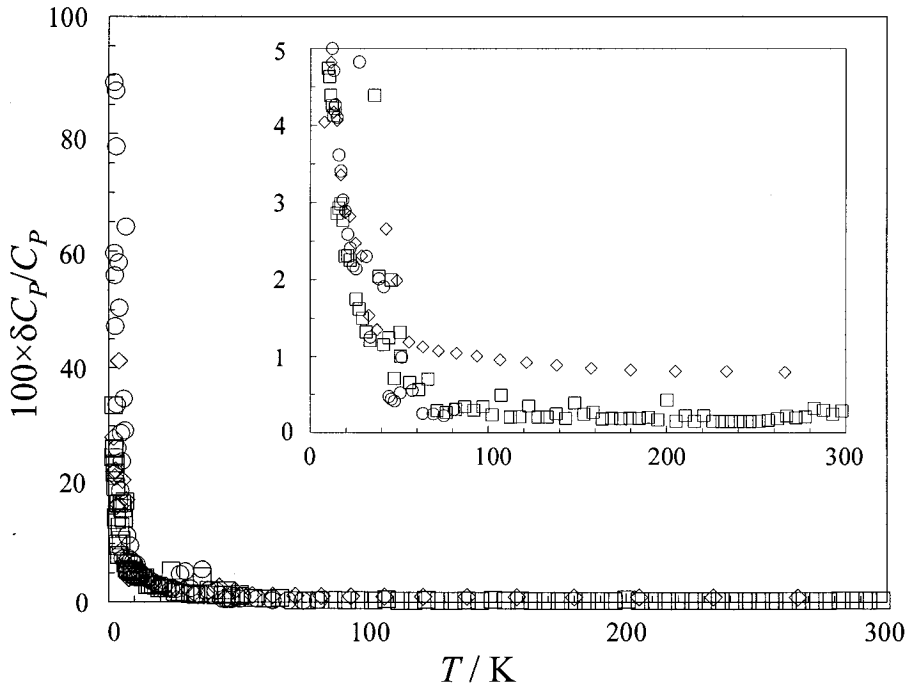

Figure 2.19. The estimated absolute uncertainty for sapphire measured with the PPMS; ◊ 15.180 ± 0.020 mg crystal; □ 13.567 ± 0.020 mg crystal; ○ 32.781 ± 0.010 mg crystal. These uncertainties have been estimated using standard propagation of error for three replicate measurements of the sample platform and the platform with the crystal.

2.3.2.3.2. PPMS ^{4}He System-Copper

High-purity polycrystalline copper Reference Material (RM 5) was obtained from NIST at 99.999+% purity in the form of a rod with dimensions of 19 mm in diameter by 120 mm in length. RM 5 is intended to be used as a comparison for heat capacity results from different laboratories. Lashley *et al.*[76] used a copper reference material from the same batch to assess the accuracy of their PPMS.

The copper rod was cut down to an appropriate size according to NIST instructions outlined in the Report of Investigation.[78] The samples were chemically etched (with 1:1 solution of nitric acid followed by 1:1 solution of hydrochloric acid) to remove any contamination introduced in the cutting process. The sample was

subsequently washed with distilled water, dried on filter paper in air and then was stored under a dry nitrogen atmosphere to prevent oxidation.

A small sample of the polycrystalline copper, mass 41.422 ± 0.010 mg, was measured using the ^{4}He system (using puck 451) from approximately T = 2 K to 150 K. The copper was kept under nitrogen atmosphere until the measurement was performed to prevent surface oxidation. The smoothest side of the copper was placed directly on the Apiezon® N grease that was used to measure the addendum. The data points were collected in triplicate, evenly spaced on a logarithmic temperature scale. The temperature rise was 2% of the absolute temperature and the Two-Tau™ method was used to calculate the heat capacity. The heat capacity and the contribution of the copper to the total heat capacity are shown in Figure 2.20.

The smoothed literature data for copper for T < 25 K are taken from a "copper reference equation" from Osborne, *et al.*[79] According to the Report of Investigation provided by NIST and the references therein, this equation gives the heat capacity of pure copper accurate to better than 1% for T < 25 K. For T > 25 K, values have been tabulated by Furukawa *et al.*[80] The reported data agree with other measurements to within better than 1% above 25 K according to Report of Investigation provided by NIST.

Figure 2.21(a) indicates that the deviation of present copper PPMS heat capacity data from the literature data is much improved for T < 60 K relative to the sapphire data shown in Figure 2.18. Copper is the superior standard for T < 60 K since copper's contribution to the total heat capacity is much larger. Figure 2.21(a) shows that the PPMS measured heat capacities that are accurate to within 4% for T < 10 K and accurate to within 1% for 10 < T < 80 K. For 80 K < T < 150 K, the copper measurements show

an accuracy of approximately 0.5%, in good agreement with the sapphire results. Copper standard results from Lashley *et al.*[76] on the ^{4}He system show that the sample deviates from literature values by 1.5% above T = 4 K, and for 1.8 K < T < 4 K, it deviates to nearly 4%.

The estimated uncertainty for the copper heat capacity measurements with the ^{4}He option of the PPMS were calculated and are shown in Figure 2.21(b). The uncertainty (or calculated reproducibility) of these measurements was within 2% for 10 < T / K < 150, but was as high as 8% at T < 10 K.

The overall analysis of the standards for the ^{4}He system shows that the system exhibits an accuracy of better than ± 1% for temperatures for T = 10 to 300 K by using samples with heat capacities that are half or greater than the calorimeter addenda heat capacity, while the accuracy diminishes to ± 4% at lower temperatures. These data confirm that the system operates within the ± 5% accuracy specified by QD.

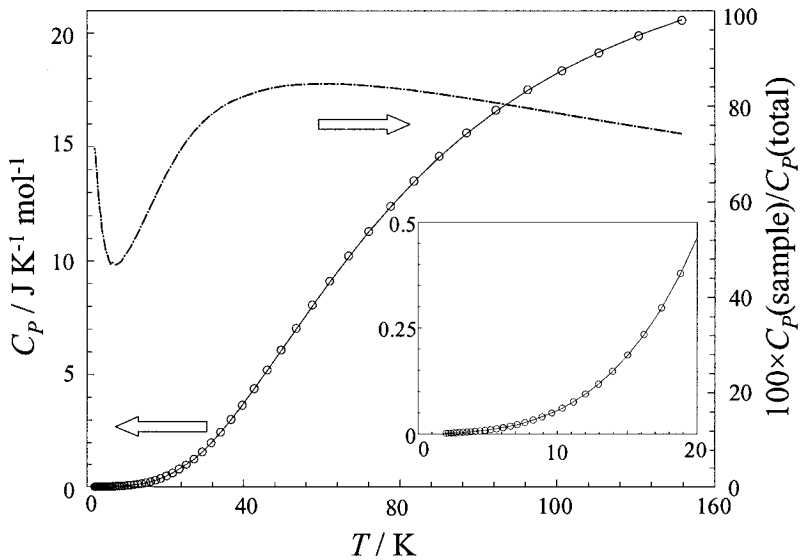

Figure 2.20. Heat capacities of the copper standard measured with the ^{4}He system and relative sample contributions to total heat capacity measurement. Error bars are not visible since the symbol is larger than calculated uncertainty.

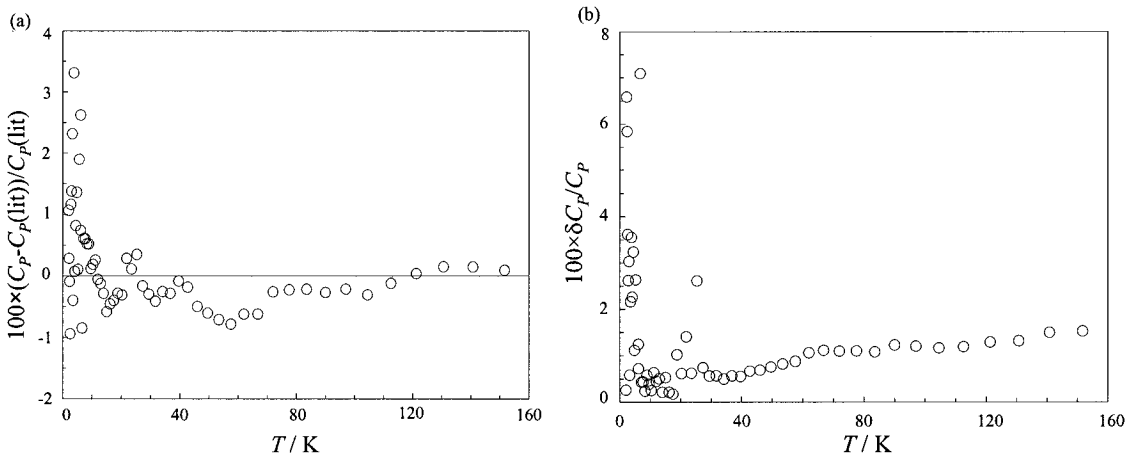

Figure 2.21. Heat capacity of copper standard measured with the ^{4}He system. (a) Relative heat capacity differences from NIST recommended smoothed data, C_p(lit). C_P(lit) has been calculated using the NIST smoothed data of Furukawa *et al.*[80] for $T > 25$ K and the equation of Osborne, *et al.*[79] for $T < 25$ K. (b) Estimated uncertainties determined using standard propagation of error for three replicate measurements of the sample platform and the platform with the crystal.

2.3.2.3.3. PPMS ^{3}He System-Copper

The copper RM 5 standard was used to test the ^{3}He system also. Two separate pucks were calibrated and verified with copper, puck 215 and puck 227. The same copper sample used in the ^{4}He system was used to assess the accuracy of the ^{3}He system with puck 215. A second copper RM 5 sample, mass 29.049 ± 0.010 mg, was prepared in the same manner as the first and was used to tested puck 227. Again, the smoothest side of the copper standards was placed directly on the Apiezon® N grease that was previously used to measure the addendum. The data points were collected in triplicate on a logarithmic temperature scale over the range of $0.4 < T / \text{K} < 10$. The heat capacity of copper and the contribution of the copper to the total heat capacity are shown in Figure 2.22 and Figure 2.23, respectively.

The smoothed literature data for copper were again taken from Osborne *et al.*[79]

Figure 2.24(a) shows that the PPMS measured heat capacities with puck 215 are accurate to within ± 2% for 2 K < T < 10 K. The estimated uncertainty shown in Figure 2.24(b), is higher than for the ^{4}He system, 10% for 2 K < T < 4 K, and 2% for T > 4 K. There were problems with the system when running the analysis for puck 215 in that the system had difficulty cooling at low temperature, and would not cool to T = 0.4 K as designated by the manufacturer. This could provide an explanation to why the accuracies and precision are less than measured with the ^{4}He system. The problem was fixed before puck 227 was tested, and the ^{3}He results in Chapter 3 and 4 were collected using puck 227, with the ^{3}He system functioning properly.

Figure 2.24(a) shows that the PPMS measured heat capacities with puck 227 are accurate to within ± 1% for 1 K < T < 10 K, but are only accurate to within ± 15% below T = 1 K. The estimated uncertainty, shown in Figure 2.24(b), is better than for puck 215, 2% for 2 K < T < 10 K, however for T < 1 K, uncertainties are very high, 35%.

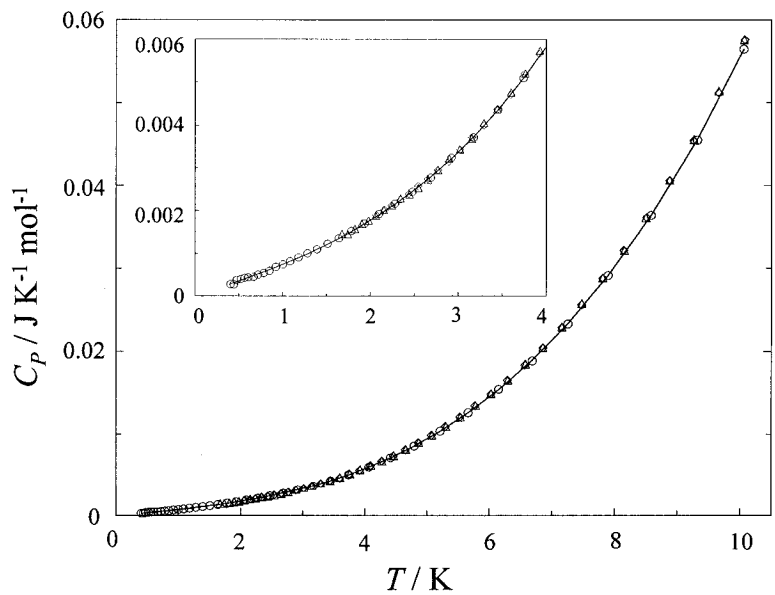

Figure 2.22. Heat capacities of the copper standard measured with the ^{3}He system, Δ puck 215, 41.422 ± 0.010 mg; ○ puck 227, 29.049 ± 0.010 mg. Error bars not visible since symbol is larger than calculated uncertainty.

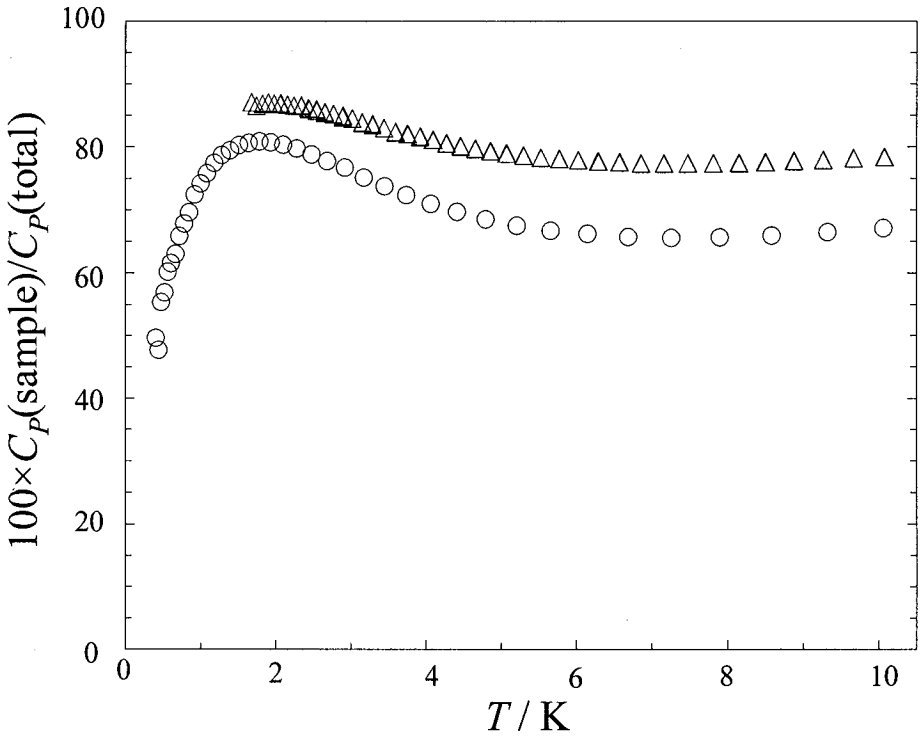

Figure 2.23. Heat capacities results for the copper standard measured with ^{3}He system, showing relative sample contributions to total heat capacity measurement for Δ puck 215, 41.422 ± 0.010 mg; ○ puck 227, 29.049 ± 0.010 mg.

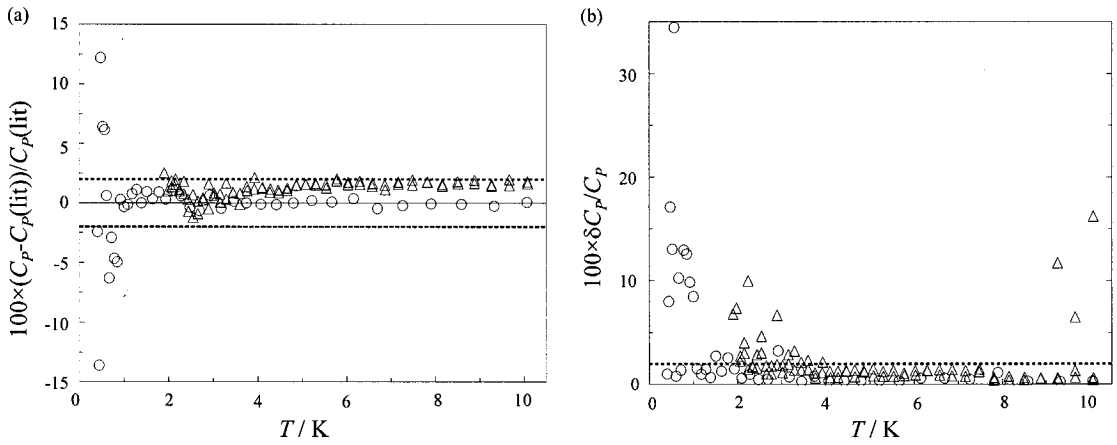

Figure 2.24. Heat capacity of the copper standard measured with the ^{3}He system, Δ puck 215, 41.422 ± 0.010 mg; ○ puck 227, 29.049 ± 0.010 mg. (a) ^{3}He system heat capacity differences from the NIST recommended smoothed data, C_P(lit). C_P(lit) has been calculated using the NIST smoothed data of Osborne, *et al.*[79] for T < 10 K. (b) Estimated uncertainties determined using standard propagation of error for three replicate measurements of the sample platform and the platform with the crystal. Dotted lines in (a) and (b) indicate 2%.

2.3.2.4. Conclusions for Relaxation Calorimeter

Using the PPMS relaxation calorimeter, the accuracy and precision of heat capacities measurements were determined by measuring Calorimetry Conference sapphire and NIST RM 5 copper standard. Heat capacities for Calorimetry Conference sapphire show accuracy of ± 0.5% for $T > 80$ K using the ^{4}He system. The random error or calculated reproducibility of these measurements was similar to the accuracy, 1% for $T > 80$ K, but much higher at lower temperature when $100 \times \delta C_P/C_P < 50\%$.

The NIST copper standard heat capacities exhibit accuracies of approximately ± 1% for 1 K < T < 10 K (with the ^{3}He system, puck 215), 1% for 10 < T < 80 K (with the ^{4}He system) and 0.5% for 80 < T < 150 K (with the ^{4}He system). For $T < 1$ K, accuracies of *ca.* 15% were obtained (with the ^{3}He system, puck 215). The random error or calculated reproducibility of these measurements was 2% for 1 K < T < 10 K (with the ^{3}He system, puck 215), 2% for $T > 10$ K (with the ^{4}He system) and 8% for $T < 10$ K (with the ^{4}He system). For $T < 1$ K, uncertainty of *ca.* 35% was obtained (with the ^{3}He system, puck 215). The systematic errors associated with poor thermal contact and sample mass measurements were not significant. These measurements of reference materials on the PPMS showed better precision and accuracy than the ± 5% certified by Quantum Design for the ^{4}He system.

The relative sample contributions to the total C_P are important to consider when determining the heat capacities of standard materials and unknown samples. In general, C_P(sample) should contribute significantly to the C_P(total) (recommendations given in Section 2.3.2.3.1). That being said, there are constraints that will limit the amount of sample that can realistically be used. Since the platform that holds the sample is only 3

mm × 3 mm, the sample must not exceed this area. Too large a sample will lead to excessive experimental time and, as will be seen in Chapter 3 and 4 for some insulating materials, will exhibit variations in their apparent C_P as a function of mass. As a result, for an unknown sample, it may be necessary to conduct several measurements on sample of various sizes in order to obtain the entire C_P curve accurately.

Each heat capacity puck in the PPMS should be tested against standard materials before use in order to gauge its operational accuracy and precision. For the C_P measurements made in Chapter 3 and 4, the overall accuracy for measurements with the ^{4}He system (with puck 451) is within 1% for $10 < T / \mathrm{K} < 300$, and within 4% for $T < 10$ K. The ^{4}He system should be used to measure C_P in the high-temperature region, however, the ^{3}He system is more accurate for $T < 10$ K so it is recommended the ^{3}He system be used to measure C_P in this low-temperature range. The accuracy with the ^{3}He system (puck 215) for $1 \mathrm{K} < T < 10$ K is within 1%, but for $T < 1$ K, the measurements can only be accurate to within 15%.

2.3.3. Comparison of Heat Capacity Methods

Two calorimeters were used to measure the temperature-dependent heat capacities in the present work. As mentioned previously, the main advantages of relaxation calorimeters are the small sample size, the speed of data collection, ease of use, and the wide accessible temperature range. The main disadvantage is limitations in the accuracy of the relaxation measurement technique that arise due to small contribution of the sample heat capacity to the total heat capacities. However, this is also a problem when performing heat capacity measurements with an adiabatic calorimeter. Another

disadvantage of the PPMS is that it is necessary to run an addendum, comprised of the heat capacity of the grease and the platform, before every sample. For the adiabatic calorimeter used in this work, the addendum only need be done once and can be used for subsequent measurements. Table 2.1 provides a more detailed comparison between the two techniques.

Table 2.1. Comparison of calorimeters used in this work for the measurement of heat capacity. (a) Advantages of our PPMS over our adiabatic calorimeter.

	PPMS	**Adiabatic calorimeter**
sample size	1 - 200 mg	5 cm^3
temperature range	^{4}He: 1.9 - 390 K ^{3}He: 0.4 - 350 K	40 - 310 K*
magnetic field	yes (0 - 9 T)	no
collection of data	~ 200 points per day (minimal supervision)	~ 8 points per day (requiring supervision)
commercially available	yes	no
cryogenic liquid	initial transfer of ~ 100 L He(l) (during installation) + ~ 2 tanks of He(g) required per month	80 K < T < 310 K - initial cool down requires ~ 15 L of N_2(l) + additional 5 L/day 10 K < T < 80 K - entire range requires ~ 100 L of He(l) + additional 5 L of N_2/day - initial cool down requires 15 L of N_2(l)

*practical working range of adiabatic calorimeter used in this work.

(b) Disadvantages of our PPMS over our adiabatic calorimeter:

	PPMS	**Adiabatic calorimeter**
addendum	must run for each sample	included in calculation of C_P
single crystal samples	must have flat bottom	no requirements
powder samples	non-volatile: - pressed into pellet volatile: - hermetically sealed in container	hermetically sealed in sample vessel

2.3.4. Differential Scanning Calorimeter (DSC)

2.3.4.1. Introduction

This technique was introduced in 1964 by Perkin-Elmer® and is one of the most widely used methods of thermal analysis.[57] A Perkin-Elmer® Pyris™ 1 power-compensated DSC, that was used for thermal analysis, will be described in this section.

DSC is a fast, commercially available technique that gives reliable thermodynamic information on relatively small sample sizes (1 to 100 mg) over a large temperature range (100 to 1500 K). Enthalpy changes, entropy changes, and the temperature associated with thermal events can be determined using this method.

2.3.4.2. Principles and Procedures

A typical DSC schematic is given in Figure 2.25. This method is based on the measurement of the differential power required to keep the temperature for a sample identical to a reference, either being either heated or cooled at the same scan rate. The sample and reference pan each reside in similar furnaces that share the same heat sink. Hermetically sealed aluminum pans from Perkin-Elmer® (kit number 0219-0041; *ca.* 20 μL) were used to contain the sample, mass known to within 0.1 mg. The empty reference pan is from the same kit as the sample pan.

Both furnaces are heated with platinum wire resistors and the temperature is measured with a platinum resistance thermometer. The DSC can be operated using either ice or liquid nitrogen to cool the heat sink, depending of the desired temperature range, and the required purge gases are nitrogen for ambient temperatures, and ultra-dry helium for sub-ambient temperatures under a flow, in either case of 20 mL min^{-1}.

The sample and the reference must be kept at the same temperature; this is

achieved through the use of feedback controls. The controlled power supplied to each furnace is $P = P_{average} + \Delta P$, where $P_{average}$ is the average power used to heat both furnaces at the fixed scan rate and ΔP is the difference in power that arises in keeping the temperatures of both furnaces the same. The difference in power to the sample and reference is related to the heat capacity of the materials.

If the heat capacity of the sample changes due to a thermal event, ΔP must change to maintain the same temperature ramp. When the power difference is plotted against the temperature, a peak represents the endothermic or exothermic events. The onset temperature can be determined and integration of the power peak gives the enthalpy change of the event. The temperature and power scales must be calibrated with appropriate standard samples in order to determine the onset temperature and enthalpy change.

A DSC can detect a wide variety of thermal events that a material could undergo when being heated or cooled. These include, but are not limited to, the heat absorbed due to the change of a phase of a material. During the course of this PhD, DSC also has been used by the author to determine the crystallinity of hybrid nanozeolite-polymer composites (discussed in references 81 and 82). DSC was used to analyze the solid-liquid phase transition for these materials and also the transition from a rigid glass to a supercooled liquid. The characteristic temperature of the latter thermal event is known as the glass transition temperature, T_g. The degree of crystallinity and the glass transition temperature are directly related to the mechanical properties of a material.[57] From the analysis of the melting events for the series of composite materials, the degree of crystallinity of each material was obtained.

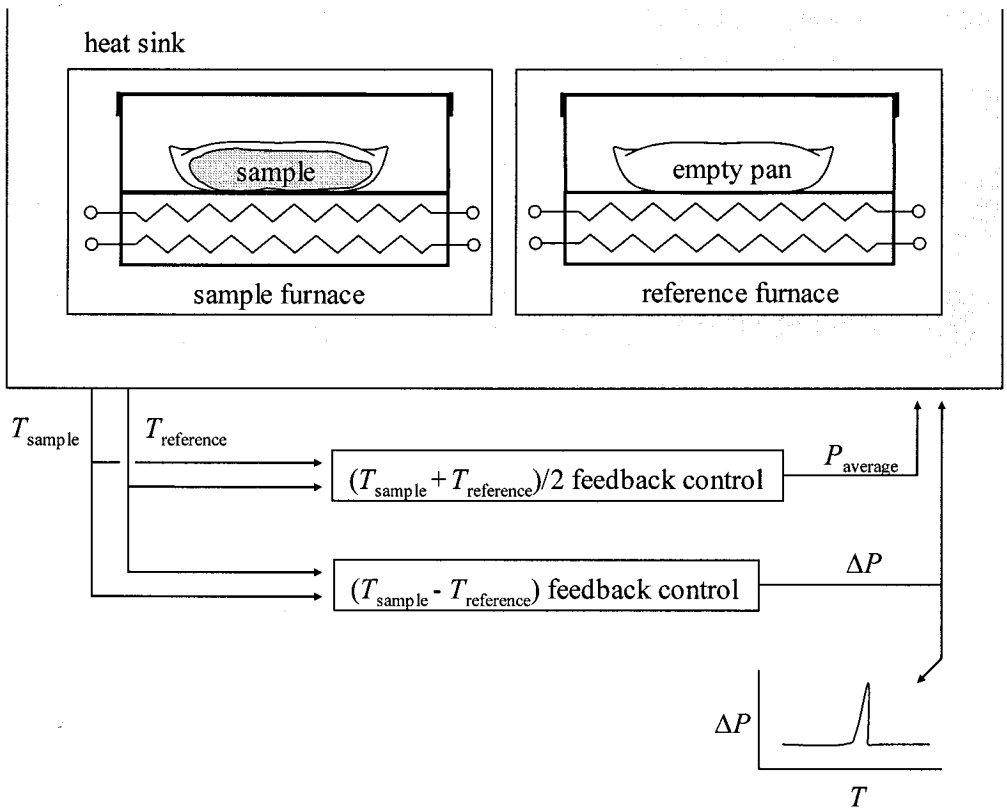

Figure 2.25. Schematic of power-compensated DSC.

2.3.4.3. Standard Materials

The measurement of thermal events using DSC requires calibration (of the temperature and heat flow) using high-purity materials as a reference. Ideally, the standard material would be well characterized and would have a thermal effect near in temperature to the thermal effect being investigated.[57] The calibration must be done using the same scan rate and the same purge gases as the sample under investigation.

Two standard materials were used to calibrate the DSC. Above room temperature, the DSC was calibrated with 99.999+% indium (T_{fus} = 429.75 K, ΔH_{fus} = 28.45 J g^{-1}). At sub-ambient temperature, the system was calibrated for temperature and enthalpy changes with the solid-solid phase transition of 99.8% pure dipentylammonium

chloride, (T_{fus} = 243.84 K, ΔH_{fus} = 6.77 J g^{-1}).[83]

2.3.5. Conclusions Concerning Calorimetry Techniques

When measuring heat capacities of materials, a significant amount of consideration must be given to the accuracy and precision of the technique. The accuracy and precision of heat capacities measurements were determined here by measuring Calorimetry Conference sapphire, NIST RM 5 copper standard and previously by Calorimetry Conference benzoic acid.[36]

The accuracy and precision for the PPMS method agree with those for the adiabatic calorimeter over common temperature ranges, however, the PPMS can be used to much lower temperatures. The resistance ratio sensitivity to temperature change, dRR/dT, for the adiabatic calorimeter is small for T < 50 K and causes more uncertainty in the ΔT measurement by adiabatic calorimetry.

2.4. Conclusions to Experimental Techniques

The experimental methods and procedures used to characterize the thermal properties of material were described in this chapter. The accuracy and precision of the techniques by comparison with standard materials or by compassion with other methods were also described.

Another important factor to thermal properties research is to insure that the materials being used are of the highest purity available, as determined using various analytical techniques available. The next chapters describe the procedures used to characterize the materials studied here, and will give comparison to other literature sources when applicable.

Chapter 3. Thermal Properties of Zirconium Tungstate, ZrW_2O_8

3.1. Materials with Unusual Thermal Expansion Properties

As discussed in Section 1.4.2, most materials expand when heated. There are several exceptions where materials either contract when heated or undergo a very small change in the cell dimensions.

Invar, named for *invar*iable in dimensions, is an iron-nickel alloy with an approximate composition of $Fe_{65}Ni_{35}$ that was discovered at the Bureau International des Poids et Measures in Paris in 1897.[84] This material essentially has a zero coefficient of thermal expansion at room temperature. Charles E. Guillaume was searching for a material to use as a reference tape, wire and/or bars that would not change in length as the temperature changed. He was awarded the Nobel Prize in 1920 for his discovery of Invar, which has a thermal expansion coefficient of 0.01×10^{-6} K^{-1} for 278 K < T < 303 K.[22] Guillaume first used Invar wire to measure the diurnal thermal expansion of the Eiffel Tower in 1912.[85]

Perhaps the earliest observation of negative thermal expansion was the density anomaly of water, a well-known material with relatively unusual behavior: water exhibits negative thermal expansion from 1 °C to 4 °C where it has its highest density. There has been a renewed interest in materials that exhibit negative thermal expansion since the mid-1990's. Negative thermal expansion materials can facilitate control of thermal expansion in composites and in principle can allow for the design of materials with specific expansion coefficients (in between the values of the pure component materials) tailored to the application.

Negative thermal expansion, NTE, has been found in various oxide systems,[86] but the contraction is usually small, anisotropic, and over a small temperature range. Both vitreous and crystalline silica (quartz) have NTE at low temperatures and vitreous silica has a maximum density near T = 193 K.[87,88] Other materials exhibit NTE over much wider temperature range, for example siliceous faujasite exhibits isotropic NTE from 25 K to 573 K and the magnitude is relatively large, $\alpha_l = -4.2 \times 10^{-6}\ K^{-1}$.[23]

NTE materials can be mixed with metals, polymers, or oxides with different properties to make materials for applications where thermal stresses associated with expansion and contraction could be lowered or avoided altogether. Being able to match coefficients of thermal expansion, CTE, in individual components of devices is important in avoiding cracks and separation at interfaces. Also, having a zero CTE is essential in electronic and optical devices when exact positioning of the components is crucial. Specific applications in electronic applications include as zero-expansion heat sinks or substrates, and composites in printed circuit boards. Substrates for high-precision optical applications and cookware are other uses.

The negative thermal expansion material ZrW_2O_8 (zirconium tungsten oxide, more commonly known as zirconium tungstate) has been used in a variety of applications and patents due to its favourable thermal expansion qualities. Cubic ZrW_2O_8 exhibits isotropic NTE over a wide temperature range.[24] It has been used along with ZrO_2 to make a low thermal expansion composite for use in optical fibre refractive index gratings.[89] A patent has recently been released whereby negative thermal expansion ceramics can be cast molded to arbitrary size and shape without press molding the starting powder and with no formation of voids and cracking in the inside.[90] Another

study explores making ZrW_2O_8 ceramic substrates with fewer microcracks and cavities by optimizing the heat treatments. This improves the mechanical properties and the variation of CTE with location.[91]

There has recently been a publication concerning the fabrication and thermal expansion properties of ZrW_2O_8 aerogels.[92] This has allowed nanoscale particles of ZrW_2O_8 to be synthesized for use in composites, an important technological step in the field since mechanical milling of ZrW_2O_8 results in an amorphous material and the loss of NTE.

Portland cement concrete has been modified with ZrW_2O_8 to control the CTE.[93] Although there is little practical significance to this application due to the expense of negative thermal expansion material, the results indicate the reduction of thermal expansion of the cement with the addition of the NTE material.

3.2. Zirconium tungstate, ZrW_2O_8

3.2.1. Introduction

The discovery of ZrW_2O_8 was somewhat serendipitous. In 1959 researchers were attempting to stabilize zirconia's crystal structure by adding cations of valency higher than two. They synthesized this metastable compound and examined it optically and by x-ray diffraction techniques.[94] Its thermal expansion properties were first reported by Martinek and Hummel in 1968.[95]

ZrW_2O_8 is a framework structure where rigid $[ZrO_6]^{8-}$ octahedra and $[WO_4]^{2-}$ tetrahedra are connected through Zr-O-W linkages. The ZrW_2O_8 structure is a network of Zr and W atoms linked by two-coordinate O atoms to give a framework formula of

$[ZrW_2O_6]^{4+}$; the two remaining O atoms complete the W coordination.[24] N.L. Ross stated in her review on framework structures[96] that three-dimensional networks of relatively rigid corner-sharing polyhedra characterize framework structures. Framework materials are studied in several different disciplines such as in materials sciences, Earth Sciences, solid-state chemistry and condensed matter physics. Materials with framework structures can be natural compounds, such as quartz and zeolites, or synthetic compounds, such as the metal organic framework materials studied by Li *et al.*[97] Quartz, which exhibits NTE as mentioned in the previous section, is also a framework structure. It consists of $[SiO_4]^{4-}$ tetrahedra linked together at their vertex oxygen atoms to give semi-infinite framework connectivity.[98]

Figure 3.1 demonstrates schematically the manner in which the $[ZrO_6]^{8-}$ and $[WO_4]^{2-}$ polyhedra are connected. Each $[ZrO_6]^{8-}$ octahedron shares all its vertex oxygen atoms with different $[WO_4]^{2-}$ tetrahedra, while the $[WO_4]^{2-}$ share only three oxygen atoms with $[ZrO_6]^{8-}$ and the fourth is bonded solely to W^{6+}.[99]

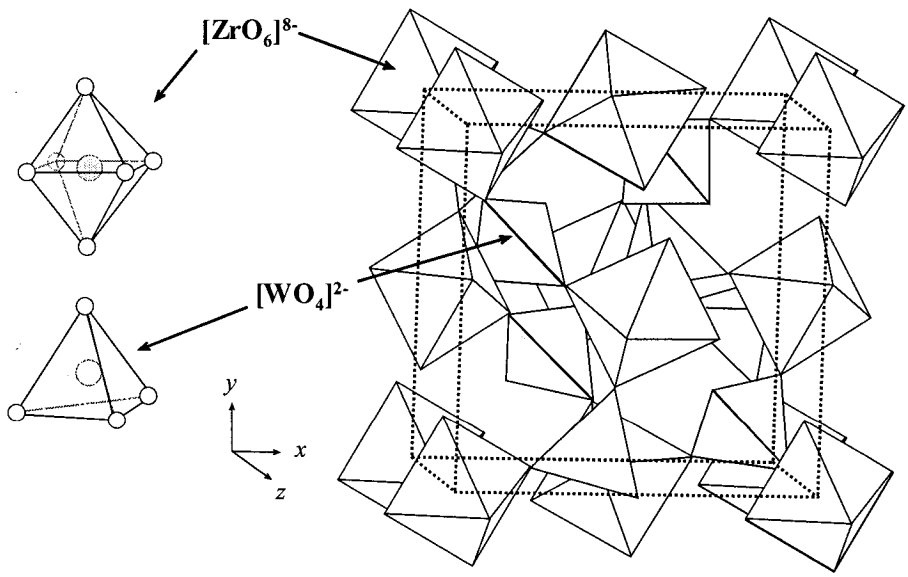

Figure 3.1. Zirconium tungstate shown as $[ZrO_6]^{8-}$ octahedra and $[WO_4]^{2-}$ tetrahedra. Unit cell schematic styled after reference 99.

3.2.2. Phase Considerations

3.2.2.1. Introduction

Chang *et al.* have reported the condensed phase relations of ZrO_2 and WO_3.[100] It was determined that ZrW_2O_8 is a metastable compound, in accordance with observations mentioned earlier,[94] and that is only thermodynamically stable between 1378 K < T < 1530 K. Therefore, the synthesis of ZrW_2O_8 must occur in this temperature range and then the sample must be quenched to room temperature where it is kinetically allowed. Heating past T = 1050 K will cause ZrW_2O_8 to decompose.[101] The binary phase diagram of ZrO_2 and WO_3 is shown in Figure 3.2.

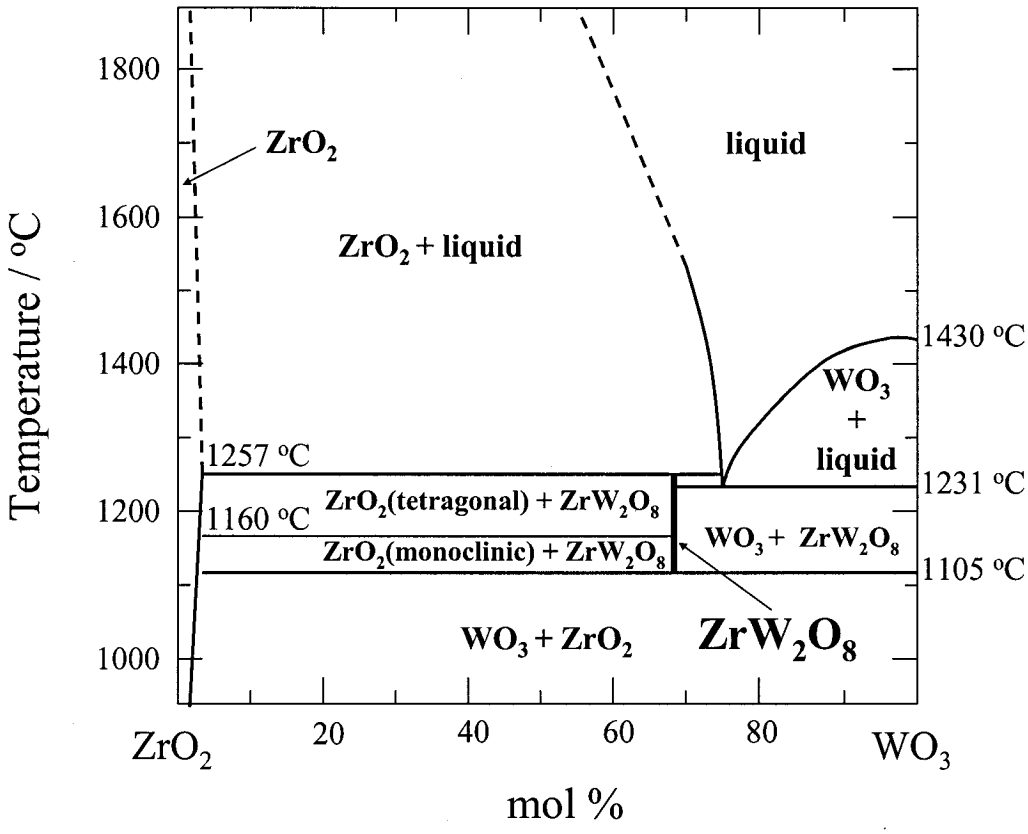

Figure 3.2. The phase diagram of ZrO_2 and WO_3 shows that the ZrW_2O_8 compound formation of occurs between 1105 °C and 1257 °C. Redrawn from original reference.[100]

There have been several reported phases of ZrW_2O_8; different phase arise due to the temperature and pressure treatment of the sample. The most studied phases are the α, β, and γ phases. Of these, the best understood phase is cubic, α-ZrW_2O_8 (space group $P2_13$, $Z = 4$) which occurs at ambient temperature and pressure. There have been several structural and thermodynamic reports on the cubic phase, some of which will be discussed in the following sections. Its negative thermal expansion,[24,95,102,103,104] Grüneisen parameter, [103,105,106,107,108,109,110] heat capacity,[111,112,113,114,108,115,116,117] and thermal conductivity (room temperature and above only)[118] have been reported by various research groups. For this cubic phase from $T = 2$ to 350 K, $\alpha_l = -9.07 \times 10^{-6}$ K^{-1}, *i.e.* $\alpha_V = -2.72 \times 10^{-5}$ K^{-1}.[104]

This CTE corresponds to a significant decrease in the volume of its unit cell with temperature. For a comparison of the magnitude, the thermal expansion coefficients of ceramics have been categorized into three different groups: (1) very low expansion, $0 \leq \alpha_l \leq 2 \times 10^{-6}$ K^{-1}; (2) low expansion, 2×10^{-6} $K^{-1} \leq \alpha_l \leq 8 \times 10^{-6}$ K^{-1}; and (3) high expansion, $\alpha_l \geq 8 \times 10^{-6}$ K^{-1}.[22] This indicates that α-ZrW_2O_8 has a very high negative CTE.

If the cubic α-phase is pressed above 0.21 GPa, it will convert to an orthorhombic phase (space group $P2_12_12_1$, $Z = 12$), γ-ZrW_2O_8.[119,120,121] The unit cell volume of the α-phase is 5% larger than the orthorhombic phase, and the basic $[ZrW_2O_6]^{4+}$ framework stays intact, but there is a change in the $[WO_4]^{2-}$ coordination environment.[120] The γ-phase is metastable at room temperature upon release of pressure; Gallardo-Amores *et al.* indicated that after seven days, the γ phase will convert to a material of α : γ ratio of 30 : 64.[122] This phase transforms back to α-ZrW_2O_8 when heated above 405 K.[120] The

negative thermal expansion properties and compressibility properties[119,123] have been investigated as well as thermodynamic calculations of the expansion properties and compressibility properties based on the phonon density of state (PDOS).[124] γ-ZrW_2O_8 shows approximately linear thermal expansion, with $\alpha_V \sim -3 \times 10^{-6}$ K^{-1}, an order of magnitude lower than α-ZrW_2O_8, $\alpha_V = \sim -3 \times 10^{-5}$ K^{-1}.[120]

A second cubic phase, β, occurs after heating ZrW_2O_8 above $T = 431 \pm 1$ K, as detected by adiabatic scanning calorimetry methods.[112] More recent results from the same research group (using adiabatic calorimetry) indicate that the transition is at $T = 440.0 \pm 1$ K.[117] This phase transition temperature is lower than those obtained with diffraction techniques, $T = 444$ K[113] and $T = 448$ K[108]. At approximately 440 K, α-ZrW_2O_8 undergoes an order-disorder phase transition[24,102] to the high temperature β phase (space group $Pa\bar{3}$, $Z = 4$).[102] The thermal expansion coefficient,[24,104,113] and heat capacity[112,113] have been reported for this phase. From the data obtained by Evans *et al.*,[102] from $T = 423$ to 693 K, $\alpha_l = -6 \times 10^{-6}$ K^{-1}.

Pressure-induced amorphization of ZrW_2O_8 also has been studied at room temperature using high-pressure x-ray diffraction[122,125] and Raman scattering experiments.[125] The study by Perottoni *et al.* indicates that ZrW_2O_8 becomes progressively amorphous from 1.5 to 3.5 GPa, above which there was no further amorphization. The amorphous phase is stable upon release of the pressure, however, the crystalline phase returns after annealing.[125] It is not known whether this phase exhibits NTE. High temperature and pressure synthesis will yield a dense hexagonal phase.[126]

This thesis focuses mainly on the thermal properties of the phase which exists at ambient temperature and pressure, α-ZrW_2O_8.

3.2.2.2. The α-β Phase Transition

The phase change at $T \sim 440$ K is volume reducing where the volume of the unit cell of the higher temperature (β) phase is smaller than that of the low-temperature (α) phase. The α-β phase transition involves a disordering of the $[WO_4]^{2-}$ tetrahedral groups that lie on the threefold axis, causing the introduction of a center of symmetry in the structure.[104] In the α-phase, the two $[WO_4]^{2-}$ tetrahedra point their unshared vertexes in the [111] direction, while in the β-phase the two tetrahedra point their unshared vertexes randomly in the [111] and $[\bar{1}\,\bar{1}\,\bar{1}]$ directions at 1:1 ratio.[112]

There is very little difference between the α and β phases in the x-ray diffraction pattern. The shifts in peak position are barely perceptible, but there are differences in the peak intensities.[24] The [310] reflection (occurring at $2\theta \sim 31^{\circ}$) is forbidden in the centric $Pa\bar{3}$ space group, but does occur in the acentric $P2_13$ space group. Other obvious differences are the disappearance of the [111] ($2\theta \sim 17^{\circ}$) and [221] ($2\theta \sim 29^{\circ}$) reflections on going from the α phase to the β phase.[102]

Figure 3.3 gives a schematic representation of the α-β phase change. Figure 3.3(a) shows α-ZrW_2O_8 where sites W1, W2, O1, O2, O3 and O4 are occupied. There is a weak interaction between the "bridging" oxygen atom at O3 and W1.[24] Figure 3.3(b) shows that the atom O4 becomes mobile and O3 becomes a bridging oxygen between the two equivalent $[WO_4]^{2-}$ units and moves to the inversion center at (0.5, 0.5, 0.5). In the β phase, the $W1^1$, $W2^1$, $O3^1$ and $O4^1$ positions become 50 % occupied (therefore the W1, W2, O3, and O4 are the other 50 % of occupied positions).

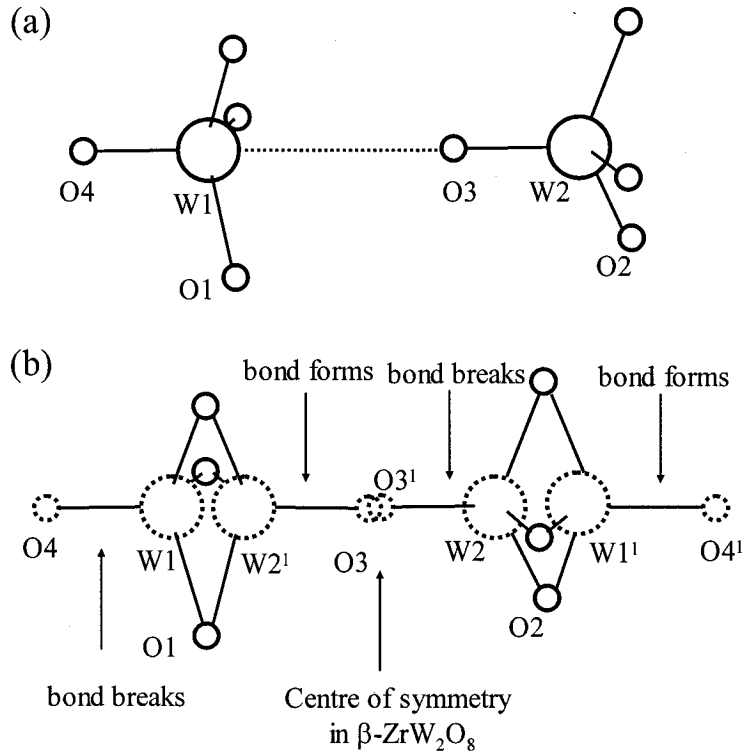

Figure 3.3. Schematic representation of (a) α-ZrW_2O_8 and (b) β-ZrW_2O_8. Atomic positions drawn with dotted lines are 50 % occupied. Redrawn from original reference.[104]

Research has shown that ZrW_2O_8 has high ionic conductivity, electrical conductivity = $\sigma \sim 10^{-5}\ \Omega^{-1}cm^{-1}$, above the α-β phase transition, in line with the high oxygen mobility in the β-phase. Conversely, at room temperature, ZrW_2O_8 acts as an electrical insulator with electrical conductivities in the range of $\leq 10^{-8}\ \Omega^{-1}cm^{-1}$.[102]

3.2.3. Mechanism of Negative Thermal Expansion

3.2.3.1. Introduction

As mentioned in Section 3.2.2, the coefficient of negative thermal expansion of ZrW_2O_8 has been well characterized experimentally over the past decade. There is a large family of oxides structurally similar to ZrW_2O_8 and many other materials in this

family also exhibit negative thermal expansion over varied ranges in temperature.[99] However, ZrW_2O_8 has the most dramatic negative thermal expansion to date. It exhibits negative thermal expansion over a wide temperature range, 0.3 K to 1050 K, and the magnitude is also significant, $\alpha_l = -8.7 \times 10^{-6}\ K^{-1}$ from $0.3 < T < 693$ K.[102] Since it is a cubic material, the NTE is isotropic over this entire range. There is a change in the magnitude due to a phase transition that starts at approximately 400 K and is evident in Figure 3.4. Approaching $T = 0$ K from room temperature, the length of the unit cell expands by about 0.3 %, while approaching $T = 1050$ K, the unit cell length shrinks by about 0.45 %.

The simplest way to explain NTE observed in open framework materials is by transverse vibrations of the bridging oxygen atoms that cause tilting of the $[ZrO_6]^{8-}$ octahedra and $[WO_4]^{2-}$ tetrahedra that make up its unique crystal structure. These polyhedra are connected at all vertices, except for one $[WO_4]^{2-}$ oxygen atom which is considered to be a terminal oxygen.

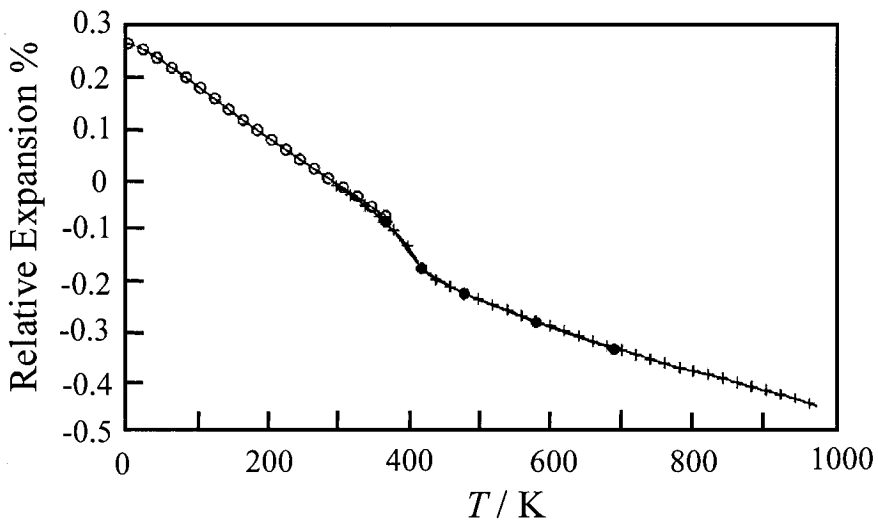

Figure 3.4. The change in unit cell length of ZrW_2O_8 as a function of temperature relative to the unit cell length at room temperature. ○,● neutron diffraction and + dilatometer data from Mary *et al.*[102] Data from reference 99.

Consider the possible vibrations of the Zr-O-W linkage for ZrW_2O_8 as shown in Figure 3.5.[127] Longitudinal vibrations along the Zr-O-W bond cause the Zr-O, W-O and the average Zr-W distances to increase (if the system was very anharmonic). However, for transverse vibrations, the average Zr-W distance would decrease as the bridging oxygen in the Zr-O-W unit vibrates with increasing amplitude, assuming a negligible change in Zr-O and W-O distance. In a three-dimensional solid, the vibration of the Zr-O-W unit will result in a rotation or rocking motion of the polyhedra that are connected by the respective oxygen atoms. In order for NTE to occur, all polyhedra must tilt back and forth in a cooperative manner without destruction of the polyhedral units.

Figure 3.6 illustrates how such a cooperative motion can result in a decrease of the metal-metal distance by considering a simplified version of four octahedra connected together at their vertexes. The bold-lined squares show the size before heating and after heating. As the system is heated, the transverse motion along the Zr-O-W linkage pulls the octahedra together and causes the structure to shrink.

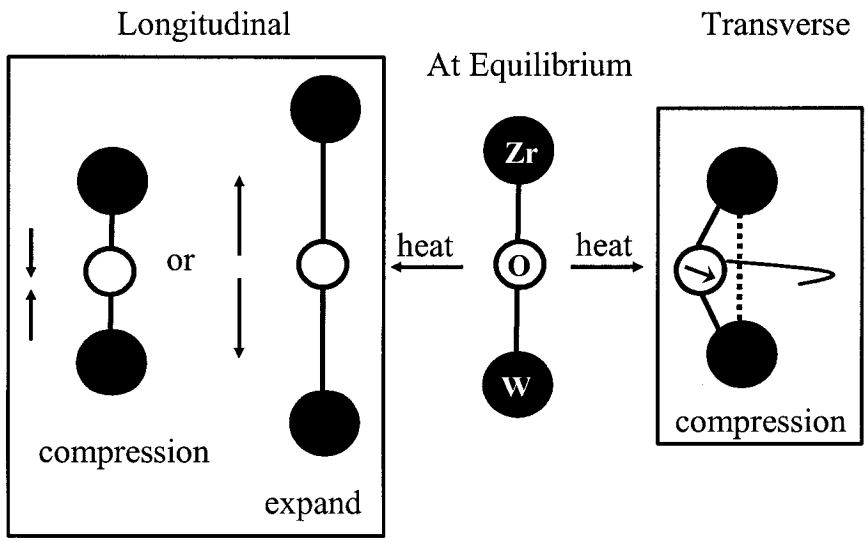

Figure 3.5. Longitudinal vibrations could lead to compression or expansion of the Zr-O-W linkage while transverse vibrations would lead to compression. Styled after reference 127.

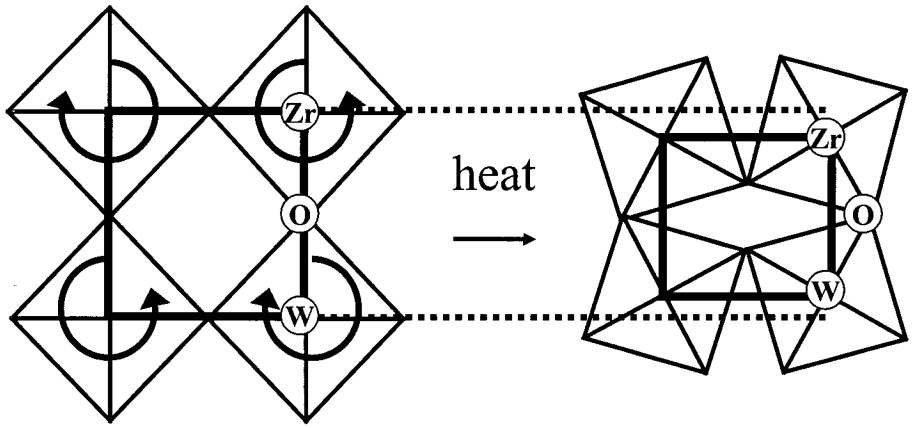

Figure 3.6. When the Zr-O-W linkage undergoes transverse librations, the polyhedra tilt back and forth in a cooperative manner that decreases the Zr-W distance. Styled after reference 128.

The mechanism for negative expansion is not yet fully understood for the systems in which NTE occurs. In 1998, Evans *et al.*[128] examined the oxygen vibrations that lead to the negative thermal expansion in the zirconium tungstate family. They were then able to generalize it to systems with specific properties and summarized some of the contributing factors recognized in compounds exhibiting low or negative thermal expansion. The list is as follows: (1) the presence of strong M-O (M = metal) bonds which themselves have inherently low thermal expansion; (2) high M-O covalency; e.g. M = W^{+6}; (3) two-coordinate oxygen to allow transverse vibrations; (4) framework structures that would support low-energy transverse vibrational modes; (5) no interstitial framework cations; (6) absence or suppression of displacive phase transitions to lower-symmetry, lower-volume structures.

Earlier work has focused on explaining NTE in ZrW_2O_8 in terms of the Rigid Unit Mode or RUM model, which was first proposed by Pyrde *et al.*[129] More recently, there has been evidence to suggest that this model is over-simplified[130,131] and the NTE and

RUMs in a system are not necessarily directly correlated.[132] The RUM model is described in the next section along with a study that discusses the lack of correlation between RUMs and NTE. The section immediately following describes a new mechanism for NTE and will give evidence to support it.

3.2.3.2. Role of RUMs in Predicting Thermal Expansion of Oxides

According to the RUM model, when the material is heated, the rigid polyhedra will rock without being distorted and thus give rise to transverse vibrations perpendicular to the M-O-M linkage axis.[129] These vibrations are anharmonic low-frequency librational (rocking) and translational modes that can be excited even at very low temperatures. This type of motion is called a "rigid unit mode" or RUM, as the polyhedra remain mostly undistorted due to their rigidity. These polyhedral librations override the positive thermal expansion and give rise to negative thermal expansion.

The RUM model was originally developed to describe the behavior of a larger class of materials that can be described as frameworks of connected polyhedra.[133] The applications of this model include interpreting the nature of high-temperature phases[133] and linking the magnitude of the transition temperature to the tetrahedral stiffness.[134,135,136] The RUM model has been used previously to provide insight into the stability and physical properties of framework silicates.[136, 137] The soft modes associated with displacive phase transitions as in the α-β transition at T = 846 K in quartz also are attributed to RUMs.[137,138,139] Hammonds *et al.* used RUMs to understand the catalytic behavior in zeolites.[140] They determined that the low-energy modes of distortion of the structure caused by the rocking of the polyhedra give rise to adsorption sites in zeolites at

which catalysis can occur.

A detailed RUM calculation was performed by Tao and Sleight on a series of framework oxides to investigate the correlation between RUMs and NTE.[132] They used a computer program called CRUSH, developed by Hammonds *et al.*,[141] to determine whether RUMs exist in the structure of oxides. They found that in some oxides the CRUSH results show RUM existence where NTE is not observed. For example in ReO_3, RUMs exist for all wavevectors corresponding to rocking motion, but ReO_3 has small, positive thermal expansion.

It also was shown that strong NTE does exist without RUMs. Another large family of NTE materials is the tungstates and molybdates in the $A_2M_3O_{12}$ family where, similar to ZrW_2O_8, the A and M cations are coordinated by oxygen octahedrally and tetrahedrally, respectively.[142] Orthorhombic $Sc_2W_3O_{12}$, $Lu_2W_3O_{12}$, and $Y_2W_3O_{12}$ are members of this family of oxides and all exhibit strong, anisotropic NTE over a large temperature range. However, these compounds do not have RUMs. The NTE in this family can still be understood in terms of the librations and tilts of the essentially rigid polyhedra.[142]

On the other hand, ZrW_2O_8 does show numerous RUMs, as does the MO_2 family to which SiO_2 belongs. Both families exhibit NTE. The results from Tao and Sleight on the RUM analysis for the framework oxide are summarized in Table 3.1. Final conclusions of the study are that even though in some oxides the presence of RUMs is accompanied by NTE, there is no simple and/or direct correlation between the presence or absence of RUMs and the thermal expansion properties. In general, having one does not predict the other.

Table 3.1. Summary of RUM analysis for framework oxides from Tao and Sleight.[132]

Structure Family	Framework Connectivity	RUM	NTE
ReO_3 type	Pure octahedral corner-sharing framework	Yes	No
ZrW_2O_8	Octahedra:tetrahedral 1:2	Yes	Yes
ZrV_2O_7	Octahedra:tetrahedral 1:2	No	Yes
AMO_5	Octahedra:tetrahedral 1:1	Yes and No	Yes
$A_2M_3O_{12}$	Octahedra:tetrahedral 2:3	No	Yes
MO_2 type	Pure tetrahedra corner-sharing framework	Yes	Yes

3.2.3.3. More Recent Mechanism

A more recent view of ZrW_2O_8 proposes that the low-energy modes responsible for NTE correspond to the correlated vibrations of the $[WO_4]^{2-}$ tetrahedra and their three nearest $[ZrO_6]^{8-}$ octahedral.[130,131] The RUM model proposed that rotation of the rigid polyhedra involving the transverse motion of the oxygen atoms of the Zr-O-W linkage as the driving force behind NTE in ZrW_2O_8. However, Cao *et al.* state that the low energies of the modes suggest that heavy atom vibrations must be involved in NTE. Also, the RUM model fails to explain why a soft-mode displacive transition does not occur, even though the low-energy modes and open structure suggest one may take place.[130]

X-ray absorption fine structure, XAFS, results show that the $[WO_4]^{2-}$ polyhedra are rigid, however, the $[ZrO_6]^{8-}$ are stiff but not rigid as temperature increases.[130,131] XAFS results indicated that due to the stiffness of the Zr-O-W linkage, the vibration of the oxygen cannot be the primary origin of NTE. Instead, correlated vibrations of the heavy atom pairs, producing low-energy optical modes, can be considered the origin.

Consider the "rigid-tent pole model" proposed by Cao *et al.* (presented in Figure 3.7) to show how the Zr-Zr distance, $d_{Zr\text{-}Zr}$, changes with temperature. The Zr-O-W linkages are assumed to be rigid (like tent poles) and the W atoms (W1 and W2 as shown in Figure 3.7(a)) are initially in the plane of the Zr atoms. The Zr atoms create an equilateral triangle which is perpendicular to the [111] axis, and W1 and W2 lie on the

[111] axis.

As the W atoms translate along the [111] plane, they move out of the plane (either up or down) of the Zr atoms making a pyramidal (tent) shape. The stiffness of the Zr-O-W linkage will not let the Zr-O-W distance ($d_{Zr\text{-}O\text{-}W}$) change, therefore, $d_{Zr\text{-}Zr}$ will decrease to preserve the equilateral shape of the base. The lattice constant, a, of ZrW_2O_8 is directly related to the Zr-Zr distance, $a = \sqrt{2}(d_{Zr\text{-}Zr})$, since the Zr atoms occupy the fcc positions in a cube. The vibrational amplitude of the $[WO_4]^{2-}$ along the [111] axis will increase with increasing temperature; consequently $d_{Zr\text{-}Zr}$ will decrease. These motions occur on all four <111> axes, thus providing isotropic contraction as diffraction results suggest.

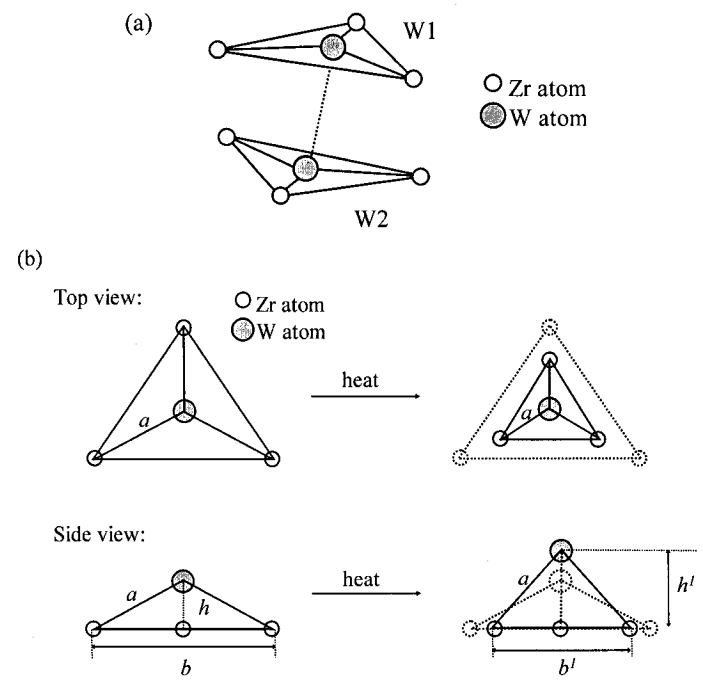

Figure 3.7. "Rigid-tent pole model" proposed by Cao *et al.* to describe NTE in ZrW_2O_8. (a) Part of the ZrW_2O_8 structure that includes W1 and W2 in the plane of the three nearest Zr atoms. (b) As the $[WO_4]^{2-}$ vibrate along the [111] axis, the W atoms move out of the plane of the Zr atoms. Increasing temperature causes the displacement of the W atoms to increase, and the distance between Zr atoms to decrease. Oxygen atoms are left out for simplicity. Restyled from reference 131.

In the real lattice, the tetrahedra and octahedral still must tilt and rotate and the Zr-O distances stretch slightly to maintain the lattice structure.[131] These motions are similar to those discussed in Evans *et al.*[102] There is however a difference in the mechanism since Evans *et al.* stress the transverse vibration of some of the oxygen atoms, whereas Cao *et al.* stress motion involving heavy atoms, and consider motions that include translation of the polyhedra. In either case, the associated motions are at low frequencies.

3.2.3.4. Final Thoughts on Mechanisms for NTE

The recent work of Tao and Sleight[132] as discussed in Section 3.2.3.3 has diminished any direct correlation between NTE and RUMs. Recent studies have concluded that the RUM model is too simplified for NTE and have provided a mechanism supported by XAFS experiments.[130,131] The motion responsible for NTE involves translation as well as libration, and the low-energy optic modes play a central role in the NTE mechanism.[143] Very recently, IR spectroscopy experiments in the low-energy region (below 10 meV) have provided evidence suggesting unconventional and anharmonic behavior.[143]

3.3. Heat Capacity of ZrW_2O_8

3.3.1. Previous Studies

The heat capacity of ZrW_2O_8 has been measured by several different groups using a variety of techniques. In 1998, the heat capacity of ZrW_2O_8 from $T = 3$ to 350 K was first reported by Ramirez and Kowach,[111] determined using a modified isothermal

calorimeter. In 2000, a second report on the heat capacity of ZrW_2O_8 was published by Yamamura *et al.*[112] from T = 340 to 550 K using adiabatic scanning calorimetry and from 300 K to 340 K using adiabatic calorimetry. At the time these were the only reports available but the C_P results were not consistent with each other. The C_P at T = 300 K reported by Ramirez and Kowach ($C_P \sim 220$ J $K^{-1}mol^{-1}$) was approximately 10% higher than that of Yamamura *et al.* ($C_P \sim 200$ J $K^{-1}mol^{-1}$). This deviation in the data is larger than is acceptable in heat capacity measurements and would indicate either a problem in the methods or with the sample used.

One difference in the experimental methods of the two research groups was that Ramirez and Kowach used a large single crystal of ZrW_2O_8 (m = 0.7 g) while Yamamura *et al.* used material in powder form. Ramirez and Kowach noted in their discussion that the relaxation times in their heat capacity measurements were long. This note and the fact that the reported heat capacity was larger than expected indicated that perhaps they were not getting an accurate measurement of C_P. Long relaxation times also indicate that the heat conduction through the material could be low; hence the material could have a low thermal conductivity.

The importance of accurate heat capacities for determination of Debye temperatures, and for understanding other thermal properties indicated a need to determine this quantity again.

In early 2002, another article on the heat capacity of a similar tungstate, hafnium tungstate, was published by Yamamura *et al.*[114] Hafnium tungstate is isostructural to its lighter cousin (atomic mass of Hf is twice that of Zr) and also exhibits NTE, albeit the magnitude is smaller than for zirconium tungstate.[113]

The measurements of C_P of HfW_2O_8 from T = 1.8 K to 330 K indicated that the $C_P(HfW_2O_8)$ values were smaller than $C_P(ZrW_2O_8)$ in the T = 300 to 330 K region, contrary to the Neumann-Kopp rule that predicts that $C_P(HfW_2O_8)$ should be larger than $C_P(ZrW_2O_8)$ by about 4 J K^{-1} mol^{-1}. They stated that more precise measurement of ZrW_2O_8 was needed to solve this discrepancy.

In June of 2002, Yamamura *et al.*[108] published another article that confirmed their heat capacity data for ZrW_2O_8 between T = 1.8 K to 330 K along with the Grüneisen function as measured with an adiabatic calorimeter and relaxation calorimeter. At room temperature, the heat capacity of ZrW_2O_8 from this study was approximately 205 J K^{-1} mol^{-1}.[108] Another study reported the heat capacity of α-ZrW_2O_8 as a function of temperature using adiabatic calorimetry from T = 0.6 K to 300 K.[116] The heat capacity of ZrW_2O_8 from this study was 207.6 J K^{-1} mol^{-1} at T = 300 K.[116] Recently, the heat capacities of ZrW_2O_8 were measured to T = 483 K and included the phase transition which was determine to occur at T = 440.0 K ± 0.5 K.[117] The heat capacity of ZrW_2O_8 from this study was ~ 205 J K^{-1} mol^{-1} at T = 300 K. The heat capacity results published for ZrW_2O_8 to date, before the present work, are summarized in Figure 3.8.

Other efforts in the literature have been spent analyzing the low-frequency modes which are responsible for NTE using the phonon density of states and the heat capacity of ZrW_2O_8.[103,144] Several groups have carried out lattice dynamical studies trying to determine specifically which low-energy modes are responsible for NTE.[124,145]

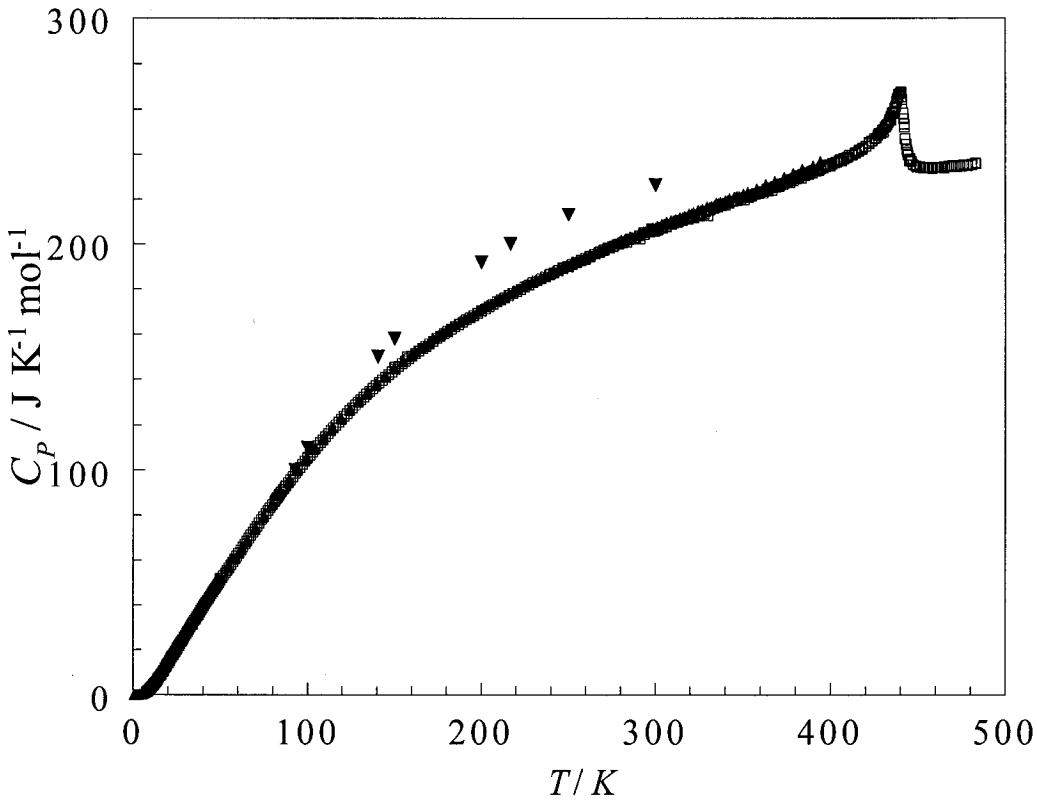

Figure 3.8. Summary of heat capacities of ZrW_2O_8. ▲Stevens *et al.*[116], □Yamamura *et al.*[114,117], ▼Ramirez and Kowach.[111]

3.3.2. Experimental Methods

Given the importance of accurate heat capacity data in understanding thermal conductivity and negative thermal expansion, the heat capacity of ZrW_2O_8 was determined here.

Zirconium tungstate was obtained as a crystalline powder from Alfa Aesar (99.7 % on metal basis excluding Hf with Hf < 3 %). Instrumental neutron activation analysis indicated Hf at 50 ppm by mass ($Zr_{1-x}Hf_xW_2O_8$ with $x = 0.00016$).

Differential scanning calorimetry (DSC) experiments, performed with a Perkin-Elmer Pyris 1 DSC calibrated with 99.999+% indium at a scan rate of 10 K min^{-1}, indicated a feature with an onset temperature of 403 K, $\Delta H = 0.97$ J g^{-1}, Figure 3.9(a),

likely due to water.[146,147] This was removed by subsequent heating (*vide infra*). The α-β phase transition at approximately 440 K was not apparent from DSC experiments; others also have found that this is not observable by DSC[102] due to the higher-order nature of the transition.

X-ray powder diffraction confirmed that the as-received sample was α-ZrW_2O_8 plus a small amount (< 5 %) of γ-ZrW_2O_8. This is evident by the broadening of the peaks at low scattering angle, evident in Figure 3.10 (γ-peaks indicated with *). The amount of the γ phase in the ZrW_2O_8 sample was approximated by measuring the ratio of the α peaks (at $2\theta = 21.75^{\circ}$) and γ peaks (at $2\theta = 22.1^{\circ}$). According to Evans *et al.*, γ-ZrW_2O_8 is stable below $T = 405$ K, but converts back to α - ZrW_2O_8 upon heating above $T = 405$ K.[119]

The heat capacity of ZrW_2O_8 was measured in a heat pulse mode from 38 K to 310 K using an automated adiabatic calorimeter. The heat capacity was determined in two separate sets of measurements, with the masses of the sample loaded into the calorimeter of 6.2905 g and 13.2544 g. The procedures for running the adiabatic calorimeter were described in detail in Section 2.3.1.

The heat capacity of ZrW_2O_8 also was measured in a heat pulse mode from 0.4 K to 300 K using a commercial relaxation calorimeter (PPMS). The procedures for running the relaxation calorimeter were described in detail in Section 2.3.2. The ZrW_2O_8 powder had to be pressed into a pellet so that it could be placed directly on the greased platform of the PPMS. The pressing procedure was outlined in Section 2.2. X-ray diffraction revealed that during the pressing step a fraction (~ 5 % more) of α-ZrW_2O_8 was transformed to the γ-phase.

DSC measurements of the as-pressed pellets showed a peak at 403 K, $\Delta H = 1.32$ J g^{-1} (attributed to water) along with a second smaller peak with an onset temperature at ~ 410 K, $\Delta_{tr}H = 0.36$ J g^{-1} (attributed to the γ-α transition[146,147]), as in Figure 3.9(c). The pressed samples were heated for 24 hours in atmosphere at 408 K. Subsequently, they were characterized by x-ray powder diffraction and DSC. The diffraction results indicated that the pressed-and-heated samples were α-ZrW_2O_8 (< 1 % γ-phase). DSC experiments of pressed-and-heated pellets, Figure 3.9(b) and (d), showed no discernable transitions indicating that pressed-and-heated pellets were converted fully back to α-ZrW_2O_8.

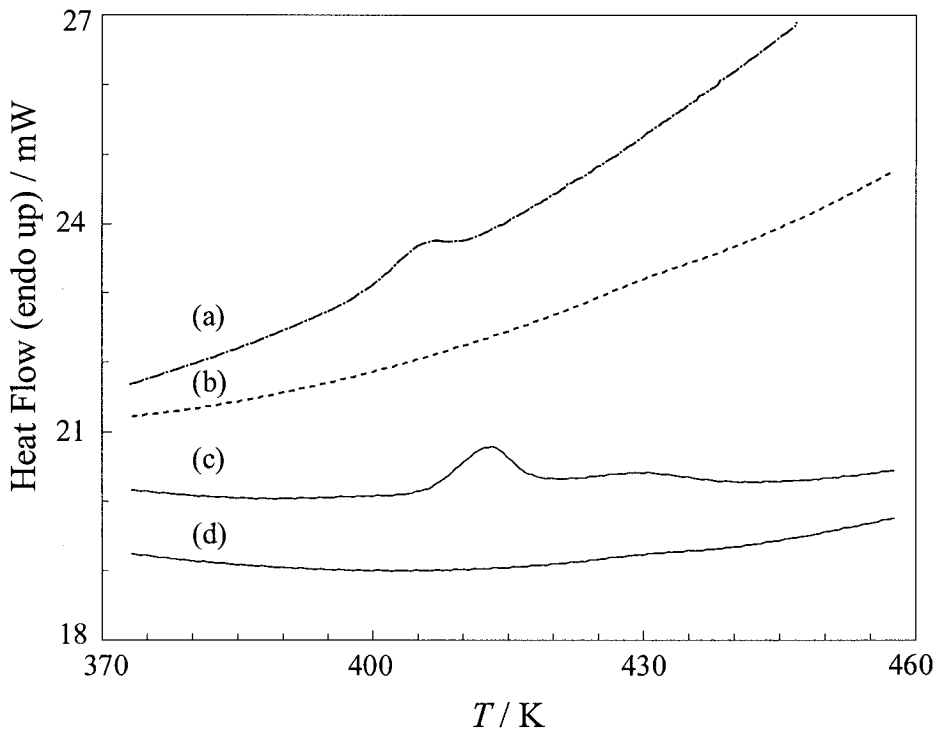

Figure 3.9. DSC scans of ZrW_2O_8. (a) As-received sample from Alfa Aesar. (b) After being pressed-and-heated to 408 K for 24 hours. (c) As-pressed pellets, 1st temperature scan indicating phase transition with an onset at $T = 406$ K. (d) As-pressed, 2nd temperature scan, no thermal event.

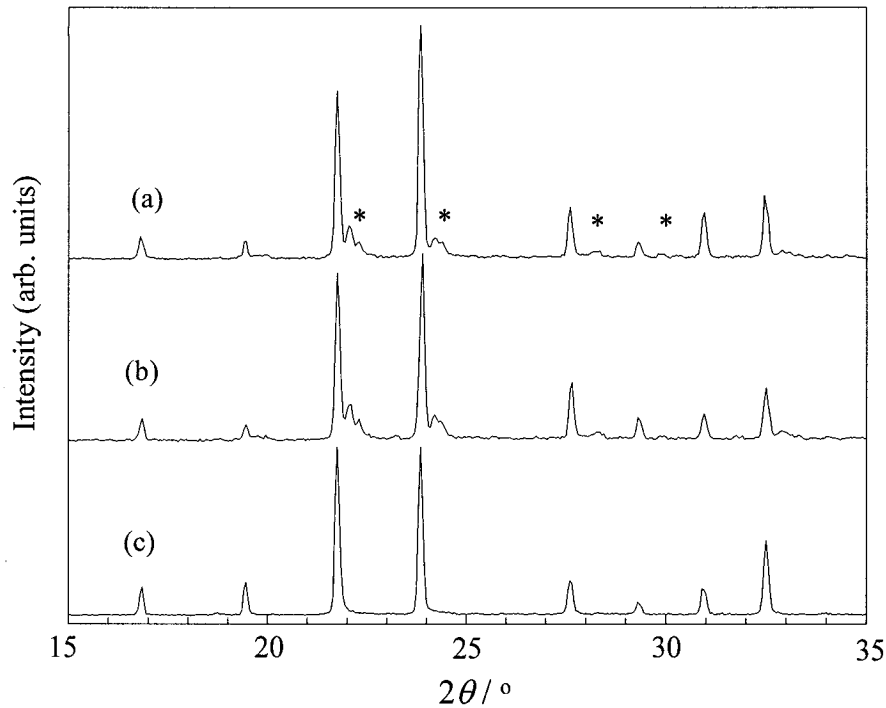

Figure 3.10. Powder x-ray diffraction pattern of ZrW_2O_8. γ-ZrW_2O_8 peaks marked with *. (a) Sample directly from Alfa Aesar, *ca.* 95 % α and 5 % γ-phase. (b) After pressing the material, *ca.* 90 % α and 10 % γ-phase are present in the sample. (c) Pressed sample after heating to $T = 408$ K; x-ray indicated primarily α phase present (< 1 % γ).

The pellets had to be broken into smaller pieces to fit onto the PPMS platform, which was 3 mm × 3 mm in area. The relaxation calorimetry method not only has a lower limit on the mass of the sample, discussed earlier in Section 2.3.2, it also has an upper limit to the amount of sample that can be used (especially for samples that have low thermal conductivity). If the sample is too massive, the result is that the apparent heat capacity is lower than the true heat capacity (when compared to other measurements). Masses of the sample used for the PPMS determination were 10.939 ± 0.005 mg, 15.548 ± 0.010 mg, 24.969 ± 0.010 mg, and 54.326 ± 0.010 mg with the ^{4}He system and 19.838 ± 0.010 mg with the ^{3}He system. A more detailed discussion on the

necessity of the number of samples will be given in the next section.

The Raman spectra for ZrW_2O_8 were obtained at room temperature on a Bruker RFS 100 spectrometer using the 1064.5 nm line of Nd:YAG laser with an incident power of 147 mW. The scattered light was collected using a Ge diode detector. The samples were prepared by packing a small amount of the powder into a small hole located in the middle of a circular metal disc. The spectra were taken using 4000 scans at a resolution of 2 cm^{-1}.

3.3.3. Heat Capacity Data

The experimental heat capacities and estimated uncertainties for ZrW_2O_8 measured using the adiabatic calorimeter and the PPMS are given in Table 3.2 and are shown in Figure 3.11. There were no phase transitions present in the 0.4 K < T < 310 K temperature region.

Table 3.2. Experimental heat capacities and estimated uncertainties of ZrW_2O_8 as measured with adiabatic calorimeter and PPMS.

T / K	C_P / J K^{-1} mol^{-1}	T / K	C_P / J K^{-1} mol^{-1}	T / K	C_P / J K^{-1} mol^{-1}
adiabatic calorimeter, 6.2905 ± 0.0005 g**					
38.41	33.2	66.44	64.7	94.53	95.0
43.10	39.6	69.07	67.9	100.85	101.7
45.60	42.0	71.64	70.2	107.11	105.8
47.28	43.8	73.96	71.6	113.27	113.0
49.63	45.1	77.42	75.2	119.39	117.3
53.15	49.8	79.29	78.4	125.47	121.3
55.18	52.2	83.05	82.5	131.53	126.4
59.21	58.1	84.88	84.8	137.43	130.6
61.29	61.1	87.95	90.1	143.28	134.6
64.20	63.4				
adiabatic calorimeter, 13.2544 ± 0.0005 g**					
41.31	38.8	136.27	130.2	228.51	176.7
47.44	43.6	139.48	132.3	231.99	179.5
50.14	46.2	139.50	132.4	234.99	178.4
55.11	51.7	145.81	136.8	237.87	181.5
60.67	59.0	148.83	139.3	241.12	183.6
64.04	61.2	158.15	143.5	244.01	183.3

...continued

T / K	C_P / J K^{-1} mol^{-1}	T / K	C_P / J K^{-1} mol^{-1}	T / K	C_P / J K^{-1} mol^{-1}
67.07	66.0	159.85	144.9	247.49	184.9
70.04	69.4	163.27	147.0	250.23	186.6
73.19	71.4	164.73	147.2	253.09	185.9
77.39	75.8	167.47	148.7	257.74	187.8
82.10	82.1	169.77	150.6	259.36	187.3
86.53	88.4	172.65	152.0	262.15	188.5
88.00	88.4	174.16	153.4	264.73	191.0
92.50	92.9	176.83	154.4	266.47	191.5
97.52	98.1	179.72	156.3	268.38	191.2
99.51	100.3	181.96	156.3	271.54	191.9
100.50	101.0	186.19	158.6	275.42	190.5
103.03	102.6	191.96	160.8	277.19	193.1
106.01	105.1	195.58	163.3	278.78	193.6
108.54	107.8	197.91	163.6	282.80	195.9
110.23	109.9	201.14	166.3	284.39	194.8
112.43	112.4	204.92	168.5	288.54	198.2
114.08	114.1	207.87	169.9	288.89	197.9
118.83	117.2	210.32	170.3	293.16	197.5
119.63	117.9	213.61	171.4	293.37	201.6
119.89	118.0	216.26	171.3	297.63	202.2
120.86	118.9	219.44	172.5	297.80	202.4
126.74	122.5	220.01	173.8	302.36	205.6
129.49	124.9	222.64	175.4	306.86	205.8
130.21	125.8	222.83	174.8		
130.22	125.9	225.54	177.1		
		^{4}He System, 10.939 ± 0.005 mg			
161.07	146.7±0.3	220.85	175.9±0.4	272.49	195.2±1.1
178.96	157.5±0.3	245.34	185.7±0.6	302.89	205.2±0.4
198.80	166.2±0.4				
		^{4}He System, 15.548 ± 0.010 mg			
1.865	0.0100±0.0001	12.13	4.32±0.04	78.63	79.3±0.3
2.070	0.0126±0.0015	13.46	5.53±0.02	87.21	88.2±0.6
2.298	0.0162±0.0016	14.93	6.95±0.03	96.76	97.7±0.4
2.555	0.0208±0.0007	16.56	8.62±0.08	107.36	107.5±0.5
2.835	0.0268±0.0012	18.38	10.6±0.1	119.10	117.4±0.7
3.141	0.0375±0.0048	22.62	15.3±0.2	132.12	127.2±0.6
3.487	0.0561±0.0035	25.09	18.2±0.1	146.57	137.0±0.6
3.868	0.0751±0.0071	27.84	21.5±0.1	162.63	146.1±0.2
4.290	0.113±0.005	30.88	25.1±0.1	180.43	154.8±0.5*
4.759	0.180±0.007	34.25	29.0±0.1	200.14	163.1±0.3*
5.281	0.280±0.006	38.00	33.4±0.2	221.99	171.7±0.6*
6.497	0.662±0.095	42.16	38.4±0.4	246.25	179.3±0.6*
7.213	0.924±0.004	46.78	43.8±0.4	282.83	190.8±6.8*
8.001	1.32±0.01	51.90	49.7±0.6	292.83	200.8±4.5*
8.879	1.84±0.01	57.58	56.2±0.4	303.06	192.6±2.0*
9.851	2.50±0.02	63.88	63.2±0.3	303.24	191.2±5.5*
10.93	3.32±0.04	70.88	71.1±0.2		

...continued

T / K	C_P / J K^{-1} mol^{-1}	T / K	C_P / J K^{-1} mol^{-1}	T / K	C_P / J K^{-1} mol^{-1}
		^{4}He System, 24.969 ± 0.010 mg,			
1.867	0.0087±0.0005*	10.88	2.97±0.02*	63.69	62.2±0.2
2.062	0.0105±0.0007*	13.40	5.03±0.03*	70.67	70.1±0.1
2.282	0.0127±0.0003*	14.87	6.37±0.04*	78.41	78.5±0.2
2.542	0.0179±0.0007*	16.49	7.96±0.07*	86.99	87.4±0.1
2.817	0.0236±0.0006*	18.30	9.78±0.12*	96.52	97.1±0.1
3.130	0.0331±0.0030*	20.30	11.9±0.0*	107.09	107.0±0.2
3.471	0.0476±0.0012*	22.53	14.4±0.1*	118.83	117.0±0.5
3.853	0.0674±0.0051*	24.99	17.3±0.3*	131.84	126.8±0.5
4.273	0.102±0.002*	27.73	20.3±0.1*	146.28	136.8±0.5
4.740	0.157±0.006*	30.77	24.0±0.2*	162.33	146.0±0.6*
5.259	0.244±0.005*	34.13	27.9±0.1*	180.13	155.0±0.4*
5.834	0.367±0.003*	37.87	32.3±0.1*	199.82	163.3±0.4*
6.472	0.548±0.016*	42.02	37.2±0.3*	221.69	171.8±0.6*
7.184	0.806±0.011*	46.63	42.6±0.3*	245.96	179.1±0.8*
7.968	1.16±0.01*	51.74	48.5±0.2*	272.81	185.3±2.0*
8.842	1.62±0.02*	57.40	55.1±0.3*	302.70	190.4±1.2*
9.808	2.22±0.02*				
		^{4}He System, 54.326 ± 0.010 mg			
1.857	0.0079±0.0004*	17.22	8.62±0.20*	153.53	139.9±1.5*
1.992	0.0097±0.0007*	18.41	9.90±0.04*	158.69	142.8±0.6*
2.130	0.0110±0.0006*	19.70	11.1±0.3*	112.43	111.6±0.2*
2.289	0.0135±0.0007*	20.39	12.8±0.1*	117.57	115.8±0.2*
2.447	0.0155±0.0010*	21.08	12.6±0.5*	122.72	119.7±0.3*
2.625	0.0184±0.0005*	22.55	14.5±0.2*	127.86	123.6±0.4*
2.802	0.0223±0.0015*	24.11	16.2±0.2*	163.83	145.5±0.6*
2.990	0.0267±0.0012*	25.80	18.2±0.2*	168.98	147.9±0.6*
3.202	0.0331±0.0067*	27.60	20.2±0.1*	174.11	150.7±0.3*
3.428	0.0419±0.0027*	29.52	22.4±0.3*	179.24	153.0±0.4*
3.670	0.0551±0.0009*	31.58	24.9±0.1*	184.36	155.0±0.5*
3.926	0.0707±0.0009*	33.77	27.5±0.1*	189.50	156.6±1.1*
4.198	0.0905±0.0010*	36.13	30.3±0.1*	194.62	158.1±0.9*
4.487	0.120±0.002*	38.64	33.2±0.1*	199.76	160.0±1.5*
4.802	0.161±0.004*	41.34	36.3±0.1*	204.89	161.8±0.7*
5.139	0.214±0.001*	44.22	39.8±0.2*	210.02	163.3±1.1*
5.490	0.281±0.002*	45.56	41.3±0.1*	215.17	165.2±0.6*
5.859	0.423±0.003*	47.31	43.4±0.1*	220.30	166.8±0.4*
5.860	0.363±0.005*	50.61	47.2±0.2*	225.43	168.2±0.4*
6.276	0.478±0.002*	50.71	47.3±0.1*	230.56	169.2±0.4*
6.726	0.623±0.003*	55.86	53.3±0.1*	235.69	170.7±0.5*
7.176	0.794±0.009*	61.01	59.1±0.4	240.83	172.0±0.7*
7.677	1.01±0.01*	66.16	65.0±0.2	245.96	172.9±0.8*
8.212	1.26±0.00*	71.31	70.9±0.2	251.08	173.8±0.9*
8.783	1.57±0.01*	76.46	76.6±0.2	256.20	174.5±0.8*
9.396	1.93±0.01*	81.57	82.0±0.2	261.33	175.1±1.2*
10.05	2.35±0.01*	86.71	87.4±0.2	266.45	176.0±0.9*
10.76	2.85±0.02*	91.86	92.7±0.2	271.56	176.9±0.8*
11.51	3.40±0.03*	97.01	97.6±0.2	273.09	187.2±1.1*
12.08	3.90±0.02*	102.15	102.6±0.2	276.68	177.6±0.9*

...continued

T / K	C_P / J K^{-1} mol^{-1}	T / K	C_P / J K^{-1} mol^{-1}	T / K	C_P / J K^{-1} mol^{-1}
12.30	4.04±0.02*	107.29	107.4±0.3	281.78	177.9±1.1*
13.16	4.77±0.03*	132.99	127.2±0.5	286.89	179.2±1.3*
14.07	5.59±0.05*	138.13	130.7±0.8	292.06	179.7±1.9*
15.05	6.51±0.03*	143.27	133.8±1.0	297.18	179.3±1.8*
16.10	7.53±0.07*	148.40	137.0±1.0	302.33	176.9±2.0*
		^{3}He System, 19.838 ± 0.010 mg			
0.4075	$(7.82\pm3.03)\times10^{-4}$	1.292	$(4.19\pm0.08)\times10^{-3}$	3.979	0.0846±0.0006
0.4607	$(1.20\pm0.16)\times10^{-3}$	1.378	$(4.72\pm0.24)\times10^{-3}$	4.253	0.111±0.001
0.4844	$(1.49\pm0.03)\times10^{-3}$	1.474	$(5.40\pm0.15)\times10^{-3}$	4.545	0.148±0.003
0.5172	$(7.98\pm0.09)\times10^{-4}$	1.574	$(6.06\pm0.17)\times10^{-3}$	4.859	0.196±0.002
0.5554	$(1.41\pm0.12)\times10^{-3}$	1.681	$(6.96\pm0.22)\times10^{-3}$	5.193	0.260±0.002
0.5906	$(1.04\pm0.01)\times10^{-3}$	1.795	$(8.03\pm0.08)\times10^{-3}$	5.549	0.343±0.002
0.6270	$(1.50\pm0.09)\times10^{-3}$	1.917	$(9.27\pm0.10)\times10^{-3}$	5.931	0.450±0.002
0.6718	$(1.53\pm0.58)\times10^{-3}$	2.050	0.0108±0.0002	6.340	0.579±0.008
0.7156	$(1.71\pm0.06)\times10^{-3}$	2.190	0.0126±0.0003	6.779	0.752±0.009
0.7650	$(2.10\pm0.48)\times10^{-3}$	2.341	0.0149±0.0001	7.244	0.961±0.003
0.8189	$(2.31\pm0.13)\times10^{-3}$	2.499	0.0176±0.0002	7.744	1.214±0.004
0.8697	$(2.21\pm0.32)\times10^{-3}$	2.672	0.0212±0.0001	8.288	1.524±0.004
0.9309	$(3.03\pm0.04)\times10^{-3}$	2.856	0.0257±0.0006	8.861	1.879±0.017
0.9916	$(2.77\pm0.04)\times10^{-3}$	3.054	0.0318±0.0004	9.459	2.274±0.02
1.061	$(3.05\pm0.21)\times10^{-3}$	3.266	0.0398±0.0003	10.07	2.725±0.009
1.130	$(3.38\pm0.10)\times10^{-3}$	3.491	0.0506±0.0006		
1.208	$(3.78\pm0.31)\times10^{-3}$	3.732	0.0663±0.0030		

*Data too uncertain and not used in further analysis (see Section 3.3.3.1 for details).
**Uncertainty for heat capacities measured with adiabatic calorimetry are ± 2% for 50 K < T < 300 K, and increase to ± 4% below T = 50 K. See Section 2.3.1.2 for details of the calculation.

In general, the uncertainty of C_P(adiabatic calorimeter) for T = 50 to 300 K was considered to be constant based on the smallest contribution to the total heat capacity which yields an uncertainty of ± 2%. This gives an uncertainty which is larger than the inaccuracy found for the benzoic acid standard.[83] This is reasonable since the benzoic acid sample contributed 50% to the total C_P, while the ZrW_2O_8 sample contribution is between 30% to 35% for the larger sample and is less than 30% for the smaller sample. The uncertainty for T < 50 K is ± 4%. The adiabatic calorimeter results deviate from optimized PPMS results by less than ± 1% for 100 K < T < 300 K, and ± 3% for T < 100 K, as shown in Figure 3.12. The optimization of the PPMS data is discussed below.

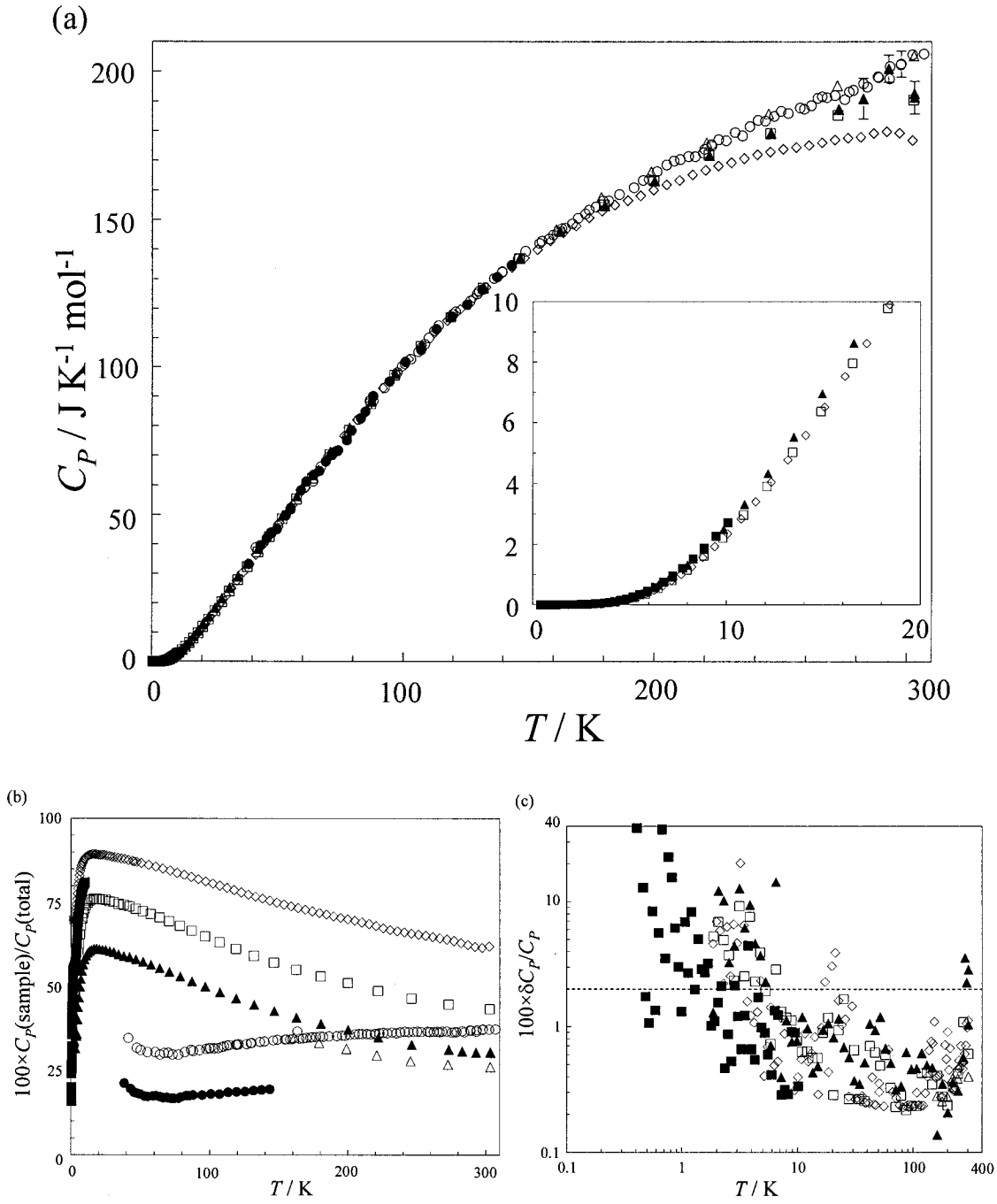

Figure 3.11. Zirconium tungstate heat capacities (a) Heat capacities, error bars are not visible where the symbol size is larger than the calculated uncertainty; (b) relative sample contributions to the total heat capacities; (c) estimated uncertainty. Adiabatic calorimeter, ● 6.2905 ± 0.0005 g and ○13.2544 ± 0.0005 g; PPMS relaxation calorimeter, ^{4}He system, Δ10.939 ± 0.005 mg, ▲15.548 ± 0.010 mg, □24.969 ± 0.010 mg, ◊54.316 ± 0.010 mg; PPMS relaxation calorimeter, ^{3}He system, ■19.838 ± 0.010 mg. Dotted line in (c) represents 2%.

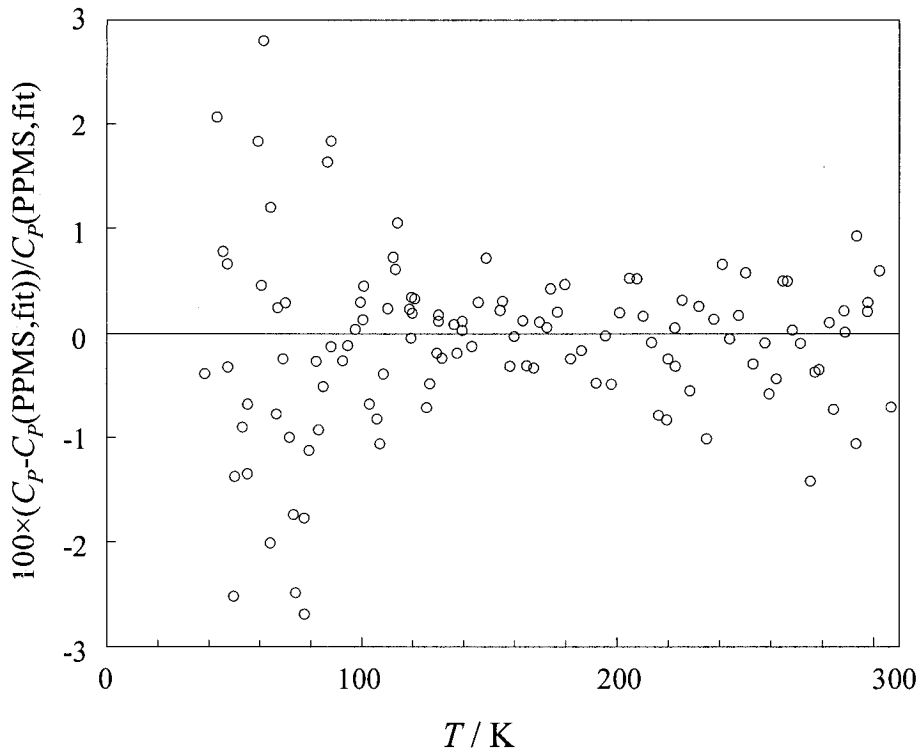

Figure 3.12. Deviation of adiabatic calorimeter results from the optimized PPMS results, (spline fit).

3.3.3.1. Optimal Heat Capacity Data

It is apparent from Figure 3.11(a) that there are deviations among the heat capacities of samples of varying masses for $T > 150$ K. An obvious trend in the deviation is the more massive the sample, the more the C_P(PPMS) deviates from C_P(adiabatic calorimeter), and from the C_P measurements from the literature.[108,115,116] The C_P for the 15.548 mg, 24.969 mg, and 54.326 mg samples all deviated over significant temperature ranges and the T range over which it deviates becomes smaller as the sample size decreases. The 54.326 mg sample exhibited the largest deviations, ~ 15% at $T = 300$ K. It converges with the other data at $T \sim 150$ K. The sample coupling was not unusual in this region, and the temperature fit by the parameters did not reveal why this deviation occurred. Careful analysis of the raw data did not indicate why this occurred. These data

are considered erroneous and are not included in the subsequent analysis and figures (including Figure 3.12).

Data with large fit deviations and with poor sample coupling (as assessed by the QD software) are also excluded. The fit deviation is determined by a mean squared deviation of the fit from model and is expressed as a normalized χ^2.[50] A value that is distinctly larger than for a specific measurement than its neighboring measurements may indicate a bad measurement.

Figure 3.11(b) gives the relative sample contribution to the total C_P. For the 10.939 mg sample, the $100\times C_P(\text{sample})/C_P(\text{total})$ is < 50%. However, it was stated in Section 2.3.2 that for relaxation calorimeters, $100\times C_P(\text{sample})/C_P(\text{total})$ should be > 50% for insulators in order to get accurate results. This is apparently not an issue for this material at higher temperatures. However, at lower temperatures, the calculated uncertainties become large where $100\times C_P(\text{sample})/C_P(\text{total})$ is low for the 10.939 mg and 15.548 mg sample as measured by the ^{4}He system and for the 19.838 mg sample measured with the ^{3}He system.

Due to these problems with sample size over different temperature ranges, the selection of the proper sample size presents a problem for analysis of previously unmeasured samples. If the sample is too massive, the measurement time becomes too long and as is the case for ZrW_2O_8, the results may not be indicative of the true C_P. However, if the sample it too small, the contribution of C_P(sample) to C_P(total) becomes an issue at lower temperatures. This could be an isolated problem due to the unusual thermal transport characteristics of these samples, however, a more definite way of choosing a sample is desirable. It is advisable that several samples of varying sizes be

run to be confident of the results.

Yamamura *et al.* also measured C_P of ZrW_2O_8 using a PPMS.[108] They used a 11.345 mg sample to measure the C_P for $T < 20$ K. They did not indicate the $100 \times C_P(\text{sample})/C_P(\text{total})$ with their results, nor did they indicate any problem with the sample size. They used an adiabatic calorimeter for $T > 10$ K, although no comparison was made between data obtained from this calorimeter, and their PPMS.

The $C_P T^{-3}$ vs. $\ln(T)$ plot is given for the present ZrW_2O_8 heat capacity measurements in Figure 3.13. This plot shows higher $C_P T^{-3}$ in the low temperature region (below $\ln(T / \text{K}) = 1$) compared to Yamamura *et al.*[108] and Stevens *et al.*[116], however, the bell-shaped part of the curve is similar and is centered around the same temperature, approximately $T = 9.5$ K.

At the peak of the bell-shaped curve, the C_P differs slightly for the C_P data from the three sources. A $C_P T^{-3}$ difference of 0.5 mJ K^{-4} mol^{-1} at $T = 9.5$ K corresponds to a difference of 0.43 J K^{-1} mol^{-1} in the C_P data. This is likely due to difference in the ZrW_2O_8 materials, as all three samples came from different sources.

Acoustic modes (approximated by a Debye function) in this type of plot would show constant $C_P T^{-3}$ at low temperature and decrease gently at higher temperatures. Optic-phonon modes (fit by an Einstein function) would show a peak similar to that in Figure 3.13. Essentially, the peak in Figure 3.13 is due to the low-energy optic modes (< 10 meV) in the material.

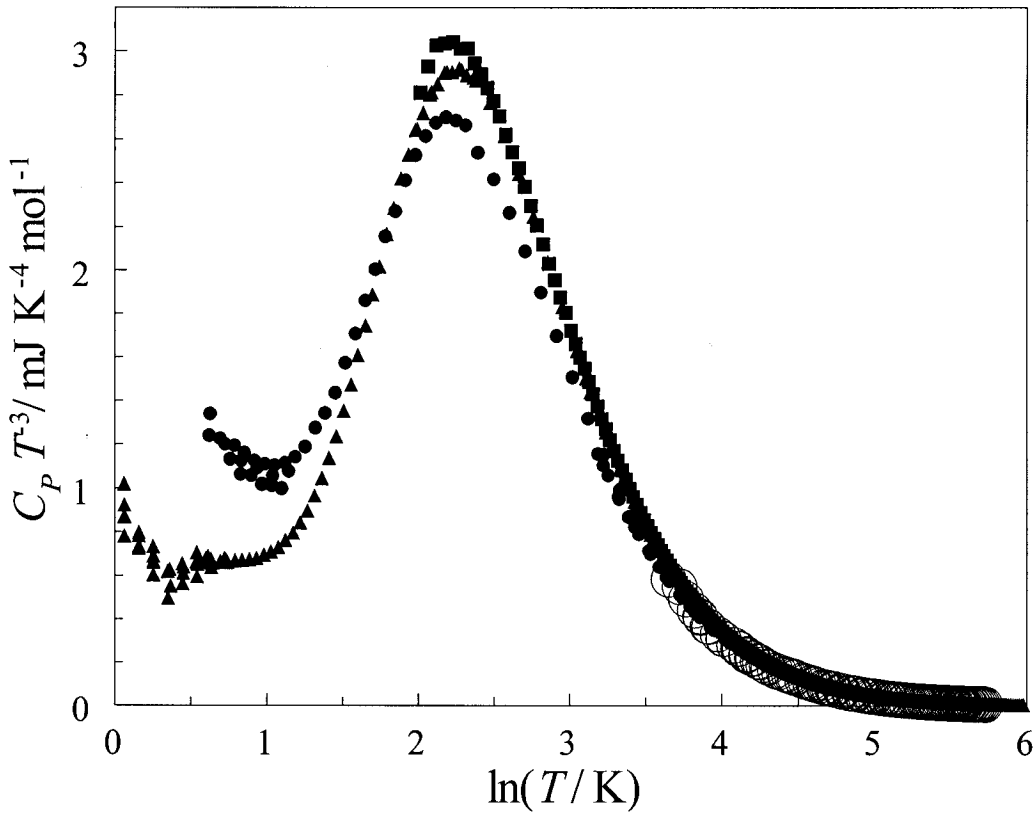

Figure 3.13. $C_P T^{-3}$ vs. ln(T) for ZrW_2O_8 heat capacities from • present PPMS and ○ present adiabatic calorimeter, ▲ Stevens *et al.*,[116] ■ Yamamura *et al.*[108,117]

3.3.4. Comparison to Previous Data

These results, both from relaxation calorimetry and from adiabatic calorimetry given in Figure 3.14, indicate good agreement with the heat capacity data of Yamamura *et al.*[108] and Boerio-Goates *et al.*[115] at high temperature but not with Ramirez and Kowach.[111] The latter measured the heat capacity of a large single crystal of ZrW_2O_8 (m = 0.7 g) while the others used powders. It is now concluded that the heat capacity discrepancy is due to thermal relaxation effects, owing to the low thermal conductivity of ZrW_2O_8, as is presented later in Section 3.5. C_P at T = 300 K from present results is 203 J K^{-1} mol^{-1}; approximately 74 % of the Dulong-Petit value given by 11 × 3R = 274.36 J K^{-1} mol^{-1}.

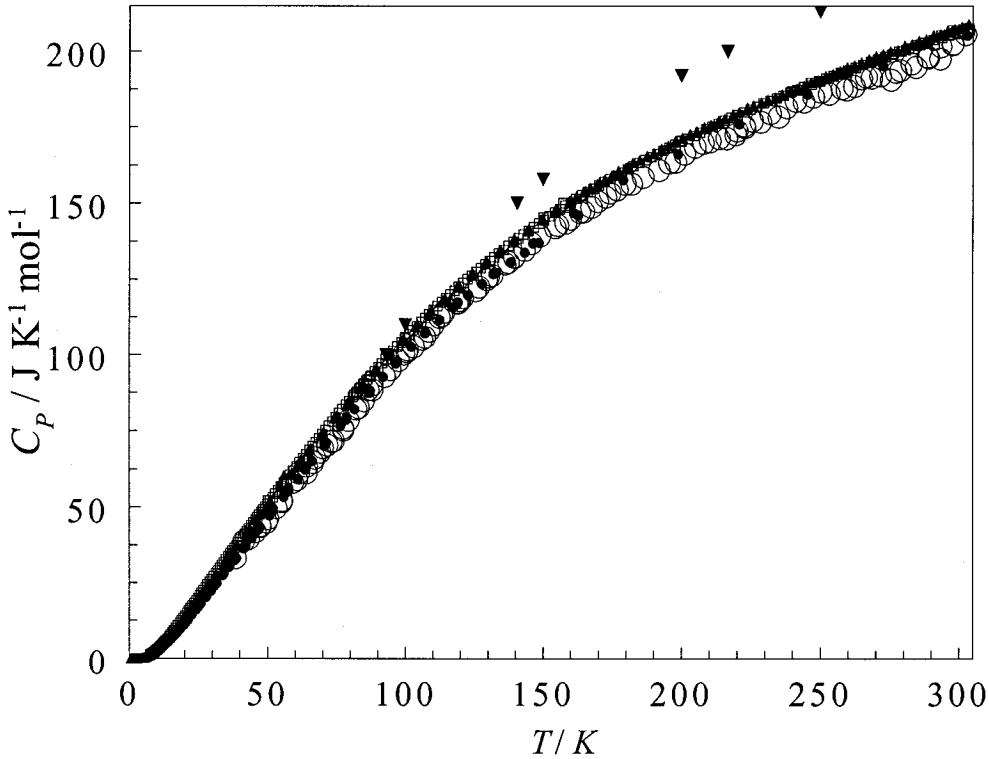

Figure 3.14. Summary of heat capacities of ZrW_2O_8. ▲Stevens *et al.*[116], □Yamamura *et al.*[114,117], ▼Ramirez and Kowach[111], ○ present adiabatic, ● present PPMS.

3.3.5. Constant Volume Heat Capacities, C_V

The C_V values were calculated as a function of temperature using Equation 1.4. The value of B_T used in the calculation was 7.25×10^{10} N m^{-2} [121] and the V and α_V were obtained from the unit cell parameters as a function of temperature determined from diffraction techniques.[102] $\alpha_V = 3 \times \alpha_l$ for a cubic solid. The (C_P - C_V) contributions, C_V, along with the smoothed C_P of zirconium tungstate are reported in Table 3.3. The (C_P - C_V) contribution is < 1% at T = 300 K.

Table 3.3. Smoothed constant pressure heat capacities, constant volume heat capacities and C_p - C_V contributions for ZrW_2O_8. Units of heat capacity are J K^{-1} mol^{-1}.

T / K	C_P	$C_P - C_V$	C_V	T / K	C_P	$C_P - C_V$	C_V
2	0.010	0.000	0.010	130	125.5	0.76	124.8
4	0.086	0.000	0.086	135	129.1	0.79	128.4
6	0.467	0.000	0.467	140	132.6	0.82	131.8
8	1.36	0.001	1.36	145	135.9	0.85	135.1
10	2.65	0.003	2.64	150	139.1	0.87	138.2
12	4.20	0.007	4.19	155	142.1	0.90	141.2
14	6.04	0.01	6.03	160	145.0	0.93	144.1
16	8.03	0.02	8.01	165	147.8	0.96	146.8
18	10.1	0.03	10.12	170	150.5	0.99	149.5
20	12.4	0.04	12.3	175	153.2	1.0	152.1
22	14.6	0.05	14.6	180	155.7	1.0	154.7
24	16.9	0.06	16.9	185	158.2	1.1	157.1
26	19.3	0.08	19.2	190	160.7	1.1	159.6
28	21.6	0.09	21.5	195	163.1	1.1	161.9
30	23.9	0.11	23.8	200	165.4	1.2	164.2
32	26.3	0.12	26.2	205	167.7	1.2	166.5
34	28.7	0.14	28.5	210	169.9	1.2	168.7
36	31.1	0.16	30.9	215	172.1	1.3	170.8
38	33.5	0.18	33.4	220	174.2	1.3	172.9
40	36.0	0.20	35.8	225	176.3	1.3	175.0
45	41.7	0.25	41.4	230	178.3	1.3	176.9
50	46.7	0.29	46.4	235	180.2	1.4	178.8
55	52.3	0.32	52.0	240	182.0	1.4	180.6
60	57.9	0.35	57.6	245	183.8	1.4	182.3
65	63.5	0.38	63.2	250	185.5	1.5	184.0
70	69.1	0.41	68.7	255	187.1	1.5	185.6
75	74.6	0.44	74.2	260	188.6	1.5	187.1
80	80.0	0.47	79.6	265	190.1	1.5	188.6
85	85.4	0.50	84.9	270	191.6	1.6	190.1
90	90.6	0.53	90.0	275	193.1	1.6	191.5
95	95.6	0.55	95.1	280	194.7	1.6	193.1
100	100.4	0.58	99.9	285	196.4	1.7	194.7
105	105.1	0.61	104.5	290	198.3	1.7	196.6
110	109.5	0.64	108.8	295	200.4	1.7	198.7
115	113.7	0.67	113.0	298.15	202.0	1.7	200.3
120	117.8	0.70	117.1	300	203.0	1.7	201.2
125	121.8	0.73	121.0				

3.3.6. Thermodynamic Parameters

Well-defined C_p data from 0 K to 300 K for ZrW_2O_8 can be used to determine thermodynamic functions such as enthalpy, entropy and Gibbs energy. For a change of

state from $T = 0$ K to any temperature T in a single phase region where C_p is known, the enthalpy of the system, H_T, can be derived from direct integration of the heat capacity,

$$H_T - H_0 = \int_0^T C_p dT \qquad 3.1$$

where H_0 is the enthalpy at a temperature of absolute zero. C_P can be directly related to entropy using the differential relation $dH_P = TdS$ which gives

$$C_P = T\left(\frac{\partial S}{\partial T}\right)_P \qquad 3.2$$

when substituted into Equation 1.2. Integration of Equation 3.2 yields an expression for entropy, S_T, is

$$S_T - S_0 = \int_0^T \frac{C_p}{T} dT \qquad 3.3$$

where S_0 is the residual entropy. Since the H and S are known, the Gibbs energy, G, relative to G at absolute zero, G_0, can be obtained from

$$G = H - TS\,. \qquad 3.4$$

The smoothed constant pressure heat capacities were integrated to yield the standard thermodynamic functions for ZrW_2O_8 below $T = 300$ K and they are listed in Table 3.4. The resultant thermodynamic functions agree with those determined by Stevens *et al.*[116] below $T = 400$ K, and with those determined by Yamamura *et al.*[117] below $T = 480$ K.

Table 3.4. Thermodynamic functions of ZrW_2O_8 as calculated from smoothed C_P, all functions are in J K^{-1} mol^{-1}.

T / K	$(H-H_o)/T$	$(S-S_o)$	$-(G-G_o)/T$	T / K	$(H-H_o)/T$	$(S-S_o)$	$-(G-G_o)/T$
2	0.005	0.005	0.00	130	62.24	109.25	47.01
4	0.03	0.03	0.00	135	64.65	114.05	49.40
6	0.11	0.13	0.02	140	67.01	118.81	51.80
8	0.31	0.38	0.07	145	69.33	123.52	54.19
10	0.65	0.81	0.16	150	71.60	128.18	56.58
12	1.11	1.43	0.32	155	73.83	132.79	58.96
14	1.68	2.21	0.53	160	76.01	137.35	61.34
16	2.35	3.14	0.79	165	78.14	141.86	63.71
18	3.10	4.21	1.11	170	80.23	146.31	66.08
20	3.92	5.39	1.47	175	82.28	150.71	68.43
22	4.79	6.67	1.89	180	84.28	155.06	70.78
24	5.71	8.05	2.34	185	86.25	159.36	73.12
26	6.66	9.49	2.83	190	88.17	163.61	75.44
28	7.64	11.00	3.36	195	90.06	167.82	77.76
30	8.65	12.57	3.92	200	91.92	171.98	80.06
32	9.68	14.19	4.51	205	93.74	176.09	82.35
34	10.72	15.85	5.13	210	95.52	180.16	84.63
36	11.79	17.56	5.77	215	97.28	184.18	86.90
38	12.87	19.31	6.44	220	99.00	188.16	89.16
40	13.96	21.09	7.13	225	100.70	192.10	91.40
45	16.73	25.66	8.93	230	102.36	196.00	93.63
50	19.47	30.30	10.83	235	104.00	199.85	95.85
55	22.20	35.01	12.81	240	105.60	203.66	98.06
60	24.94	39.81	14.86	245	107.18	207.43	100.25
65	27.70	44.67	16.97	250	108.73	211.16	102.44
70	30.46	49.58	19.12	255	110.25	214.85	104.61
75	33.22	54.53	21.32	260	111.74	218.50	106.76
80	35.97	59.52	23.55	265	113.20	222.11	108.90
85	38.72	64.53	25.81	270	114.64	225.68	111.03
90	41.46	69.56	28.10	275	116.06	229.21	113.15
95	44.18	74.59	30.42	280	117.45	232.70	115.25
100	46.87	79.62	32.75	285	118.82	236.16	117.35
105	49.53	84.63	35.10	290	120.17	239.60	119.42
110	52.16	89.62	37.47	295	121.52	243.01	121.49
115	54.74	94.58	39.84	298.15	122.36	245.14	122.79
120	57.28	99.51	42.23	300	122.85	246.40	123.54
125	59.78	104.40	44.62				

The thermodynamic parameters for production of ZrW_2O_8(s) from ZrO_2(s) and WO_3(s) have not been previously studied. These parameters can be obtained by considering the thermodynamic cycle shown in Figure 3.15.

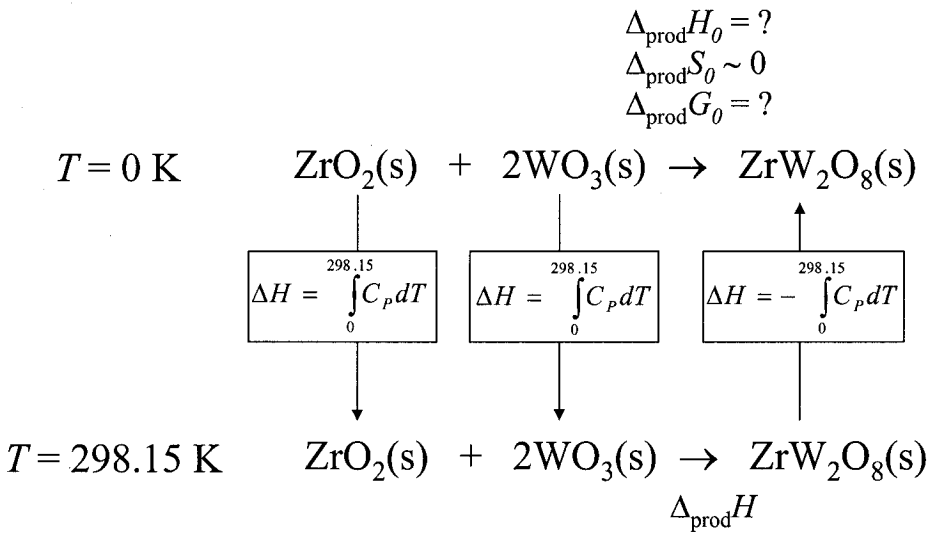

$$\Delta_{prod}H = \Delta_f H^o(ZrW_2O_8) - \Delta_f H^o(ZrO_2) - 2\times\Delta_f H^o(WO_3)$$

Figure 3.15. Thermodynamic cycle for production of $ZrW_2O_8(s)$ from $ZrO_2(s)$ and $WO_3(s)$.

The heat capacity data for $ZrO_2(s)$[148,149,150] and $WO_3(s)$[151,152,153] were obtained from previously published results. The smoothed heat capacities for $ZrW_2O_8(s)$ are reported in Table 3.3. The enthalpies of formation at 298.15 K have been reported for $ZrW_2O_8(s)$, $ZrO_2(s)$ and $WO_3(s)$. They are 64.82 ± 3.60 kJ mol^{-1} [154], -1097.46 kJ mol^{-1} [150] and -842.9 ± 0.8 kJ mol^{-1} [155], respectively. The enthalpy, entropy and Gibbs energy changes for production of $ZrW_2O_8(s)$ from $ZrO_2(s)$ and $WO_3(s)$ as functions of temperature were determined using the cycle in Figure 3.15 along with literature values of heat capacity experiments and heat of formation data. Figure 3.16 is a graphic representation of the thermodynamic functions with respect to temperature.

The Gibbs energy of formation of ZrW_2O_8 from the oxides, $ZrO_2(s)$ and $WO_3(s)$, using the thermodynamic cycle derived here, was found to be positive at room temperature. This is consistent with what is already known about the thermodynamic stability of ZrW_2O_8, that it is unstable in this temperature range, ($\Delta_{prod}G > 0$).

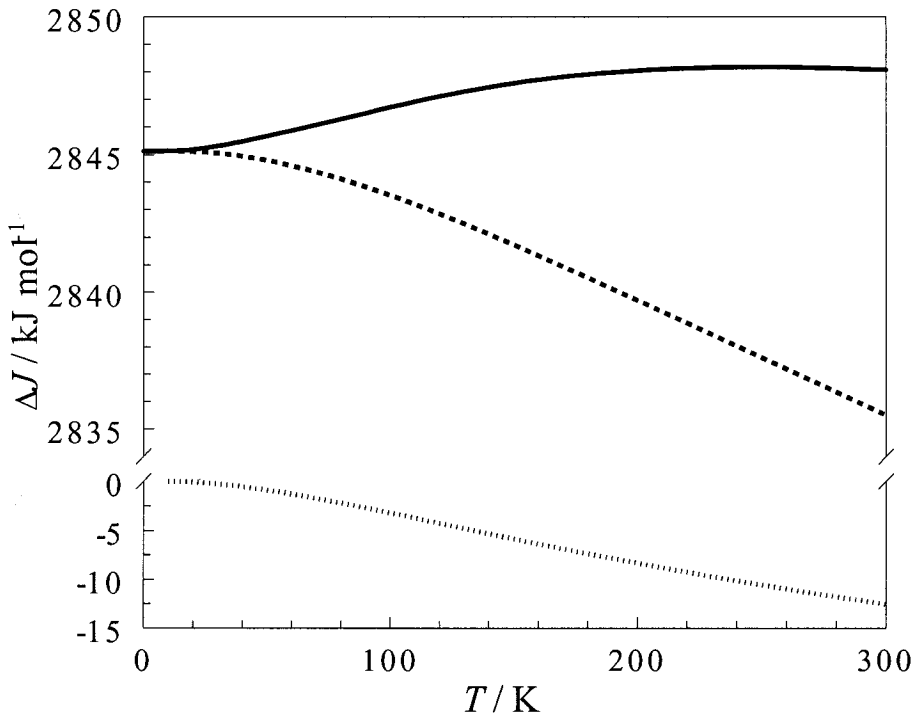

Figure 3.16. The values of $\Delta_{prod}H$ (—), $-T\times\Delta_{prod}S$ (| | | |), and $\Delta_{prod}G$ (----) for production of ZrW_2O_8(s) from ZrO_2(s) and WO_3(s) as functions of temperature. $\Delta J = \Delta_{prod}H$, $-T\times\Delta_{prod}S$, and $\Delta_{prod}G$.

3.4. Theoretical Calculation of Heat Capacity

3.4.1. Introduction

The heat capacity is calculated using the Einstein and Debye formulas, Equations 1.8 and 1.9, along with spectroscopic analysis and can be compared with the experimental data. By doing this, one can better understand the modes that contribute to the heat capacity over specific temperature ranges. This will help identify the modes that are leading to NTE in ZrW_2O_8.

3.4.2. Raman, IR and Phonon Density of States Spectroscopic Analysis

The α-ZrW_2O_8 crystallizes in the $P2_13$ space group (T^4) and has four formula units per unit cell. This gives a total of 4 × 11 = 44 atoms per unit cell, and 3 × 44 = 132

degrees of freedom per unit cell, of which three are acoustic and 129 are optic. Ravindran *et al.*[156] have given a classification of the phonons in this system. They can be classified as acoustic, lattice modes arising from Zr atom motion, translational and librational (hindered rotation) modes of $[WO_4]^{2-}$ ions and internal modes of distorted $[WO_4]^{2-}$ tetrahedra. The irreducible representation for the various classes of modes as follows: acoustic(3) = T; lattice(9) = $A + E + 2T$; translational(24) = $2A + 2E + 6T$; librational(24) = $2A + 2E + 6T$; internal(72) = $6A + 6E + 18T$; total(132) = $11A + 11E + 33T$.

Of the 54 predicted optically active modes, Ravindran *et al.* observed 21 in the Raman spectrum at room temperature, given in Table 3.5. The Raman spectrum has been measured by other groups; Evans *et al.*[102] observed 18 phonon modes and Perottoni and da Jornada[125] observed 13 in their Raman spectra. Yamamura *et al.*[108] observed 26 in their Raman spectrum. The present Raman analysis yielded 31 peaks, see Figure 3.17 for Raman peaks from current study and Table 3.5 for Raman modes observed by Ravindran *et al.* and Yamamura *et al.* with those from present modes.

Based on the assignment by Ravindran *et al.*, there should be 32 degrees of freedom in the high-frequency region (628 to 1034 cm^{-1}) from 14 modes, however only 13 are apparent from the present Raman spectroscopy results at $T = 300$ K. In the low-frequency region (< 433 cm^{-1}) there should be 97 (optic) degrees of freedom from 40 modes; only 18 are apparent from Raman and one from infrared analysis[143] at $T = 300$ K. In total, 32 optic modes were observed and used in the analysis. There are no peaks in the Raman spectrum between 433 and 736 cm^{-1}.

The phonon density of states, PDOS, of ZrW_2O_8 has been measured at $T = 300$ K

using inelastic neutron scattering, shown in Figure 3.18.[103] There is a gap in the PDOS where there are no peaks, between 433 and 628 cm^{-1}, similar to the results of the Raman spectrum.

Table 3.5. Observed frequencies from Raman and IR spectroscopy.

Ravindran *et al.*[156] cm^{-1}	**Yamamura *et al.*[108] cm^{-1}**	**Present work, T = 298 K cm^{-1}**	**meV**	**Assigned degrees of freedom (present work)**
-	-	28.5*	3.5*	1
41	40.9	41	5.1	1
-	51.7	-	-	-
65	65.8	65	8.1	2
74	75.6	74	9.2	4.5
84	86.2	84	10.4	4.5
-	-	107	13.3	4.5
144	143	145	18.0	6
-	-	182	22.6	6
-	-	210	26.0	6
235	235	237	29.4	6
244	245	247	30.6	6
-	-	271	33.6	6
-	284	281	34.8	6
-	300	296	36.7	7.7
310	308	310	38.4	7.7
-	331	-	-	-
333	334	333	41.3	7.7
-	-	362	44.9	4.8
382	384	383	47.5	4.8
-	-	414	51.3	4.8
737	735	736	91.3	2.4615
746	744	749	92.9	2.4615
773	774	773	95.8	2.4615
790	790	789	97.8	2.4615
861	862	862	106.9	2.4615
-	-	868	107.6	2.4615
886	888	892	110.6	2.4615
904	903	904	112.1	2.4615
932	931	931	115.4	2.4615
967	967	968	120.0	2.4615
-	996	980	121.5	2.4615
1020	1019	1020	126.5	2.4615
1029	1029	1029	127.6	2.4615
			Total	**129**

* From IR study by Hancock *et al.*[143]

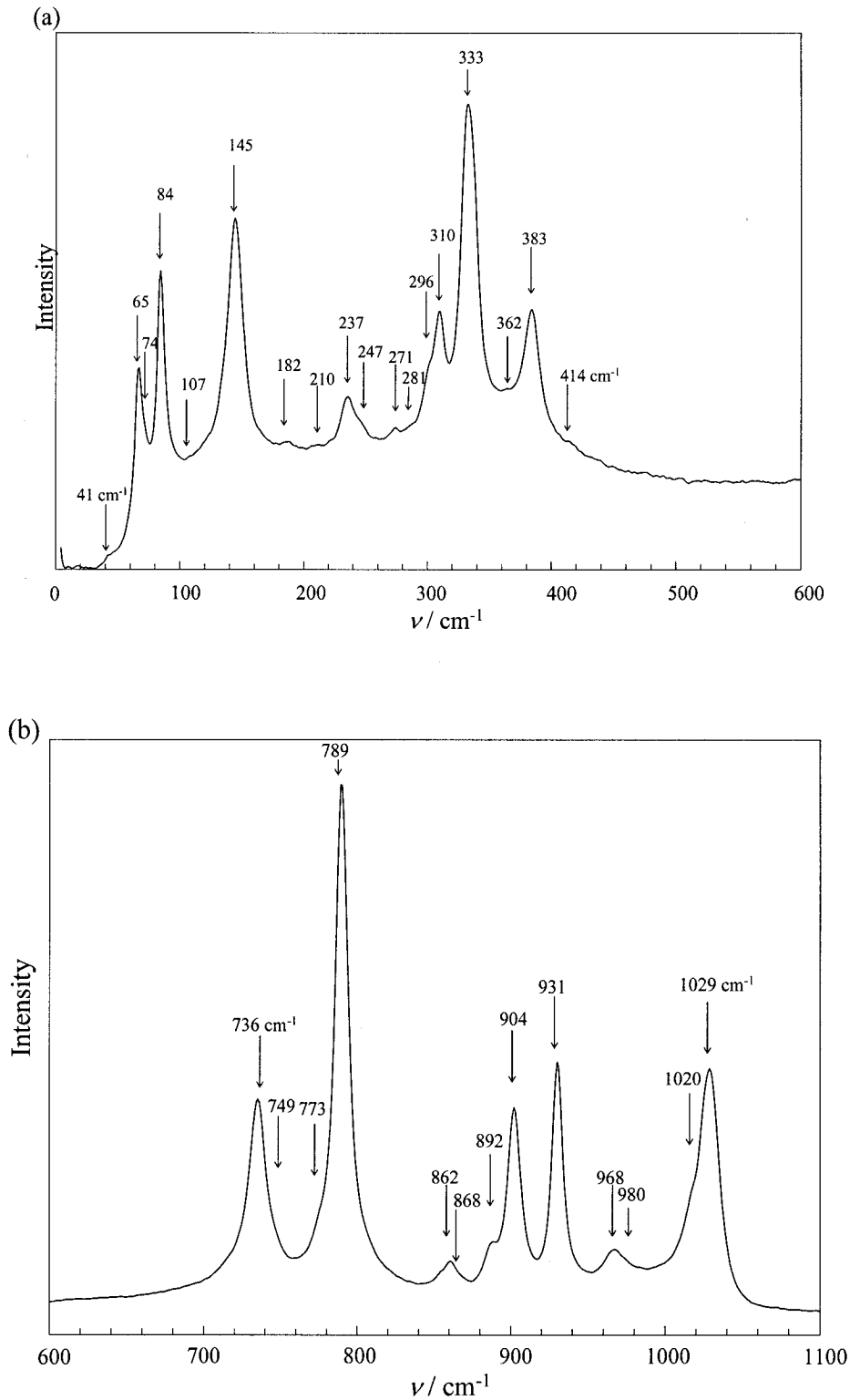

Figure 3.17. Raman spectrum of ZrW_2O_8 from the present study at T = 300 K with assigned peaks shown for (a) the low-frequency region, and (b) the high-frequency region.

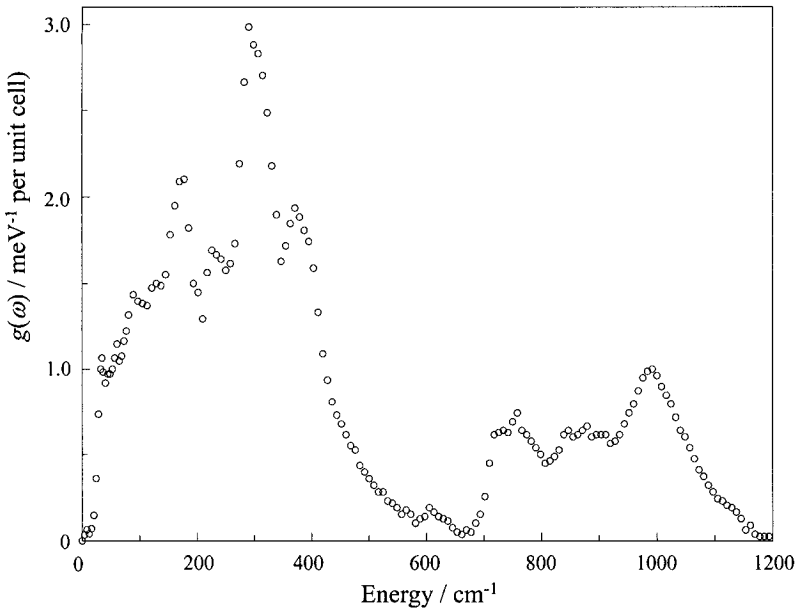

Figure 3.18. Phonon density of states, $g(\omega)$, of ZrW_2O_8 at $T = 300$ K from inelastic neutron scattering. Redrawn after original reference.[103]

3.4.3. Calculation of C_V(optic) from Spectroscopic Analysis

3.4.3.1. Previous Models

Several approaches have been taken to determine the heat capacity using Einstein and Debye terms along with spectroscopic analysis. Some of these reports have compared their calculated heat capacity to measurements obtained by Ramirez and Kowach that have been shown above to be overestimated.[108,115,116] Previous methods used to calculate heat capacity will briefly be described before introducing a new attempt at modeling the heat capacity of ZrW_2O_8.

Early analysis include Ramirez and Kowach's protocols published in 1998 which involved using Einstein and Debye modes with the oscillator strength/formula unit approximated from experimental PDOS. Their models fit their data well; however, the protocols only use two or three low-frequency Einstein modes, while from Raman analysis in the present study, 31 optic modes were found. Ramirez and Kowach used

several Debye modes that deviate from those determined experimentally[111] and the assigned oscillator/f.u. contribution for the Debye modes is too large. It should be three per unit cell, therefore 3/4 per formula unit. See Table 3.6 and Figure 3.19 for the parameters they used.

The most physically realistic calculations would use Raman and IR spectroscopy to determine the optic modes, and then use the experimental PDOS to estimate the oscillator strength per formula unit. Ravindran *et al.* measured the Raman spectrum and assigned optic modes.[156] These are given in Table 3.5 along with those measured for present work.

Table 3.6. Parameters used by Ramirez and Kowach[111] for their calculation of the heat capacity of ZrW_2O_8 with Einstein modes ($E1$, $E2$, and $E3$) and Debye modes (θ_{D1}, and θ_{D2}) for fit (a) and fit (b).

(a)			(b)		
Mode	Energy	Oscillator/f.u.	Mode	Energy	Oscillator/f.u.
1	3.1 meV	0.44	$E1$	3.3 meV	0.52
$E2$	5.0 meV	1.7	$E2$	5.8 meV	1.7
$E3$	12 meV	6.9	θ_{D1}	650 K	22.5
θ_{D1}	650 K	22.5	θ_{D2}	200 K	7.2
θ_{D2}	20 K	0.008			

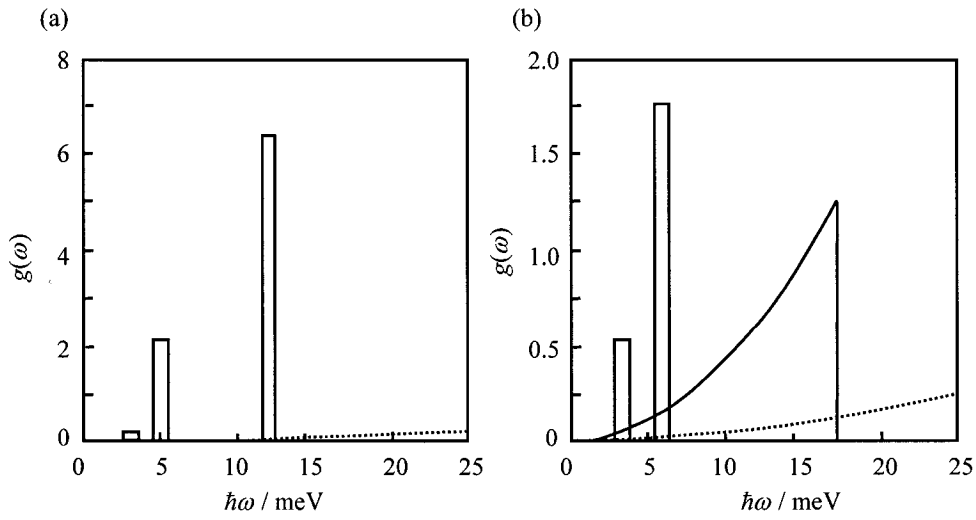

Figure 3.19. The derived three-dimensional phonon spectrum from Ramirez and Kowach for fit (a) and fit (b).[111] Parameters are given in Table 3.6.

To calculate the heat capacity from these frequencies, the oscillator strength per formula unit was estimated by drawing vertical lines in the PDOS at the corresponding Raman frequencies assigning a number of phonons to each branch of frequency. This was achieved by determining the relative heights of the lines and optimizing the height so that the degrees of freedom in total equaled 129 for all of the optic modes. They used a Debye temperature of 200 K from the remaining three acoustic modes and their results were compared to the Ramirez and Kowach heat capacity data.[111]

Ravindran *et al.* calculated a heat capacity of 200 J K^{-1} mol^{-1}, which is 10% lower than Ramirez and Kowach's data, however, it fits well with more recent measurements[108,115,116] and present heat capacity measurements. However, the Debye temperature is not physically accurate since it is now known from low-temperature heat capacity analysis that θ_D = 88 K, (see later for details). Also, they failed to recognize an important mode at 28 cm^{-1} obtained from IR[143] and other modes that are apparent from the present Raman spectrum.

Hancock *et al.*[143] carried out an analysis similar to that done by Ravindran *et al.*[156] They included the low Einstein mode at 28 cm^{-1} and used θ_D = 89 K. Their analysis also provides a good fit to the heat capacity reported previously by Ramirez and Kowach.[111]

Yamamura *et al.* devised a very effective method to calculate the C_V to fit their experimental data (measured with adiabatic and relaxation calorimetry).[108] They used two Einstein modes, *E*1 and *E*2, one Debye mode, *D*, and two rectangular shaped functions, *R*1 and *R*2, to calculate the effective DOS. Table 3.7 and Figure 3.20 give the parameters they used to analyze the heat capacity of ZrW_2O_8.

The lowest-frequency Einstein mode $E1$, corresponds to the lowest-frequency peak of $g(\omega)$. The Debye temperature was calculated from their low temperature heat capacity data. They calculated θ_D from the slope of the plot of $C_P T^{-1}$ vs. T^2 assuming three degrees of freedom for four formula units. The degrees of freedom and characteristic temperature were assigned and optimized by using a nonlinear least-squares method.

Table 3.7. Parameters of each mode obtained for the analysis of heat capacity of ZrW_2O_8 used by Yamamura *et al.*[108] D is Debye mode, E is Einstein mode and R is a rectangular contribution to PDOS.

Mode	Degrees of freedom	θ / K
D	3	88.1
$E1$	3.12	41.8
$E2$	2.08	111
$R1$	90	59.6-608
$R2$	33.6	831-1747

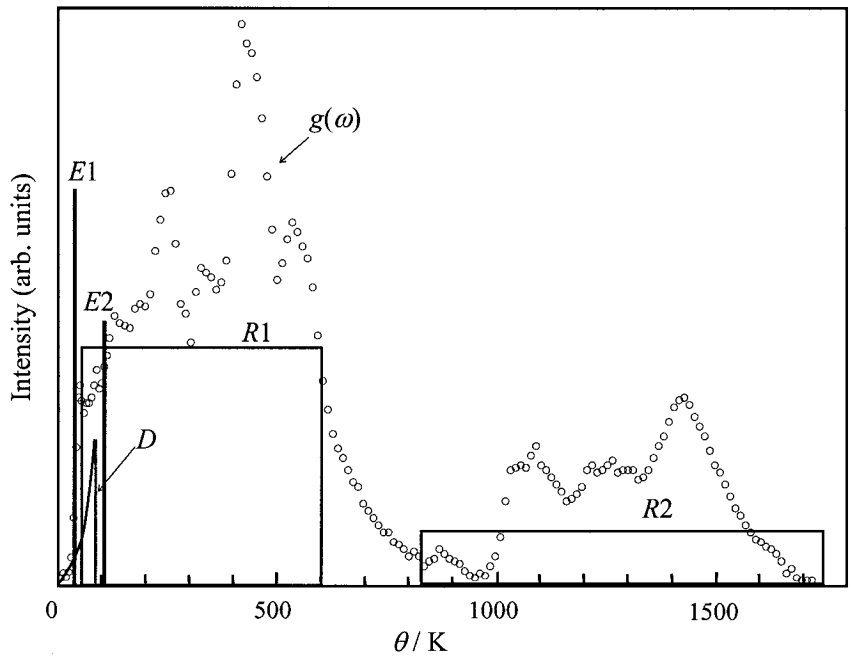

Figure 3.20. Calculated effective phonon density of states (parameters given in Table 3.7) and experimental PDOS[103] from inelastic neutron scattering , $g(\omega)$. Redrawn from original reference.[108]

3.4.3.2. Present Model

The analysis used in the present model is similar in parts to previous analyses; however, my goal in calculating the effective PDOS and heat capacity of ZrW_2O_8 was to be as physically accurate as possible. The assignment of the degrees of freedom per observed IR and Raman mode was achieved by separating the experimental PDOS into frequency bins. Integrating over $g(\omega)$ from the PDOS spectrum, five modes up to $\hbar\omega =$ 8.5 meV (68.6 cm^{-1}) were found, of which at least two out of three are acoustic.[103] Therefore, four degrees of freedom were assigned to the three modes below $\hbar\omega$ = 8.5 meV and θ_D = 88 K was used for the acoustic modes.

Integration of the PDOS in the high-frequency region yielded 32 degrees of freedom which were divided evenly between the 13 modes in the high-frequency region. The sum of the optic degrees of freedom in the low-frequency region is 129 - 32 = 97. The low-frequency degrees of freedom were distributed among the 19 optic modes and were optimized by using a nonlinear least-squares method. The PDOS frequency distribution is given in Table 3.5 and is shown in Figure 3.21.

The Einstein equation for heat capacity (Equation 1.8 and Equation 1.11) was used to calculate C_V(optic) with the degrees of freedom and frequencies as explained above. C_V(optic) for one formula unit was compared with C_V(exp). These are shown along with other contribution to the calculated C_V(cal) are shown graphically in Figure 3.22.

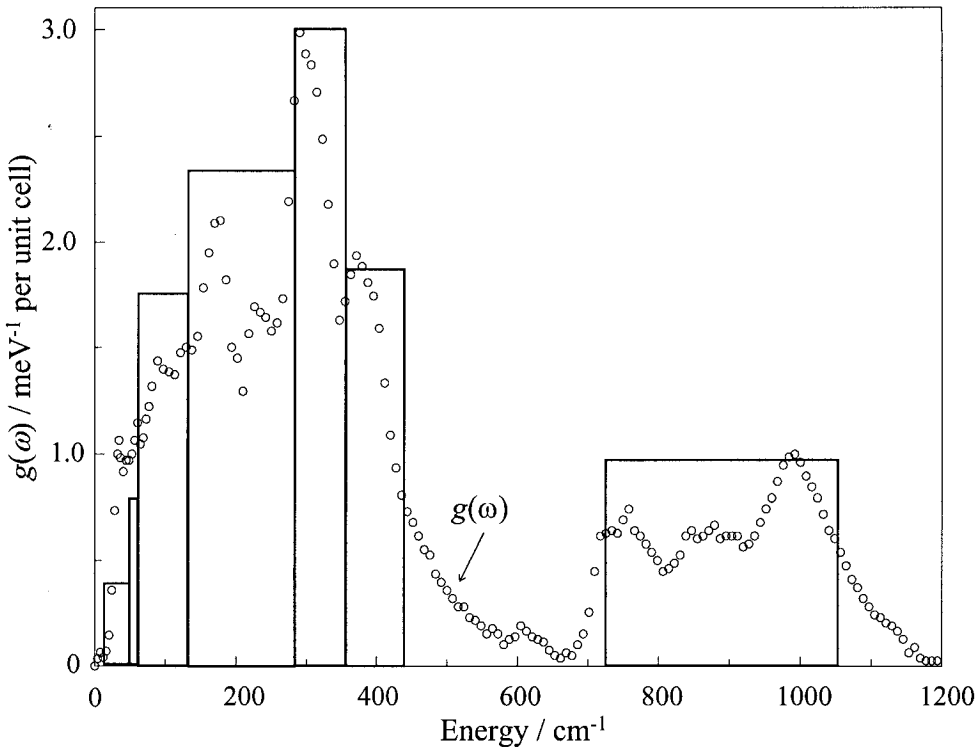

Figure 3.21. Calculated effective phonon density of states, $g(\omega)$, (parameters given in Table 3.5) and ○ experimental PDOS[103] from inelastic neutron scattering.

The fit shown in Figure 3.22 (total calculated) works well for $T > 100$ K but deviates from C_V (exp) for $T < 100$ K. This is due to a poor estimation of C_V(total optic) using the method described earlier. The fit could be improved by adjusting the distribution of frequencies. For example, one improvement would be to make the lower-frequencies modes account for more degrees of freedom. However, this would not be consistent with the results of the experimental PDOS which state that below 8.5 meV, there can only be five degrees of freedom, of which at least two are acoustic. Of most concern is the behavior of the optic modes below 8.5 meV (68.6 cm^{-1}) since these are the modes that have been deemed responsible for negative thermal expansion.[103]

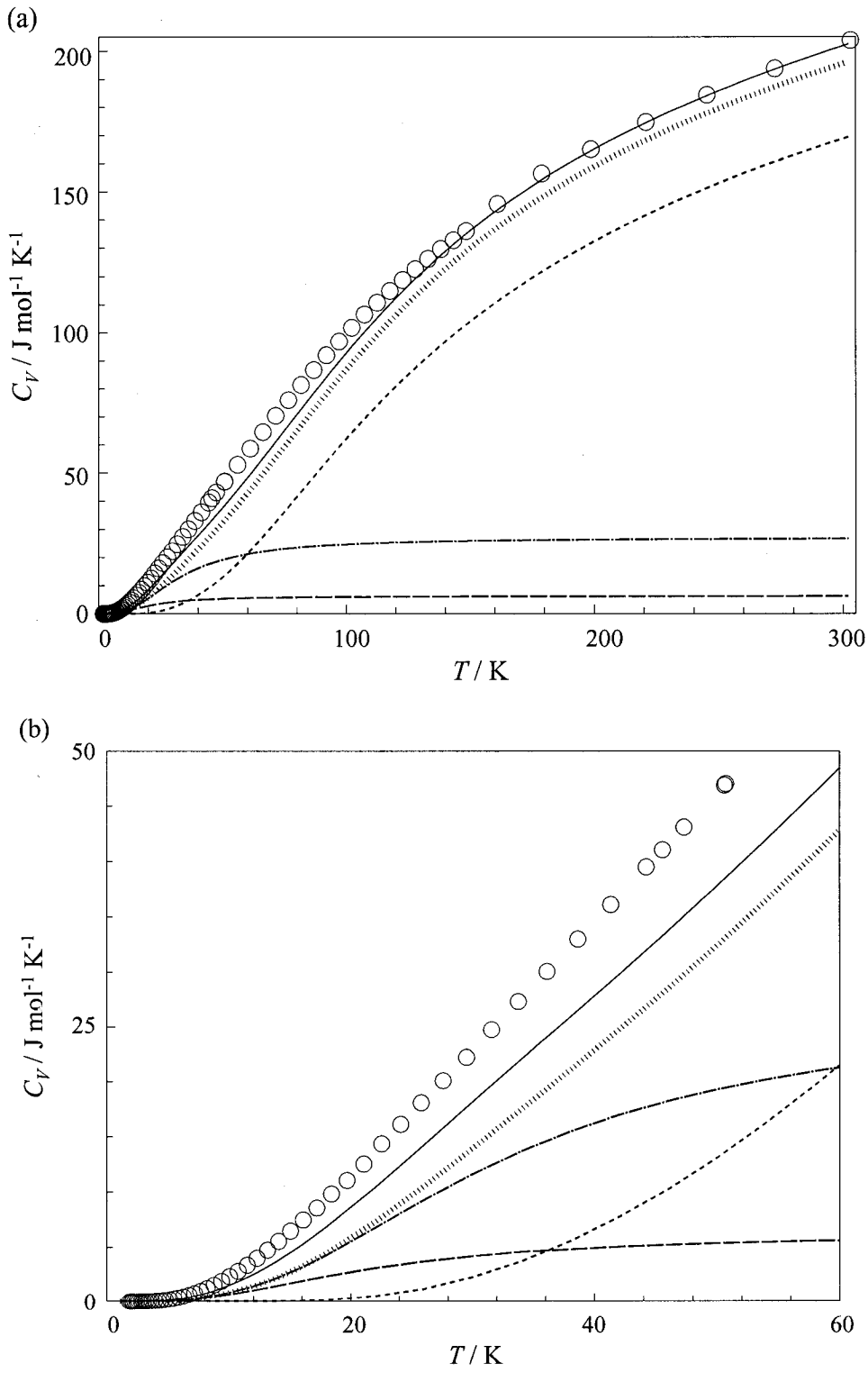

Figure 3.22. (a) Calculated heat capacity of ZrW_2O_8. ○ experimental data, (—) total calculated, (|||||) total optic, (— - —) optic with energies < 10 meV, (----) optic with energies > 10 meV) and (— —) acoustic. Close-up view given in (b).

3.4.4. Conclusions

My analysis of the contributions of various modes to the heat capacity of ZrW_2O_8 (Figure 3.22) indicates that for $T > 60$ K the modes below 10 meV which are most relevant for negative thermal expansion,[103] are essentially fully excited. These modes are so low in frequency that they can be highly anharmonic, essentially fully coupling with each other. This could lead to short phonon mean free paths, high resistance to heat flow, and low thermal conductivity. In the following sections, the thermal conductivity and the Grüneisen parameter (used to quantify anharmonicity) of ZrW_2O_8 will be discussed.

3.5. Thermal Conductivity

3.5.1. Introduction

A perfect harmonic solid has no thermal expansion, and normal (positive) thermal expansion in solids arises from anharmonicity in lattice dynamics. Peierls determined that thermal resistance in insulators arises from phonon-phonon interactions which cause the phonons to turn back onto themselves.[25] Phonon-phonon coupling requires anharmonic interactions. As mentioned previously, the negative thermal expansion of ZrW_2O_8 has been attributed to the presence of highly anharmonic low-frequency vibrational modes.[103,106,107,109] Therefore, both NTE and thermal resistance have their origins in anharmonic terms in the lattice dynamics.

There have been several comments on zirconium tungstate's ability to conduct heat. Ramirez and Kowach[111] commented on the long time constant for internal thermal equilibrium for their heat capacity measurements above $T = 20$ K. In their heat capacity

study on ZrW_2O_8, Stevens *et al.* also mentioned that their techniques required semi-adiabatic conditions below T = 30 K due to poor thermal conductivity of their samples.[116]

As already mentioned above, ZrW_2O_8 acts as an electrical insulator at room temperature.[102] Until very recently, there were no reports of its thermal conductivity at room temperature or below, nor was the trend in the thermal conductivity below room temperature known. If ZrW_2O_8 exhibits the temperature dependence of a "normal", simple crystalline solid, the thermal conductivity would show a peak below room temperature, and a negative temperature coefficient at room temperature.

The thermal conductivity of $Zr_{1-x}Y_xW_2O_8$ (x = 0.00, 0.01) above room temperature (from T = 300 K to 550 K) has been reported very recently by Hashimoto *et al.*[118] from thermal diffusivity measurements (estimated from the laser-flash technique)[157] and heat capacity measurements using power-compensated differential scanning calorimetry. The heat capacity data were in agreement with previous measurements using adiabatic scanning calorimetry.[112] Hashimoto *et al.*[118] calculated the thermal conductivity from thermal diffusivity measurements and heat capacity. Thermal diffusivity (D, units of m^2 s^{-1}) describes the rate at which heat is conducted through a material. It is related to the thermal conductivity, κ, heat capacity at constant pressure (C_P), and density (ρ) of a material through the following function:

$$D = \kappa\, C_P \rho \qquad 3.5$$

This report has shown unusually low thermal conductivity for ZrW_2O_8 at and above room temperature.

For this thesis, the goal was to carry out low-temperature measurements of the

thermal conductivity of ZrW_2O_8 to delineate the origins of its unusually low thermal conductivity. The latter was accomplished through consideration of the theoretical minimum thermal conductivity, the phonon mean free path, the Grüneisen parameter, and the contributions of various modes to the heat capacity.[158]

3.5.2. Thermal Conductivity of Crystalline Oxides

A review of the thermal conductivity of various crystalline oxide ceramics is needed to understand the significance of the κ results for AB_2O_8 NTE materials. Zirconia (ZrO_2) has one of the lowest thermal conductivities in a ceramic (typically ~2 to 3 W m^{-1} K^{-1}), and as such, it has been used widely in applications where a thermal insulator is needed at high temperatures.[159] An example of such an application is in thermal barrier coatings where yttria (Y_2O_3)-stabilized zirconia (YSZ) is used to protect and insulate hot-section metallic components in engines.[160] The thermal conductivity of YSZ and ZrO_2 stabilized with MgO are shown in Figure 3.23 along with other oxides.

Data for Al_2O_3, MgO, $BaTiO_3$, Fe_3O_4, $SrTiO_3$, NiO, SiO_2, TiO_2, MnO, Y_2O_3, and $MgO{\cdot}3.5Al_2O_3$ were taken from Touloukian *et al.*[28] The κ data for BeO were obtained from Slack[161], and $MgAl_2O_4$ data were from Burghartz and Schulz.[162] Most of these oxides show typical crystalline behavior with a maximum in the thermal conductivity (as discussed in Section 1.4.3).

Figure 3.24 gives the thermal conductivities for oxides that have relatively low κ values. Data for $MnZnFe_2O_4$, $MnFe_2O_4$, $ZnFe_2O_4$, $CoZnFe_2O_4$, ThO_2, SnO_2, $CaTiO_3$, and $SrZrO_3$ were from Touloukian *et al.*[28] Data for $Y_3Fe_5O_{12}$ and $Y_3Al_5O_{12}$ were from Padture and Klemens[163]; $ZrO_2{\cdot}3mol\%Y_2O_3$ data were from Stevens[164]; data for

ZrO_2·5.3mass%Y_2O_3 and ZrO_2·5mass%MgO were from Hasselman *et al.* [165]; and data for YBa_2ZrO_6 were obtained by Sreekumar et al.[166]

For most of the oxides, it seems that there is a peak in the temperature dependence of κ, however it is difficult to tell since not all the κ data were available in the temperature range needed to make this assessment. For $ZnFe_2O_4$, YBa_2ZrO_6, and the various stabilized zirconia compounds, it seems that there would not be a peak in the κ. YBa_2ZrO_6 has very low thermal conductivity at room temperature, 0.4 W m^{-1} K^{-1}.[166]

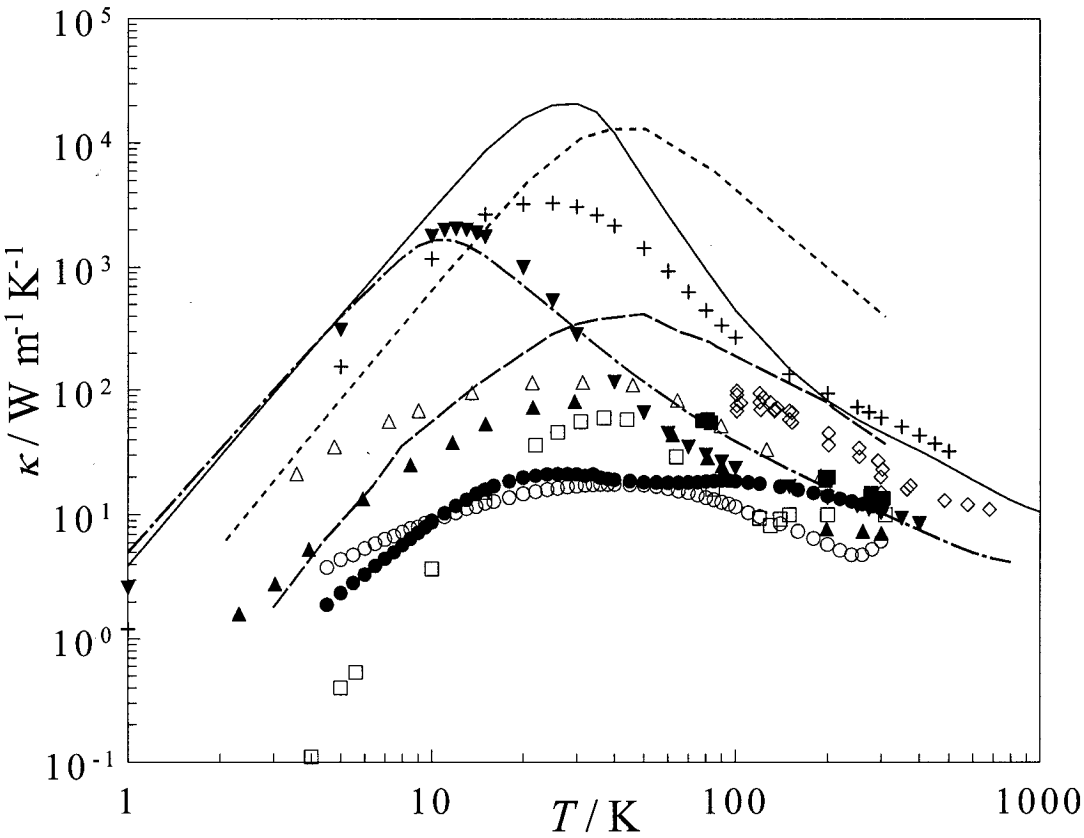

Figure 3.23. Thermal conductivities of crystalline oxide materials with relatively high κ values. (—) Al_2O_3, (— - —) SiO_2, (----) BeO, (— — —) NiO, + MgO, ○ $BaTiO_3$, ▲ Fe_3O_4, ◊ $MgAl_2O4$, Δ MgO·3.5Al_2O_3, ● $SrTiO_3$, ▼ TiO_2, ■ Y_2O_3, and □ MnO.

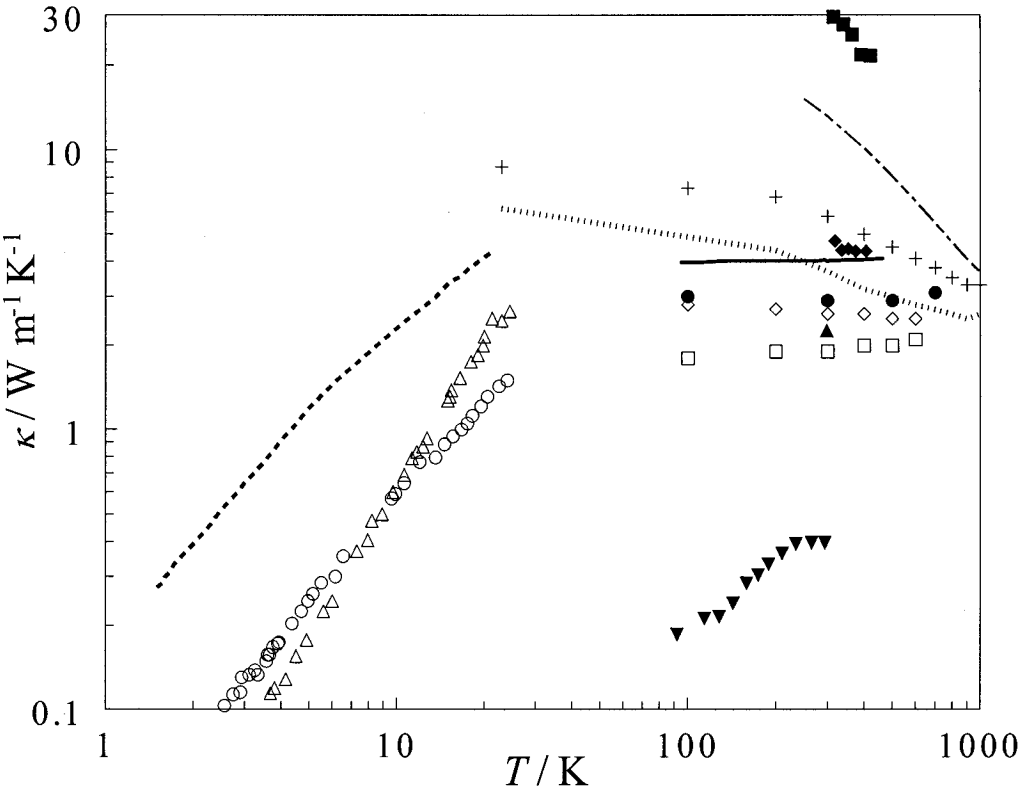

Figure 3.24. Thermal conductivities of crystalline oxide materials with relatively low κ values. (— - —) ThO_2, (—) $ZnFe_2O_4$, (‖‖‖)$Y_3Fe_5O_{12}$, (----) $MnZnFe_2O_4$, ◊ ZrO_2·5.3mass%Y_2O_3, +$Y_3Al_5O_{12}$, □ ZrO_2·5 mass%MgO, ○ $CoZnFe_2O_4$, ▲ $SrZrO_3$, Δ $MnFe_2O_4$, ■ SnO_2, ● ZrO_2·3mol%Y_2O_3, ▼ YBa_2ZrO_6, and ♦ $CaTiO_3$.

3.5.3. Experimental Methods

The samples were pressed into disk-shaped pellets with a diameter of 4.74 mm using a load of 2000 lbs (0.5 GPa). The pressing step was required to create sample morphologies suitable for thermal conductivity (and also relaxation heat capacity measurements, see Section 3.3.2) and also to decrease grain boundaries effects between the crystallites. The samples were heated for 24 hours in atmosphere at 408 K to ensure only α-ZrW_2O_8, as for the heat capacity measurement. Table 3.8 gives the dimensions and the density of the ZrW_2O_8 pellets used in this study and compares the density to the ideal density.

Temperature-dependent thermal conductivities of α-ZrW_2O_8 were determined using the thermal transport option of the QD PPMS. A two-probe configuration (heater and hot thermometer shared one lead while the coldfoot and cold thermometer shared the other) was used and the pellets were epoxied (0.2 mm of silver-loaded epoxy, Tra-Bond 816H01 from Tra-Con, Inc.) to two disc-shaped copper leads (diameter of 6.30 mm). The thermal conductivities were measured under vacuum of 10^{-4} Torr. Thermal conductivities were measured using both continuous and single methods; the principles of operation for these techniques are based on a pulse method and are described in Section 2.2.

Table 3.8. Size, actual density and % of theoretical density of ZrW_2O_8 pellets used to measure thermal conductivity with the PPMS.

Sample	Thickness / mm	Density / g cm^{-3}	% Density
1	1.24	3.78	74.4
2	1.05	3.96	78.0
3	1.00	3.79	74.6
4	1.18	3.79	74.6
5	1.22	3.82	75.2

The geometry of the thermal conductivity sample was constrained in several ways. The thickness of the sample, l, is limited by the thermal diffusion time constant for the sample defined as $\tau \sim C \times l^2/\kappa$. Too thick a sample would result in excessively long measurement times; the minimum thickness is governed by the optimal temperature drop across the sample ($\Delta T \sim 0.03 \times T$). The maximum heater power, P, for the 2 kΩ heater in the PPMS is 50 mW where $P = \kappa \times \Delta T \times (A/l)$ and A is the sample area. The optimal height of the pellets was determined to be approximately 1 to 1.2 mm.

3.5.4. Results and Discussion

3.5.4.1. Comparison of Single and Continuous Mode

For zirconium tungstate sample 1, measurements were taken both in the continuous scanning mode (measurements taken continuously as the software adjusts parameters, such as the heater power and period, to optimize the measurements) and the step-wise mode (more direct than the continuous mode since the system is required to reach a steady state when the heater is in both the "on" and "off" states). The two measurement modes should yield results that are the same within the uncertainty of the technique.

Figure 3.25(a) is a graph of the ΔT vs. time collection during the heat at approximately $T = 263$ K using single mode. As is evident from the data, it took more than 10 minutes to reach temperature stability equal to 0.1 dT/T, and the entire cycle was approximately 15 minutes at this temperature. The actual data used to calculate T_{hot} and T_{cold} are only approximately 60 points at a collection rate of 1 point per second shown in Figure 3.25(b).

The data shown in Figure 3.25(c) and (d) are for the same sample as measured in single mode in Figure 3.25(a) and (b), but the data are recorded in continuous mode. When the continuous measurement mode is selected, the user must define the scan rate, usually between 0.1 and 1 K min^{-1}. The data are collected over an optimized period. Data were recorded for approximately 8 minutes and the temperature changed by approximately 8 K. The data were then fit with the model, Equation 2.1, and the thermal conductivity was calculated. Sample 1 in Table 3.8 was measured using both methods, the results of which are shown in Figure 3.26.

The long time needed to reach steady state is a disadvantage of the step-wise method compared with the continuous, but an advantage is that the method is more direct and there is no need for relaxation curve-fitting calculation. The continuous mode determined 188 thermal conductivity points in 7.3 hours and the single mode determined 33 data points in 18 hours. There was no difference in the results obtained by the two methods, within the uncertainty of the measurements, and therefore the faster continuous method was used for the other samples.

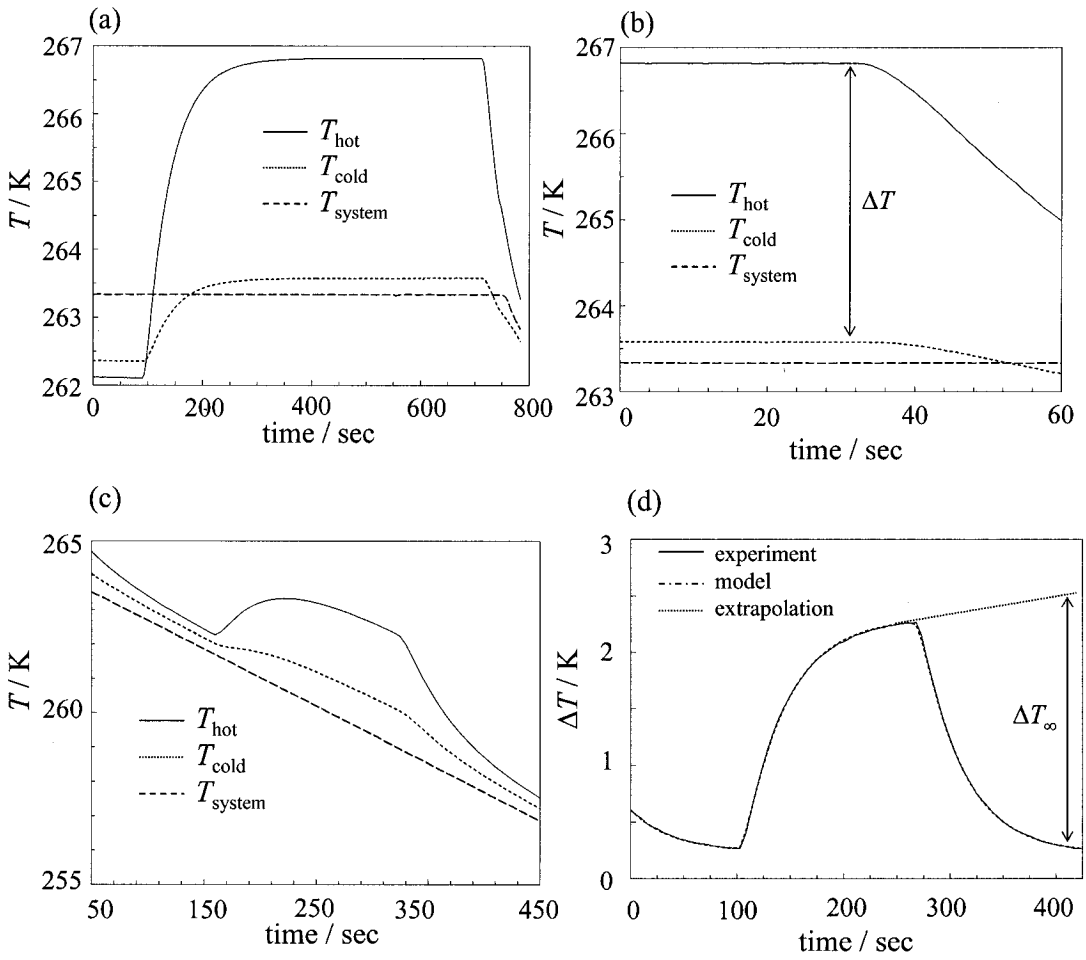

Figure 3.25. Measurement of thermal conductivity. Single mode (a) T vs. time, box indicates data used for calculation of ΔT, data shown in (b). Continuous mode scan rate of 1 K min^{-1} (c) T vs. time (d) ΔT vs. time.

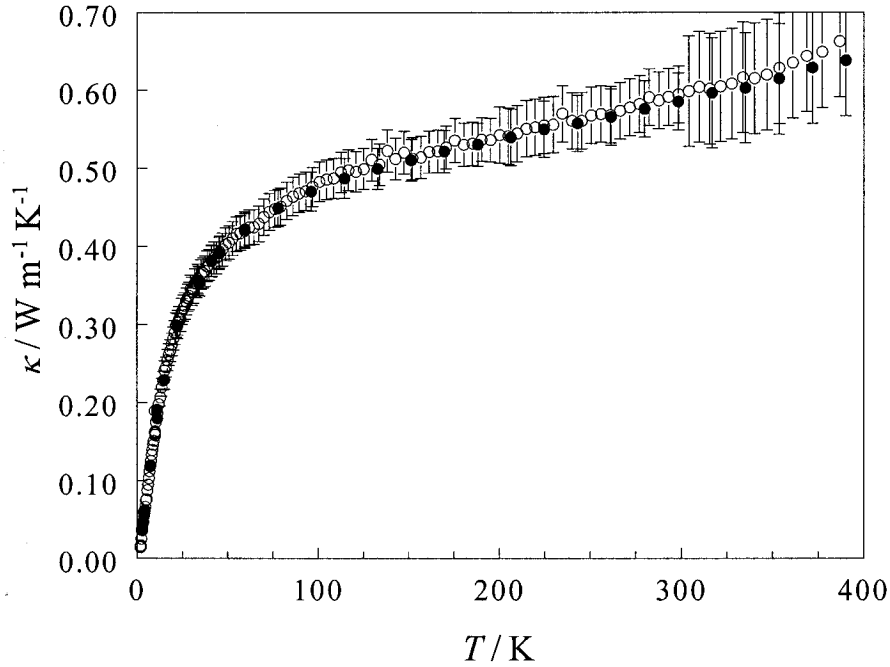

Figure 3.26. The thermal conductivity of ZrW_2O_8, sample 1, measured in ● single mode and ○ continuous mode. Error bars are not shown where the symbol is larger than calculated uncertainty.

3.5.4.2. Continuous Measurement Results

Figure 3.27 shows the temperature dependence of the thermal conductivity, κ, of ZrW_2O_8 for the five samples measured, while Table 3.9 gives the numerical values. Sample 1 was run twice (run 2 not shown in Figure 3.27 or Table 3.9). The results of the two runs are within 2% of each for entire temperature range tested, $33 < T / K < 390$. The uncertainties in κ were estimated from the accuracies in thermal conductance reported by QD, see Section 2.2.6, along with the uncertainties in measuring the diameter and the height of the pellet since $\kappa = (K \times l)/A$. In general, the results are in good agreement with each other (within 20 %) at temperatures above 30 K but there is some sample dependence at lower temperatures, possibly due to either sample differences or slight variations in the sample-epoxy adhesion.

Table 3.9. Smoothed thermal conductivity data of ZrW_2O_8 for five samples measured and average value.

T / K	κ(sample 1) / W m^{-1} K^{-1}	κ(sample 2) / W m^{-1} K^{-1}	κ(sample 3) / W m^{-1} K^{-1}	κ(sample 4) / W m^{-1} K^{-1}	κ(sample 5) / W m^{-1} K^{-1}	Average κ / W m^{-1} K^{-1}
2	0.016	0.0040	0.0051	0.0078	0.0069	0.0080
2.25	0.021	0.0055	0.0070	0.011	0.0095	0.011
2.5	0.027	0.0069	0.0088	0.014	0.012	0.014
2.75	0.032	0.0084	0.011	0.017	0.015	0.016
3	0.037	0.0099	0.012	0.020	0.017	0.019
3.5	0.046	0.013	0.016	0.025	0.022	0.025
4	0.056	0.016	0.020	0.031	0.028	0.030
4.5	0.065	0.020	0.024	0.037	0.033	0.036
5	0.074	0.024	0.028	0.044	0.039	0.042
5.5	0.083	0.028	0.032	0.050	0.045	0.048
6	0.093	0.032	0.037	0.056	0.051	0.054
6.5	0.10	0.036	0.042	0.062	0.057	0.060
7	0.11	0.041	0.046	0.068	0.064	0.066
7.5	0.12	0.046	0.052	0.074	0.070	0.072
8	0.13	0.051	0.057	0.080	0.076	0.079
8.5	0.14	0.056	0.062	0.086	0.083	0.085
9	0.15	0.062	0.068	0.092	0.089	0.092
9.5	0.16	0.067	0.073	0.098	0.095	0.098
10	0.17	0.072	0.079	0.10	0.10	0.10
11	0.18	0.083	0.090	0.12	0.11	0.12
12	0.20	0.094	0.10	0.13	0.13	0.13
13	0.21	0.10	0.11	0.14	0.14	0.14
14	0.22	0.11	0.12	0.15	0.15	0.15
16	0.25	0.13	0.14	0.17	0.17	0.17
18	0.26	0.15	0.16	0.19	0.19	0.19
20	0.28	0.17	0.18	0.20	0.20	0.21
22	0.30	0.18	0.19	0.22	0.22	0.22
24	0.31	0.20	0.21	0.23	0.23	0.24
26	0.32	0.21	0.22	0.24	0.24	0.25
28	0.33	0.22	0.23	0.25	0.25	0.26
30	0.34	0.23	0.24	0.26	0.26	0.27
35	0.36	0.26	0.26	0.28	0.28	0.29
40	0.38	0.28	0.28	0.30	0.29	0.31
45	0.39	0.29	0.30	0.31	0.30	0.32
50	0.40	0.31	0.31	0.32	0.31	0.33
55	0.41	0.32	0.32	0.33	0.32	0.34
60	0.42	0.33	0.33	0.34	0.32	0.35
65	0.43	0.34	0.34	0.35	0.33	0.36
70	0.44	0.35	0.35	0.35	0.34	0.37
75	0.45	0.36	0.36	0.36	0.34	0.37
80	0.45	0.37	0.37	0.36	0.35	0.38
85	0.46	0.38	0.38	0.37	0.35	0.39
90	0.47	0.39	0.39	0.38	0.36	0.39
95	0.47	0.39	0.40	0.38	0.36	0.40
100	0.48	0.40	0.40	0.39	0.36	0.41

...continued

T / K	κ(sample 1) / W m^{-1} K^{-1}	κ(sample 2) / W m^{-1} K^{-1}	κ(sample 3) / W m^{-1} K^{-1}	κ(sample 4) / W m^{-1} K^{-1}	κ(sample 5) / W m^{-1} K^{-1}	Average κ / W m^{-1} K^{-1}
120	0.50	0.42	0.42	0.40	0.38	0.42
140	0.51	0.43	0.43	0.42	0.39	0.44
160	0.52	0.45	0.44	0.42	0.41	0.45
180	0.53	0.46	0.46	0.43	0.42	0.46
200	0.54	0.47	0.47	0.44	0.43	0.47
220	0.55	0.48	0.47	0.45	0.43	0.48
240	0.56	0.49	0.48	0.46	0.44	0.49
260	0.57	0.50	0.49	0.47	0.45	0.50
280	0.58	0.51	0.50	0.47	0.46	0.50
300	0.59	0.51	0.51	0.48	0.47	0.51
320	0.61	0.52	0.52	0.49	0.48	0.52
340	0.62	0.53	0.53	0.50	0.49	0.53
360	0.63	0.55	0.54	0.51	0.50	0.55
380	0.65	0.58	0.56	0.52	0.52	0.57
385	0.66	0.58	0.57	0.53	0.53	0.57

* Uncertainty of κ values is discussed in text.

There is no apparent trend in κ with respect to the density of the pellet. However, the determined thermal conductivities are specific to the sample since the porosity of the pellets most certainly has an effect on the magnitude of the κ values. The porosity, ϕ, is defined as $\phi = [100\times[(\rho_{bulk}-\rho_{eff})/\rho_{bulk}]$, so it is [100-(% theoretical density)]. Studies have shown that significant porosity in the material can affect κ, and methods have been developed to estimate the correction for the porosity if the bulk κ is known.[167] The bulk κ is not known for ZrW_2O_8. Another method developed by Klemens[168] allows the calculation of the ratio of κ_{porous} to κ_{dense} from the porosity of the material,

$$\frac{\kappa_{porous}}{\kappa_{dense}} = 1 - \frac{4}{3}\phi . \qquad 3.6$$

This approximation has been used recently by Schlickting *et al.* to determine the effect of porosity in yttria-stabilized zirconia.[169]

For ZrW_2O_8, when the theoretical density is 74.4% (as in sample 1), κ_{dense} =

$1.52 \times \kappa_{porous}$, so the approximate κ assuming 100% theoretical density would be 1.52×0.60 W m^{-1} K^{-1} or 0.91 W m^{-1} K^{-1} at T = 300K. The average room-temperature value of the thermal conductivity of ZrW_2O_8 samples (κ_{porous}) is 0.51 ± 0.10 W m^{-1} K^{-1} (with an average theoretical density of 75.4%), while average κ_{dense} is 0.76 W m^{-1} K^{-1}.

Since repeat measurements on the same sample yielded results within 2% of each other, the differences in κ for the ZrW_2O_8 pellets are more likely due to poor thermal contact between pellet and copper lead than differences in the measurement technique. For such low thermally conductive materials, the epoxy layer attaching the pellet to lead is an important factor that could limit the measured κ, as discussed in Section 2.2.4. Therefore, the best room temperature value of κ_{dense} will be taken from the sample pellet that yielded the highest κ since this material probably provided the best epoxy layer thermal contact, therefore κ_{dense} = 0.91 W m^{-1} K^{-1}at T = 300 K.

The room-temperature thermal conductivity as determined by Hashimoto *et al.* from laser-flash thermal diffusivity was 0.80 W m^{-1} K^{-1} for a sample with 77.8 % density which is similar to those reported here,[118] however the value is uncorrected for porosity. The κ value at T = 300 K from Hashimoto *et al.* corrected to 100% theoretical density is 1.1 W m^{-1} K^{-1}.

A recent investigation of accuracy of laser flash determination of thermal diffusivity shows that special precautions are required to get high accuracy.[170] The differences likely arise from a number of factors, including radiative heat loss in laser flash methods (here a shield was used to reduce radiation), slight differences in sample density, and conversion of thermal diffusivity to thermal conductivity.

The most remarkable finding here is that the thermal conductivity of ZrW_2O_8 does

not exhibit the temperature dependence of a "normal" crystalline solid. In that case, the thermal conductivity would show a peak below room temperature, and a negative temperature coefficient at room temperature as shown in Figure 1.10(a). Indeed, the temperature dependence of the thermal conductivity of ZrW_2O_8 is more like that of a glass, despite being a crystalline material.

Glass-like thermal conductivity also has been observed for crystalline clathrates, in which guest species can rattle inside cages and reduce the mean free path of the heat-carrying acoustic phonons.[171] Indeed, this has been the basis for the suggestion[172] and realization[173] of materials with low thermal conductivity, as required for thermoelectric applications.

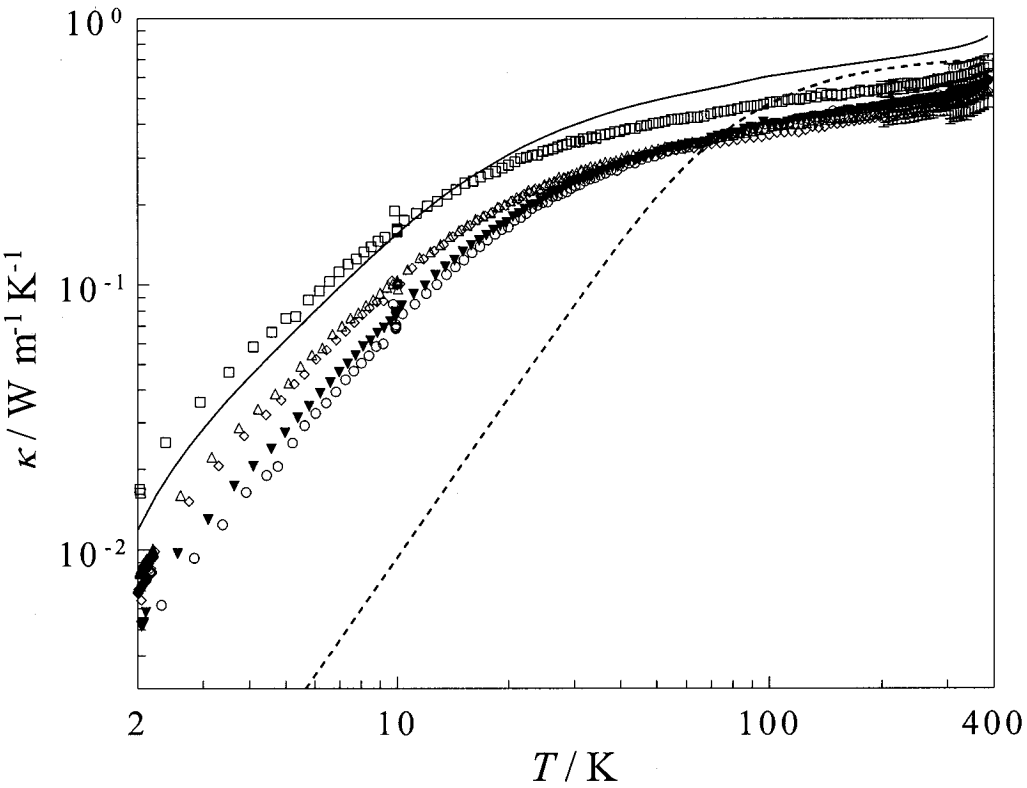

Figure 3.27. Temperature dependence of thermal conductivity of ZrW_2O_8 pellets measured directly using PPMS.□ 1, ○ 2, ▼ 3, Δ 4, ◊ 5, (—)κ_{dense} of average values of κ, and (----) κ_{min}. Error bars are not visible since symbol size is larger than calculated uncertainty.

At one theoretical extreme, a perfect lattice governed by purely harmonic interatomic interactions has infinite thermal conductivity. At the other extreme, one can imagine fully coupled phonons, leading to the concept of theoretical minimum thermal conductivity, κ_{min}. κ_{min} for ZrW_2O_8 was calculated from an equation based on fully coupled oscillators[27], using Equations 1.24 and 1.25, and is also shown in Figure 3.27.

For the calculation of κ_{min}, the average velocity of sound was determined from the bulk modulus, B, and shear modulus, G, which were calculated from experimental elastic constants of ZrW_2O_8.[110] The transverse and longitudinal velocities, v_t and v_l respectively are calculated from Equation 1.26. The mean velocity is v_m = 2900 m s^{-1} (averaged for T = 0 K and T = 300 K elastic data). Using v_m, the effective Debye temperature, θ_D^e, is calculated from Equation 1.25. This yields a θ_D^e = 333 K. The unit cell dimensions used for the calculation of θ_D^e and κ_{min} were those reported by Evans *et al.*[102]

The analysis of my heat capacity data leads to θ_D = 88 K, where θ_D represents only the acoustic modes (3 out of 132 degrees of freedom in the unit cell). This value of θ_D is in good agreement with a recent lattice dynamical analysis.[143] While there are several reports of θ_D values *ca.* 320 K,[108,110] these are not truly Debye characteristic temperatures for the acoustic modes. Instead, they are effective Debye characteristic temperatures (referred to above as θ_D^e) where all the lattice modes (3 acoustic and 129 optical) have been treated as Debye-like, and they are in good agreement with the value of the mean θ_D^e as calculated from v_m.

The observed thermal conductivity of ZrW_2O_8 is very low, and is close to the theoretical minimum value for T > 60 K (see Figure 3.27). This indicates highly

anharmonic lattice dynamics, in agreement with other investigations.[103,106,107,109]

Using the experimental thermal conductivity data, the phonon mean free path, λ, was calculated from Equation 1.17. The results are shown in Figure 3.28. The mean free path at $T > 40$ K is *ca.* 10 Å or less, on the same order as the mean free path for non-crystalline materials such as amorphous SiO_2[27] despite the fact that ZrW_2O_8 is crystalline; see Figure 1.10(b) for comparison.

The minimum particle size of the polycrystalline ZrW_2O_8 powder was determined to be > 40 μm as determined by mesh sifters. Even at low temperatures, the size of the particles would not affect the thermal conductivity since the maximum value of λ calculated from experimental data and Equation 1.17 (~3000 Å at 2 K) is less than the minimum grain size. Therefore, the particle size does not limit the thermal conductivity by grain boundary scattering. Grain boundary scattering can limit the κ values at low temperatures as was seen for Al_2O_3 and BeO.[174,175]

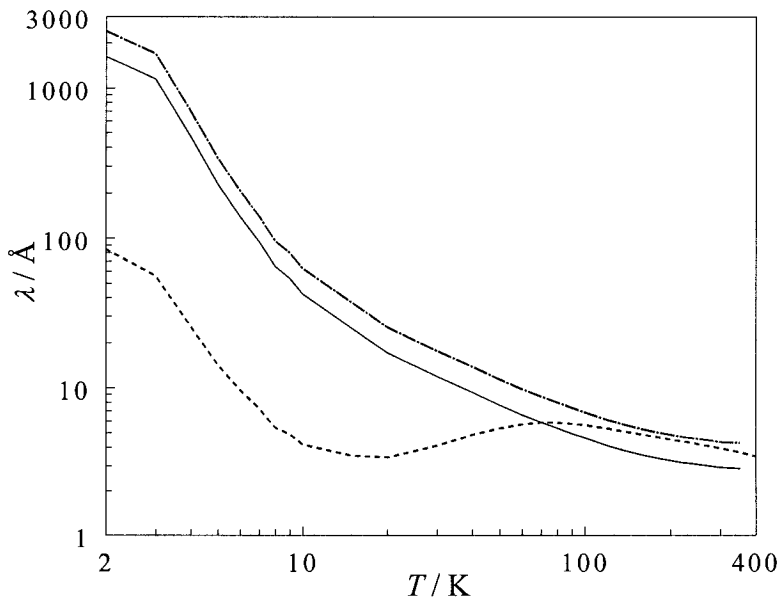

Figure 3.28. Phonon mean free path of ZrW_2O_8; (—) from the average porous experimental thermal conductivity, (— - —) from the average dense experimental thermal conductivity, (----) from the minimum thermal conductivity.

3.6. Grüneisen Parameter and Anharmonicity in ZrW_2O_8

The Grüneisen parameter, γ, can be used to quantify the degree of anharmonicity in a material. The average value of γ as a function of temperature can be calculated for a cubic solid from the volume coefficient of thermal expansion, α_V, the specific heat, C_V, the bulk modulus, B_T (= 72.5 GPa for ZrW_2O_8 [121]), and the volume of the unit cell, V_m, as in Equation 1.28.

Figure 3.29 shows the Grüneisen parameter for ZrW_2O_8 as a function of temperature and indicates large values (always negative due to its negative thermal expansion), especially at very low temperatures. My results agree with other experimental and calculated values for the average Grüneisen parameter.[103,107,144] Deviations of γ from zero indicate an anharmonic system. C_{60} was thought to be remarkably anharmonic with $\gamma \approx 3$ at low temperatures,[176] but clearly ZrW_2O_8 is even more so. Note that below T < 60 K, γ deviates significantly from zero.

The large deviation of γ from zero fits with the conclusions made in Section 3.4.4. The analysis of the contributions of various modes to the heat capacity of ZrW_2O_8 (Figure 3.22) indicates that for $T > 60$ K the modes below 10 meV which are most relevant for negative thermal expansion,[103] are essentially fully excited. From the calculation of γ, we know that these modes are highly anharmonic, as γ deviates significantly from zero as shown in Figure 3.29. Furthermore, the modes are essentially fully coupling with each other leading to short phonon mean free paths (Figure 3.28), high resistance to heat flow, and low thermal conductivity (Figure 3.27).

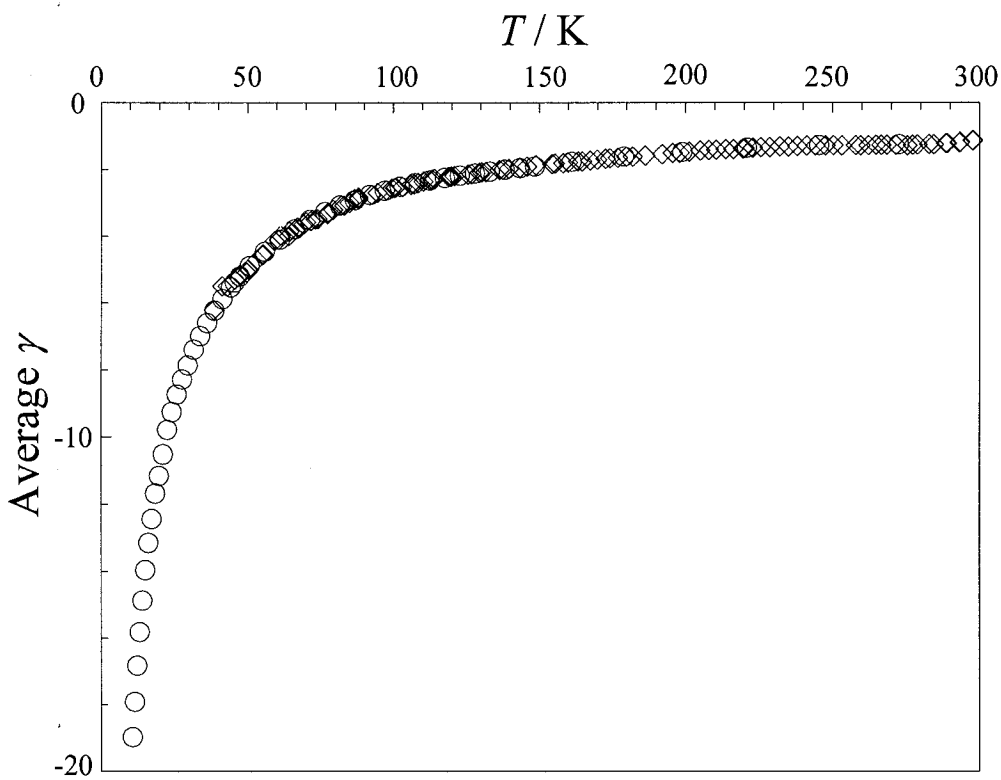

Figure 3.29. Grüneisen parameter for ZrW_2O_8, ○ PPMS results, ◊ adiabatic calorimetry results.

3.7. Conclusions

The same highly anharmonic, low-frequency modes which lead to negative thermal expansion in ZrW_2O_8 give rise to highly coupled phonons which reduce the phonon mean free path and, hence, the thermal conductivity. This remarkable finding could provide a basis for design of new materials with low thermal conductivity.

Chapter 4. Thermal Properties of Hafnium Molybdate, $HfMo_2O_8$

4.1. Structure and NTE Properties of $HfMo_2O_8$

Many structural analogues of zirconium tungstate have been studied and their thermal expansion properties explored to determine whether they also exhibit NTE. Lind outlines the synthesis and characterization of the solid solution system $Zr_{1-x}Hf_xMo_{2-y}W_yO_8$ ($0 \leq x \leq 1$, $0 \leq y \leq 2$) in her doctoral dissertation.[154] There are several different polymorphs of each of these compounds, but for the present work, the focus is on the cubic polymorph of hafnium molybdate which is isostructural to β-ZrW_2O_8.

According to Lind, above $y \geq 1.2$, the structure of $Zr_{1-x}Hf_xMo_{2-y}W_yO_8$ has the α-ZrW_2O_8 phase at room temperature, while compositions with $y \leq 1$ crystallize in the disordered β-ZrW_2O_8 phase.[154] Therefore, $HfMo_2O_8$ (also known as hafnium molybdenum oxide) is isostructural to β-ZrW_2O_8 but will be referred to here as cubic-$HfMo_2O_8$ or simply $HfMo_2O_8$. This name is given to reduce confusion with the recently synthesized monoclinic polymorph β-$HfMo_2O_8$ reported in the literature.[177] $HfMo_2O_8$ does not exhibit the cubic-to-cubic phase transition observed in ZrW_2O_8, as the former is already in the high-temperature disordered phase;[154] however, like α and β-ZrW_2O_8, it is a metastable compound.[177] Synthesis is achievable through a nonconventional low-temperature preparation.[154, 178]

Cubic-$HfMo_2O_8$ has a structure with space group of $Pa\bar{3}$, with $Z = 4$, and has a lattice constant $a = 9.1015$ Å at $T = 30$ °C.[154] Cubic-$HfMo_2O_8$ exhibits negative thermal expansion with a $\alpha_l = -4.0 \times 10^{-6}$ K^{-1} obtained for $T = 77$ K to 573 K by means of

powder x-ray diffraction.[154] The magnitude of this CTE fits into the low expansion category for ceramics, $2 \times 10^{-6}\ K^{-1} \leq |\alpha_l| \leq 8 \times 10^{-6}\ K^{-1}$, as described in Section 3.2.2.1.[22]

The published research to date on hafnium molybdate consists mainly of synthetic and structural studies of the various polymorphs. The cubic form of $HfMo_2O_8$ being used in the present study is metastable. There is a stable form of $HfMo_2O_8$; it crystallizes in a trigonal lattice at ambient temperature and pressures.[179] Under high-pressure and high-temperature conditions, a monoclinic polymorph is obtained.[180,181] There has also been interest in the thermodynamic properties[182,183,184] and vaporization behavior[185] of $HfMo_2O_8$ since hafnium and zirconium molybdate are major fission products in nuclear reactors.

4.2. Heat Capacity of $HfMo_2O_8$

4.2.1. Introduction

Given the importance of accurate heat capacity data in understanding thermal conductivity and negative thermal expansion, the heat capacity of $HfMo_2O_8$, which has not yet been reported in the literature, was determined here. The heat capacities of $HfMo_2O_8$ are compared to the heat capacities of ZrW_2O_8 which were reported in Section 3.3.

4.2.2. Experimental Methods

The sample of cubic-$HfMo_2O_8$ was obtained from the laboratory of Dr. Angus P. Wilkinson at the Georgia Institute of Technology. It was synthesized according to the methods discussed by Lind *et al.*[154,178] The analysis done by Dr. Wilkinson and his

colleagues indicated that the $HfMo_2O_8$ was 95% by weight cubic phase. The other 5% by weight consists of less than 0.5% water, less than 0.1% trigonal $HfMo_2O_8$ and an amorphous content of about 4% according to x-ray diffraction. Thermogravimetric analysis gave a Hf : Mo ratio of 1 : 2.03. The sample was kept under vacuum except when making pellets and loading into the PPMS pucks for C_P and κ measurements.

The heat capacity of $HfMo_2O_8$ was measured for T = 0.4 K to 300 K using a commercial relaxation calorimeter (PPMS). The procedures for running the relaxation calorimeter were described in detail in Section 2.3.2. The $HfMo_2O_8$ powder had to be pressed into a pellet so that it could be placed directly on the greased platform of the PPMS. Upon doing so, the samples experienced pressures of approximately 0.5 GPa. The pressing procedure was outlined in Section 2.2.5. High-pressure x-ray diffraction studies have shown that cubic-$HfMo_2O_8$ undergoes a fully reversible first-order phase transition between 0.7 and 2.0 GPa.[180] Also, Lind *et al.* establish that under nonhydrostatic conditions, cubic-$HfMo_2O_8$ starts to amorphize above 0.3 GPa.[180] Lind *et al.* recognized the new (high-pressure) phase by a reduction in unit-cell volume and from broadening of the peaks in the x-ray diffraction pattern. They were unable to determine the structure of the high-pressure phase. The x-ray diffraction results from the present study, shown in Figure 4.1 and Figure 4.2, indicate that the samples studied here did not change on pressing. There is no evidence of peak broadening, and no new peaks appear in the diffraction pattern.

DSC experiments, shown in Figure 4.3, performed with a Perkin-Elmer Pyris 1 DSC calibrated with 99.999+% indium at a scan rate of 10 K min^{-1}, show no visible transitions from room temperature to T = 460 K (limit of detection 0.1 J g^{-1}).

The pellets had to be broken into smaller pieces to obtain suitable sizes for calorimetry. Masses of the sample used for the PPMS heat capacity determination were 10.781 ± 0.005 mg, 14.002 ± 0.010 mg, with the ^{4}He system and 10.230 ± 0.010 mg and 25.804 ± 0.005 mg with the ^{3}He system.

The Raman spectra for $HfMo_2O_8$ were obtained at room temperature on a Bruker RFS 100 spectrometer using the 1064.5 nm line of Nd:YAG laser with an incident power of 147 mW. The scattered light was collected using a Ge diode detector. The samples were prepared by packing a small amount of the powder into a small hole located in the middle of a circular metal discs. The spectra were taken using 6000 scans at a resolution of 2 cm^{-1}.

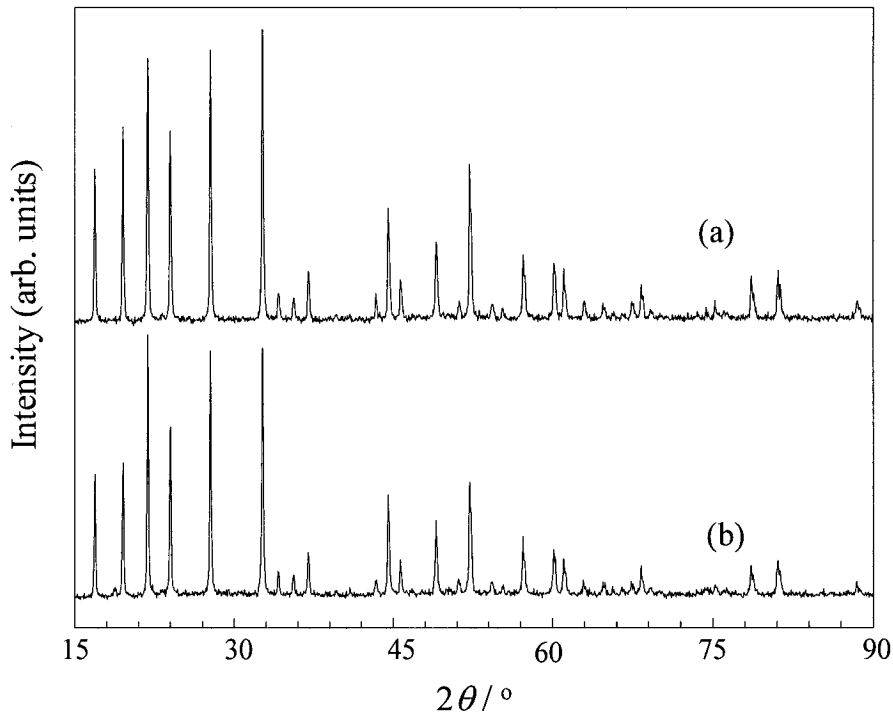

Figure 4.1. X-ray powder diffraction of $HfMo_2O_8$. (a) As-received from Georgia Institute of Technology. (b) As-pressed sample, to a pressure of ~0.5 GPa.

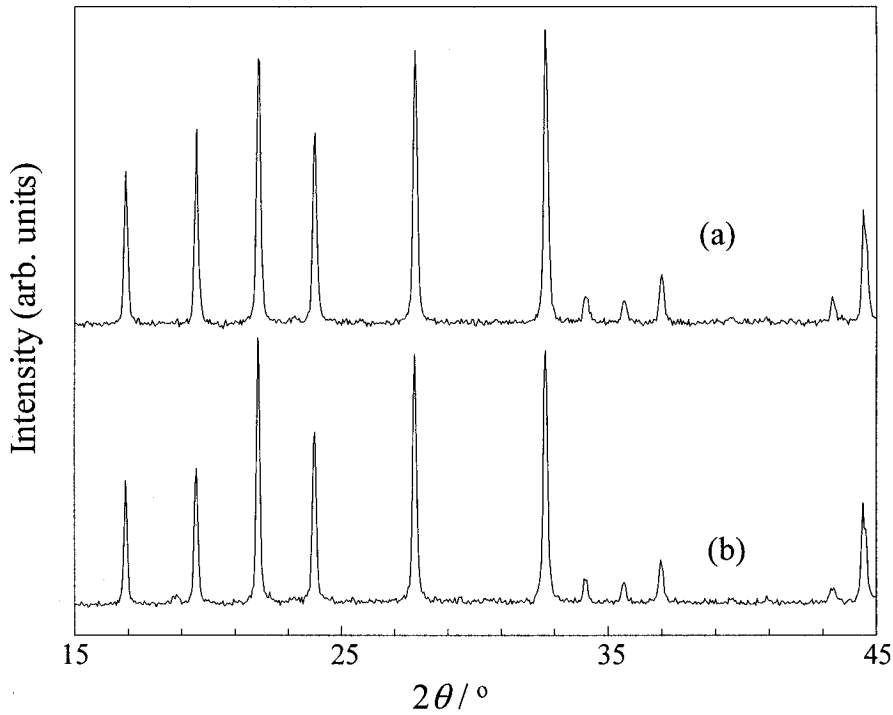

Figure 4.2. X-ray powder diffraction of $HfMo_2O_8$ from 2θ=15 to 45°. (a) As-received sample from Georgia Institute of Technology. (b) As-pressed sample, to a pressure of ~0.5 GPa.

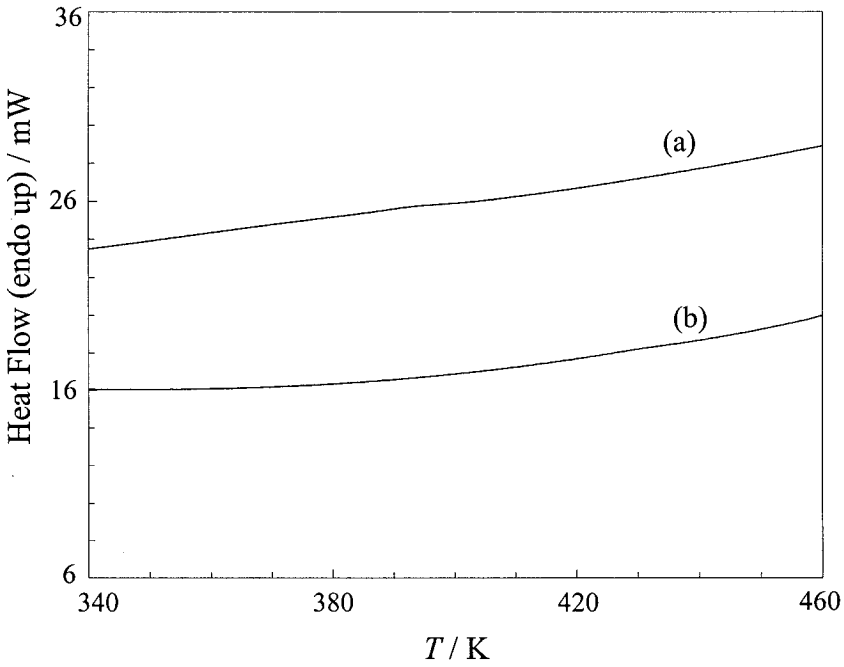

Figure 4.3. DSC scans of $HfMo_2O_8$. (a) As-received sample from Georgia Institute of Technology. (b) As-pressed pellets, to a pressure of ~0.5 GPa.

4.2.3. Heat Capacity Data

The experimental heat capacities of $HfMo_2O_8$ measured using the PPMS are given in Table 4.1 and are shown in Figure 4.4, along with the estimated uncertainties (determined as described in Section 2.3.4.3), and the relative contribution of the sample to the total heat capacity. There were no phase transitions present for 0.4 K < T < 305 K temperature region. Four samples were measured to characterize the sample over the entire temperature range. However, some of the results are considered too uncertain due to low sample contribution to the total C_P (< 50%), poor sample contact, or large fit deviation. In these cases, the data were not used in further analysis. This will be described further in the section discussing optimal heat capacities of $HfMo_2O_8$, Section 4.2.3.1.

Table 4.1. Experimental heat capacities and estimated uncertainties of $HfMo_2O_8$ as measured by the PPMS.

T / K	C_P / J K^{-1} mol^{-1}	T / K	C_P / J K^{-1} mol^{-1}	T / K	C_P / J K^{-1} mol^{-1}
			PPMS ^{4}He, 10.781 ± 0.010 mg		
2.061	0.0071±0.0005	12.06	4.23±0.02	63.68	66.4±0.4
2.283	0.0100±0.0001	13.38	5.45±0.02	70.66	74.6±0.3
2.535	0.0151±0.0005	14.85	6.91±0.03	78.40	83.1±0.4
2.811	0.0226±0.0016	16.48	8.64±0.07	86.99	92.2±0.3
3.121	0.0306±0.0035	18.29	10.7±0.0	96.52	101.7±0.7
3.462	0.0488±0.0166	20.29	13.0±0.1	107.10	111.9±0.6
3.846	0.0754±0.0022	22.51	15.8±0.2	118.84	121.7±0.6
4.264	0.120±0.002	24.98	18.9±0.1	131.85	131.6±0.4
4.731	0.174±0.007	27.71	22.3±0.1	146.30	141.4±0.5
5.248	0.275±0.014	30.75	26.2±0.2	162.35	150.9±0.2
5.822	0.416±0.010	34.12	30.4±0.1	180.14	160.1±0.2
6.474	0.638±0.004	37.86	35.3±0.1	199.86	168.7±0.4
7.173	0.900±0.009	42.01	40.4±0.2	221.72	177.4±0.5
7.956	1.28±0.00	46.62	46.2±0.2	245.97	185.5±0.5
8.828	1.77±0.01	51.72	52.4±0.2	272.82	194.2±1.3
9.794	2.42±0.01	57.39	59.3±0.1	302.67	198.7±1.3
10.87	3.23±0.01				
			PPMS ^{4}He, 14.002 ± 0.010 mg		
2.035	0.0075±0.0003	11.48	3.72±0.05	64.22	67.1±0.5
2.221	0.0097±0.0002	12.52	4.64±0.02	70.01	73.7±0.5
2.425	0.0124±0.0009	13.64	5.68±0.07	76.29	80.3±0.3
2.648	0.0163±0.0013	14.85	6.93±0.05	83.17	87.7±0.6

...continued

T / K	C_P / J K^{-1} mol^{-1}	T / K	C_P / J K^{-1} mol^{-1}	T / K	C_P / J K^{-1} mol^{-1}
2.888	0.0210±0.0010	16.18	8.33±0.10	90.65	95.3±0.9
3.154	0.0315±0.0030	17.64	9.93±0.04	98.83	103.5±0.1
3.443	0.0466±0.0011	19.22	11.7±0.1	107.73	111.7±0.3
3.758	0.0641±0.0055	20.96	13.8±0.2	117.44	119.8±0.4
4.099	0.0958±0.0028	22.84	16.1±0.4	128.01	127.9±0.3
4.466	0.140±0.006	24.88	18.6±0.2	139.53	136.0±0.3
4.865	0.205±0.010	27.12	21.6±0.2	152.09	143.8±0.6
5.309	0.279±0.014	29.57	24.7±0.1	165.81	151.3±0.2
5.785	0.411±0.004	32.22	28.1±0.1	180.76	158.9±0.2
6.300	0.579±0.016	35.12	31.7±0.2	197.01	165.7±0.2
6.886	0.759±0.250	38.29	35.8±0.1	214.73	173.0±0.2
7.453	1.02±0.01	41.74	40.0±0.1	234.00	178.4±0.5
8.128	1.37±0.00	45.50	44.7±0.1	255.04	185.3±0.4
8.858	1.80±0.01	49.59	49.7±0.1	277.93	191.4±0.8
9.658	2.32±0.01	54.06	55.0±0.1	303.02	200.0±1.0
10.53	2.96±0.01	58.92	60.7±0.1		
		PPMS ^{3}He, 10.230± 0.010 mg			
0.3921	(6.29±0.11)×10^{-5}*	1.469	(4.61±0.05)×10^{-3}*	3.980	0.0903±0.0009
0.4199	(2.79±0.01)×10^{-4}*	1.568	(5.28±0.05)×10^{-3}*	4.254	0.119±0.001
0.4742	(5.47±0.22)×10^{-4}*	1.676	(6.06±0.05)×10^{-3}*	4.546	0.155±0.002
0.5083	(4.37±0.07)×10^{-4}*	1.791	(7.01±0.12)×10^{-3}*	4.858	0.204±0.001
0.5470	(1.86±0.02)×10^{-4}*	1.913	(8.07±0.10)×10^{-3}*	5.194	0.268±0.001
0.6641	(7.67±0.11)×10^{-4}*	2.045	(9.55±0.08)×10^{-3}*	5.549	0.349±0.002
0.7082	(9.65±0.13)×10^{-4}*	2.179	0.0111±0.0001*	5.929	0.451±0.002
0.7551	(1.11±0.01)×10^{-3}*	2.335	0.0133±0.0001*	6.340	0.575±0.009
0.8089	(1.25±0.11)×10^{-3}*	2.497	0.0159±0.0001*	6.775	0.738±0.004
0.9218	(1.63±0.02)×10^{-3}*	2.667	0.0194±0.0002*	7.240	0.935±0.004
0.9860	(2.22±0.03)×10^{-3}*	2.853	0.0243±0.0002*	7.743	1.18±0.01
1.054	(2.31±0.13)×10^{-3}*	3.050	0.0307±0.0002*	8.280	1.47±0.01
1.126	(2.62±0.06)×10^{-3}*	3.261	0.0133±0.0004*	8.850	1.81±0.02
1.203	(3.03±0.04)×10^{-3}*	3.488	0.0522±0.0005*	9.440	2.18±0.01
1.285	(3.48±0.04)×10^{-3}*	3.732	0.0691±0.0011	10.02	2.54±0.02
1.374	(3.94±0.05)×10^{-3}*				
		PPMS ^{3}He, 25.804 ± 0.005 mg			
0.5330	(2.07±0.14)×10^{-4}	1.398	(2.50±0.11)×10^{-3}	105.52	109.0±1.4
0.5667	(2.52±0.14)×10^{-4}	1.498	(3.20±0.08)×10^{-3}	116.10	117.8±1.4
0.6025	(3.82±0.89)×10^{-4}	1.609	(3.68±0.36)×10^{-3}	127.73	126.1±1.0
0.6962	(4.08±0.06)×10^{-4}	1.726	(4.57±0.18)×10^{-3}	140.53	134.7±1.5
0.7441	(8.52±0.09)×10^{-4}	1.852	(5.44±0.48)×10^{-3}	154.60	142.4±0.6*
0.7992	(9.95±0.16)×10^{-4}	1.984	(6.78±0.18)×10^{-3}	170.07	149.5±0.8*
0.8550	(1.03±0.02)×10^{-3}	2.130	(8.39±0.44)×10^{-3}	187.20	155.3±0.5*
0.9185	(1.11±0.18)×10^{-3}	2.287	0.0103±0.0001	205.93	160.4±1.2*
0.9860	(1.32±0.20)×10^{-3}	2.454	0.0129±0.0005	226.56	164.2±3.0*
1.056	(1.50±0.06)×10^{-3}	2.636	0.0162±0.0004	249.28	167.5±3.3*
1.131	(1.94±0.08)×10^{-3}	2.830	0.0208±0.0002	274.34	168.4±4.0*
1.215	(2.01±0.19)×10^{-3}	3.035	0.0273±0.0002	301.89	167.7±0.3*
1.302	(2.29±0.18)×10^{-3}	95.91	100.5±1.0		

*Data too uncertain and not used in further analysis (see Section 4.2.3.1 for details).

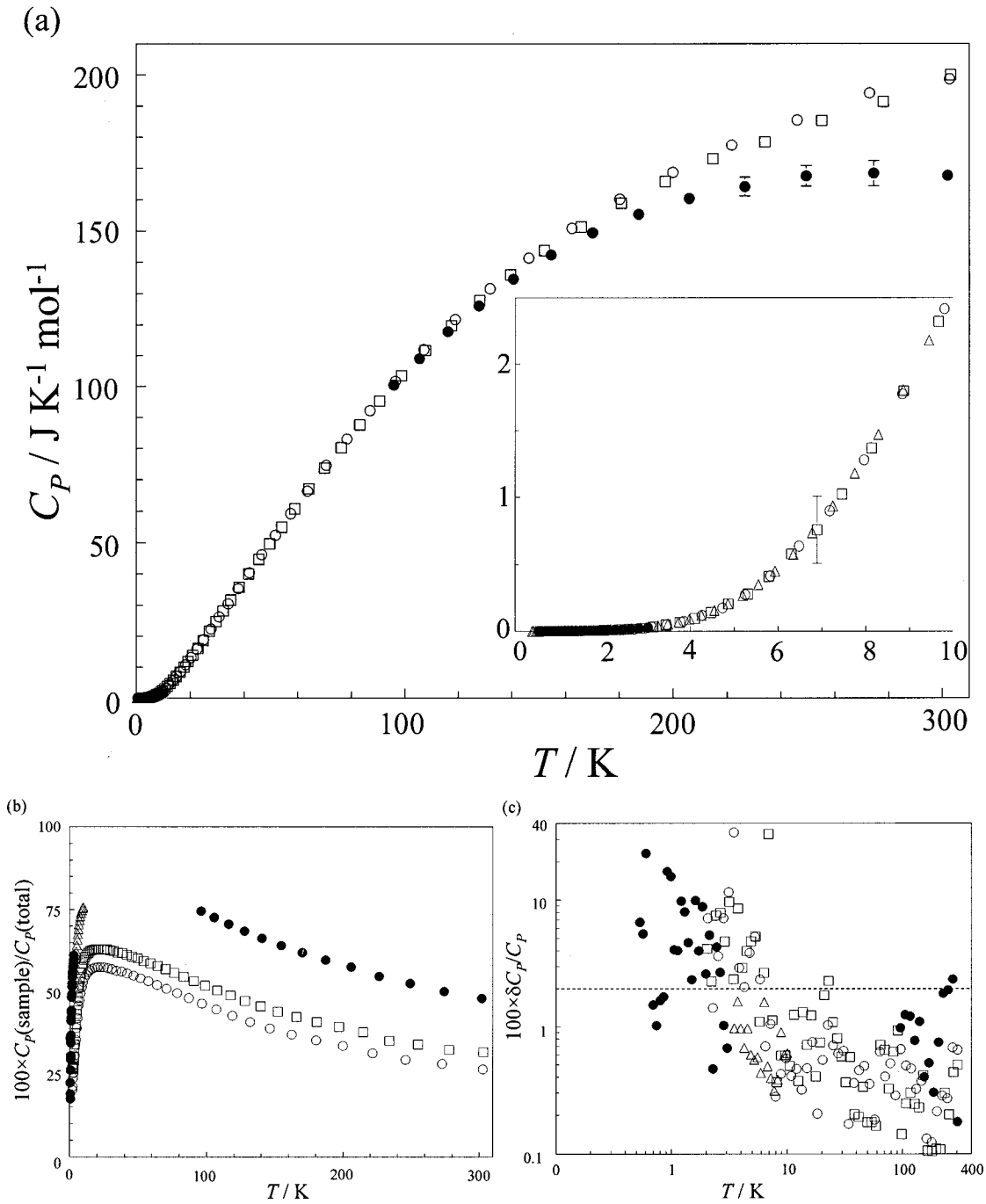

Figure 4.4. Hafnium molybdate heat capacities (a) Heat capacities; (b) relative sample contributions to the total heat capacities; (c) estimated uncertainty. PPMS relaxation calorimeter, ^{4}He system, ○10.781 ± 0.010 mg, □14.002 ± 0.010 mg. ^{3}He system, Δ10.230 ± 0.010 mg, ●25.804± 0.005 mg. Error bars are not visible where the symbol size is larger than the calculated uncertainty. Dotted line in (c) represents 2%.

4.2.3.1. Optimal Heat Capacity Data

For $HfMo_2O_8$, it is apparent from Figure 4.4(a) that there are deviations among the heat capacity determinations of samples of varying masses. However, only the largest sample size used, ~25 mg, deviates greatly from the other data. These data converge with the other data for $T < 150$ K. As was the case for ZrW_2O_8, the sample coupling was not unusual in this region, and the temperature fit by the parameters gave no indication as to why this deviation occurred, however, this deviation is most likely due to the low thermal conductivity of this material, see Section 4.3. The data for the ~25 mg sample for $T > 150$ K are considered erroneous and are not included in the subsequent analysis and figures.

Figure 4.4(b) gives the relative sample contribution to the total C_P. At low temperatures, the calculated uncertainties for samples as measured by the ^{4}He system and ^{3}He system become large where $100 \times C_P(\text{sample})/C_P(\text{total})$ is small. Data for which $100 \times C_P(\text{sample})/C_P(\text{total}) < 50$ are not included in the subsequent analysis and figures.

Data with large fit deviations and with poor sample coupling (as assessed by the QD software) are also excluded. The fit deviation is determined by a mean squared deviation of the fit from model and is expressed as a normalized χ^2.[50] A value that is distinctly larger for a specific measurement than its neighboring measurements could indicate a bad measurement. Figure 4.5 gives the optimal C_P data used for subsequent analysis.

Figure 4.6 shows C_P vs. T^3 for $HfMo_2O_8$ in the low-temperature range. The Debye temperature was calculated with the Debye-T^3 law (Equation 1.10) using data in the range $T = 0.4$ K to 2.6 K. At these low temperatures, $(C_P - C_V) \sim 0$ so C_P was used in

this determination. The calculation of (C_P - C_V), non-negligible at higher temperatures, is described later in Section 4.2.3.4. The solid line (slope = 8.7967 × 10^{-4} J K^{-4} mol^{-1}) in Figure 4.6 was obtained by fitting the data below T = 2.6 K using a linear least squares method. Above T = 3 K, the C_P data deviate from the T^3 law. A value of θ_D = 82 K was obtained considering 3 degrees of freedom for 4 formula units, assuming that the optic modes contribute negligibly for T < 2.6 K, as shown later (Section 4.2.4). This value of θ_D is similar but slightly less than the value obtained for ZrW_2O_8 using the same methods, θ_D = 88 K.

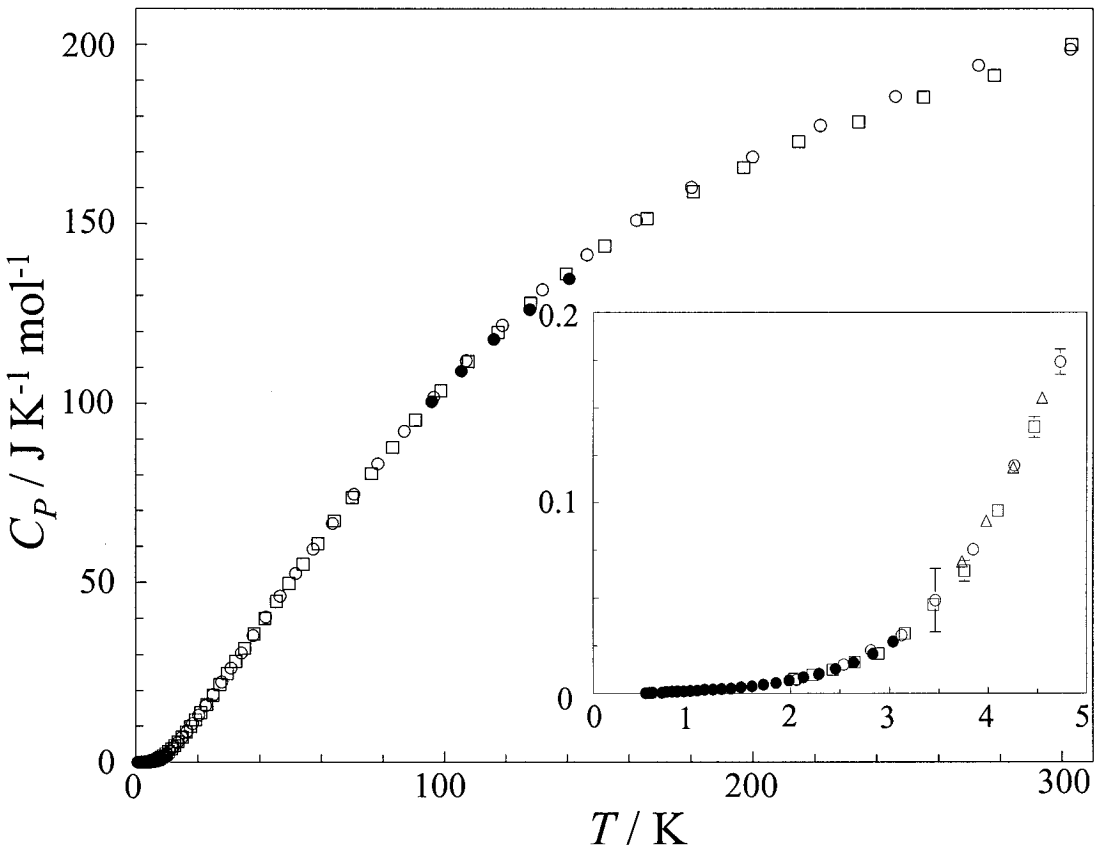

Figure 4.5. Optimal heat capacities of $HfMo_2O_8$ using the PPMS relaxation calorimeter, ^{4}He system, ○10.781 ± 0.010 mg, □14.002 ± 0.010 mg. ^{3}He system, Δ10.230 ± 0.010 mg, ●25.804± 0.005 mg. Error bars are not visible where the symbol size is larger than the calculated uncertainty.

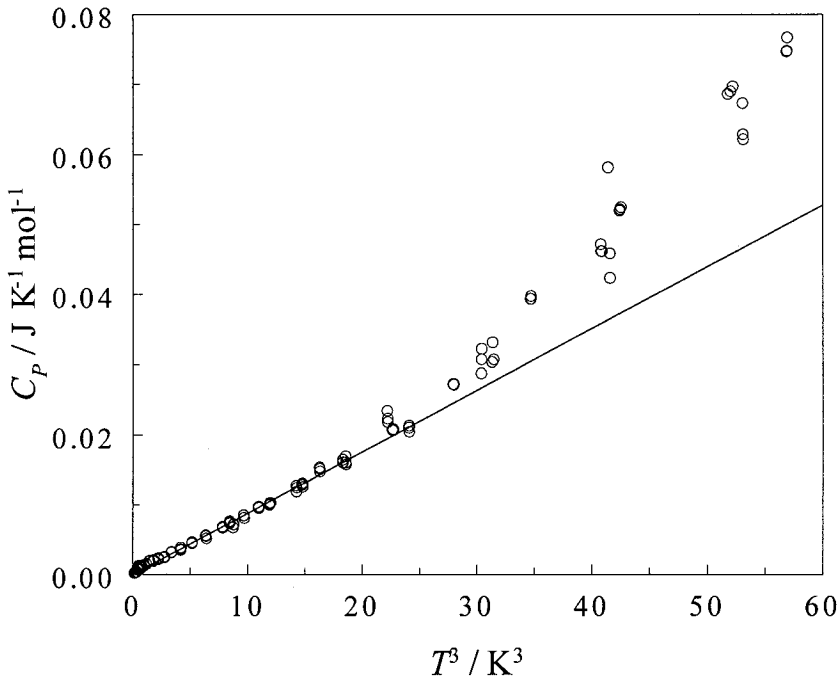

Figure 4.6. C_P vs. T^3 of $HfMo_2O_8$ for $T < 4$ K. The solid line shows Debye-T^3 law fit of data below $T = 2.6$ K, slope is 8.7967×10^{-4} J K^{-4} mol^{-1}. Determination of θ_D is described in the text.

As discussed in Chapter 1, the Debye theory of lattice heat capacity takes into account only the acoustic modes of lattice vibrations and solids are represented as an elastic continuum. As such, the Debye temperature will depend only on the sound velocity (relationship shown in Equation 1.25). The sound velocity is determined by bulk elastic constants and density, $v_m = (E_Y/\rho)^{1/2}$ where E_Y is Young's modulus.

Yamamura *et al.*[108] showed that for HfW_2O_8 and ZrW_2O_8, the densities are proportional to the formula mass (FM) since the lattice parameters of the compounds are nearly the same values at room temperature. The relative (averaged) bond strength for HfW_2O_8 compared to that of ZrW_2O_8 can be deduced from the experimental θ_D from C_P, as $[\theta_D(ZrW_2O_8)/\theta_D(HfW_2O_8)]^2 \sim FM(HfW_2O_8)/FM(ZrW_2O_8) \sim 1.15$. This illustrates that bonds in HfW_2O_8 are 1.15 times stronger on average than in ZrW_2O_8, in terms of the

force constant. Yamamura *et al.* concluded that this increased bond strength is responsible for the hardening of the high-frequency intrapolyhedra vibrations observed in their Raman spectra since interpolyhedra coupling via the bond linking them would contribute positively to frequencies.[108]

The lattice parameters of $HfMo_2O_8$ and ZrW_2O_8 are also nearly the same value at room temperature, 9.10 Å[154] vs. 9.16 Å[102] for $HfMo_2O_8$ and ZrW_2O_8, respectively. The relative (averaged) bond strength for $HfMo_2O_8$ compared to that of ZrW_2O_8 from the experimental θ_D from C_P, as $[\theta_D(ZrW_2O_8)/\theta_D(HfMo_2O_8)]^2 \sim (88/82)^2 \sim 1.15$, as seen for $(ZrW_2O_8)/(HfW_2O_8)$ but in this case it is not equal to the reciprocal of the ratio of the formula mass, 498/587 ~ 0.85, indicating that the effect is due to more than the mass.

4.2.3.2. Comparison of $C_P(HfMo_2O_8)$ and $C_P(\alpha\text{-}ZrW_2O_8)$

The heat capacity of $HfMo_2O_8$ is very similar to that of α-ZrW_2O_8. The two materials crystallize in different space groups. ZrW_2O_8 undergoes an order-disorder transition above room temperature and $HfMo_2O_8$ crystallizes in a phase with the same structure as the same high-temperature disordered phase of ZrW_2O_8. The disorder arises from the random orientation of the two $[WO_4]^{2-}$ tetrahedra. In the ordered phase, the two $[WO_4]^{2-}$ lie along the [111] body diagonal with their unshared W-O both pointing along the [111] direction. In the disordered phase, as in cubic-$HfMo_2O_8$, the $[MoO_4]^{2-}$ tetrahedra will point their unshared vertices randomly either in the [111] or $[\bar{1}\bar{1}\bar{1}]$ direction at a 1:1 ratio.[112] High oxygen mobility has been documented in the disordered β phase of ZrW_2O_8.[102]

Previous comparisons of ZrW_2O_8 with analogues such as $ZrMo_2O_8$[116]

(isostructural with disordered β-ZrW_2O_8) and HfW_2O_8[108] (isostructural with ordered α-ZrW_2O_8) have shown that the heat capacities are similar, however more so for HfW_2O_8 and α-ZrW_2O_8 than for $ZrMo_2O_8$ and β-ZrW_2O_8. It is therefore reasonable that $HfMo_2O_8$ should have C_P values similar to ZrW_2O_8.

Proposed mechanisms for NTE in ZrW_2O_8 were described in Section 3.2.3. Cao *et al.*[130,131] stressed the importance of heavy atom vibrations in NTE and it has been shown that vibrations of the $[WO_4]^{2-}$ and $[ZrO_6]^{8-}$ units are important for understanding NTE. Cao *et al.* have shown that $[WO_4]^{2-}$ polyhedra are rigid, however, the $[ZrO_6]^{8-}$ are stiff but not rigid as temperature increases. The low-energy vibrations of the undistorted polyhedra strongly depend on the type of cation at the center of the polyhedra, because the center cation determines the mass and the size of the polyhedra.[108] This suggests that the AB_2O_8 type materials with differing cations, *A* and *B*, could have different lattice vibrations than ZrW_2O_8.[108]

A study by Yamamura *et al.* compared the lattice dynamics of cubic α-HfW_2O_8 to α-ZrW_2O_8.[108] α-HfW_2O_8 has the same structure as α-ZrW_2O_8. They compare the two compounds, which differ only by exchanging the zirconium ions for hafnium ions, in terms of their C_P and CTE values. Zirconium and hafnium have similar chemical properties despite the large difference in their atomic number.[108] The ionic radii of the two atoms in the sixfold coordination sites are quite similar (86 pm for Zr^{4+} and 85 pm for Hf^{4+}).[186] However the atomic mass of hafnium (178.5 g mol^{-1}) is approximately twice that of zirconium (91.2 g mol^{-1}). The large difference in atomic mass could be expected to lead to different lattice vibrations for ZrW_2O_8 and HfW_2O_8 and therefore affect the NTE since negative thermal expansions of these compounds originate from

lattice vibrations.[108] However, their CTEs are very similar, $\alpha_l(HfW_2O_8)$ is -8.8×10^{-6} K^{-1} determined from x-ray diffraction for $T = 90$ K to 300 K and $\alpha_l(\alpha\text{-}ZrW_2O_8)$ is -9.6×10^{-6} K^{-1} determined from the same study over the same temperature range.[113] Their results also show that the heat capacity curves are similar, although there are atomic mass effects at low temperatures. The values of $\Delta C_P = C_P(HfW_2O_8) - C_P(ZrW_2O_8)$ are maximal at approximately 3 J K^{-1} mol^{-1} at $T = 80$ K and ΔC_P went from positive to negative above $T \sim 200$ K.[108]

A study from Stevens *et al.*[116] compared the heat capacities of $\alpha\text{-}ZrW_2O_8$ and cubic-$ZrMo_2O_8$. Cubic-$ZrMo_2O_8$ has the same structure as $\beta\text{-}ZrW_2O_8$. The ionic radii of the two atoms in the fourfold coordination sites are similar to each other, 56 pm for W^{6+} and 55 pm for Mo^{6+}, and the atomic mass of tungsten (183.8 g mol^{-1}) is approximately twice that of molybdenum (95.9 g mol^{-1}).[186] However, their results show $C_P(\alpha\text{-}ZrW_2O_8) > C_P(ZrMo_2O_8)$ over the entire temperature range. From Stevens *et al.*, at $T = 298.15$ K, $C_P(\alpha\text{-}ZrW_2O_8) = 207.01$ J K^{-1} mol^{-1} and $C_P(ZrMo_2O_8) = 210.06$ J K^{-1} mol^{-1}. On the basis of thermal expansion, $ZrMo_2O_8$ is similar to $\beta\text{-}ZrW_2O_8$: $\alpha_l(ZrMo_2O_8) = -5.0 \times 10^{-6}$ K^{-1} for $T < 600$ K[178] and $\alpha_l(\beta\text{-}ZrW_2O_8) = -6.2 \times 10^{-6}$ K^{-1} for $T = 500$ K to 560 K.[113]

The mass should also be expected to affect the CTE and C_P for ZrW_2O_8 compared with $HfMo_2O_8$. $HfMo_2O_8$ has a smaller absolute thermal expansion coefficient than $\beta\text{-}ZrW_2O_8$, $\alpha_l(HfMo_2O_8)$ is -4.0×10^{-6} K^{-1} for $T = 77$ K to 573 K[154] versus $\alpha_l(\beta\text{-}ZrW_2O_8) = -6.2 \times 10^{-6}$ K^{-1} for $T = 500$ K to 560 K.[113]

The present heat capacities of $HfMo_2O_8$ and ZrW_2O_8 are shown in Figure 4.7 and Figure 4.8. The heat capacities do not differ significantly for 100 K < T < 200 K, however for $T < 200$ K there is a difference in C_P. The best $HfMo_2O_8$ heat capacities

were spline fit and were compared to the present ZrW_2O_8 heat capacities, as shown in Figure 4.9 and Figure 4.10. The values of $\Delta C_P = C_P(HfMo_2O_8) - C_P(ZrW_2O_8)$ are positive at low temperature and negative at high temperature (as was the case for $C_P(HfW_2O_8) - C_P(ZrW_2O_8)$).[108] The maximum value of ΔC_P is ~5 J K^{-1} mol^{-1} at approximately $T = 100$ K.

The value of θ_D of $HfMo_2O_8$ is smaller than the value of θ_D of ZrW_2O_8, 82 K vs. 88 K. This will affect the ΔC_P of $HfMo_2O_8$ vs. ZrW_2O_8. At low temperatures, a smaller value of θ_D will result in a larger C_P at given temperature. Therefore, at lowest T $C_P(HfMo_2O_8) > C_P(ZrW_2O_8)$ because of the Debye (acoustic lattice) modes. At higher temperatures, the opposite will occur. The Einstein (optic) modes of $HfMo_2O_8$ generally move to slightly higher wavenumbers which reduces C_P and the magnitude of CTE.

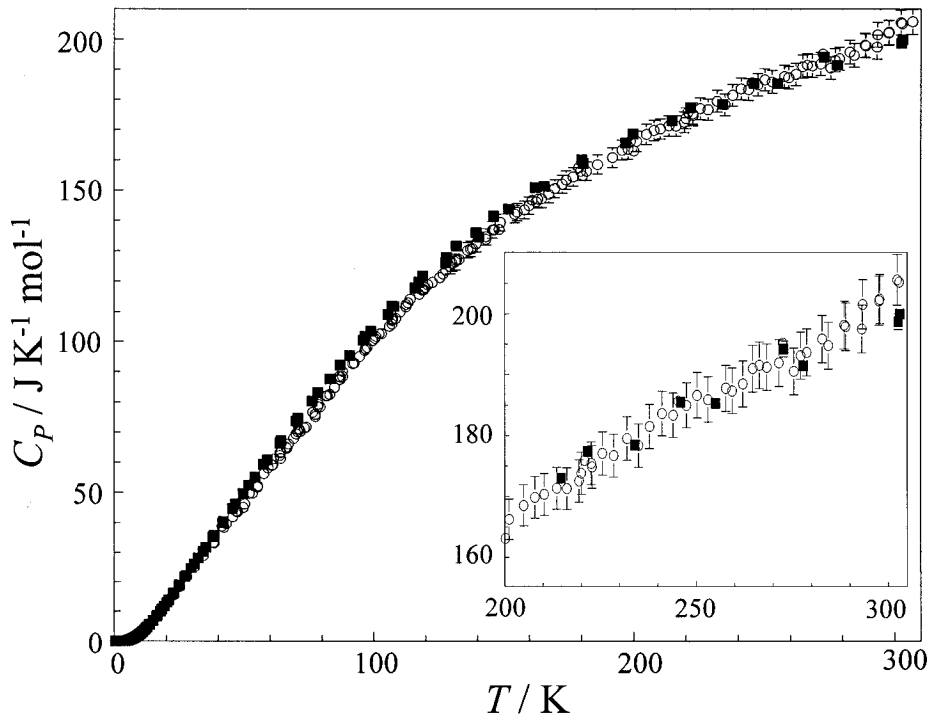

Figure 4.7. Heat capacities of hafnium molybdate, ■, and zirconium tungstate, ○. Inset shows $T = 200$ K to 300 K. Error bars are not visible where the symbol size is larger than the calculated uncertainty.

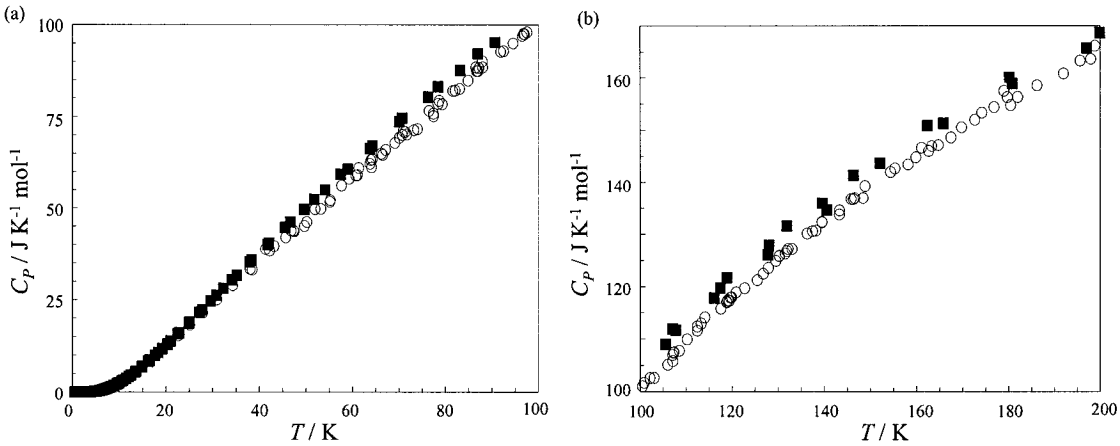

Figure 4.8. Heat capacities of hafnium molybdate, ■, and zirconium tungstate, ○. (a) T = 0 K to 100 K, (b) T = 100 K to 200 K. Error bars are not visible where the symbol size is larger than the calculated uncertainty.

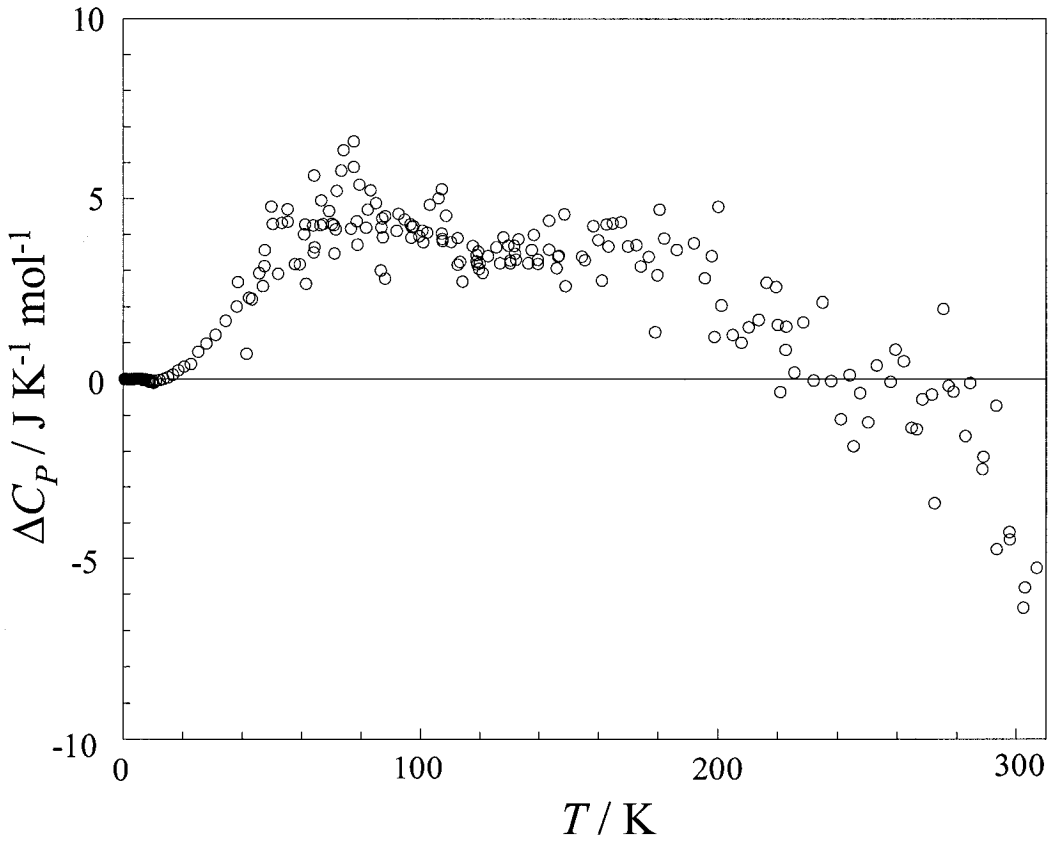

Figure 4.9. Difference in heat capacity between $HfMo_2O_8$ and ZrW_2O_8. $\Delta C_P = C_P(HfMo_2O_8) - C_P(ZrW_2O_8)$.

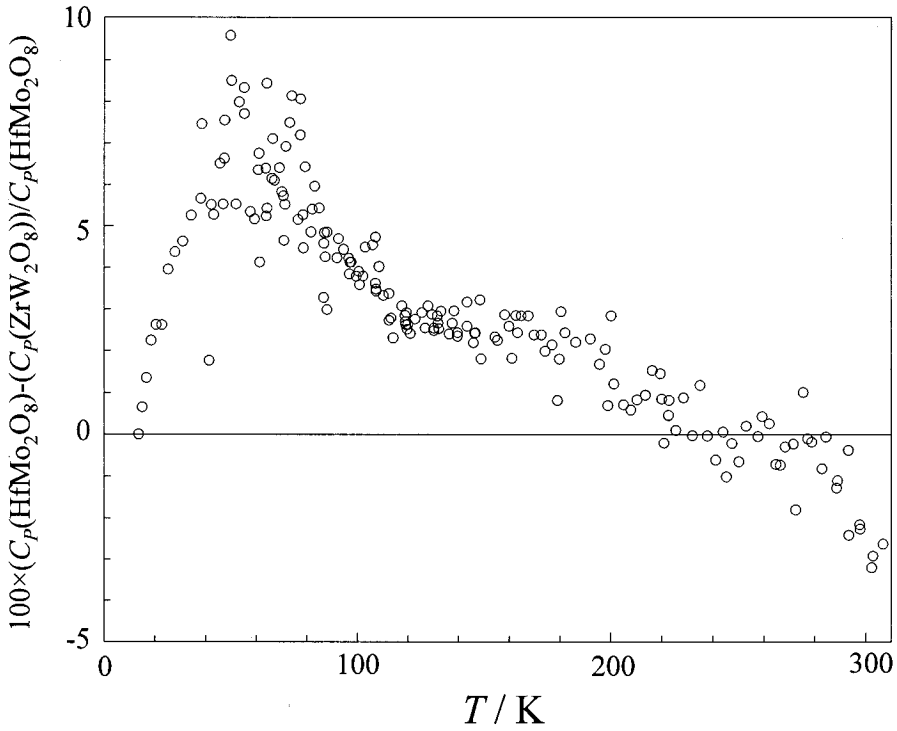

Figure 4.10. Relative heat capacity differences between $HfMo_2O_8$ and ZrW_2O_8.

To date, the heat capacities of several NTE materials with the structure AB_2O_8 (isostructural to either α or β-ZrW_2O_8) have been reported. A plot of the C_PT^{-3} vs. ln(T) is given in Figure 4.11 for the AB_2O_8 NTE materials for which the C_P has been measured. The C_P data for α-ZrW_2O_8[108,117] and cubic-HfW_2O_8[114,187] (isostructural to α-ZrW_2O_8) were reported by Yamamura *et al.*, C_P for α-ZrW_2O_8 and cubic-$ZrMo_2O_8$ (isostructural to β-ZrW_2O_8) were reported by Stevens *et al.*,[116] and the present C_P results include α-ZrW_2O_8 and cubic-$HfMo_2O_8$ (isostructural to β-ZrW_2O_8). The bell-shaped part of the C_PT^{-3} curves are similar for all AB_2O_8 compounds, and are centered at approximately T = 9.5 K, except for $ZrMo_2O_8$. The peak of that curve is centered at approximately T = 8 K. The difference in peak location and shape suggests that the distribution of low-frequency optic modes is different in $ZrMo_2O_8$ compared with the other AB_2O_8 compounds. A

detailed analysis of the phonon density of states has not been reported for $ZrMo_2O_8$, nor have there been any reports on analysis by spectroscopic techniques.

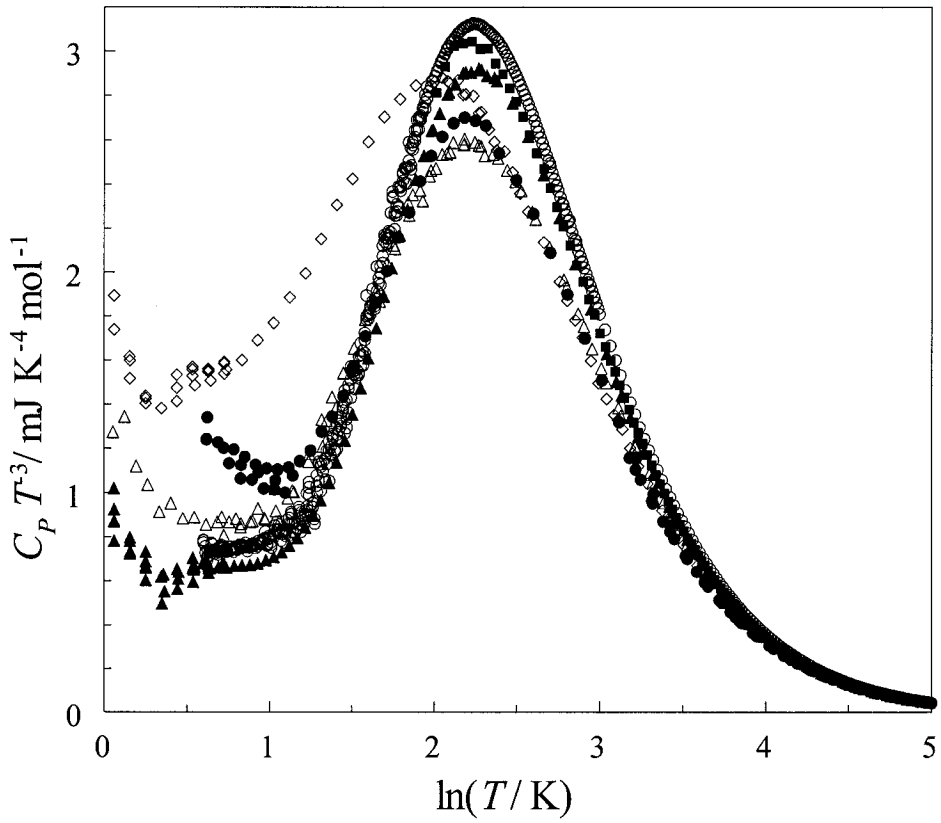

Figure 4.11. C_PT^{-3} vs. ln(T) for AB_2O_8 NTE materials. α-ZrW_2O_8: ● present PPMS, ■ Yamamura *et al.*[108,117], and ▲ Stevens *et al.*[116]. Cubic-HfW_2O_8: ○Yamamura *et al.*[114,187]; cubic-$ZrMo_2O_8$: ◊ Stevens *et al.*[116]; cubic-$HfMo_2O_8$: Δ present study.

4.2.3.3. Constituent Additvity

As was discussed in Section 1.3.2.1, the Neumann-Kopp law is based on the additivity of the heat capacity properties of the constituent atoms to estimate the heat capacity of a solid. A similar approach concerned with thermodynamic contribution from the "constituent group" of a compound has been used with considerable success to estimate the heat capacity and thermodynamics of complex inorganic compounds.[188,189,190] For example sodalite, $Na_8Al_6Si_6O_{24}Cl_2$, has an experimental value

of C_P/R = 97.7 at T = 298.15 K while constituent additivity from C_P of Na_2O, Al_2O_3, SiO_2, and NaCl yield C_P/R = 98.0.[188] Calculation of C_P of $Na_8Al_6Si_6O_{24}Cl_2$ via constituent additivity provides a fit to experimental C_P values to within a few percent for 100 K < T < 1000 K.[188]

Stevens *et al.* have used this technique to calculate the C_P of α-ZrW_2O_8 and cubic-$ZrMo_2O_8$ from the weighted sums of the constituent binary oxides.[116] They found for both compounds that the C_P from the sum of the binary oxides was larger than the experimental C_P. $\Delta C_P = C_P(\text{NTE}) - C_P(AO_2) - 2\times C_P(BO_3)$ was at the maximum ~27 J K^{-1} mol^{-1} for α-ZrW_2O_8, and was at the maximum ~23 J K^{-1} mol^{-1} cubic-$ZrMo_2O_8$. The maximum for ΔC_P for both NTE materials occurred at approximately T = 80 K. This led Stevens *et al.* to infer that there exist a significant number of low-energy vibrational modes in the NTE materials relative to the binary oxides.

Stevens *et al.* have also carried out this analysis for another NTE oxide, Zn_2GeO_4.[191] They reported the heat capacity results for this material, which exhibits NTE below ambient temperatures, for T = 0.5 to 400 K and calculated the C_P from the binary oxides, hexagonal ZnO and tetragonal GeO_2. They found that there was an excess C_P with a maximum of ~ 12 J K^{-1} mol^{-1} at approximately T = 100 K due to low-frequency modes that do not exist in the binary oxides. The average CTE for Zn_2GeO_4 below ambient temperature is -3.4 × 10^{-6} K^{-1}, and +3.9× 10^{-6} K^{-1} above ambient temperatures. Stevens *et al.* also point out the consistency between the lower magnitude of CTE for Zn_2GeO_4 than ZrW_2O_8 and $ZrMo_2O_8$, and the lower magnitude of the excess C_P (decreasing excess C_P with CTE magnitude).

Here, the heat capacities of $HfMo_2O_8$ are compared with the sum of the C_P values

of its binary oxides, HfO_2 and MoO_3. $C_P(HfO_2)$ for 52 K < T < 300 K is from Todd.[192] Experimental data for T < 50 K appear not to have been published, however, Todd's data were extrapolated to lower temperatures by Westrum *et al.*[193] The heat capacities of MoO_3[194] have recently been measured and were used in the additive calculation for $ZrMo_2O_8$ by Steven *et al.*[116] Figure 4.12(b) gives the results of $\Delta C_P = C_P(HfMo_2O_8) - C_P(HfO_2) - 2\times C_P(MoO_3)$ which shows that for T < 200 K, there is a large excess in C_P of $HfMo_2O_8$ (as much as ~20 J K^{-1} mol^{-1}at about 50 K) relative to the sum of its binary oxides. This leads to the conclusion that there exist a significant number of low-energy vibrational modes in $HfMo_2O_8$ relative to the binary oxides, as was seen for $ZrMo_2O_8$ and ZrW_2O_8,[116] and to a lesser extent Zn_2GeO_4.[191]

Since the C_P data for the $Hf_xZr_{(1-x)}Mo_yW_{(2-y)}O_8$ for x = 0, 1 and y = 0, 2 have been reported, one can compare the $C_P(HfMo_2O_8)$ data with a calculation of $C_P(HfMo_2O_8)$ from the other oxides *i.e.* $C_{P,exp}(HfMo_2O_8)$ vs. $C_{P,calc}(HfMo_2O_8) = C_P(HfW_2O_8) - C_P(ZrW_2O_8) + C_P(ZrMo_2O_8)$. The numerical data for $C_P(HfW_2O_8)$, published in figure form by Yamamura *et al.*[114], were obtained from the authors.[187] The results of the calculation are shown in Figure 4.13. The values of $C_{P,calc}(HfMo_2O_8)$ are larger than $C_{P,exp}(HfMo_2O_8)$ for T > 40 K and the deviation is (at a maximum) approximately 5% at 300 K. At lower temperatures, $C_{P,calc}(HfMo_2O_8) < C_{P,exp}(HfMo_2O_8)$ for $20 < T / K < 40$, and for T < 20 K, $C_{P,calc}(HfMo_2O_8) > C_{P,exp}(HfMo_2O_8)$ and deviates considerably at the lowest temperature. Using the NTE AB_2O_8 materials provides a better fit (Figure 4.13) than using the binary oxides (Figure 4.12). This is reasonable since the AB_2O_8 materials all exhibit NTE and therefore would have the low-frequency modes (attributed to NTE) that the binary oxides do not have.

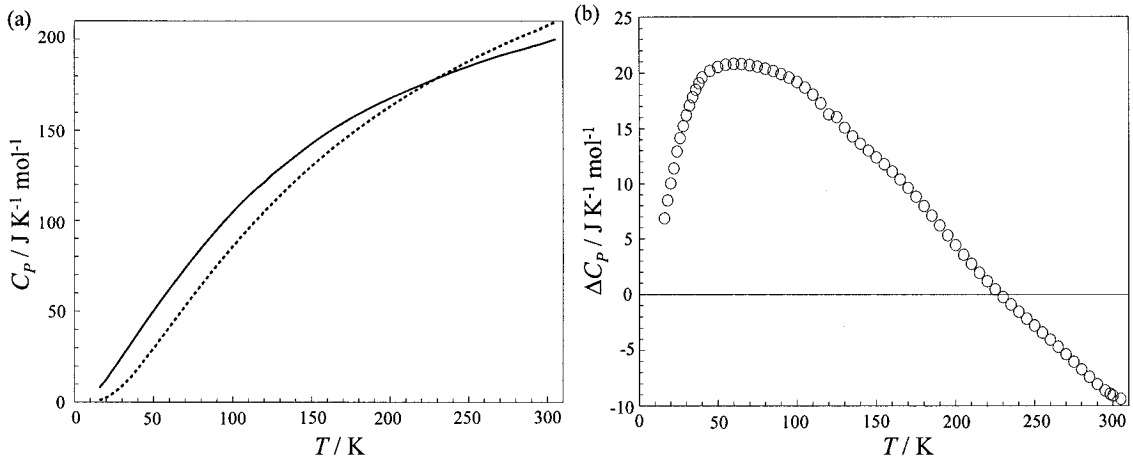

Figure 4.12. Heat capacity of hafnium molybdate relative to the sum of its binary oxides. (a) Experimental C_P of $HfMo_2O_8$ (—), constituent additivity of binary oxides *i.e.* $C_P(HfO_2) + 2\times C_P(MoO_3)$ (----). (b) $\Delta C_P = C_P(HfMo_2O_8) - C_P(HfO_2) - 2\times C_P(MoO_3)$.

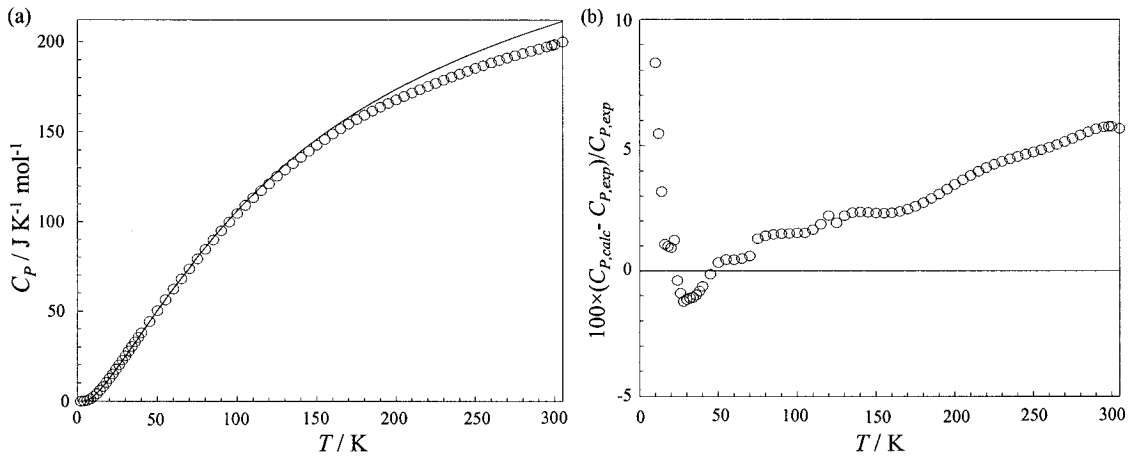

Figure 4.13. (a) Heat capacity of hafnium molybdate from sum of its AB_2O_8 oxides, $C_P(HfW_2O_8) - C_P(ZrW_2O_8) + C_P(ZrMo_2O_8)$, (—), and o smoothed experimental $C_P(HfMo_2O_8)$. (b) Deviation of calculated C_P from measured C_P.

4.2.3.4. Constant Volume Heat Capacities and Thermodynamic Functions

The C_V values for $HfMo_2O_8$ were calculated as a function of temperature using Equation 1.4 for $T > 77$ K where α_l is known from x-ray diffraction.[154] The value of B_T used in the calculation was 43×10^9 N m^{-2}. This was determined from high pressure x-ray experiments specifically for $ZrMo_2O_8$, however, the relative volume expansion vs.

pressure results for $ZrMo_2O_8$ and $HfMo_2O_8$ from this study were almost identical.[154,180] The temperature-dependent molar volumes were calculated from the unit cell parameter at $T = 300$ K and the α_V[154] using $V(T) = V(300\text{ K})[1+\alpha_V(T - 300\text{ K})]$.

For $T < 77$ K, because there were no data for α_l, the Nernst-Lindemann relationship (Equation 1.6) was used to approximate $(C_P - C_V)$. The values of $(C_P - C_V)/C_P$ was less than 0.5 % at $T = 300$ K. The $(C_P - C_V)$, C_V, and the smoothed C_P of $HfMo_2O_8$ are reported in Table 4.2. The smoothed constant pressure heat capacities were integrated to yield the standard thermodynamic functions for $HfMo_2O_8$ for $T = 2$ K to 300 K and these are listed in Table 4.3. Residual entropy of $R\times\ln 2$ was included in the calculation of entropy since $HfMo_2O_8$ is a disordered phase.

Table 4.2. Smoothed constant pressure heat capacities, constant volume heat capacities and C_P-C_V contributions for $HfMo_2O_8$. Units of heat capacity are J K^{-1} mol^{-1}.

T / K	C_P	$(C_P - C_V)$	C_V	T / K	C_P	$(C_P - C_V)$	C_V
2	0.007	0.000	0.007	130	129.0	0.09	128.9
4	0.089	0.000	0.089	135	132.5	0.10	132.4
6	0.471	0.000	0.471	140	135.9	0.10	135.8
8	1.30	0.000	1.30	145	139.4	0.10	139.3
10	2.56	0.000	2.56	150	142.6	0.11	142.5
12	4.18	0.000	4.18	155	145.8	0.11	145.7
14	6.05	0.000	6.05	160	148.8	0.11	148.7
16	8.13	0.000	8.13	165	151.7	0.12	151.6
18	10.4	0.000	10.4	170	154.4	0.12	154.2
20	12.7	0.000	12.7	175	156.9	0.12	156.8
22	15.0	0.000	15.0	180	159.3	0.13	159.2
24	17.6	0.000	17.6	185	161.6	0.13	161.5
26	20.1	0.000	20.1	190	163.8	0.13	163.6
28	22.7	0.000	22.7	195	165.9	0.14	165.7
30	25.2	0.000	25.2	200	167.9	0.14	167.7
32	27.7	0.000	27.7	205	169.8	0.14	169.6
34	30.3	0.001	30.3	210	171.7	0.15	171.5
36	32.8	0.001	32.8	215	173.5	0.15	173.3
38	35.4	0.001	35.4	220	175.3	0.15	175.1
40	37.9	0.001	37.9	225	177.1	0.16	176.9
45	44.2	0.002	44.1	230	178.8	0.16	178.6
50	50.3	0.002	50.3	235	180.5	0.17	180.3

...continued

T / K	C_P	$(C_P - C_V)$	C_V	T / K	C_P	$(C_P - C_V)$	C_V
55	56.3	0.003	56.3	240	182.1	0.17	182.0
60	62.2	0.004	62.2	245	183.8	0.17	183.6
65	68.0	0.005	68.0	250	185.3	0.18	185.2
70	73.6	0.007	73.6	255	186.9	0.18	186.7
75	79.1	0.008	79.1	260	188.3	0.18	188.2
80	84.5	0.06	84.5	265	189.7	0.19	189.6
85	89.8	0.06	89.8	270	191.1	0.19	190.9
90	94.9	0.06	94.9	275	192.4	0.19	192.2
95	99.9	0.07	99.8	280	193.6	0.20	193.4
100	104.7	0.07	104.6	285	194.8	0.20	194.6
105	109.2	0.07	109.2	290	196.0	0.20	195.8
110	113.5	0.08	113.5	295	197.2	0.21	197.0
115	117.5	0.08	117.5	298.15	198.0	0.21	197.8
120	121.2	0.08	121.2	300	198.5	0.21	198.3
125	125.5	0.09	125.4				

Table 4.3. Thermodynamic functions for $HfMo_2O_8$ as calculated from smoothed C_P; all functions in J K^{-1} mol^{-1}.

T / K	$(H - H_o)/T$	$(S - S_o)$	$-(G - G_o)/T$	T / K	$(H - H_o)/T$	$(S - S_o)$	$-(G - G_o)/T$
2	0.00	5.77	5.76	130	65.18	120.36	55.18
4	0.02	5.79	5.77	135	67.61	125.29	57.68
6	0.11	5.89	5.78	140	69.99	130.17	60.19
8	0.30	6.13	5.83	145	72.32	135.00	62.68
10	0.63	6.55	5.92	150	74.61	139.78	65.17
12	1.09	7.16	6.07	155	76.86	144.51	67.66
14	1.66	7.94	6.28	160	79.06	149.19	70.13
16	2.34	8.88	6.54	165	81.21	153.81	72.60
18	3.11	9.96	6.85	170	83.33	158.38	75.06
20	3.95	11.17	7.22	175	85.39	162.89	77.50
22	4.85	12.49	7.64	180	87.41	167.35	79.93
24	5.80	13.90	8.10	185	89.39	171.74	82.36
26	6.81	15.41	8.60	190	91.32	176.08	84.77
28	7.85	16.99	9.14	195	93.20	180.36	87.16
30	8.92	18.64	9.72	200	95.04	184.59	89.55
32	10.02	20.35	10.33	205	96.84	188.76	91.92
34	11.14	22.11	10.97	210	98.60	192.87	94.27
36	12.27	23.91	11.64	215	100.32	196.93	96.61
38	13.42	25.75	12.33	220	102.00	200.94	98.94
40	14.58	27.63	13.05	225	103.65	204.90	101.25
45	17.52	32.45	14.93	230	105.27	208.81	103.54
50	20.49	37.42	16.93	235	106.85	212.67	105.83
55	23.47	42.50	19.02	240	108.40	216.49	108.09
60	26.45	47.65	21.19	245	109.92	220.26	110.34
65	29.42	52.85	23.43	250	111.41	223.99	112.58
70	32.38	58.09	25.72	255	112.88	227.68	114.80
75	35.31	63.36	28.05	260	114.32	231.32	117.01

...continued

T / K	$(H - H_o)/T$	$(S - S_o)$	$-(G - G_o)/T$	T / K	$(H - H_o)/T$	$(S - S_o)$	$-(G - G_o)/T$
80	38.22	68.64	30.42	265	115.73	234.92	119.20
85	41.10	73.92	32.82	270	117.11	238.48	121.37
90	43.95	79.20	35.25	275	118.47	242.00	123.54
95	46.76	84.47	37.71	280	119.80	245.48	125.68
100	49.54	89.72	40.18	285	121.10	248.92	127.81
105	52.27	94.93	42.66	290	122.38	252.31	129.93
110	54.96	100.12	45.15	295	123.64	255.68	132.04
115	57.59	105.25	47.66	298.15	124.42	257.78	133.35
120	60.17	110.33	50.16	300	124.88	259.00	134.12
125	62.70	115.37	52.67				

As for ZrW_2O_8(s), the thermodynamic parameters for production of $HfMo_2O_8$(s) from HfO_2(s) and MoO_3(s) have not been previously studied. These parameters can be obtained by considering a thermodynamic cycle similar to the one used for ZrW_2O_8, but replacing for the proper oxides (see Figure 4.14).

The heat capacity data for HfO_2(s) were obtained from Todd[192] and C_P data for MoO_3(s) were obtained from Boerio-Goates.[194] The smoothed heat capacities for $HfMo_2O_8$(s) are reported in Table 4.1. The enthalpies of formation at 298.15 K have been reported for $HfMo_2O_8$(s), HfO_2(s) and MoO_3(s). They are 44.45 ± 3.94 kJ mol^{-1},[180] -1145 kJ mol^{-1},[195] and -745 kJ mol^{-1},[150] respectively. The enthalpy, entropy and Gibbs energy changes for production of $HfMo_2O_8$(s) from HfO_2(s) and MoO_3(s) as functions of temperature were determined using the cycle in Figure 4.14 along with literature values of heat capacity experiments and heat of formation data. Figure 4.15 is a graphic representation of the thermodynamic functions with respect to temperature.

The Gibbs energy of production of $HfMo_2O_8$(s) from the oxides, HfO_2(s) and MoO_3(s), using the thermodynamic cycle derived here was found to be positive at room temperature. This is consistent with what is already known about the thermodynamic stability of cubic-$HfMo_2O_8$, that it is an unstable form[179] in this temperature range, ($\Delta_{prod}G > 0$).

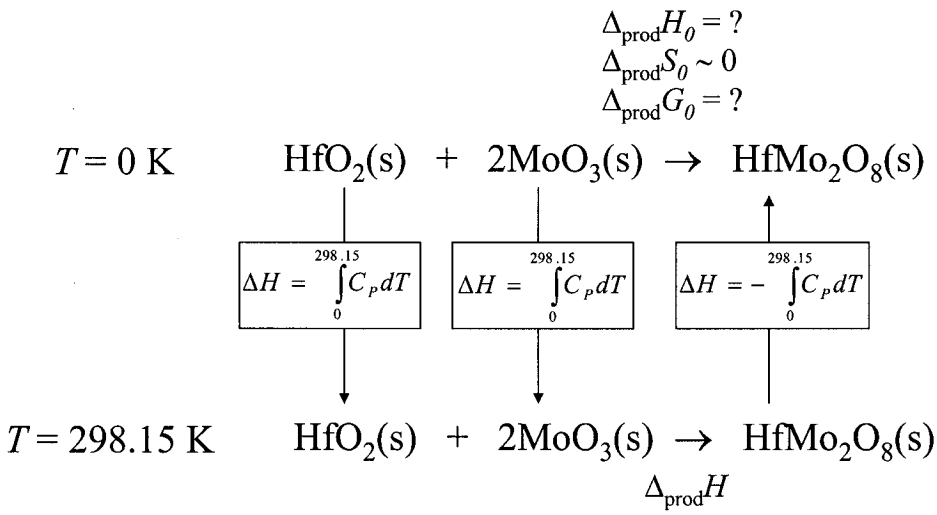

$$\Delta_{prod}H = \Delta_f H^o(HfMo_2O_8) - \Delta_f H^o(HfO_2) - 2\times\Delta_f H^o(MoO_3)$$

Figure 4.14. Thermodynamic cycle for production of $HfW_2O_8(s)$ from $HfO_2(s)$ and $MoO_3(s)$.

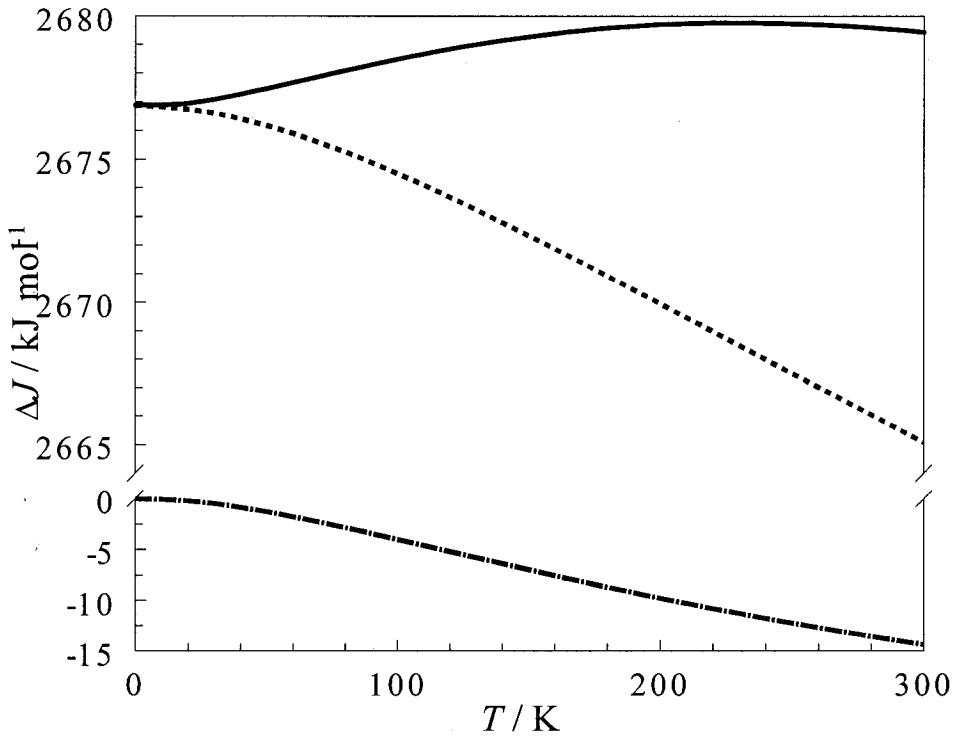

Figure 4.15. The values of $\Delta_{prod}H$ (—), $-T\times\Delta_{prod}S$ (— - —), and $\Delta_{prod}G$ (----) for production of $HfMo_2O_8(s)$ from $HfO_2(s)$ and $MoO_3(s)$ as functions of temperature. $\Delta J = \Delta_{prod}H$, $-T\times\Delta_{prod}S$, and $\Delta_{prod}G$.

4.2.4. Theoretical Calculation of Heat Capacity

4.2.4.1. Introduction

The heat capacity of $HfMo_2O_8$ can be calculated using the Einstein and Debye formulas, Equations 1.8 and 1.9, along with spectroscopic analysis and compared with the experimental data. By doing this, one could better understand the modes that contribute to the heat capacity over specific temperature ranges. This could help identify the modes that are leading to NTE in $HfMo_2O_8$.

4.2.4.2. Calculation of C_V(optic) from Spectroscopic Analysis

Cubic-$HfMo_2O_8$ crystallizes in the $Pa\bar{3}$ (T_h) space group and has four formula units per unit cell. This gives a total of $4 \times 11 = 44$ atoms per unit cell, and $3 \times 44 = 132$ degrees of freedom per unit cell, of which three are acoustic and 129 are optic.

The Raman spectrum of $HfMo_2O_8$ had not been reported prior to the present study. From group theory analysis, not all of the modes are Raman active. There are 20 peaks observed in the Raman spectrum at room temperature, shown in Figure 4.16. The strong peak at 84 cm^{-1} is likely due to a side band from the YAG Raman laser in the spectrometer used in this study. However, another study[108] indicates that ZrW_2O_8 and HfW_2O_8 both shows peaks at approximately this energy at room temperature, so this mode will be included in the C_V(optic) analysis.

A mode at 28.5 cm^{-1} was added to the C_V(optic) calculation. Evidence for a mode this low is seen for ZrW_2O_8 (from IR spectroscopy[143]), however, the optics of the Raman spectrometer used here do not allow for determination of modes this low in frequency. As was the case for α-ZrW_2O_8, $HfMo_2O_8$ shows no peaks in the Raman

spectrum between 433 and 736 cm^{-1}, aside from a weak peak at 667 cm^{-1}.

The PDOS of $HfMo_2O_8$ has not been measured so an effective PDOS has been determined in order to calculate C_V(optic) for $HfMo_2O_8$. The similarities in the C_P curves of ZrW_2O_8 and $HfMo_2O_8$ indicate that the lattice vibrations of the two compounds are comparable. The experimental PDOS of ZrW_2O_8[103] was used as a guideline to determine the effective PDOS of $HfMo_2O_8$, and the same distribution of degrees of freedom was used for $HfMo_2O_8$.

Four degrees of freedom were assigned to the three modes below $\hbar\omega = 8.5$ meV (= 68.6 cm^{-1}) and $\theta_D = 82$ K (calculated from low-temperature C_P data) was used for the acoustic modes. In the high-frequency region, 32 degrees of freedom were divided evenly among the nine observed modes in the high-frequency region. The remaining 97 optic degrees of freedom were distributed among the 12 optic modes in the low-frequency region and were optimized using a nonlinear least-squares method. The PDOS frequency distribution is given in Table 4.4 and is shown in Figure 4.17.

Table 4.4. Observed frequencies from Raman for $HfMo_2O_8$.

T = 298 K		**Assigned**	**T = 298 K**		**Assigned**
cm^{-1}	**meV**	**degrees of freedom**	**cm^{-1}**	**meV**	**degrees of freedom**
28.5*	3.5*	1	667	82.7	3.556
43	5.3	1	750	93.0	3.556
65	8.1	2	781	96.8	3.556
74	9.1	9	819	101.5	3.556
84	10.4	9	852	105.6	3.556
120	14.9	9	876	108.6	3.556
159	19.7	9	904	112.1	3.556
223	22.6	9	945	117.2	3.556
296	36.7	13	998	123.7	3.556
330	40.9	13			
349	43.3	11			
382	47.4	11			
Sub-Total		**97**	**Sub-Total**		**32**
Total: 129					

* From IR study of ZrW_2O_8 by Hancock *et al.*[143]

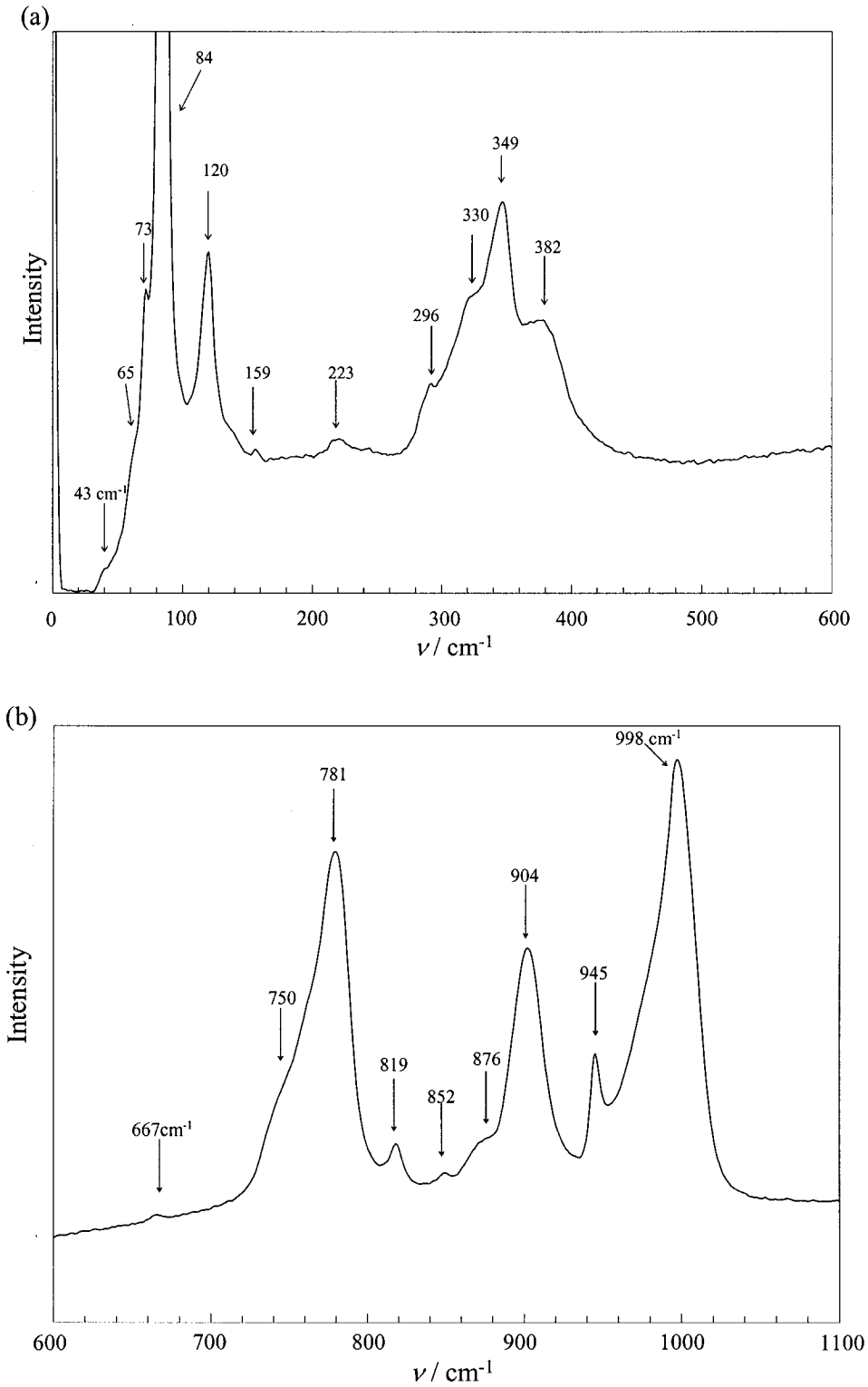

Figure 4.16. Raman spectrum of $HfMo_2O_8$ from the present study at $T = 300$ K with assigned peaks, (a) low-frequency region, and (b) high-frequency region.

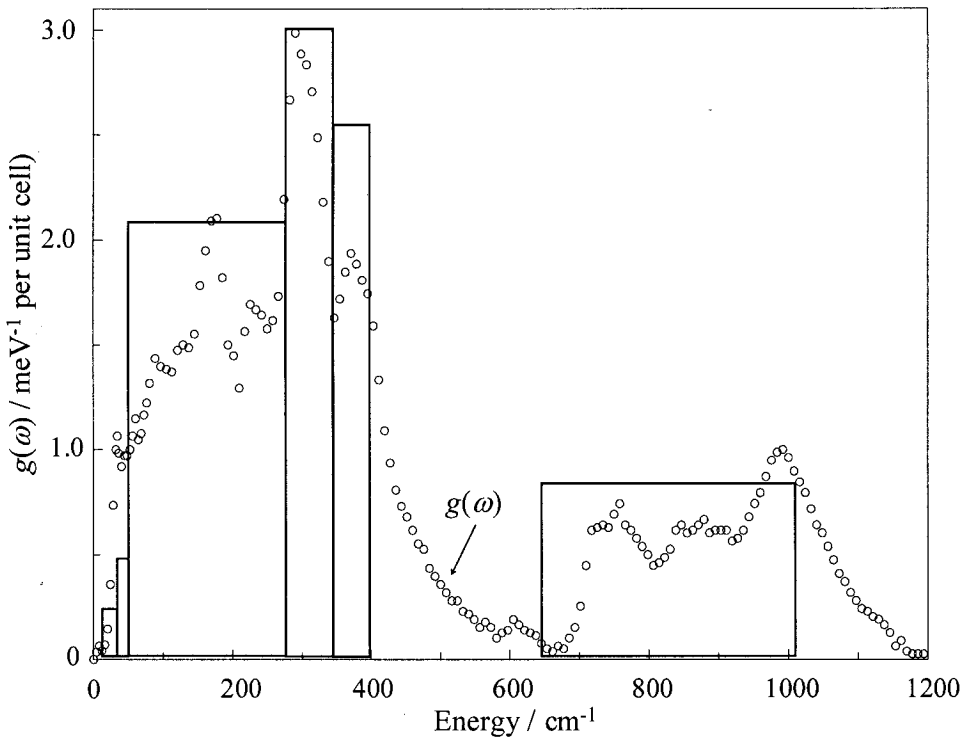

Figure 4.17. Calculated effective phonon density of states, $g(\omega)$, of cubic-$HfMo_2O_8$ (parameters given in Table 4.4) and o experimental PDOS of ZrW_2O_8 from inelastic neutron scattering.[103]

The Einstein equation for heat capacity (Equation 1.8 and Equation 1.11) was used to calculate C_V(optic) for $HfMo_2O_8$ with the degrees of freedom and frequencies as explained above. C_V(optic) for one formula unit was compared with C_V(exp). These are shown along with other contributions to the calculated C_V(cal) in Figure 4.18.

The total calculated heat capacity shown in Figure 4.18 works reasonably well for most of the temperature range, but deviates from C_V(exp) for $T > 250$ K (by less than 5%) and for $T < 20$ K (by more than 10%). The C_V(total calculated) fitting procedure yields a better fit than was obtained for ZrW_2O_8.

The present analysis of the contributions of various modes to the heat capacity of $HfMo_2O_8$ (Figure 4.18) indicates that for $T > 60$ K the modes below 10 meV which are most relevant for negative thermal expansion,[103] are essentially fully excited.

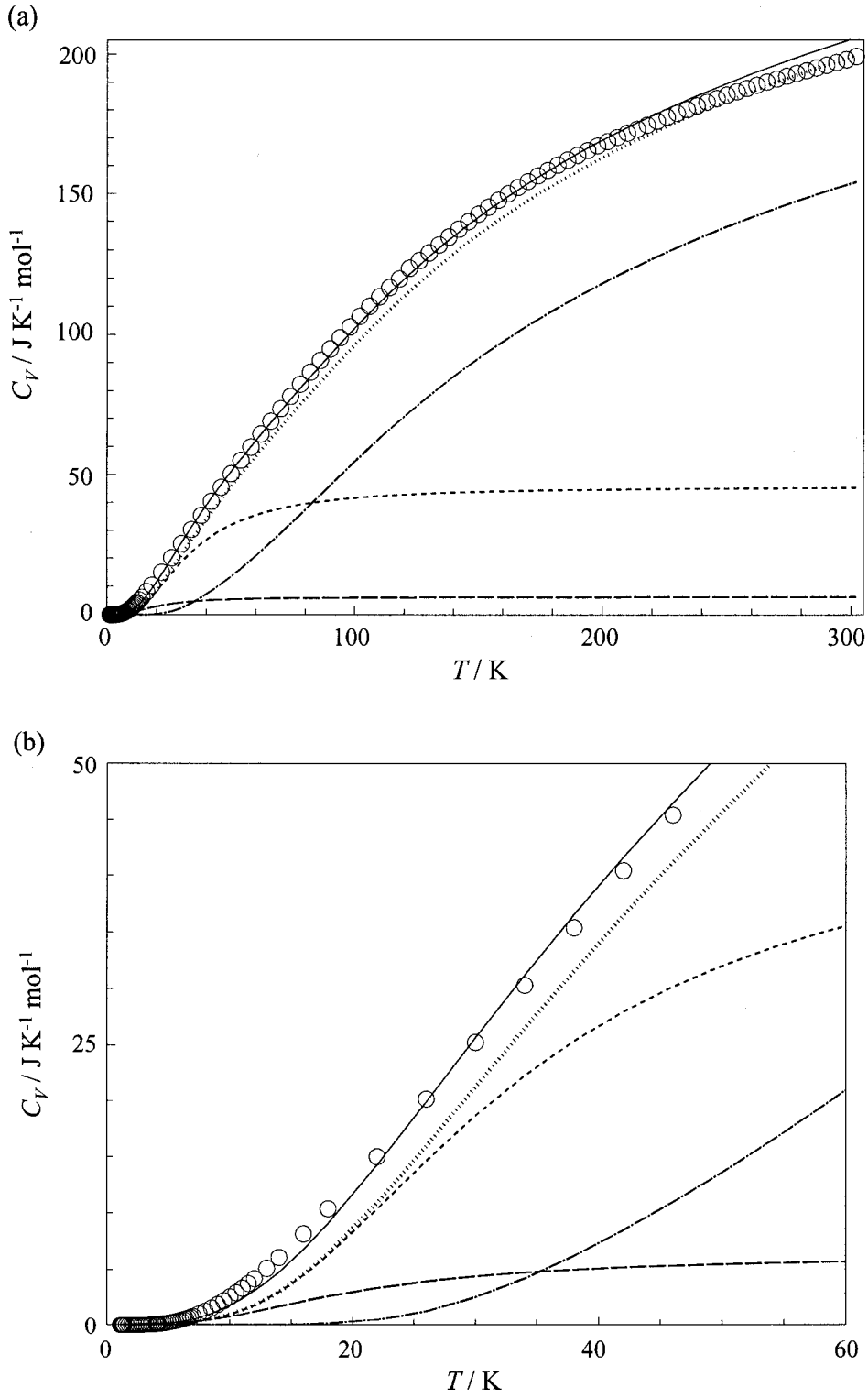

Figure 4.18. (a) Calculated heat capacity of $HfMo_2O_8$. ○ experimental data, (—) total calculated, (.....) total optic, (----) optic with energies < 10 meV, (— - —) optic with energies > 10 meV, and (— —) acoustic. (b) Close-up of low temperature region.

4.2.5. Conclusions

The heat capacities of the cubic form of hafnium molybdate are reported from T = 0.4 to 300 K. Results indicate that the C_P values of $HfMo_2O_8$ are very similar to α-ZrW_2O_8, although slight differences are apparent below T = 200 K. Therefore, the lattice dynamics of these two materials are very similar. The constituent additivity calculation of $C_P(HfMo_2O_8)$ from $C_P(HfO_2)$ + 2× $C_P(MoO_3)$ demonstrates that there are additional low-energy vibrations present in this material not present in its binary oxides.

The analysis of the contributions of various modes to the heat capacity of $HfMo_2O_8$ (Figure 4.18) indicates that, for T > 60 K the modes below 10 meV, which are most relevant for negative thermal expansion,[103] are essentially fully excited. This was also the case for ZrW_2O_8[158] as shown in Section 3.5. These modes are so low in frequency that they can be highly anharmonic, essentially fully coupling with each other. As was shown for ZrW_2O_8, this could lead to short phonon mean free paths, high resistance to heat flow, and low thermal conductivity. In the following sections, the thermal conductivity and the Grüneisen parameter (used to quantify anharmonicity) of $HfMo_2O_8$ will be presented and discussed.

4.3. Thermal Conductivity

4.3.1. Introduction

The thermal conductivity of $HfMo_2O_8$ has not been reported previously. Due to the similarities in C_P and α_l for $HfMo_2O_8$ and ZrW_2O_8, one would expect the temperature dependent thermal conductivities of the two materials to be similar. The goal of this thesis was to see if low-temperature κ of materials that exhibit NTE was unusual in

comparison with other materials. In Chapter 3, consideration of the theoretical minimum thermal conductivity, the phonon mean free path, the Grüneisen parameter, and the contributions of various modes to the heat capacity was employed to delineate the origins of its unusually low thermal conductivity in ZrW_2O_8. For comparison purposes, the same analysis is performed to delineate the origins of the unusual low thermal conductivity of $HfMo_2O_8$.

4.3.2. Experimental Methods

The procedures described in Section 3.5.3 (for κ of ZrW_2O_8) were followed to press the $HfMo_2O_8$ powder into pellets of the appropriate dimensions. $HfMo_2O_8$, in powder obtained directly from the Georgia Institute of Technology, was pressed into disk-shaped pellets with a diameter of 4.74 mm using a load of 2000 lbs (0.5 GPa). DSC and x-ray diffraction confirmed that the pressing step did not change the phase of $HfMo_2O_8$; see Section 4.2.2.

The $HfMo_2O_8$ pellets were very fragile and often broke while the κ measurements were underway. Often the samples would break at the sample-epoxy interface, but in other instances, the pellet itself would fracture. This could be due to thermal stresses in the compound that overcome the mechanical integrity of the pellets, possibly arising from differences in thermal expansion of the samples relative to the epoxy and copper leads.

When the sample puck was loaded into the PPMS, it was not possible to visually confirm if the pellet was broken; however, it was obvious from a significant drop in the κ values as the measurement progressed that there was a problem. This drop in κ occurred at different temperatures for each case in which the sample broke. It was not due to a

phase transition since no anomalous behavior was present in the C_P curve of this material. Upon removing the TTO puck from the PPMS, it became clear that the samples had broken. This breakage also occurred when measuring κ for ZrW_2O_8. In that case, 22 samples were made in order to obtain reliable results for five ZrW_2O_8 samples for the temperature range of 2 to 390 K. In total, 27 samples were made to collect the data for $HfMo_2O_8$. The data presented below are for pellets before the samples had broken.

The optimal height (for pulse period : τ_1 ratio to be 8 : 1) for the pellets was approximately 0.8 mm. Table 4.5 gives the dimensions and densities of the $HfMo_2O_8$ pellets used successfully in this study.

Temperature-dependent thermal conductivities of cubic-$HfMo_2O_8$ were determined using the thermal transport option of the QD PPMS. A two-probe configuration (heater and hot thermometer shared one lead while the coldfoot and cold thermometer shared the other) was used and the pellets were epoxied (0.2 mm of silver-loaded epoxy, Tra-Bond 816H01 from Tra-Con, Inc.) to two disc-shaped copper leads (diameter of 6.30 mm). The thermal conductivities were measured under vacuum of 10^{-4} Torr. Thermal conductivities were measured using continuous methods; the principles of operation for this technique are based on a pulse method and are described in Section 2.2.

Table 4.5. Size and density (at T = 300K) of $HfMo_2O_8$ pellets used to measure thermal conductivity with the PPMS.

Sample	Thickness / mm	Density / g cm^{-3}	% Theoretical Density
1	0.74	2.74	62.4
2	0.74	2.75	62.6
3	0.80	2.68	61.0
4	0.84	2.49	56.7
5	0.78	2.65	60.4

4.3.3. Results and Discussion

Figure 4.19 shows the temperature dependence of the thermal conductivity, κ, of $HfMo_2O_8$ for the samples measured, while Table 4.6 gives the smoothed numerical data for each run along with the average values. The uncertainties in κ were estimated from the accuracies in thermal conductance reported by QD, described in Section 2.2.6, along with the uncertainties in measuring the diameter and the height of the pellet since $\kappa = (K \times l)/A$. For the κ of ZrW_2O_8 given in Section 3.5.4, it was found that in general, the results were in good agreement with each other (within 20 %) at temperatures above 30 K but there was some sample dependence at lower temperatures, possibly due to either sample differences or slight variations in the sample-epoxy adhesion. The same will be considered for $HfMo_2O_8$, the overall uncertainty is 20% for temperatures above 30 K but uncertainty will be larger below 30 K. The thermal conductivity at $T = 300$ K for sample 1 is 0.32 ± 0.06 W m^{-1} K^{-1}, but the average value is lower, 0.28 ± 0.06 W m^{-1} K^{-1}.

Table 4.6. Smoothed thermal conductivity data of $HfMo_2O_8$ for five samples measured and average value.

T / K	κ / W m^{-1} K^{-1}	T / K	κ / W m^{-1} K^{-1}	T / K	κ / W m^{-1} K^{-1}	T / K	κ / W m^{-1} K^{-1}
sample 1(a)		**sample 1(a)**		**sample 2**		**Average**	
2	0.00061	240	0.30	380	0.51	6.5	0.0095
2.25	0.0012	260	0.31	385	0.53	7	0.011
2.5	0.0017	280	0.31	**sample 3**		7.5	0.012
2.75	0.0023	300	0.32	220	0.23	8	0.013
3	0.0028	320	0.33	230	0.24	8.5	0.014
3.5	0.0037	340	0.34	240	0.25	9	0.016
4	0.0046	350	0.35	250	0.25	9.5	0.017
4.5	0.0055	**sample 1(b)**		260	0.25	10	0.018
5	0.0065	2	0.0012	270	0.26	11	0.021
5.5	0.0074	2.25	0.0016	280	0.26	12	0.023
6	0.0085	2.5	0.0019	290	0.26	13	0.026
6.5	0.0096	2.75	0.0023	300	0.27	14	0.028
7	0.011	3	0.0027	310	0.28	16	0.033
7.5	0.012	3.5	0.0036	320	0.28	18	0.038

...continued

T / K	κ / W m^{-1} K^{-1}	T / K	κ / W m^{-1} K^{-1}	T / K	κ / W m^{-1} K^{-1}	T / K	κ / W m^{-1} K^{-1}
8	0.013	4	0.0045		**sample 4**	20	0.042
8.5	0.015	4.5	0.0054	220	0.236	22	0.047
9	0.016	5	0.0063	230	0.242	24	0.051
9.5	0.017	5.5	0.0073	240	0.247	26	0.056
10	0.019	6	0.0083	250	0.252	28	0.060
11	0.022	6.5	0.0094	260	0.257	30	0.064
12	0.024	7	0.011	270	0.261	35	0.074
13	0.027	7.5	0.012	280	0.265	40	0.082
14	0.030	8	0.013	290	0.269	45	0.090
16	0.035	8.5	0.014	300	0.272	50	0.098
18	0.039	9	0.015	310	0.277	55	0.11
20	0.044	9.5	0.016	320	0.286	60	0.12
22	0.049	10	0.017		**sample 5**	65	0.12
24	0.054	11	0.020	210	0.23	70	0.13
26	0.058	12	0.022	220	0.24	75	0.14
28	0.063	13	0.025	230	0.24	80	0.15
30	0.067	14	0.027	240	0.24	85	0.15
35	0.078	16	0.032	250	0.25	90	0.16
40	0.086	18	0.036	260	0.25	95	0.17
45	0.094	20	0.041	270	0.26	100	0.17
50	0.10	22	0.045	280	0.26	120	0.20
55	0.11	24	0.049	290	0.26	140	0.23
60	0.12	26	0.053	300	0.27	160	0.24
65	0.12	28	0.057	310	0.27	180	0.26
70	0.13	30	0.061	320	0.28	200	0.27
75	0.14	35	0.071		**Average**	220	0.25
80	0.15	40	0.079	2	0.00090	240	0.26
85	0.15	45	0.087	2.25	0.0014	260	0.27
90	0.16	50	0.094	2.5	0.0018	280	0.27
95	0.17		**sample 2**	2.75	0.0023	300	0.28
100	0.17	315	0.40	3	0.0027	320	0.32
120	0.20	320	0.41	3.5	0.0036	340	0.39
140	0.22	330	0.43	4	0.0045	360	0.47
160	0.24	340	0.44	4.5	0.0054	380	0.51
180	0.26	350	0.46	5	0.0064	385	0.53
200	0.27	360	0.47	5.5	0.0074		
220	0.29	370	0.48	6	0.0084		

* Uncertainty of κ values is discussed in text.

** Refer to Table 4.5 for sample descriptions. Sample 1(a) is first run of sample 1, while (b) is second run.

As also found for ZrW_2O_8, the present results indicate that $HfMo_2O_8$ does not exhibit the temperature dependence of a "normal" crystalline solid. The temperature dependence of the thermal conductivity of both $HfMo_2O_8$ and ZrW_2O_8 is more like that

of a glass, despite being a crystalline material. The κ data for sample 1(a) at temperatures below ~9 K are scattered due to problems with the PPMS temperature controller in stabilizing the temperature in this region. This problem was ultimately fixed and the pellet was run a second time to obtain improved results, shown as sample 1(b) in Figure 4.19. The two runs are within 5% of each other where the deviation is a maximum.

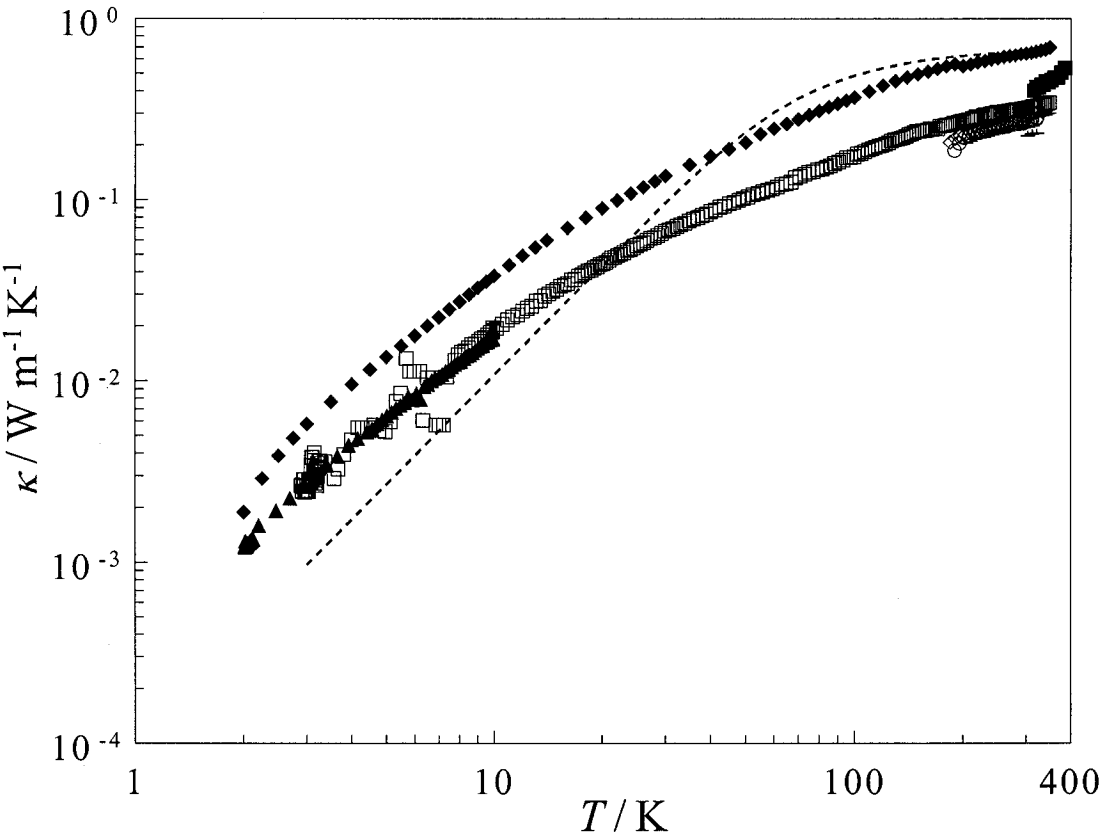

Figure 4.19. Temperature dependence of thermal conductivity of $HfMo_2O_8$ pellets measured directly using PPMS. □ 1(a) which was first cooling of sample 1, ▲1(b) which was second cooling of sample 1, ■ 2, ○ 3, Δ 4 ◊ 5, ♦ κ_{dense} of average values of κ, and (----) κ_{min}. Error bars indicate uncertainty in measurement, and are not visible when the symbol size is larger than the calculated uncertainty.

κ_{min} for $HfMo_2O_8$ was calculated from an equation based on fully coupled oscillators,[27] using Equations 1.24 and 1.25, and is shown in Figure 4.19. The analysis of the present low-temperature heat capacity data leads to $\theta_D = 82$ K, where θ_D represents only the acoustic modes (3 out of 132 degrees of freedom in the unit cell). Instead, if the effective Debye characteristic temperature (θ_D^e) is considered where all the lattice modes (3 acoustic and 129 optical) are treated as Debye-like, the result is a higher effective Debye temperature, $\theta_D^e = 290$ K. For ZrW_2O_8, the same analysis (treating all modes as Debye-like) yields a $\theta_D^e \sim 320$ K,[108,110] in good agreement with the value of the mean $\theta_D^e = 333$ K as calculated from elastic constants.[110] The elastic constant results were used to calculate κ_{min} for ZrW_2O_8 in Section 3.5.4.2. Since there are no reports of elastic measurements of $HfMo_2O_8$ at this time and since θ_D^e obtained from the elastic constants is not significantly different than θ_D^e obtained using C_P measurements for ZrW_2O_8, the elastic constant determination of $\theta_D^e = 333$ K was used for the κ_{min} calculation for $HfMo_2O_8$.

The mean velocity of sound ($v_m = 2900$ m s^{-1}) was calculated from the Debye temperature using Equation 1.25. The unit cell dimensions used for the calculation of V_m were used as in Section 4.2.3.4. The observed thermal conductivity of $HfMo_2O_8$ is very low, but it is lower than the theoretical minimum value for $T > 20$ K (Figure 4.19). The values based on 100% theoretical density are higher, but are still less than the κ_{min} for $T >$ 30 K. This low κ values indicates highly anharmonic lattice dynamics, in agreement with the investigation for ZrW_2O_8.

The density of the pellets as-made and the amount of amorphous material in the

cubic-$HfMo_2O_8$ might provide an explanation as to why the κ values of this material are lower than the κ values for ZrW_2O_8, and also lower than the theoretical κ_{min}. The cubic-$HfMo_2O_8$ sample from Georgia Institute of Technology has approximately 4% of amorphous material in it, and approximately 1% of other contaminants. This could lower the κ since amorphous materials generally have lower κ values than crystalline materials.

However, this is probably not the most significant lowering of κ. The larger contribution to the low κ values is probably the density of the pellets. As was shown in Table 4.5, the pellets used in this investigation were only 56 to 63% of the theoretical density, lower than the theoretical density of the ZrW_2O_8 pellets (74 to 78%). Using methods developed by Klemens[168] shown in Equation 3.6, the relationship of κ_{dense} to κ_{porous} for pellet sample 1 (62.4% density) would be $\kappa_{dense} = 2.0 \times \kappa_{porous} = 2.0 \times 0.32 = 0.64$ W m^{-1} K^{-1} at $T = 300$ K. The average value of κ assuming an average theoretical density of 60.6% at $T = 300$ K is 0.28 W m^{-1} K^{-1}, and $\kappa_{dense} = 0.60$ W m^{-1} K^{-1}. The κ_{dense} (for the average value of κ) of $HfMo_2O_8$ is shown in Figure 4.19 along with the measured κ, and κ_{min}. The best room temperature value of κ_{dense} is taken from the sample pellet that yielded the highest κ since this material probably provided the best epoxy layer thermal contact, therefore $\kappa_{dense} = 0.64$ W m^{-1} K^{-1} at $T = 300$ K for $HfMo_2O_8$.

Using the experimental thermal conductivity data, the phonon mean free path, λ, was calculated from Equation 1.17. The results are shown in Figure 4.20. The mean free path at $T > 40$ K is *ca.* 10 Å or less, on the same order as the mean free path for non-crystalline materials such as amorphous SiO_2[27] despite the fact that $HfMo_2O_8$ is crystalline. This was also the result for ZrW_2O_8 (see Section 3.5.4).

The minimum particle size of the polycrystalline $HfMo_2O_8$ powder was determined to be > 50 μm as determined by mesh sifters. Even at very low temperatures, the size of the particles would not affect the thermal conductivity since the maximum value of λ calculated from experimental data and Equation 1.17, ~200 Å at 2 K (shown in Figure 4.20) is less than the minimum grain size. Therefore, similar to what was seen for ZrW_2O_8, the $HfMo_2O_8$ particle size does not limit the thermal conductivity by grain boundary scattering.

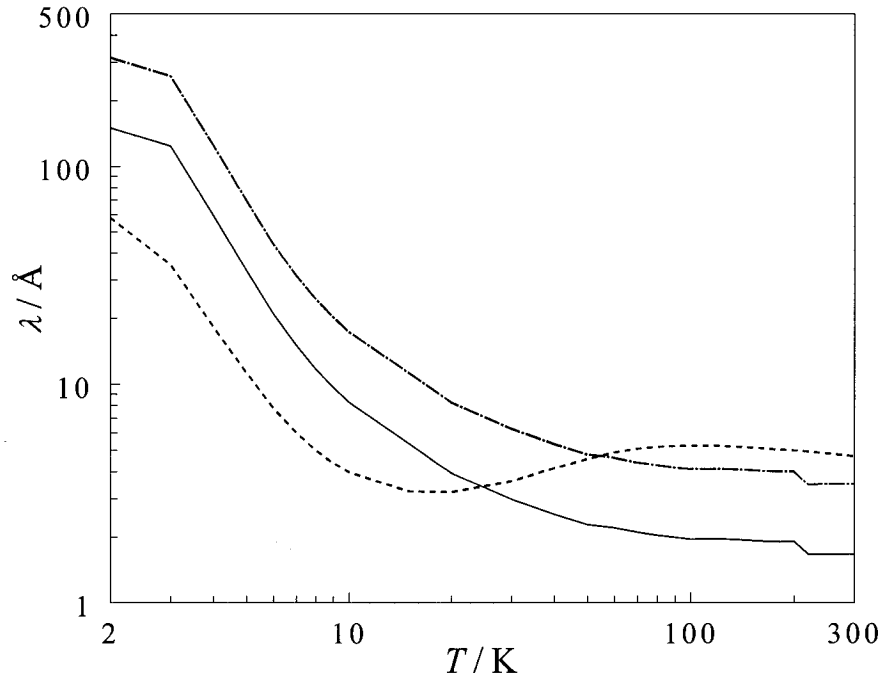

Figure 4.20. Phonon mean free path of $HfMo_2O_8$; (—) from the average porous experimental thermal conductivity, (— - —) from the average dense experimental thermal conductivity, (----) from the minimum thermal conductivity.

4.4. Grüneisen Parameter and Anharmonicity in $HfMo_2O_8$

The average value of γ for $HfMo_2O_8$ is given as a function of temperature in Figure 4.21 for $T > 77$ K where α_l is known. The average γ value was calculated from Equation 1.28 using smoothed C_V data (from Table 4.2), $B_T = 43 \times 10^9$ N m^{-2} [154,180]

(considered constant over the entire temperature range), and volumes calculated as in Section 4.2.3.4. There are no α_l data available for $T < 77$ K. The average Grüneisen parameters for $HfMo_2O_8$ are large in magnitude, and the magnitude starts to increase for $T < 150$ K, as for ZrW_2O_8.

The large deviation of γ from zero fits with the conclusions made for ZrW_2O_8. The analysis of the contributions of various modes to the heat capacity of ZrW_2O_8 (Figure 3.22) indicates that for $T > 60$ K the modes below 10 meV which are most relevant for negative thermal expansion,[103] are essentially fully excited. From the calculation of γ, we know that these modes are highly anharmonic, as γ deviates significantly from zero as shown in Figure 4.21, however, $HfMo_2O_8$ deviates to a lesser extent. Furthermore, the modes are essentially fully coupled with each other leading to high resistance to heat flow, and low thermal conductivity (Figure 4.19).

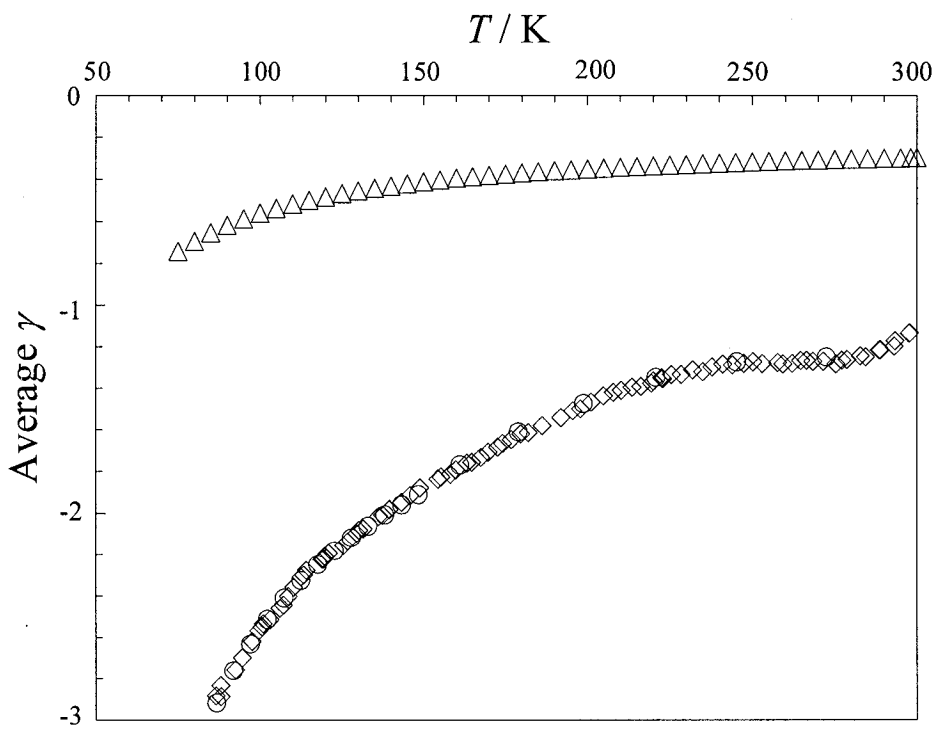

Figure 4.21. Grüneisen function of Δ $HfMo_2O_8$, ○ ZrW_2O_8 PPMS results, ◊ ZrW_2O_8 adiabatic calorimetry results.

4.5. Conclusions

The same highly anharmonic low-frequency modes which lead to negative thermal expansion in $HfMo_2O_8$ give rise to highly coupled phonons which reduce the phonon mean free path and, hence, the thermal conductivity. This is also the case for ZrW_2O_8. This remarkable finding indicates that negative thermal expansion in materials with AB_2O_8 structures could generally lead to low glass-like thermal conductivities.

Chapter 5. Conclusions and Future Directions

Thermal properties are among the most fundamental characteristics of materials. Studying thermal properties of a material such as heat capacity, thermal expansion, and thermal conductivity can lead to better understanding of the theories in chemistry, physics, and engineering, can help uncover links between structure and properties, and can help provide insight into applications of materials.

The measurement of thermal conductivity allows for the study of interesting physical phenomenon; however it is also an important property from a technological aspect. Materials that exhibit thermal conductivities from both the high and low end of the spectrum are of special interest for various applications. As mention in Chapter 2, high-thermally conductive materials such as diamonds and silicon are extensively studied for their use in thermal management devices for electronics,[37] while low-thermally conductive materials such as skutterudites, clathrates, half-Heuslers, and novel oxides are studied for their use in high-efficiency thermoelectric applications.[37,39] Advancing the understanding of the mechanisms that lead to thermal resistivity can be used as a basis for new materials design.

Thermal conductivity can be reduced in materials through several different structural and dynamic mechanisms. By reducing the particle size of crystallite, the mean free path of the phonons can be reduced thus reducing κ. Also, having large unit cell can also lower κ, such as in AlPdMn quasicrystals.[196] Introduction of defects in the lattice can also effectively reduce κ. Amorphous materials have lower κ values than crystalline materials due to lack of periodicity, thus providing another mechanism for

thermal resistance. Dynamic features, such as having rattlers in cages of clathrates, can lower the κ values by optic modes which scatter the heat carrying-acoustic phonons.[197]

The coefficient of thermal expansion of a material is important to consider for many engineering applications. The CTE is based on the intrinsic nature of the material, as described in Chapter 1; its magnitude can vary greatly from material to material. Having a mismatch in thermal expansion can lead to useful applications such as in bimetallic strips in thermometers, but it also can lead to problems and potentially failure in a system. Materials with low thermal expansion coefficients are desirable since they will exhibit favorable thermal shock resistance. Temperature gradients on rapid cooling or heating would be minimized, and so fewer cracks would result. For engineering purposes, control of the coefficient of thermal is also desirable. Being able to tailor materials with specific CTE would be useful for applications in which having close to identical CTE would be favorable. For example, interfaces shared by two materials with different thermal expansion properties could result in thermal stress leading to cracks or separation at the interfaces. If the materials had the same CTEs, the thermal stresses of the interface would be less, and destruction of the interface would be less likely. For these applications, NTE materials could be mixed with positive thermal expansion materials to obtain a material with a CTE tailored to the application.

For NTE materials with the AB_2O_8 structure, there is a relationship between NTE and low-frequency modes. These modes are unique to the AB_2O_8 form, and are not present in their constituent binary oxides. This has been shown by comparing the C_P of the AB_2O_8 materials to the C_P calculated from the binary oxides. This could be used as a method to assess whether materials with structural similarities have low-frequency

modes, the presence of which could indicate that the material has the potential to exhibit NTE.

This thesis shows for the first time that for the NTE materials, ZrW_2O_8 and $HfMo_2O_8$, highly anharmonic low-frequency modes (responsible for negative thermal expansion) also give rise to highly coupled phonons which reduce the phonon mean free path and, hence, the thermal conductivity. This was shown through the consideration of the heat capacity, phonon mean free path, and Grüneisen parameter. This remarkable finding suggests that negative thermal expansion in framework NTE oxides with similar structures could generally lead to low glass-like thermal conductivities. The coupled low-frequency modes are a necessary condition for the mechanism of low, glass-like thermal conductivity in these materials.

ZrW_2O_8 has been synthesized as a large single crystal,[198] and will become amorphous when pressed above 3.5 GPa.[122,125] It would be useful to determine the κ of a single crystal to have a better idea of the effect of density of the pellets on the κ of this material. Also, investigation of κ of amorphous ZrW_2O_8 would allow comparison with maximum thermal resistance, as one would expect for the amorphous material.

Recently ZrW_2O_8 aerogels have been prepared and have been shown to exhibit negative thermal expansion.[92] Aerogels have very low thermal conductivities, for example, a typical silica aerogel has a $\kappa = 0.017$ W m^{-1} K^{-1} at $T = 300$ K.[30] Studying the thermal properties of the ZrW_2O_8 aerogels in more detail would show if the low-frequency modes and concomitant unusual thermal properties still exist in the aerogel form.

Another area for further investigation is the variation in κ for framework materials

as a function of density of the pellet. This was not possible here due to limitations of the pressing procedure (increase the load would break the pressing assembly) and constraints on the sample geometries needed. Having less dense pellets would make the samples even more fragile during κ measurements. Ideally, the materials should be synthesized as boules from which pellets could be machined.

In general terms of future directions, there is large family of NTE materials with AB_2O_8 structure whose thermal properties (heat capacity and thermal conductivity) have not been studied. It would be worth investigating the generality of low, glass-like κ in other NTE framework oxides similar to those studied here.

In conclusion, a new mechanism for low-thermal conductivity has been found in that low-frequency modes in these framework oxide materials lead to low glass-like thermal conductivity. This mechanism could provide a basis for design of new materials with low thermal conductivity.

References

1. http://history.nasa.gov/rogersrep/51lcover.htm last accessed 10/07/2004.

2. C.H.P. Lupis, *Chemical Thermodynamics of Materials*, Elsevier Science Publishing Co., Inc.: New York, **1983**.

3. R.S. Berry, S.A Rice, and J. Ross, *Physical Chemistry*, 2nd Ed., Oxford University Press, Inc.: New York, **2000**.

4. A. Navrotsky, *Physics and Chemistry of Earth Materials*, Cambridge University Press: Cambridge, **1994**.

5. J.F. Nye, *Physical Properties of Crystals, Their Representation by Tensors and Matrices*, Oxford University Press: New York, **1985**.

6. A.I. Kitaigorodsky, *Molecular Crystals and Molecules*, Academic Press: New York, **1973**.

7. W. Nernst and F.A. Lindemann, *Z. Electrochem.*, **1911**, *17*, 817-827.

8. G.K. White, *Experimental Techniques in Low-Temperature Physics*, 3rd Ed., Oxford University Press: Oxford, **1979**.

9. E.S.R. Gopal, *Specific Heats at Low Temperatures*, Plenum Press: New York, **1966**.

10. P.L. Dulong and A.T. Petit, *Ann. Chim. Phys.*, **1819**, *10*, 395.

11. J.B. Ott and J. Boerio-Goates, *Chemical Thermodynamics Vol. 1, Principles and Applications*, Academic Press: San Diego, **2000**.

12. A. Einstein, *Ann. Phys.*, **1907**, *22*, 180-190.

13. P. Debye, *Ann. Phys.*, **1912**, *39*, 789-839.

14. T.H.K. Barron and G.K. White, *Heat Capacity and Thermal Expansion at Low Temperatures*, Kluwer Academic/Plenum Publishers: New York, **1999**.

15. Y. Fujii, N.A. Lurie, R. Pynn, and G. Shirane, *Phys. Rev. B*, **1974**, *10(8)*, 3647-3659.

16. M.T. Dove, *Introduction to Lattice Dynamics*, Cambridge University Press: Cambridge, **1993**.

17. N.W. Ashcroft and N.D. Mermin, *Solid State Physics*, Holt, Rinehart and Winston: New York, **1976**.

18. M.T. Dove, *Structure and Dynamics, An Atomic View of Materials*, Oxford University Press, Inc.: New York, **2003**.

19. M.A. White, *Properties of Materials*, Oxford University Press, Inc.: New York, **1999**.

20. C. Kittel, *Introduction to Solid State Physics*, 7th Ed., John Wiley & Sons, Inc.: New York **1996**.

21. M.A. White, *Can. J. Chem.*, **1996**, *74*, 1916-1921.

22. R. Roy, D.K. Agrawal, and H.A. McKinstry, *Annu. Rev. Mater. Sci.*, **1989**, *19*, 59-81.

23. M.P. Attfield and A.W. Sleight, *Chem. Commun.*, **1998**, *5*, 601-602.

24. T.A. Mary, J.S.O. Evans, T. Vogt, and A.W. Sleight, *Science*, **1996**, *272*, 90-92.

25. R. Peierls, *Ann. Phys.* **1929**, *3*, 1055-1101.

26. R.C. Zeller and R.O. Pohl, *Phys. Rev. B*, **1971**, *4(6)*, 2029-2041.

27. D.G. Cahill and R.O. Pohl, *Ann. Rev. Phys. Chem.*, **1988**, *39*, 93-121.

28. Y.S. Touloukian, R.W. Powell, C.Y. Ho, and P.G. Klemens, Ed. *Thermophysical Properties of Matter Vol. 2, Thermal Conductivity: Nonmetallic Solids*, Plenum: New York, **1970**.

29. G.E. Childs, L.J. Ericks, and R.L. Powell, Eds., *Thermal Conductivity of Solids at Room Temperature and Below, A Review and Compilation of the Literature*, National Bureau of Standards Monograph 131, **1973**.

30. E. Hümmer, Th. Rettelbach, X. Lu, and J. Fricke, *Thermochim. Acta*, **1993**, *218*, 269-276.

31. M. Zakrzewski and M.A. White, *Phys. Rev. B*, **1992**, *45*, 2809-2817.

32. D. Michalski and M.A White, *J. Phys. Chem.*, **1995**, *99*, 3774-3780.

33. D. Michalski and M.A. White, *J. Chem. Phys.*, **1997**, *106(14)*, 6202-6203.

34. L.D. Landau and E.M. Lifshitz, *Statistical Physics*, Pergamon: London, **1969**.

35. H.M. Ledbetter, *J. Phys. D: Appl. Phys.* **1980**, *13*, 1879-1884.

36. M.J.M. Van Oort and M.A. White, *Rev. Sci. Instrum.*, **1987**, *58(7)*, 1239-1241.

37. J. Yang, "Theory of thermal conductivity" in *Thermal Conductivity*, T.M. Tritt, Ed.,

Kluwer Press, **2005**, in press.

38. www.mathisinstruments.com, last accessed 01/06/2005.

39. G.S. Nolas, J. Yang, and H.J. Goldsmid, "Semiconductors and thermoelectric materials" in *Thermal Conductivity*, T.M. Tritt, Ed., Kluwer Press, **2005**, in press.

40. D.G. Cahill, H.E. Fischer, T. Klitsner, E.T. Swartz, and R.O. Pohl, *J. Vac. Sci. Technol. A*, **1989**, *7(3)*, 1259-1266.

41. B. Yang and G. Chen, "Experimental studies on thermal conductivity of thin films and supperlattices" in *Thermal Conductivity*, T.M. Tritt, Ed., Kluwer Press, **2005**, in press.

42. D.G. Cahill, W.K. Ford, K.E. Goodson, G.D. Mahan, A. Majumdar, H.J. Maris, R. Merlin, and S.R. Phillpot, *J. Appl. Phys.*, **2003**, *93(2)*, 793-818.

43. T.M. Tritt and D. Weston, "Measurement techniques and considerations for determining thermal conductivity of bulk materials" in *Thermal Conductivity*, T.M. Tritt, Ed., Kluwer Press, **2005**, in press.

44. M.A. White, *J. Therm. Anal. Calor.*, **1999**, *57*, 765-771.

45. www.nist.gov, last accessed 01/06/2005.

46. O. Maldonado, *Cryogenics*, **1992,** *32(10)*, 908-912.

47. N.R. Dilley, R.C. Black, L. Montes, A. Wilson, and M.B. Simmonds, *Mat. Res. Soc. Symp. Proc.*, **2002**, *691*, 85-90.

48. D.V.S. Muthu, B. Chen, A.W. Sleight, J.M. Wrobel, and M.B. Kruger, *Solid State Commun.*, **2002,** *122(1-2)*, 25-28.

49. L. Ouyang, Y.-N. Xu, and W.Y. Ching, *Phys. Rev. B*, **2002**, *65(11)*, 113110/1-4.

50. Quantum Design, *PPMS Hardware and Options Manual*, 2nd Ed., 1999.

51. *CRC Handbook of Chemistry and Physics*, CRC Press Inc., Boca Raton.

52. www.qdusa.com/products/ppms.html last accessed 24/01/2005.

53. H. Preston-Thomas, *Metrologia*, **1990**, *27(1)*, 3-10.

54. R.L. Rusby, M. Durieux, A.L. Reesink, R.P. Hudson, G. Schuster, M. Kühne, W.E. Fogle, R.J. Soulen, and E.D. Adams, *J. Low Temp. Phys.*, **2002**, *126(1-2)*, 633-642.

55. American Society for Testing Materials, www.astm.org.

56. R.W. Powers, D. Schwartz, and H.L Johnston, *TR 264-265*, **1951**, reference in *Thermophysical Properties of Matter Vol. 1, Thermal Conductivity: Metallic Elements and Alloys*, Y.S. Touloukian, R.W. Powell, C.Y. Ho, and P.G. Klemens, Eds., Plenum: New York, **1970**.

57. M.A. White, "Thermal analysis and calorimetry" in *Physical Methods in Supramolecular Chemistry, Vol. 8*, J.E.D. Davies and J.A. Ripmeester, Eds., in *Comprehensive Supramolecular Chemistry*, J.-M. Lehn, J.L. Atwood, D.D. McNicol, J.E.D. Davies, and F. Vogtle, Eds., Elsevier Science Ltd.: Oxford, **1996.**

58. W.H. Brock, *The Norton History of Chemistry*, W.W. Norton & Company: New York **1993**.

59. S. Kopperl and J. Parascandola, *J. Chem. Educ.*, **1971**, *48(4)*, 237-242.

60. R.A. Marriott, *PhD dissertation: Thermodynamic stability studies of racemic and conglomerate enantiomeric crystals*, Dalhousie University, **2004.**

61. P.W.R. Bessonette and M.A. White, *J. Chem. Phys.*, **1999**, *110(8)*, 3919-3925.

62. D.C. Ginnings and G.T. Furukawa, *J. Am. Chem. Soc.*, **1953**, *75*, 522-527.

63. L. Qiu, *PhD dissertation: Thermal properties of framework materials: Selected zeolites, clathrates and an organic diol*, Dalhousie University, **2001.**

64. Unpublished results, M.A. White.

65. J.S. Hwang, K.J. Lin, and C. Tien, *Rev. Sci. Instrum.*, **1997**, *68(1)*, 94-101.

66. W. Schnelle, J. Engelhardt, and E. Gmelin, *Cryogenics*, **1999**, *39*, 271-275.

67. R.N. Goldberg and R.D. Weir, *Pure and Appl. Chem.*, **1992**, *64*, 1545-1562.

68. D.A. Ditmars, S. Ishihara, S.S. Chang, G. Bernstein, and E.D. West, *J. Res. Natl. Bur. Std.*, **1982**, *87*, 159-163.

69. R.Q. Fugate and C.A. Swenson, *J. Appl. Physics*, **1969**, *40*, 3034-3036.

70. D.G. Archer, *J. Phys. Chem. Ref. Data*, **1993**, *22(6)*, 1441-1453.

71. D.A. Ditmars and T.B. Douglas, *J. Res. Natl. Bur. Std. A*, **1971**, *75*, 401-420.

72. M. Sorai, K. Kaji, and Y. Kaneko, *J. Chem. Thermodyn.*, **1992**, *24*, 167-180.

73. R. Viswanathan, *J. Appl. Physics*, **1975**, *46*, 4086-4087.

74. G.K. White and M.L. Minges, *Int. J. of Thermophysics*, **1997**, *18*, 1269-1327.

75. R. Castanet, *High Temp.-High Pressures*, **1984**, *16*, 449-457.

76. J.C. Lashley, M.F. Hundley, A. Migliori, J.L. Sarrao, P.G. Pagliuso, T.W. Darling, M. Jaime, J.C. Cooley, W.L. Hults, L. Morales, D.J. Thoma, J.L. Smith, J. Boerio-Goates, B.F. Woodfield, G.R. Stewart, R.A. Fisher, and N.E. Phillips, *Cryogenics*, **2003**, *43*, 369-378.

77. D.G. Archer and D.R. Kirklin, *Thermochim. Acta*, **2000**, *347*, 21-30.

78. W.P. Reed, *National Institute of Standards and Technology, Report of investigation, RM 5*, Standard Reference Materials Program: Gaithersburg, **1992**. https://srmors.nist.gov/certificates/view_cert2gif.cfm?certificate=RM5 Last accessed 12/16/04.

79. D.W. Osborne, H.E. Flotow, and F. Schreiner, *Rev. Sci. Instrum.*, **1967**, *38*, 159-168.

80. G.T. Furukawa, W.G. Saba, and M.L. Reilly, *National Standard Reference Data Series, National Bureau of Standards 18*, U.S. Government Printing Office: Washington, D.C., **1968**.

81. B.-Z. Zhan, M.A. White, P. Fancy, C.A. Kennedy, and M. Lumsden, *Macromolecules*, **2004**, *37*, 2748-2753.

82. C.A. Kennedy, B.-Z. Zhan, and M.A. White, *J. Comp. Mater.*, **2005**, *39*, 193-198.

83. M.J.M. Van Oort and M.A. White, *Ber. Bunsenges. Phys. Chem.*, **1988**, *92(2)*, 168-176.

84. D.G. Rancourt, *Phys. in Canada*, **1989**, *45*, 3-10.

85. C.E. Guillaume, *Proc. Phys. Soc., London*, **1920**, *32*, 374-404.

86. C.N. Chu, N. Saka, and N.P. Suh, *Mater. Sci. Eng.*, **1987**, *95*, 303-308.

87. K. Scheel, *Verh. Dtsch. Phys. Ges.*, **1907**, *7*, 3-23.

88. K. Scheel, *Verh. Dtsch. Phys. Ges.*, **1907**, *7*, 719-721.

89. D.A. Fleming, D.W. Johnson Jr., and P.J. Lemaire, *Lucent Technologies Inc.*, U.S. Patent 5,694,503, **1998**.

90. Y. Morito, K. Takahashi, and T. Hashimoto, *Moritex Corporation*, U.S. Pat. Appl.

Publ., 20030218271, **2003**.

91. J.-C. Chen, G.-C. Huang, C. Hu, and J.-P. Weng, *Scripta Mater.*, **2003**, *49*, 261-266.

92. L.D. Noailles, H.-h. Peng, J. Starkovich, and B. Dunn, *Chem. Mater.* **2004**, *16(7)*, 1252-1259.

93. M. Kofteros, S. Rodriguez, V. Tandon, and L.E. Murr, *Scripta Mater.*, **2001**, *45* 369-374.

94. J. Graham, A.D. Wadsley, J.H. Weymouth, and L.S. Williams, *J. Am. Ceram. Soc.*, **1959**, *42(11)*, 570.

95. C. Martinek and F.A. Hummel, *J. Am. Ceram. Soc.*, **1968**, *51(4)*, 227-228.

96. N.L. Ross, "Framework structures" in *Reviews in Mineralogy and Geochemistry, Vol.41, High-Temperature and High-Pressure Crystal Chemistry*, R.M. Hazen and R.T. Downs, Eds., Mineralogical Society of America: Washington, **2000**.

97. H. Li, M. Eddaoudi, M. O'Keeffe, and O.M. Yaghi, *Nature*, **1999,** *402*, 276-279.

98. A.P. Giddy, M.T. Dove, G.S. Pawley, and V. Heine, *Acta Cryst. A*, **1993**, *49*, 697-703.

99. A.W. Sleight, *Annu. Rev. Mater. Sci.*, **1998**, *28*, 29-43.

100. L.L.Y. Chang, M.G. Scroger, and B. Phillips, *J. Am. Ceram. Soc.*, **1967**, *50(4)*, 211-215.

101. N. Duan, U. Kameswari, and A.W. Sleight, *J. Am. Chem. Soc.*, **1999**, *121(44)*, 10432-10433.

102. J.S.O. Evans, T.A. Mary, T. Vogt, M.A. Subramanian, and A.W. Sleight, *Chem. Mater.*, **1996**, *8(12)*, 2809-2823.

103. G. Ernst, C. Broholm, G.R. Kowach, and A.P. Ramirez, *Nature*, **1998**, *396*, 147-149.

104. J.S.O. Evans, W.I.F. David, and A.W. Sleight, *Acta. Cryst. B*, **1999**, *55*, 333-340.

105. K. Wang and R.R. Reeber, *Appl. Phys. Lett.*, **2000**, *76(16)*, 2203-2204.

106. (a) T.R. Ravindran, A.K. Arora, and T.A. Mary, *Phys. Rev. Lett.*, **2000**, *84(17)*, 3879-3882.
(b) T.R. Ravindran, A.K. Arora, and T.A. Mary, *Phys. Rev Lett.*, **2000**, *85(1)*, 225.
(c) S.L. Chaplot and R. Mittal, *Phys. Rev. Lett.*, **2001**, *86(21)*, 4976.
(d) T.R. Ravindran and A.K. Arora, *Phys. Rev. Lett.*, **2001**, *86(21)*, 4977.

107. R. Mittal, S.L. Chaplot, H. Schober, and T.A. Mary, *Phys. Rev. Lett.*, **2001**, *86(20)*, 4692-4695.

108. Y. Yamamura, N. Nakajima, T. Tsuji, M. Koyano, Y. Iwasa, S. Katayama, K. Saito, and M. Sorai, *Phys. Rev. B*, **2002**, *66(1)*, 014301/1-9.

109. T.R. Ravindran, A.K. Arora, and T.A. Mary, *Phys. Rev. B*, **2003**, *67*, 064301/1-4.

110. F.R. Drymiotis, H. Ledbetter, J.B. Betts, T. Kimura, J.C. Lashley, A. Migliori, A.P. Ramirez, G.R. Kowach, and J. Van Duijn, *Phys. Rev. Lett.*, **2004**, *93(2)*, 025502/1-4.

111. A.P. Ramirez and G.R. Kowach, *Phys. Rev. Lett.*, **1998**, *80(22)*, 4903-4906.

112. Y. Yamamura, N. Nakajima, and T. Tsuji, *Solid State Commun.*, **2000**, *114(9)*, 453-455.

113. Y. Yamamura, N. Nakajima, and T. Tsuji, *Phys. Rev. B*, **2001**, *64*, 184109/1-5.

114. Y. Yamamura, N. Nakajima, T. Tsuji, Y. Iwasa, K. Saito, and M. Sorai, *Solid State Commun.*, **2002**, *121(4)*, 213-217.

115. J. Boerio-Goates, R. Stevens, B. Lang, and B.F. Woodfield, *J. Therm. Anal. Calor.*, **2002**, *69*, 773-783.

116. R. Stevens, J. Linford, B.F. Woodfield, J.Boerio-Goates, C. Lind, A.P. Wilkinson, and G. Kowach, *J. Chem. Thermodyn.*, **2003**, *35*, 919-937.

117. Y. Yamamura, T. Tsuji, K. Saito, and M. Sorai, *J. Chem. Thermodyn.*, **2004**, *36*, 525-531.

118. T. Hashimoto, J. Kuwahara, T. Yoshida, M. Nashimoto, Y. Takahashi, K. Takahashi, and Y. Morito, *Solid State Commun.*, **2004**, *131*, 217-221.

119. J.S.O. Evans, J.D. Jorgensen, S. Short, W.I.F. David, R.M. Ibberson, and A.W. Sleight, *Phys. Rev. B*, **1999**, *60(21)*, 14643-14648.

120. J.S.O. Evans, Z. Hu, J.D. Jorgensen, D.N. Argyriou, S. Short, and A.W. Sleight, *Science*, **1997**, *275*, 61-65.

121. J.D. Jorgensen, Z. Hu, S. Teslic, D.N. Argyriou, S. Short, J.S.O. Evans, and A. W. Sleight, *Phys. Rev. B*, **1999**, *59(1)*, 215-225.

122. J.M. Gallardo-Amores, U. Amador, E. Morán, and M.Á. Alario-Franco, *Int. J. Inorg. Mater.*, **2000**, *2*, 123-129.

123. Z. Hu, J.D. Jorgensen, S. Teslic, S. Short, D.N. Argyriou, J.S.O. Evans, and A.W. Sleight, *Physica B*, **1998**, *241-243*, 370-372.

124. R. Mittal and S.L. Chaplot, *Solid State Commun.*, **2000**, *115*, 319-322.

125. C.A. Perottoni and J.A.H. da Jornada, *Science*, **1998**, *280*, 886-889.

126. A. Grzechnik, W.A. Crichton, K. Syassen, P.Adler, and M. Mezouar, *Chem. Mater.*, **2001**, *13*, 4255-4259.

127. J.S.O. Evans, *J. Chem. Soc., Dalton Trans.*, **1999**, *19*, 3317-3326.

128. J.S.O. Evans, T.A. Mary, and A.W. Sleight, *Physica B*, **1998**, *241-243*, 311-316.

129. A.K.A. Pryde, K.D. Hammonds, M.T. Dove, V. Heine, J.D. Gale, and M.C. Warren, *J. Phys.: Condens. Matter*, **1996**, *8(50)*, 10973-10982.

130. D. Cao, F. Bridges, G.R. Kowach, and A.P. Ramirez, *Phys. Rev. Lett.*, **2002**, *89(21)*, 215902/1-4.

131. D. Cao, F. Bridges, G.R. Kowach, and A.P. Ramirez, *Phys. Rev. B*, **2003**, *68*, 14303/1-14.

132. J.Z. Tao and A.W. Sleight, *J. Solid State Chem.*, **2003**, *173*, 442-448.

133. M.T. Dove, K.O. Trachenko, and M.G. Tucker, *Rev. Mineral Geochem.*, **2000**, *39*, 1-33.

134. M.T. Dove, A.P. Giddy, and V. Heine, *Trans. Am. Crystallogr. Assoc.*, **1991**, *27*, 65-75.

135. M.T. Dove, M. Gambhir, and V. Heine, *Phys. Chem. Minerals*, **1999**, *26(4)*, 344-353.

136. M.T. Dove, V. Heine, and K.D. Hammonds, *Mineral. Mag.*, **1995**, *59*, 629-639.

137. K.D. Hammonds, M.T. Dove, A.P. Giddy, V. Heine, and B. Winkler, *Am. Mineral.*, **1996**, *81*, 1057-1079.

138. T.H.K. Barron, J.F. Collins, T.W. Smith, and G.K. White, *J. Phys. C: Solid State Phys.*, **1982**, *15(20)*, 4311-4326.

139. M.T. Dove, *Am. Mineral.*, **1997**, *82(3-4)*, 213-244.

140. K.D. Hammonds, H. Deng, V. Heine, and M.T. Dove, *Phys. Rev Lett.*, **1997**, *78(19)*, 3701-3704.

141. K.D. Hammonds, M.T. Dove, A.P. Giddy, and V. Heine, *Am. Mineral.*, **1994**, *79(11-12)*, 1207-1209.

142. J.S.O. Evans, T.A. Mary, and A.W. Sleight, *J. Solid State Chem.*, **1997**, *133*, 580-583.

143. J. N. Hancock, C. Turpen, Z. Schlesinger, G.R. Kowach, and A.P. Ramirez, *Phys. Rev. Lett.* **2004**, *93*, 225501/1-4.

144. W.I.F. David, J.S.O. Evans, and A.W. Sleight, *Europhys. Lett.*, **1999**, *46(5)*, 661-666.

145. R. Mittal and S.L. Chaplot, *Phys. Rev. B*, **1999**, *60(10)*, 7234-7237.

146. T. Hashimoto, T. Katsube, and Y. Morito, *Solid State Commun.*, **2000**, *116*, 129-132.

147. T. Hashimoto and Y. Morito, *J. Ceram. Soc. Jpn*, **2002**, *110(9)*, 823-825.

148. J.G. Collins, S.J. Collocott, and G.K. White, *Aust. J. Phys.*, **1985**, *38(4)*, 617-622.

149. M.V. Nevitt, Y. Fang, and S.-K. Chan, *J. Am. Ceram. Soc.*, **1990**, *73(8)*, 2502-2504.

150. M.W. Chase Jr., *J. Phys. Chem. Ref. Data Monograph 9*, **1998**, 1-1951.

151. E.G. King, W.W. Weller, and A.U. Christensen, *U.S. Depart. of the Int., Bur. of Mines*, **1960**, 1-29.

152. F.R. Sale, *Thermochim. Acta*, **1979**, *30(1-2)*, 163-171.

153. H. Seltz, F.J. Dunkerley, and B.J. DeWitt, *J. Am. Chem. Soc.*, **1943**, *65*, 600-602.

154. C. Lind, *PhD dissertation: Negative thermal expansion materials related to cubic zirconium tungstate*, Georgia Institute of Technology, **2001**.

155. A.D. Mah, *J. Am. Chem. Soc.*, **1959**, *81*, 1582-1583.

156. T.R Ravindan, A.K. Arora, and T.A. Mary, *J. Phys.: Condens. Matter*, **2001**, *13(50)*, 11573-11588.

157. Y. Takahashi, *Int. J. Thermophys.*, **1984**, 5(1), 41-52.

158. C.A. Kennedy and M.A. White, *Solid State Commun.*, **2005**, *134*, 271-276.

159. K.W. Schlichting, N.P. Padture, and P.G. Klemens, *J. Mater. Sci.*, **2001**, *36*, 3003-3010.

160. R.L. Jones in *Metallurgical and Ceramic Coatings*, K.H. Stern, Ed., Chapman & Hall: London, **1996**.

161. G.A. Slack, *J. Phys. Chem. Solids*, **1973**, *34*, 321-335.

162. St. Burghartz and B. Schulz, *J. Nuclear Mater.*, **1994**, *212-215*, 1065-1068.

163. N.P. Padture and P.G. Klemens, *J. Am. Ceram. Soc.*, **1997**, *80*, 1018-1020.

164. R. Stevens, "Engineering properties of zirconia" in *Engineered Materials Handbook, Vol. 4*, S.J. Schneider and C.A. Dostal, Eds., ASM Int.: Metals Park, **1991**.

165. D.P.H. Hasselman, L.F. Johnson, L.D. Bentsen, R. Syed, H.L. Lee, and M.V. Swain, *Am. Ceram. Soc. Bull.*, **1987**, *66*, 799-806.

166. R. Sreekumar, J. Isaac, J. Philip, K.V. Paulose, M.T. Sebastian, and A.D. Damodaran, *Physica Status Solidi*, **1992**, *133*, 341-347.

167. V.V. Murashov and M.A. White, *J. Mater. Sci.*, **2000**, *35*, 649-653.

168. P.G. Klemens, *High Temps. -High Press.*, **1991**, *23*, 241-248.

169. K.W. Schlichting, N.P. Padture, and P.G. Klemens, *J. Mater. Sci.*, **2001**, *36*, 3003-3010.

170. T. Baba and A. Ono, *Meas. Sci. Technol.*, **2001**, *12*, 2046-2057.

171. J.S. Tse and M.A. White, *J. Phys. Chem.*, **1988**, *92*, 5006-5011.

172. G.A. Slack, "New materials and performance limits for thermoelectric cooling" in *CRC Handbook of Thermoelectrics*, Ed. D.M. Rowe, CRC Press Inc.: Boca Raton, **1995**.

173. B. Sales, B.C. Chakoumakos, R. Jin, J.R. Thompson, and D. Mandrus, *Phys. Rev. B*, **2001**, *63*, 245113/1-8.

174. R. Berman, *Proc. Phys. Soc. A*, **1952**, *65*, 1029-1040.

175. G.A. Slack, S.B. Austerman, *J. App. Phys.*, **1971**, *42*, 4713-4717.

176. M.A. White, C. Meingast, W.I.F. David, and T. Matsuo, *Solid State Commun.*, **1995**, *94*, 481-484.

177. S.N. Achary, G.D. Mukherjee, A.K. Tyagi, and B.K. Godwal, *Phys. Rev. B*, **2002**, *66(18)*, 184106/1-5.

178. C. Lind, A.P. Wilkinson, Z. Hu, S. Short, and J.D. Jorgensen, *Chem. Mater.*, **1998**, *10*, 2335-2337.

179. M. Auray, M. Quarton, and P. Tarte, *Powder Diffraction*, **1987**, *2(1)*, 36-38.

180. C. Lind, D.G. VanDerveer, A.P. Wilkinson, J. Chen, M.T. Vaughan, and D.J. Weidner, *Chem. Mater.*, **2001**, *13*, 487-490.

181. S.N. Achary, G.D. Mukherjee, A.K. Tyagi, and B.K. Godwal, *Powder Diffraction*, **2003**, *18(2)*, 147-149.

182. S.R. Bharadwaj, M.S. Samant, R. Mishra, S.R. Dharwadkar, S.S. Savant, and R. Kalyanaraman, *J. Alloy Comp.*, **1995**, *230(1)*, 13-15.

183. R. Pankajavalli and O.M. Sreedharan, *J. Nucl. Mater.*, **1990**, *175(3)* 194-196.

184. Z. Singh, S. Dash, R. Prasad, and V. Venugopal, *J. Alloy Comp.*, **1996**, *244*, 85-89.

185. M.S. Samant, S.R. Bharadwaj, A.S. Kerkar, and S.R. Dharwadkar, *J. Nucl. Mater.*, **1993**, *207*, 98-102.

186. R.D. Shannon, *Acta Cryst. A*, **1976**, *32*, 751-767.

187. Private communication with Profs. Y. Yamamura and M. Sorai, January, 2005.

188. B.J. Wood, "Crystal field electronic effects on the thermodynamic properties of Fe^{2+} minerals" in *Advances in physical geochemistry Vol. 1, Thermodynamics of minerals and melts*, R.C. Newton, A. Navrotsky, and B.J. Wood, Eds., Springer-Verlag: New York, **1981**.

189. B.F. Woodfield, J. Boerio-Goates, J.L. Shapiro, R.L. Putnam, and A. Navrotsky, *J. Chem. Thermodyn.*, **1999**, *31*, 245-253.

190. L. Qiu and M.A. White, *J. Chem. Educ.*, **2001**, *78(8)*, 1076-1079.

191. R. Stevens, B.F. Woodfield, J. Boerio-Goates, and M. Crawford, *J. Chem. Thermodyn.*, **2004**, *36*, 349-357.

192. S.S. Todd, *J. Am. Chem. Soc.*, **1953**, *75*, 3035-3036.

193. E.F. Westrum Jr., B.H. Justice, J.A. Sommers, and D.A. Johnson, *J. Therm. Anal. Calor.*, **1999**, *57*, 659-667.

194. Private communication with Prof. J. Boerio-Goates, January 2005.

195. E.J. Huber, Jr. and C.E. Holley, Jr., *J. Chem. Engin. Data*, **1968**, *13*, 252-253.

196. A. L. Pope and Terry M. Tritt, "Thermal Conductivity of Quasicrystalline Materials" in *Thermal conductivity*, T.M. Tritt, Ed., Kluwer Press, **2005**, in press.

197. G.S. Nolas, J.-M. Ward, J. Gryko, L. Qiu, and M. A. White, *Phys. Rev. B*, **2001**, *64*, 153201/1-3.

198. G.R. Kowach, *J. Cryst. Growth*, **2000**, *212*, 167-172.